BEHAVIOUR OF DISCONTINUOUS PRECAST CONCRETE BEAM-COLUMN CONNECTIONS

by

Sarakot Asaad Hasan

Thesis submitted to the University of Nottingham for the degree of Doctor of Philosophy

Department of Civil Engineering

October 2011

ABSTRACT

The study investigates experimentally and theoretically the behaviour of an internal precast concrete beam-column connection, where both the column and beam are discontinuous in construction terms. The aim was to modify the behaviour mechanisms within the connection zone by introducing a beam hogging moment resistance capacity under dead loads and limiting the damage within the connection. This is to offer permanent dead load hogging moments that could counterbalance any temporary sagging moment generated under sway loads, enhance the rotational stiffness, balance the design requirements for the beam-end and beam mid-span moments, provide efficient continuity across the column, and reduce the deflection at the beam mid-span.

Three full-scale beam-column connection tests subjected to gravity loads were conducted taking the connection reinforcement detail as the main variable. The configuration of the three main interfaces within the connection was based on the experimental results of small-scale tests. The results of the full-scale tests showed that, by using the strong connection concept, it was possible to produce equivalent monolithic behaviour, control the crack width within the connection zone, and force the final damage to occur outside of this zone, which comprises the interfaces and parts of the adjoining elements. The strong connection consisted of using additional short steel bars crossing the connection at the top of the beam, horizontal U-shaped links at the beam-ends, and additional column links.

In addition, the experimental programme included two full-scale tests to investigate the behaviour of the connection under sway loads using two different connection reinforcement details. The results of this study showed that the proposed modification in the reinforcement details was able to mobilise the beam sagging moment through the dowel action of the column main bars but it was also accompanied by large relative beam-column rotations (low rotational stiffness).

The evaluation of the behaviour of the connections was carried out by incorporating the experimental rotational stiffnesses in semi-rigid frame analyses using the ANSYS software package and a Visual Basic program based on the conventional semi-rigid analysis approach. In addition, a simplified technique has been validated against these two methods to replicate the semi-rigid behaviour. In the same respect, the study is proposing a new approach for classifying precast concrete beam-column connections as rigid by relating the connection fixity factor with the moment redistribution. It has been shown that the connection could be classified as rigid if the fixity factor is not less than 0.73 and the available moment redistribution from the mid-span to the supports is not less than the required moment redistribution resulting from semi-rigid frame analysis.

In the theoretical part, an analytical tool has been calibrated to predict the rotational stiffness of the specimens with semi-rigid behaviour under gravity loads. The model showed a reasonable agreement with the experimental results. To help the modelling, two pull-out tests were conducted to determine the bond-slip relation of steel bars embedded in cement-based grout. Moreover, a finite element numerical simulation model using the ANSYS software package was carried out to replicate the experimental results of the semi-rigid specimens tested under gravity loads. In spite of providing results close to experimental values prior to yielding, the FE model was not able to predict the failure mode and consequently the correct ultimate load. This is due to the simplified way of modelling the interaction between the corrugated sleeves and the surrounding concrete as perfect bond.

The research concludes that the precast beam-column connection investigated in the current study can be treated as an emulative monolithic connection under gravity loads through using the strong connection concept; however, it is not suitable to resist beam net sagging moments. Besides, the study concludes that to consider a precast concrete beam-column connection as rigid, it is required to correlate the fixity factor with the moment redistribution.

PUBLICATIONS

Hasan, S.A., Elliott, K.S. , Ferreira, M.A. 2011, 'An Experimental Investigation on the Moment Continuity of Precast Concrete Beam-Column Connections under Gravity Loads', *Proceedings of fib Symposium, Concrete Engineering for Excellence and Efficiency*, Prague.

Hasan, S.A., Ferreira, M.A., Elliott, K.S. 2011, 'A Theoretical Investigation on the Moment Continuity of Precast Concrete Beam-Column Connections under Gravity Loads', *Proceedings of fib Symposium, Concrete Engineering for Excellence and Efficiency*, Prague.

ACKNOWLEDGMENT

I would like to express my deep thanks to my supervisors Dr Kim S. Elliott, Dr. Marcelo Ferreira and Professor Carlo Sansour for their knowledge, guidance and support during my time as a research student at the University of Nottingham. I should mention the special role of my principal supervisor Dr. Elliott who kept his commitment towards the research and continued to offer his kind help and advice even after his retirement, for which I'm indebted.

I greatly appreciate the Civil Engineering Laboratory technical staff: Mr. Nigel Rook; Mr. Bal Loyla; and Mr. Michael Jones at Nottingham University for their assistance throughout the experimental work.

I am also very grateful to extend my sincere thanks to Ministry of Higher Education- Iraq and Technical College-Erbil for their sponsorship and granted study for which I am very grateful.

Finally, I would like to thank my parents for their blessing, encouragement during the period of study, to my wife Zinah, and my children Lana, Sarwar and Huda for the patience, understanding and love throughout our stay in England, which without their support these accomplishments would not have been possible.

DECLARATION

I declare that, unless otherwise cited in the texts, the contents of this thesis are the results of my own work conducted at the University of Nottingham, Department of Civil Engineering between January 2008 and July 2011. No part of this thesis has been submitted to any other University or other educational institution for a Degree, Diploma or other qualifications.

Sarakot Asaad Hasan

TABLE OF CONTENTS

CHAPTER 3
BIAXIAL LOADING TEST RESULTS AND DISCUSSION

CHAPTER 4
FULL-SCALE TEST PROGRAM

CHAPTER 5
FULL-SCALE TEST RESULTS AND DISCUSSIONS : GRAVITY LOADS

CHAPTER 6
FULL-SCALE TEST RESULTS AND DISCUSSIONS : SWAY LOADS

CHAPTER 7
FINITE ELEMENT MODELLING

CHAPTER 8
ANALYSIS AND DESIGN CONSIDERATIONS

CHAPTER 9
CONCLUSIONS AND RECOMMENDATIONS

APPENDICES

LIST OF FIGURES

CHAPTER 4

CHAPTER 5

LIST OF TABLES

ACRONYMS/ ABBREVIATIONS

ABNT	Brazilian association for technical standards
ACI	American Concrete Institute
AISC	American Institution of Steel Construction
ANSYS	FE software package
BSi	British Standard institute
Cal	Calculated
CEB	Comité Euro-international du Betón (European-international committee of concrete)
CEN	Comité Européen de Normalisation (European committee for standardization)
CERIB	Concrete industry study and research centre, France
CR	Centre of Rotation
EC0	Eurocode 0, EN 1990
EC1	Eurocode 1, EN 1991
EC2	Eurocode 2, EN 1992
EC3	Eurocode 3, EN 1993
Exp	Experimental
FE	Finite Element
fib	fédération internationale du béton (International federation for structural concrete)
GR	GRavity
ICBO	International Conference of Building Officials
LT	Left Top beam-column interface
LB	Left Bottom beam-column interface
M-θ	Moment-rotation
NBR	Norma Brasileira Registrada (Brazilian standard specification)
PCI	Precast/Prestressed Concrete Institute
POT	Linear voltage displacement potentiometer
RB	Right Bottom beam-column interface
RT	Right Top beam-column interface
SG	Electrical resistance strain gauges
SW	SWay
UBC	Uniform Building Code
UDL	Uniformly Distributed Load
1D	One Dimension
3D	Three Dimension

SYMBOLS

Δ1	Beam deflection due to flexure deformation of beam
Δ2	Beam deflection due to rotation in connection
Δ_c	Calculated deflection
Δ_e	Experimentally measured deflection
α	Efficiency factor of jointed precast column
α_t	Factor relates τ_{max} with τ_a
γ	Fixity factor
δ	Deflection
δ_c	Compressive deformation
δ_S	Modified mid-span deflection due to semi-rigid effects
δm	Ratio of maintaining moment after redistribution (in EC2, it is called δ)
δm_a	Avaliable δm

δm_r	Required δm for semi-rigid connections
θ	Relative beam-column rotation (connection rotation)
θ_e	Beam end-rotation due to unit end-moment
θ_t	Total beam end rotation
θ_{cr}	Relative beam-column rotation at apperance of 1st crack
θ_{se}	Relative beam-column relative rotation at service load
θ_y	Relative beam-column relative rotation at yield load
θ_u	Relative beam-column rotation at ultimate state
θ_R	End rotation of simply supported beam under UDL (θ_R=W L^3 / 24 EI)
θ_E	Modified beam-end rotation due to semi-rigid effects
θ_{LT}	Relative beam-column rotation at left top interface
θ_{LB}	Relative beam-column rotation at left botom interface
θ_{RT}	Relative beam-column rotation at right top interface
θ_{RB}	Relative beam-column rotation at right bottom interface
ε	Strain
ε_{cr}	Strain at cracking moment in concrete/steel
ε_y	Strain at yield moment in concrete/steel
ε_c	Concrete compression strain
ε_{cu2}	Ultimate compressive strain in concrete
ε_s	Steel strain
ε_{sy}	Steel yielding strain
ρ	Reinforcement ratio of longitudinal tension reinforcement ($\rho = A_s / (b . d)$)
σ	Stress
σ_s	Steel stress
σ_u	Ultimate stress
σ_Y	Yielding stress
τ	Bond stress
τ_{max}	Maximum local bond stress
τ_a	Average/nominal bond stress
τ_f	Residual bond stress at faliure
Ø	Bar diameter
a	Minimum dimension of column
b	Beam width
b_c	Column width
d	Effective depth of main tension reinforcement
c_1,.., c_6	Modification factors in semi-rigid stiffness matrices
f	Compressive strength of concrete
f_c	Cylinder compressive strength of concrete
f_{cd}	Design value of concrete compressive strength
f_{ck}	Characteristic compressive cylinder concrete strength at 28 days
f_{cm}	Mean value of compressive strength f_c at an age of 28 days
$f_{c,max}$	Compressive strength of concrete at stronger side of dowel bar
$f_{c,min}$	Compressive strength of concrete at weakest side of dowel bar
f_{ct}	Axial direct tensile strength of concrete
$f_{ct,fl}$	Flexural tensile strength of concrete
f_{ctm}	Mean axial direct tensile strength of concrete
f_{cu}	Cube concrete/grout compressive strength
f_j	load-bearing capacity of a system of precast concrete column with mortar joint
f_m	Compressive strength of mortar

f_p	Compressive strength of precast concrete column
f_y	Yield strength of reinforcement
f_u	Ultimate strength of reinforcement
h	Overall depth of beam
h_c	Column depth
k	Ratio of column compressive strength to mortar compressive strength (f_p / f_m)
l_a	Embedded length of steel bar
l_p, l_d	Beam-end length that represents a part from connection zone.
l_e	Available anchorage length within column
l_t	Transmission bond length
n	Number of main bars surounded by stirrups
r	Ratio of column depth to mortar joint thickness (h_c/t)
t	Mortar joint thickness
u	displacement
w	Crack width
x	Distance from the compression side to the neutral axis of the transformed section (including the reinforcement)
x_I	x for uncracked section
x_{II}	x for fully cracked section
x_{III}	x at ultimate stage
x_d	x at column dowel bars yielding
x_u	x at ultimate state
xr	Distnace from a beam section where M/EI is calculated to the location of calcuating deflection based on moment-area theorem
y	Distance from neutral axis to location of measuring beam strain
y_t	Distance from neutral axis to extreme fibre in tension side of beam

A_s,A_{s1}	Area of tension reinforcement
A_{s2}	Area of compression reinforcement
A_{st}	Area of transvese reinforcement
C	Concrete cover
C_{clear}	Clear distance between steel bar ribs
E	Modulus of elasticity
E_b	Elastic modulus of beam
E_c	Elastic modulus of concrete
E_{col}	Elastic modulus of column
E_s	Elastic modulus of steel reinforcement
F_c	Resulted compressive force at compression zone of beam under flexure
F_t	Tension force in steel bars
F_x	Member end axial force
F_y	Member end shear force
F_{VR}	Yield shear strength of steel bar under dowel action
I	Second moment of area
I_I	Second moment of area of uncracked section (including the reinforcement)
I_{II}	Second moment of area of fully cracked section (including the reinforcement)
I_{eff}	Effective concrete's second moment of area
I_s	Assigned second moment of area to stubs in the simplified semi-rigid analysis
K	Sriffness matrix
L	Span length
Ls	Stub length

Lr	Reference beam length in Bjorhovde classification system
M	Bending moment
M_b	Beam bending moment at column face
M_{b1}	M_b of beam 1
M_{b2}	M_b of beam 2
M_c	Column bending moment at beam face
M_{c1}	M_c of top colum
M_{con}	Beam-column design moment resistance
M_{cr}	Cracking bending moment
M_E	Modified beam-end moment due to semi-rigid effects
M_S	Modified mid-span moment due to semi-rigid effects
M_F	Fixed end moment
M_u	Ultimate bending moment
M_y	Yield bending moment
M_{yd}	Beam sagging moment capacity contolled by yielding of column dowel bars
M_{se}	Service end-moment
M_{po}	Potential fixed end moment of member taken to have rigid ends
P	Applied load
R	Load reaction
Rm	Moment redistribution
Rm_a	Available moment redistribution
Rm_r	Required moment redistribution for semi-rigid connections
S	Beam-column rotational stiffness
S_{in}	Initial beam-column rotational stiffness
S_{cr}	Secant beam-column rotational stiffness prior to cracking
S_{se}	Secant beam-column rotational stiffness at service stage
S_y	Secant beam-column rotational stiffness at point of yielding of reinforcement
S_u	Secant beam-column rotational stiffness at ultimate moment
S_E	Secant stiffness due to semi-rigid effects
Sb	Bond slip
Sb_{end}	Bond slip at active steel bar end
Sd_{max}	Shear displacement of dowel bars at ultimate shear capacity
U_x	End displacements in x-direction at each member end (i,j)
U_y	End displacements in y-direction at each member end (i,j)
V	Conjugated beam-end shear
Vt	Volt
W	Uniformly distributed load
Y	Angle of rotation due to relative dispacements of member-ends
Z	Beam section lever arm
Z_I	Beam section lever arm for uncracked beam section
Z_{II}	Beam section lever arm at yielding stage
Z_{III}	Beam section lever arm at ultimate stage
Z_d	Beam section lever arm at column dowel bars yielding

* The FE symbols will be introduced within Chapter 7

CHAPTER 1
INTRODUCTION

1.1 Introduction

In the construction industry, the challenge is always about the speed and cost of the performance. Precast concrete, as a construction method, ensures high quality control, and durable, fast and economic buildings compared with cast in situ construction; therefore, it is widely used as a proper alternative to the latter.

The efficiency of precast concrete structures in resisting gravity or lateral loads relies on the behaviour of jointing systems including beam-column connections. The connection configuration and response including strength, rotational stiffness and ductility affect building frames in several ways. For instance, under gravity loads, the beam-column connection response affects mostly the behaviour of adjoining beams, while under lateral loads it affects the moment-distribution and the global stability (2^{nd} order effects).

Beam-column connections should be designed to transfer all types of forces: compression, tension, shear, bending and torsion. This could be achieved by ensuring a proper assemblage of joined members, and adequate continuity of the reinforcement. However, this goal is not easy because the design should take into account the simplicity and the practice of making the connections. Therefore, it is essential to consider both requirements of structural performance and buildability within the design of connections.

Among the connection types used in practice, the discontinuous (in construction terms only) precast concrete beam-column connection has been used in the precast concrete industry for many years in braced systems (Figure 1.1). This connection

configuration is also called '*beam to column head connection'* according to *fib* (2011). It has advantages over other jointing methods as it is simple, needs no corbels, bolting or welding, and is efficient in providing reasonable continuity between adjoining elements. However, it still requires a generous tolerance for construction, which is related mainly to the process of housing the dowel bars protruding from the bottom column in preformed sleeves in the beam and top column, which could reach ±12.5 mm according to ACI (2008b).

Figure 1.1 Discontinuous beam-column connection used in a braced frame car park project – Preconco Ltd., Barbados, 2010

1.2 Problem statement

Despite the use of the discontinuous precast concrete beam-column connection in practice, no design rules or guides were found within the available sources. In addition, the connection configuration used in practice (see the car park building in Figure 1.1, for example) does not offer any beam-end negative (hogging) moment resistance capabilities for dead loads. This is because the continuity bars at the top of the beam are provided later within the topping concrete, meaning that the moment continuity is only active for imposed loads (*fib*, 2011), even though, in most cases, this feature is not considered in the design and the beam-ends are treated as pinned connections.

Also, in the practical detail (Figure 1.1), the gap between the beams is too narrow for the infill grout to be structural, and therefore the load transfer in compression will be forced to pass through the dowels in the head of the lower column, something for which it is not designed.

Based on the above-mentioned observations, there is scope to modify the discontinuous beam-column connection behaviour and to establish main design principles. The modifications in the connection configuration include (Figure 1.2):

- locating the continuity top bars within the precast concrete beams and casting the trough before constructing the slab. This is to provide beam-end hogging moment resistance capacity under dead loads, which counterbalances reversals of positive (sagging) moment generated under sway loads;
- using a new connection reinforcement detail under gravity loads to strengthen the connection, limit the crack width within the connection zone and move the final damage to a point outside the connection zones. The new reinforcement detail also includes bending the beam bottom bars around the column dowel bars to mobilise beam-end sagging moments under sway loads;
- grouting the vertical joint between the beams to provide a direct path to transfer the compressive stress in the beam.

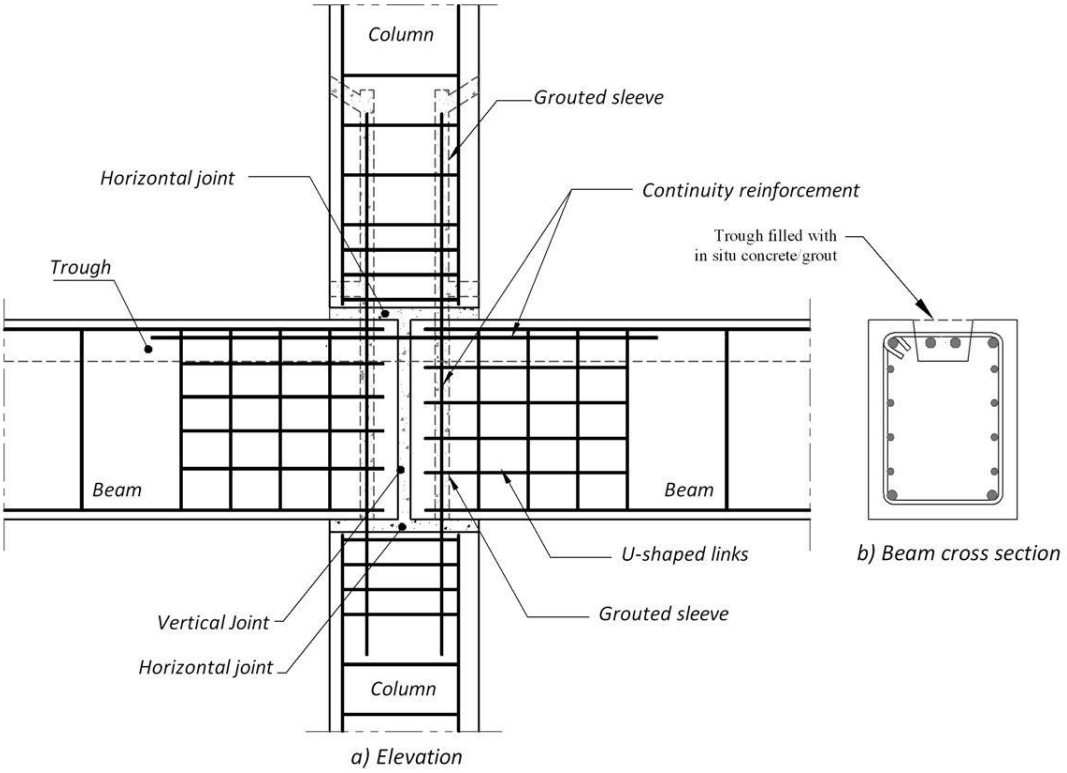

Figure 1.2 Proposed discontinuous beam-column connection configuration

1.3 Hypotheses

The hypotheses of the current study with respect to the discontinuous beam-column connection are: (i) the full beam-end hogging moment capacity can be mobilised as a result of providing continuity in the beam top reinforcement and altering the reinforcement details; (ii) the interaction between the beam bottom bars and the column bars provides the dowel action mechanism required to mobilise the beam-end sagging moment.

1.4 Aims and objectives

The aims of the current study are to:

- determine the effects of connection reinforcement details on the moment continuity across the connection;
- develop the basis for establishing main design principles for the connection type investigated in the current study.

In order to achieve the aims of the study, the following objectives are set.

- To determine experimentally the thickness and status of the joints within the connection needed to be used in the full-scale tests.
- To determine experimentally the effects of using different reinforcement details for the connection on the moment-rotation response (M-θ), crack propagation, crack width and the failure mode under separate gravity and sway loadings.
- To implement M-θ data in frame analyses to show the effects of the connection flexibility on the moment distribution and the sway.
- To calibrate simplified semi-rigid frame analyses that incorporate the effects of the flexibility of the beam-column connections.
- To establish a new approach for classifying precast concrete beam-column connections as rigid.
- To use the finite element modelling tool to replicate the experimental response of the connection.

1.5 Research methodology

For a reliable assessment of the behaviour of precast concrete beam-column connections, laboratory testing is recommended due to the complexity of the involved details (Catoia et al, 2008; Elliott et al, 1998; Loo and Yao, 1995) and to ensure that the connection has the necessary non-linear response characteristics (Ghosh et al, 1997). These complexities include: many contact regions of concrete-to-grout and steel bars-to-grout, possible irregularity in contact conditions, and construction initial imperfections, all of which restrict performing a straightforward analytical simulation for the connection. Therefore, before any attempt to develop analytical solutions for connections, experimental validation is required (Elliott et al, 2003b).

In this respect, the structural behaviour of the discontinuous beam-column connection will be examined by a mix of experimental and analytical methods using the following steps.

- Conducting preliminary small-scale biaxial loading tests to assess the ability of the connection to transfer axial loads with/without joint infill.
- Conducting full-scale beam-column connection tests subjected to separate gravity and sway loads taking the connection reinforcement detail as the main parameter.
- Performing semi-rigid frame analyses to find out the effects of the flexibility of the discontinuous beam-column connection in real frames.
- Modelling the semi-rigid behaviour of the connections tested under gravity loads using analytical and finite element modelling.

1.6 Limitations of the study

The investigation has been carried out by examining a full-scale beam-column using dimensions, reinforcement and beam and column loads resulting from a rigid frame analysis of a four-storey prototype building. The study moved towards modifying the connection to justify its use. Based on that, there are certain limitations in this study:

- the reported results are with respect to certain column and beam sizes and column axial load;
- the reported results are with respect to a certain range of concrete, grout and steel bar strength;
- in spite of using different continuity reinforcement within the connections whilst aiming to improve the behaviour, no attempts were made to investigate a wider range of reinforcement ratios;

- the rotational stiffnesses reported in the current study are with respect to the discontinuous precast concrete beam-column connection type investigated in the current study.

1.7 Behaviour of precast concrete beam-column connections

As connections in precast concrete construction are considered as the most critical locations in building frames, proper attention needs to be taken in designing them. CEB-FIP Model Code 1990 (1993) stated that, to ensure the performance of the precast concrete connections, the joints are required to:

1- accommodate the relative displacement required to mobilise the resistance of the joint;

2- resist all the action effects resulting from the analysis of the structure as a whole and from the analysis of the individual members;

3- secure robust and stable behaviour of the structure through the strength and deformability of the joints;

4- take into consideration the anticipated required tolerances during manufacture and erection.

1.7.1 Elementary behaviour

In ordinary frame analysis, beam-column connections are designed either as nominally pinned (free to rotate with no moment capacity) or fixed (zero rotation with definite moment capacity). This assumption does not match the actual practice even in monolithic construction, where there is a limited beam-column relative rotation (Baharuddin et al, 2008; Ferreira, 1999) that is not considered as a result of incomplete knowledge about moment-rotation behaviour or not having the required modelling tools.

In precast concrete construction, the beam-column connection could be categorised into simple (pinned) connections, which transmit purely shear forces, and moment resisting connections, which mobilise moments in addition to the shear. For design convenience, precast concrete connections are strictly dealt with as either pinned or fixed, in spite of the majority of the connections behave in a semi-rigid manner (Elliott et al, 2003b), which mobiles a certain amount of the beam moment depending on the connection stiffness. Further, the moment resisting connections could be divided into 'equivalent monolithic' systems, where the connections are stronger than the adjacent precast concrete elements, and 'jointed' systems, where the connections are weaker (*fib*, 2003).

The equivalent monolithic system (the connection type studied in this research is intended to be among them) could be either strong (with limited ductility) or ductile (with normal strength). In the first type, the connection is sufficiently stronger than the adjacent members and the connection remains in an elastic region while the yielding occurs elsewhere in the frame. In ductile connections, the connection is designed for the required strength but with sufficient ductility to ensure non-brittle failure.

1.7.2 Semi-rigid behaviour

In order to evaluate the rigidity of a connection under gravity loads, a beam-line analysis could be used, which provides a convenient way to determine the influence of the semi-rigid connection on the behaviour of an elastic beam.

To obtain the beam-line (Figure 1.3) for a particular single beam subjected to uniformly distributed load 'w', the moment-rotation diagram is constructed considering the extreme conditions. The first condition is a pinned beam to determine point A, which represents the rotation ($\frac{W\ L^3}{24\ EI}$) of the beam at supports under distributed load. The

second condition is a fully-rigid beam to determine point B, which represents the hogging moment of the beam ($\frac{W L^2}{12}$) at the supports under distributed load. The line that connects points A and B is known as the "beam-line".

In Figure 1.3, line 1 represents the behaviour of a fully-rigid connection, and line 2 represents the behaviour of an ideally pinned connection. To assess any connection, the moment-rotation plot needs to be verified against the beam-line. If a moment-rotation relation (e.g. line 3) fails to cross the beam line, then the connection is considered as pinned due to the lack of the exhibited ductility.

On the other hand, if the moment-rotation relation (e.g. line 4) crosses the beam-line, the connection will have sufficient ductility and achieve the required strength to be considered as a semi-rigid connection, and might be considered as a fully-rigid connection when the difference is negligible in comparison to line 1. For full assessment of plot 4, the classification limits for the semi-rigid zone given by the codes of practices need to be verified, which will be presented in detail in Chapter 2.

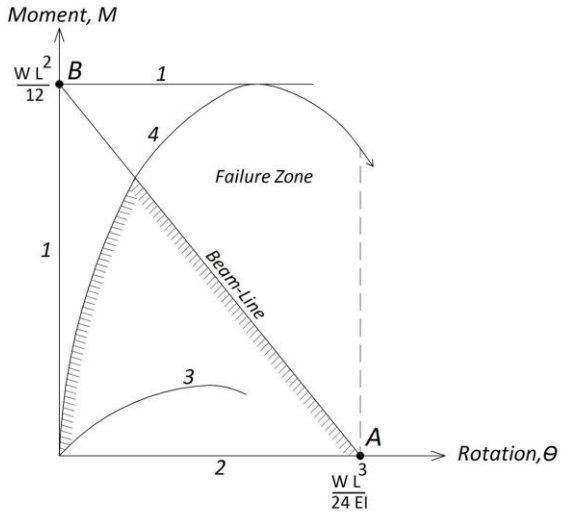

Figure 1.3 Moment-rotation characteristic of beam-column connections

1.7.3 Strong connection concept

As mentioned in Section 1.7.1, an equivalent monolithic beam-column connection could be achieved by designing the connection to be stronger than the adjoining members; the connection is designed to remain elastic while inelastic action takes place away from the connection. Beam-column joints should to be designed in such a way to force the failure to happen in the beam outside the joint (Hegger et al, 2004); it is especially advised to adopt this concept in buildings subjected to seismic loads (Ghosh et al, 1997; ICBO, 1997). The non-linear yielding region should be separated from the column by a distance not less than one half of the member's depth, as recommended by UBC code of practice (ICBO, 1997).

In the current study the concept of a strong connection has been used to strengthen the semi-rigid beam-column connection to control the crack width within the connection zone under gravity loads. This will guarantee avoiding yielding and slippage within the connection and move the final failure away from the connection.

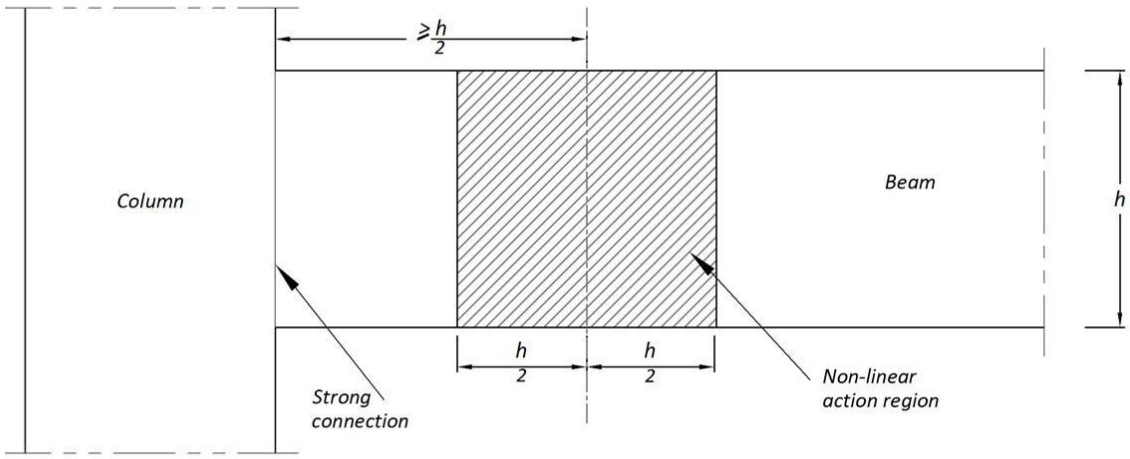

Figure 1.4 Non-linear action region and location (Ghosh et al, 1997)

1.8 Layout of thesis

This thesis structure is organised into nine chapters, as follows.

A) Chapter 1 introduces the research background and significance, in addition to the aims and objectives.

B) Chapter 2 presents the literature review related to the current investigation.

C) Chapter 3 presents the test set up and the results of the small-scale biaxial compression tests for beam-column connections.

D) Chapter 4 describes the test set up for the full-scale beam-column connection under gravity and sway loads.

E) Chapter 5 presents and discusses the results obtained from the full-scale tests under gravity loads.

F) Chapter 6 presents and discusses the results obtained from the full-scale tests under sway loads.

G) Chapter 7 introduces the finite element method with the application of the ANSYS software. This is to produce a 3D FE model simulating the semi—rigid behaviour of the connections tested under gravity loads.

H) Chapter 8 presents the analysis and design considerations for the tested beam-column connection configuration, including performing semi-rigid frame analysis using different techniques to quantify the sufficiency of the connection in real frames.

I) Chapter 9 highlights the main research findings, conclusions and recommendations, in addition to suggestions for further research.

CHAPTER 2

REVIEW OF LITERATURE

2.1 Introduction

The main purpose of this chapter is to gather the existing knowledge that would be useful for the current investigation of discontinuous beam-column connections in precast concrete construction. A review of the existing literature regarding discontinuous precast concrete connections is presented in Section 2.2. In the following four sections (as referred to in Figure 2.1), the behaviour mechanism and design provisions for mortar joint infill, grouted reinforcing bars, bond of steel bars, and dowel action are presented. In Section 2.7, the semi-rigid response is evaluated; in addition, the available classification systems are presented and discussed. Finally, the available theoretical models for precast concrete beam-column connections with continuity reinforcement crossing the connection are reviewed in Section 2.8.

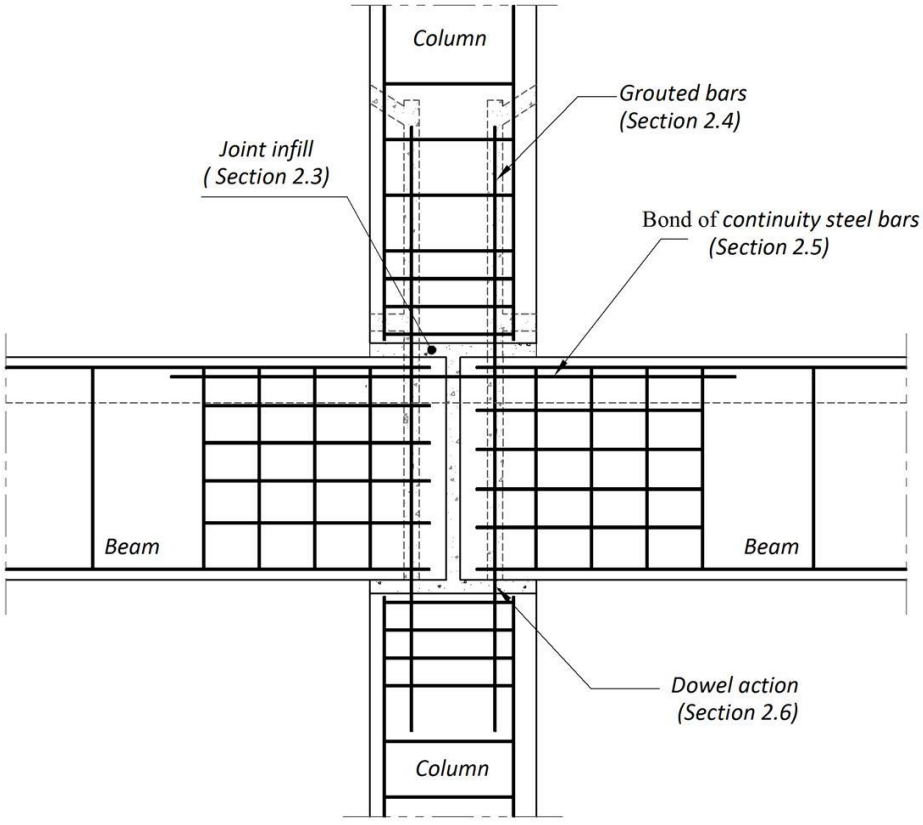

Figure 2.1 Discontinuous beam-column behaviour components

2.2 Discontinuous beam-column connections

As pointed out in Chapter 1, the available literature showed that only a little research has been carried out on the discontinuous beam-column connection type, the few exceptions being by Stanton et al (1986), Lindberg et al (1992), de Chefdbien and Dardare (1994), and Restrepo et al (1995). The main difference with the beam-column connection configuration investigated in the current study is that the connections in these researches did not provide hogging moment resistance capability under dead loads. This is in addition to differences in the reinforcement details and the amount and location of the in situ infill in comparison with the current study. In this section, the details of these experimental researches will be presented to show the available knowledge in the studied field and to avoid using details shown to be insufficient in these researches.

Stanton et al (1986) and Dolan et al (1987) reported the results of the PCI 1/4 study (Specially Funded Research and Development Programs 1 and 4), which examined the most common types of moment resisting precast concrete beam-column connections. Among the specimens, a discontinuous column connection (BC25) and a roof corner connection (BC29) were tested (Figure 2.2).

The BC25 connection was constructed using bolts to connect plates cast at the ends of the columns. The specimen was subjected to 1330 kN vertical load and cyclic reversed lateral loads. The failure happened at the third cycle by bursting the ties and buckling of the reinforcement. The final strength of the connection should have been covered by the strength of the bolts. Therefore, as it was concluded, this connection could develop the full strength capacity of the bolts by using additional column ties confinement. It was recommended to use 135^{o} hooks as column ties near the connection

plates and avoid locating the connection at the points of the maximum moments and shift it towards the inflection point. It was suggested that connection BC25 is not reliable to be used as a moment resistant joint due to the sudden buckling failure of the column bars and the implication on the frame collapse.

The BC29 was constructed by erecting the beam over dowels extending from the column. The dowels extended through ducts (sleeve) and filled with cement grout in the beam. The connection was tested to sustain moments, and it was found that the moment resistance of the connection is low; however, it showed very ductile behaviour. Therefore, it was advised to use this connection as a supplemental moment restraint, and to provide additional lateral restraint for the structure.

These connections differ from the connection investigated in the current study by being used at roof level (BC29) and having the beam continuous and using different bolts and steel plates for continuity of the column (BC25).

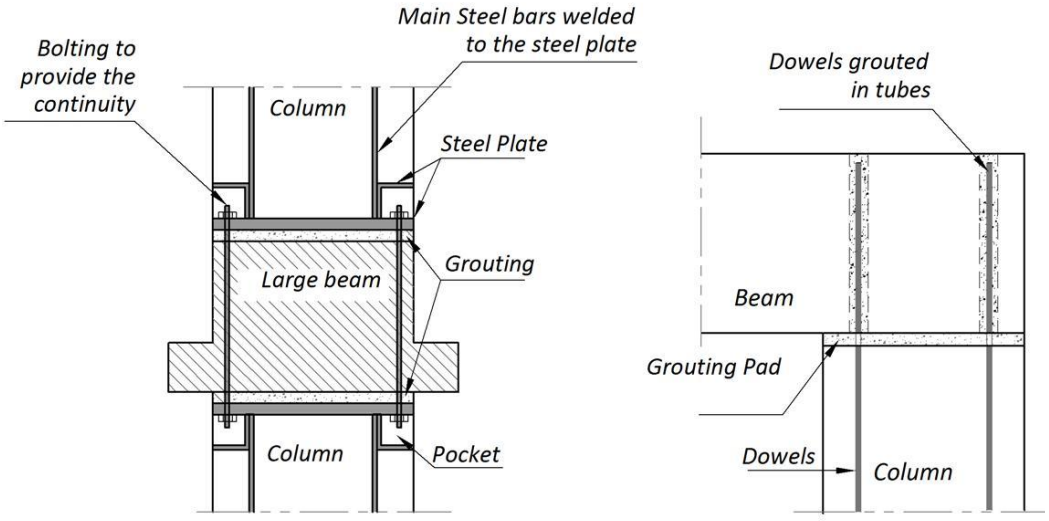

a) BC25 b) BC29

Figure 2.2 Configuration of specimens BC25 and BC29 tested by Stanton et al (1986)

Lindberg et al (1992) performed four tests on a storey height concrete frame that consisted of discontinuous beams and columns, as shown in Figure 2.3. The test specimens had different properties regarding geometry, reinforcement details, use of

hollow core slab slices, use of horizontal joint steel, and direction of loads. The most similar tests were 2 and 3. Even so, there was a difference in the direction of applying the loads, which theoretically reported to have no considerable effects.

Test 1 was designed to find out the ultimate compression strength of the connection without any loads on the beams. The beam sections were prismatic without using hollow core slices and without any continuity steel bars in the horizontal direction. The failure happened in the top column at 2500 kN load, which was lower than the theoretical ultimate loads (3000 kN for the top column and 3800 kN for the lower column). This behaviour was attributed to the rotation of the beam ends under the column, without sufficient steel bars in the lower part of the top column; therefore, additional reinforcement steel ties were added at the column ends near the connection in the other three tests. However, this justification does not seem to be realistic as there were no applied loads on the beams.

Test 2 (Figure 2.3b) aimed to find out the bending moment capacity of the connection under constant column load. T beams and four hollow core slab slices were used with horizontal continuity steel bars embedded in the joints between the hollow core and beam. The results were 90 kN ultimate loads at beams with a constant 180 kN column axial load.

The purpose of test 3 was initially to find out the compressive strength of the connection while subjected to a constant bending moment at the beams. The geometry of test 3 was similar to test 2 except for applying loads from beneath rather than on top. At first, a 600 kN load had been applied to the column, then it was proposed to apply a 100 kN load at the beams before applying the monotonic load on the column. Nevertheless, the connection failed at the 95 kN beam load, even though it was

theoretically supposed to sustain a 171.9 kN beam load. This behaviour was referred to the bond failure of the joint steels between the beams and the hollow core slices.

Test 4 aimed to solve the early failure in tests 1 and 3 by providing steel plates at the column-ends near the connection, as shown in Figure 2.3 (the terms upper, lower and top should be read in conjunction with Figure 2.3c). No hollow core slices or joint steels had been provided; this was to examine the efficiency of the connection without them. In this test, it was required to investigate the compressive strength of the connection while subjecting to constant bending moment from the beams. The ultimate axial force on the column was 3600 kN with a constant 50 kN beam load.

The outcomes of Lindberg's (1992) research showed that there was unfavourable behaviour in the column and beam, which the researcher attempted to solve by providing steel plates at the beam and column ends in test 4. It could be claimed that this test solved the problem in test 1 regarding the shortage in the connection to sustain the estimated axial force. However, it did not examine the moment capacity of the beam, as the beam load did not reach 171.9 kN (the theoretical limit) or even 100 kN (the proposed applied load in test 3).

Providing the steel plates with additional welded steel bars (test 4) made the connection details more complex and might be considered as impractical for construction purposes. Therefore, in the current research, the intention was towards avoiding such complexity in the detail and, as an alternative, to use the full continuity in the beam and column main bars.

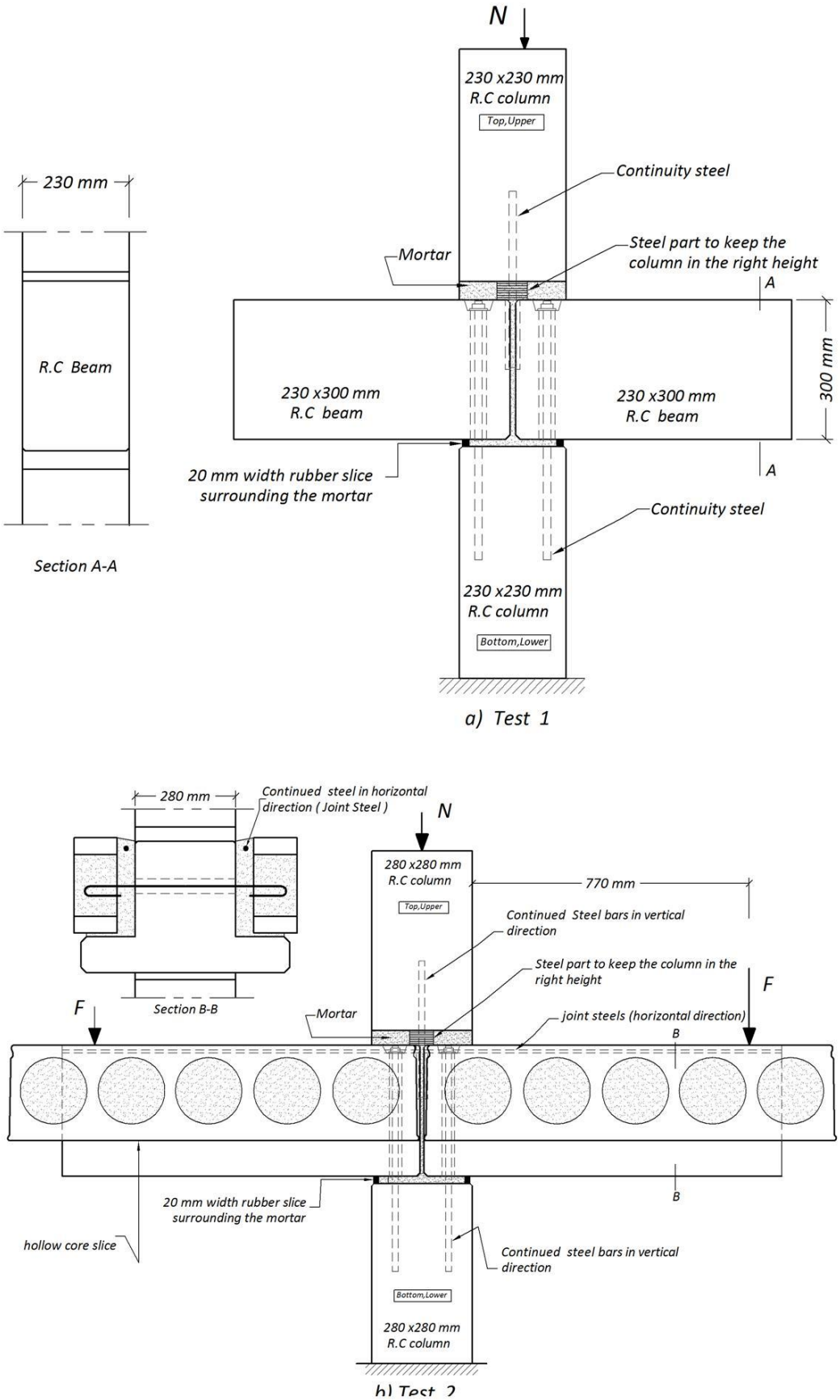

Figure 2.3 Beam-column connection specimens tested by Lindberg et al (1992)

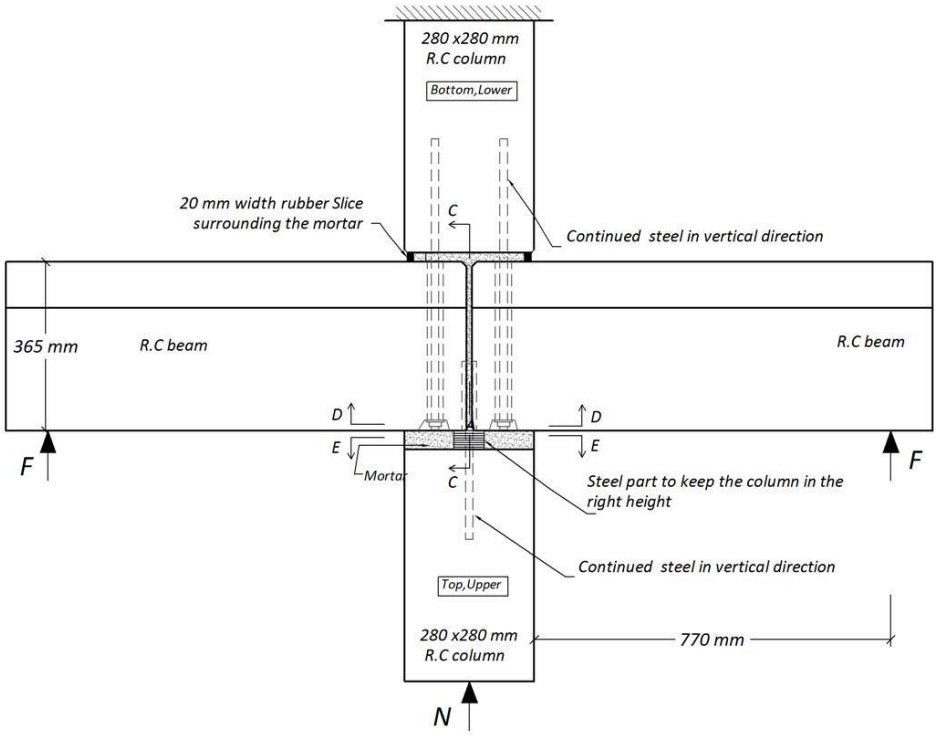

c) Test 4

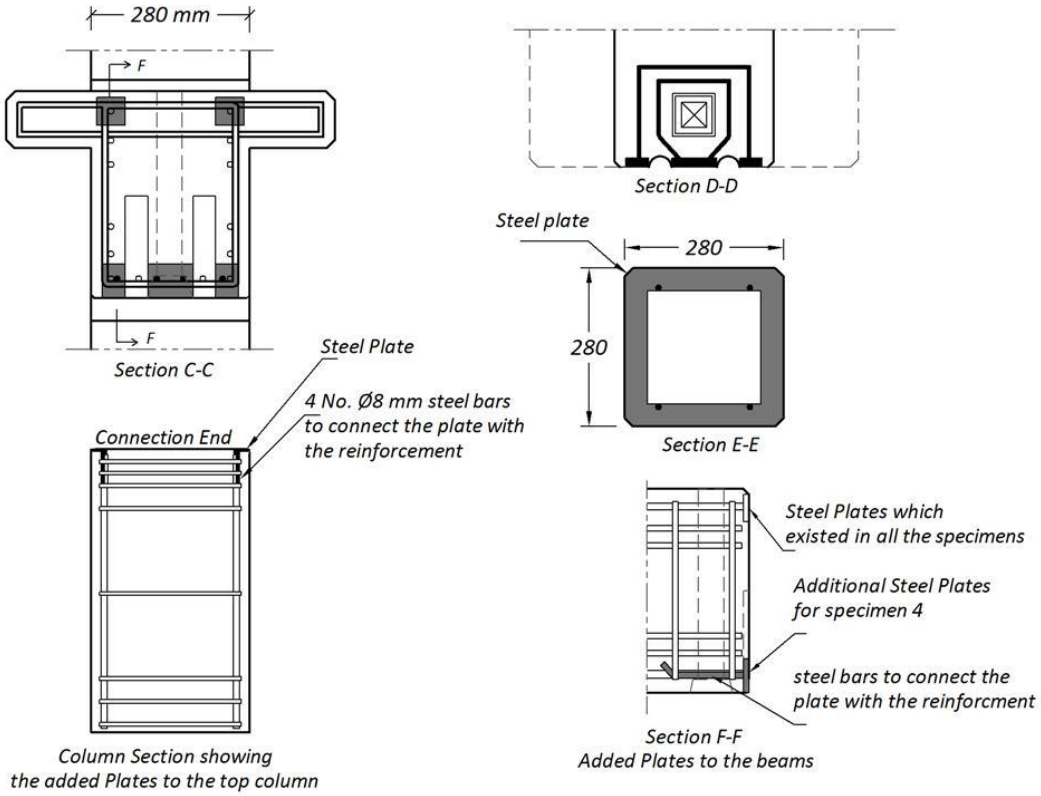

d) Test 4 sections

Figure 2.3 (Cont.) Beam-column connection specimens tested by Lindberg et al (1992)

Comair and Dardare (1992) and de Chefdbien and Dardare (1994) presented a research conducted by CERIB in 1990, which aimed to classify the connections according to their location and used technology, presenting the test data and experimental work, including the details and the findings. One of the tested connections consisted of a column with two beam parts connected with the column by four threaded pins that pass through grouted sleeves in the beam, as shown in Figure 2.4. The connection included 100 mm cast in situ topping concrete with three steel bars as continuity top reinforcement for the beam. This connection type was considered as the most economical system in France.

The main variables in the study were the type of the bedding materials (mortar or neoprene), vertical infill materials (concrete or expanded polystyrene) and the amount of the top continuity reinforcement in the concrete topping. The test was conducted by applying a constant loading of 200 kN to the column, simulating the upper storey column load, followed by applying monotonic beam loads to failure.

The first cracks were vertical flexural cracks appeared between the precast concrete beam and the vertical cast in situ concrete due to the loss of interlock between them. At this stage the continuity bars tensioned immediately. The failure initiated by yielding of the continuity steel after flexure-shear cracks that started from the concrete topping and extended towards the precast concrete beams. By this yielding, the strain in the threaded bars between the column and beam increased significantly. The failure occurred by the yielding of the threaded bars accompanied with very large deflections.

It was concluded that the continuity moment could be increased by 30% of the bending moment capacity of a simply supported beam. Two different types of behaviour were observed: quasi-bilinear for connections with solid materials in the bedding and

vertical infill, and non-linear for connections with soft bedding and/or vertical infill materials. While the existence of the soft elements as a beam bedding (Neoprene) or an infill between beams (Polystyrene sheet) did not affect the ultimate strength, it did introduce a complicated load-rotation curve as a result of the thrust between beams at large deflections. This behaviour is clear in Figure 2.5, as test BC3 included soft materials for both the bedding and the vertical infill between the beams. Based on that, in the current study, only the rigid filling option will be considered.

Restrepo et al (1995) presented the results of six precast concrete moment resisting beam-column connection types used at the perimeter frames of buildings, which intended to emulate the behaviour of conventional cast-in-place reinforced concrete structures. Two of the tested connection systems had the connection in the beam-column region which comprised of discontinuous members (in construction terms).

Figure 2.6a shows the details of the first type (system 1), where the lower part of the beam (580 mm height) was precast concrete and the top part (120 mm) was cast in situ concrete with the beam seated on 30 mm of the column below. The top column and the connection core were cast in situ also. Figure 2.6b shows the details of the second type (system 2), where precast concrete beams cross the column and the column main bars pass through 70 mm corrugated steel ducts (sleeves) preformed in the beam, and protrude to the above. The duct holes and the horizontal joints are filled with non-shrinkage grouts.

System 1 showed excellent performance with respect to strength and ductility with main beam cracks at the column faces, not at the vertical cold joint. Neither of the horizontal, vertical construction joints nor the anchorage of the beam bottom bars

affected the cyclic load performance. This system was rather flexible due to poor bond condition within the connection core, where it was reported that, after the concrete set, excessive bleeding and plastic settlement of the fresh concrete was observed in the beam-column connection, which in turn affected the bond condition of the top beam bars. Regarding system 2, it displayed excellent performance, and it showed that the grouted ducts (sleeves) and the construction joints had insignificant effect on the behaviour. Both systems were tested under quasi-static cyclic reversed lateral loading, and the results showed that the connections could be designed and constructed to emulate cast-in-place construction.

It has been reported that, to recognise the beam and column rotations at the joint faces caused by the penetration of strains in longitudinal bars into the joint and the curvature distribution in the beam, a suitable value for the second moment of area needs to be considered; this is necessary in order to conduct the elastic analysis. However, no relative beam-column rotations were reported in the paper to quantify this flexibility.

From the research conducted by Restrepo et al (1995), it could be concluded that the horizontal and vertical construction joints in the proposed beam-column connection in the current study will not affect the behaviour as long as there is full continuity of the longitudinal bars across the joints. Also, the grouted ducts could have insignificant effect on the behaviour if they are confined with horizontal steel links. In the current beam-column configuration, it is not possible to provide such horizontal links; therefore, the effect of not providing such links will be investigated.

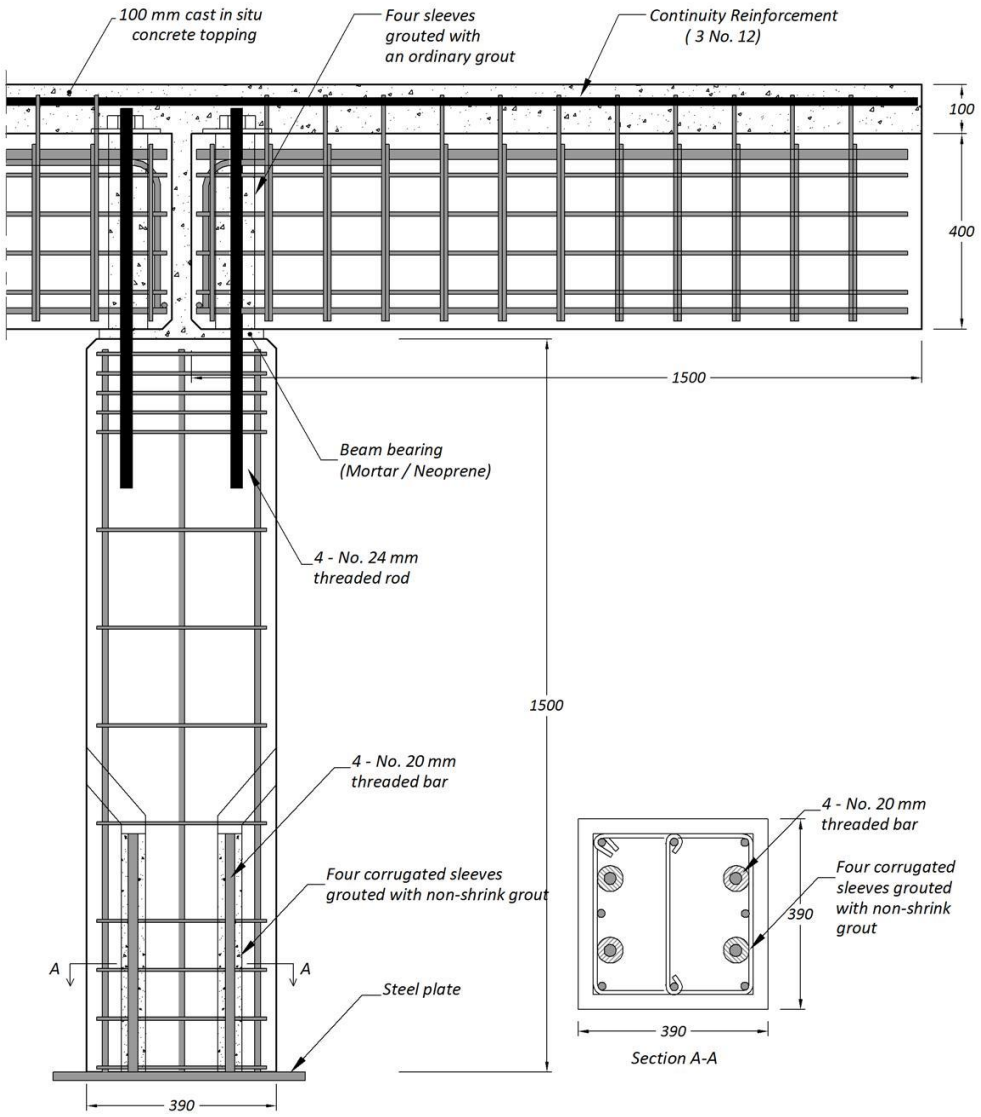

Figure 2.4 CERIB beam-column connection (de Chefdbien and Dardare, 1994)

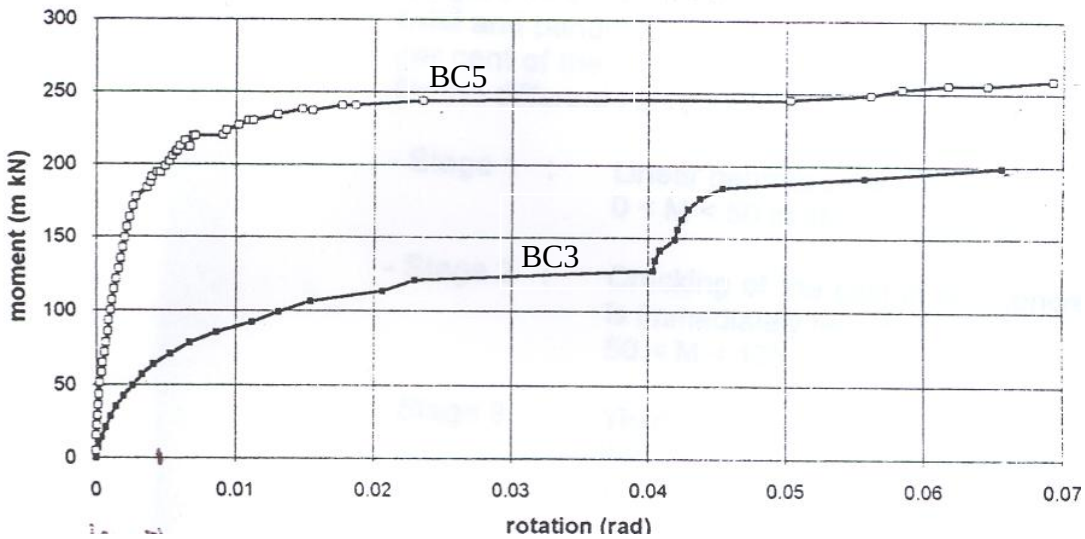

Figure 2.5 Moment-rotation relations of tests BC3 and BC5 (de Chefdbien and Dardare, 1994)

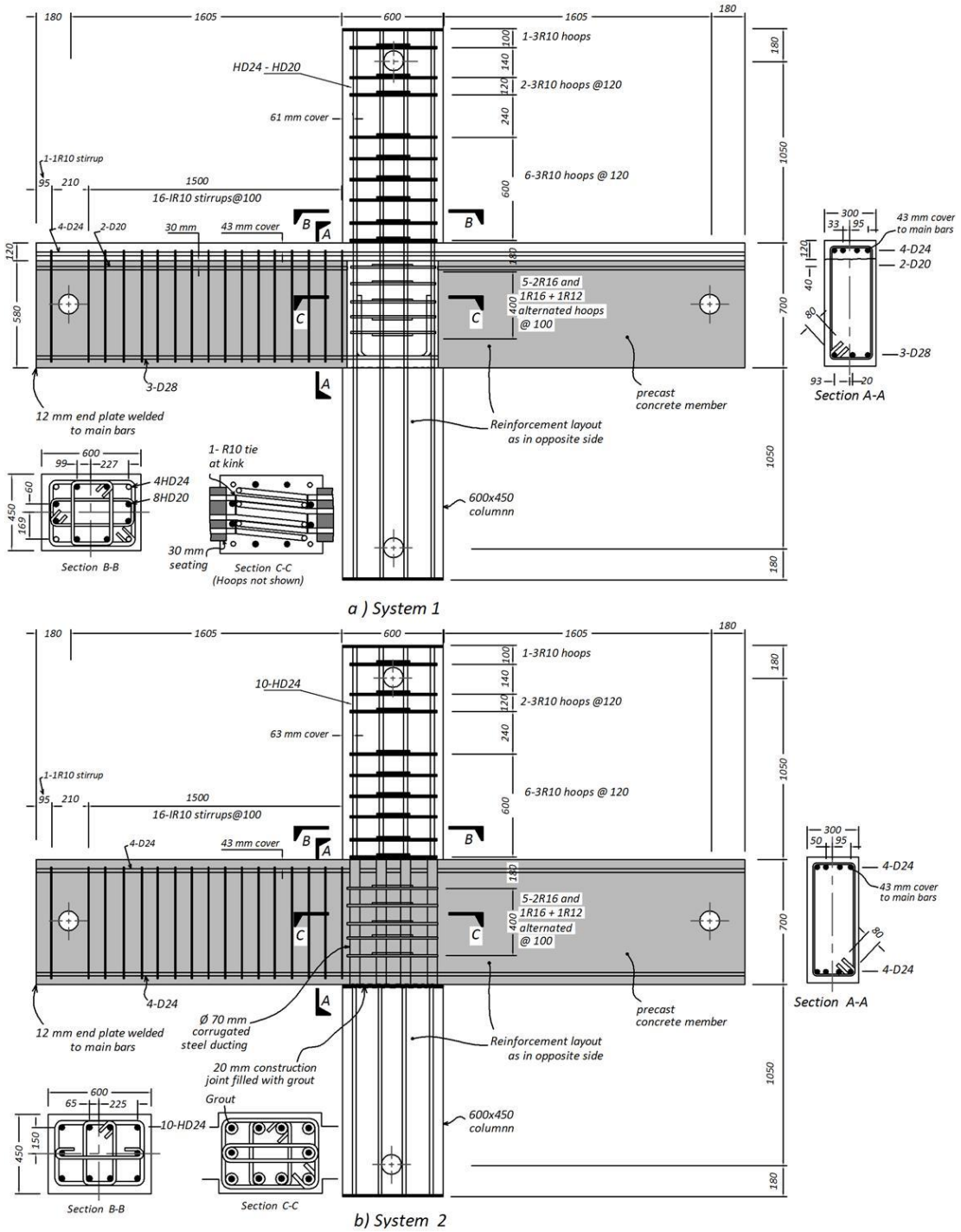

Figure 2.6 Beam-column connection specimens tested by Restrepo et al (1995)

Hughes and Crisp (2010) presented the beam-column connection configuration that is shown in Figure 2.7, within the common precast concrete construction used in Melbourne, Australia. This configuration does not provide moment continuity for dead loads; in addition, it requires the beam to be clamped to the column by nuts and washers installed to coarse threaded column bars. In spite of this connection configuration being

used in real frames (Figure 2.7), the paper did not present any experimental or numerical invistigation for the behaviour.

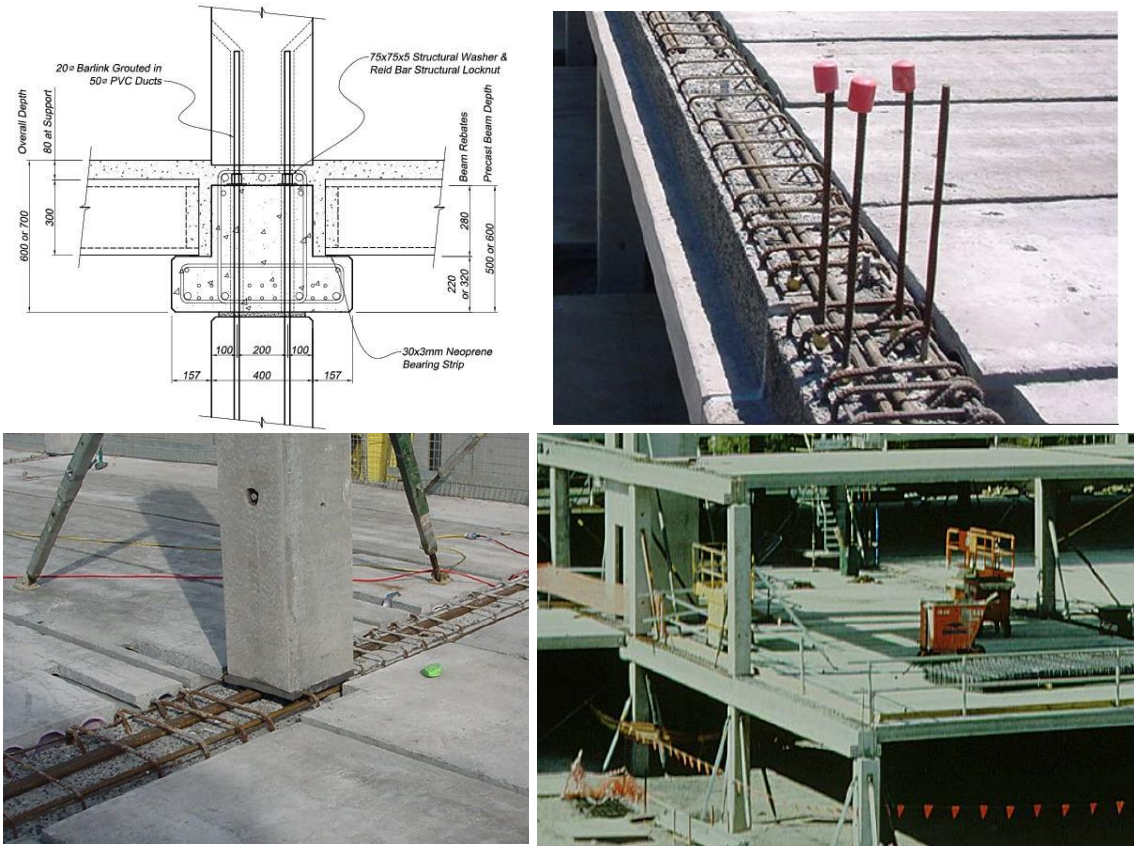

Figure 2.7 Beam-column connection configuration used in Australia (Hughes and Crisp, 2010)

2.3 Precast concrete joint infill

As mentioned earlier, the joint between precast concrete members has a significant effect on the behaviour of beam-column connections. It is required to set the thickness of the joints to zero but, due to construction reasons, some space should be provided between the elements. The space is usually filled with cement-based grout/mortar or concrete with small gravel sizes by using expansive cement to assure a full contact with the precast concrete elements and using shrinkage reducing admixture to control shrinkage cracks.

In the case of using a semi-rigid joint infill layer, such as cement mortar, the load-bearing capacity of a jointed connection 'f_j' is governed by the splitting stress of

the precast concrete elements (Figure 2.8). This mechanism of failure is attributed to the expelling of the mortar to outside the joint, as there is no confinement at the borders. This expelling produces friction forces in the contact area between the precast concrete members and the mortar, which comes entirely from different strain responses of the contacted materials (different elastic modulus). These friction forces cause tensile splitting cracks in the precast concrete members (Figure 2.8b).

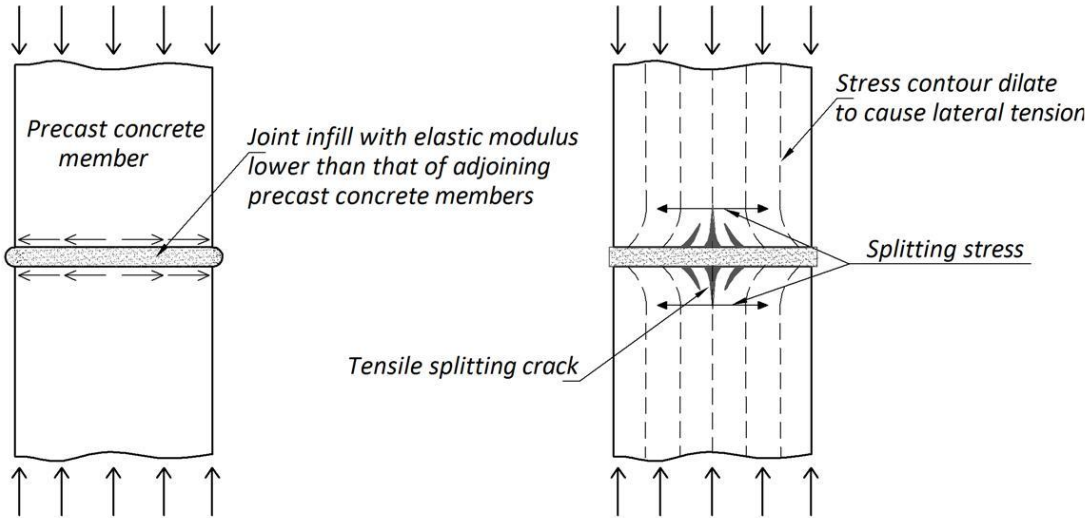

a) Frictional forces due to relative movement between mortar and concrete

b) Splitting stress in the column (Elliott, 2002)

Figure 2.8 Stress distribution at joint area using semi-rigid joint infill

In the beam-column connection investigated in the current study, there are three locations of joint infill layers, which might undergo compressive stresses, within the connection zone (Figure 2.1). For these locations, *fib* (2008) recommended that:

(i) the horizontal joint between the beam and lower column should be of a 3 mm minimum thickness sand/cement mortar;

(ii) the horizontal joint between the beam and top column should be of a 10-30 mm thickness to allow for deviations in beam level;

(iii) the vertical gap between the beam-ends to be filled with a well-compacted expanding grout or a fine concrete depending on the available space.

In the *fib* (2008) recommendations, the compressive strength of the mortar 'f_m' was advised to be equal to the compressive strength of the precast concrete column 'f_p', but without specifying any maximum thickness limit. Generally, the load-bearing capacity of a jointed column system 'f_j' is related to the thickness of mortar layer 't' and f_m (Dragosavic, 1978; Vambersky, 1990), as listed below.

- If f_m is greater than f_p, the mortar layer will not reduce f_j, and $f_j = f_p$
- *If* f_m is less than f_p, then f_j is given as a proportion to f_p through an efficiency factor 'α' (Eq. (2.1)), which is varied according to the variation in k and r (Figure 2.9)

$$f_j = n_o \ \alpha \ f_p \tag{2.1}$$

$$\alpha = k \frac{5\,(1-k)+r^2}{5\,(1-k)+k\ r^2} \quad ;\ k = f_m / f_p \ ;\ r = h_c / t \tag{2.2}$$

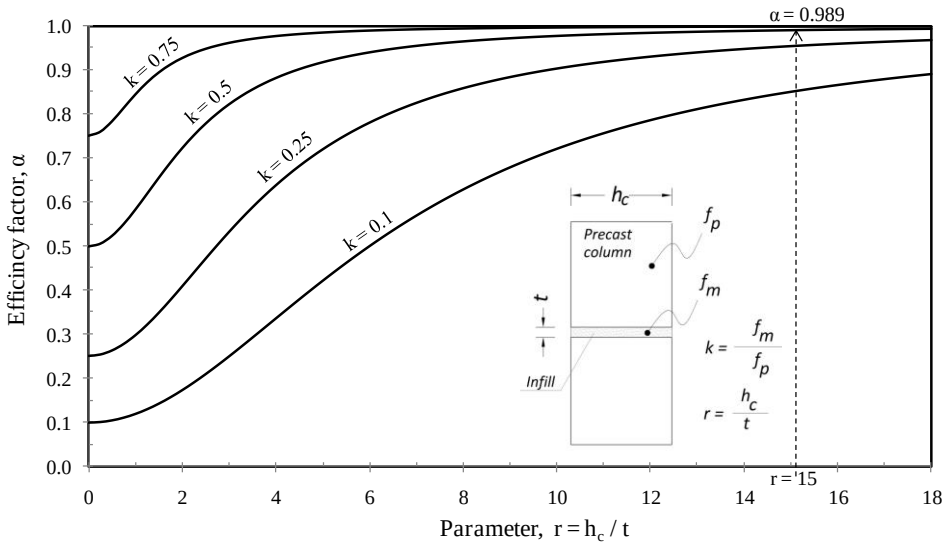

Figure 2.9 Efficiency factor of joint

Eq. (2.1) includes also a reduction factor 'n_o', which is related to the quality of preparation of mortars under site conditions. The value of n_o was recommended to be taken equal to 0.9 for a pouring mortar, which is applicable to the current research, and equal to 0.7 for a dry packed mortar; However, higher values for n_o could be used if confirmed by tests (Vambersky, 1990). For r equal to 15, k equal to 0.5, and n_o equal to 1, the efficiency factor is 0.989 according to Eq. (2.2) and Figure 2.9 , meaning that at

this geometry and material strength proportions, f_m has almost no effect on f_p. In the current study, the mortar joint will be aimed to be within this limit to minimise any influence of the mortar joint on the load-bearing capacity of the system (f_j).

In the same study presented above, Vambersky (1990) carried out a numerical modelling of a joint region to investigate the effect of using steel plates of different thicknesses (10 mm and 40 mm) on f_j. The research concluded that using steel plates at the column-ends does not result in a significant increase in f_j; also, it was shown that the splitting tensile stress in the column have nearly the same value, independent of the steel plate thickness.

However, contracting to the above results, Minnert (1997) found that high strength concrete columns with steel plates adjacent to the mortar joint could develop full bearing capacity of a column without joint. This was attributed to the role of these plates in providing an effective confinement to the column ends which restrict the lateral strains and consequently leads to prevent destruction or spalling of concrete adjacent to the joint. On the other hand, providing transverse reinforcement mesh led to development of 90% of the load capacity of the system. In contrast to the model with steel plates, the failure happened by spalling of the column concrete cover near the joint and spalling of mortar outside the joint. Therefore, it was concluded that it is necessary to adopt a new model design for the transverse reinforcement at the joint. With respect to the concrete strains, it was recorded that the longitudinal compressive strain across the joint is greater than the strains in the normal concrete area (far from the joint). In addition, it was concluded that the existence of the steel plates at the joint enhance the ability of the longitudinal steel bars to transfer the compressive stress (Figure 2.10).In the beam-column connection configuration investigated in the current study, there is no

need for such steel plates to achieve this function; this is because the main steel bars are crossing the joint interfaces that ensure a direct transfer of the stress.

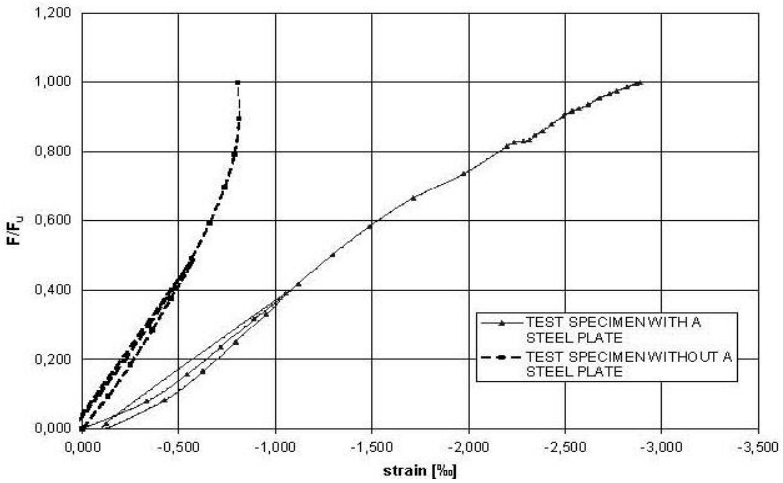

Figure 2.10 Compressive strains at the end of longitudinal bars (Minnert, 1997)

Saleh (2000) performed an experimental study on normal strength precast concrete columns with cement mortar joints incorporating two methods for jointing: (i) using steel plates, which were welded to the steel bars of the columns at the joint; and (ii) using reinforcement mats at the end of the columns. The specimens consisted of two parts of 200 x 400 mm cross section columns in 1000 mm and 500 mm heights for the lower and the upper part, respectively. The used mortar was 20 mm in thickness with compressive strength not less than that of the concrete columns. The experimental results showed the splitting stress in the presence of a steel plate is smaller in comparison with using transverse reinforcement. This feature using steel plates enhance the bearing capacity of the system. The research also presented a significant difference in the deformation across the joint in comparison to other column area. Figure 2.11 shows the longitudinal strains in the column parts. From the graph, it is clear that the strain across the connection zone grew up rapidly at the beginning. This shows that there is a large deformation in this zone during the early stage of the loading due to self-rearrangement of the connection parts.

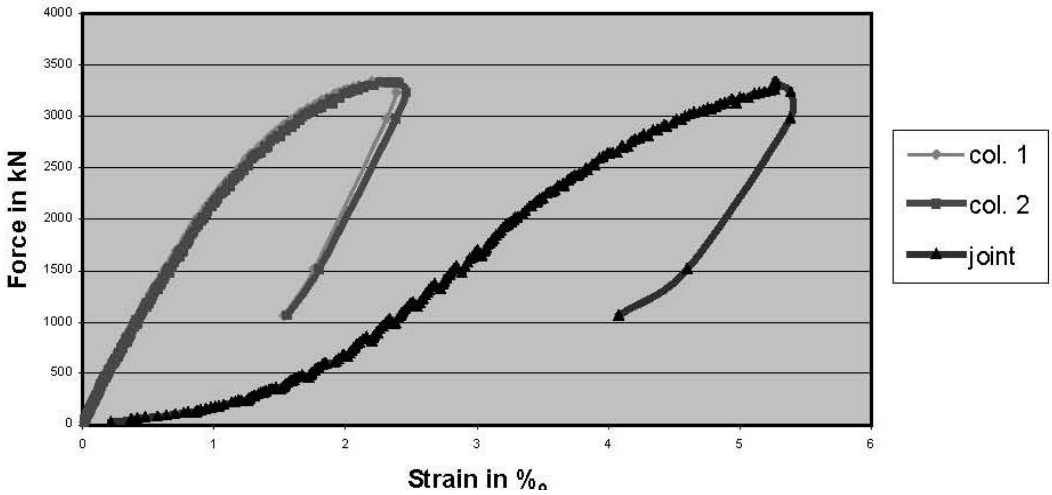

Figure 2.11 Vertical strain progress of column parts (Saleh, 2000)

Gorgun (1997) performed five tests on 100 x 100 mm cross-section prismatic specimens with different in situ concrete infill thicknesses. The original aim of the study was to simulate the behaviour of the bottom in situ infill in the billet beam-column connection type. However, the configuration of the specimens was such that it produced a uniaxial stress distribution in the specimens similar to column configuration. Table 2.1 shows the results of the tests, where the effect of the infill is clear with a maximum reduction of 29% (as a percentage of the cube concrete strength) in case of using in situ infill with thickness equal to the width of the tested specimens. As well, it is notable from the table that the bearing capacity is the highest when the two parts of the specimen were put directly on each other without in situ infill; even the difference is slight (4%) in comparison with the 25 mm thickness joint.

Table 2.1 Results of axial compression tests conducted by Gorgun (1997)

Test Reference	**A1**	**A2**	**A3**	**A4**	**A5**
Infill depth, mm	-----	0	25	50	100
Precast cube strength (N/mm^2)	40.8	40.8	40.8	40.8	40.8
Infill strength (N/mm^2)	21.2	21.2	21.2	21.2	21.2
Effective secant modulus (kN/mm^2)	26.3	20.0	18.7	13.9	13.3
Ultimate strength (N/mm^2)	31.8	30.0	28.0	24.0	20.0
Ratio of ultimate strength to precast concrete cube strength	0.78	0.73	0.69	0.59	0.49

* Specimen A1 represents solid precast specimen without joint.
Specimen A2 represents a two-piece specimen with a 0 thickness joint between them.
The effective secant moduli measured at 2/3 of the ultimate load.

Barboza et al (2006) performed a study concerning load-bearing capacity of mortar joints between precast concrete members considering several variables. The model consisted of two segments of 175 mm square cross-section columns reinforced with 4 Ø 10 mm as the main reinforcement, Ø 5 mm each 90 mm as stirrups, with 15 mm, 22.5 mm, and 30 mm mortar joint between them. The model was loaded axially by compression load, and the outcomes of the research included the following.

- Compared with a system of a column made of two separate parts without joint, the load-bearing capacity of the jointed column system increased by 9-10% with the presence of mortar joint when the thickness not greater than 12.8% of the column width (the specimens with 15 and 22.5 mm mortar joint).
- Using 30 mm thickness for the mortar joint (17.1% of column width) led to a 6% reduction in the load-bearing capacity.
- Increasing the mortar strength had no significant effect on the bearing capacity
- Using column links with closer spacing at the connection area did not increase the load-bearing capacity; however, the ductility of the system increased, which led to restricting the rupture.

Commenting on the first conclusion, the increase in the load-bearing capacity is related to the role of the thin mortar joint in achieving the full contact at the interfaces. In the case of the column of separate parts without joint, it is difficult to achieve such full contact, which is the reason for achieving lower load-bearing capacity in comparison with the case of thin mortar layer. Theoretically, the thinner the joint (up to the direct contact), the less the effect of the joint, as Gorgun (1997) has showed. The other conclusion regarding the effect of the mortar strength does not seem to be realistic as the used ratio of k (f_m/f_p) was between 0.75 and 2.36, and the value of h_c/t was equal

to or less than 11.67 (175 mm /15 mm). By projecting these values in Figure 2.9, this range represents only a very small zone in the graph, which is the zone that is very close to achieving 1 as an efficiency factor. However, as the practical values of k and h_c/t in real construction practice are around these figures, the above conclusions could be valid for the joint behaviour in practice.

From the above review of literature, it appears that there is less agreement regarding the effects of the joint infill thickness, joint infill strength and the use of steel plates on the ultimate bearing capacity of precast concrete axial members. However, there is a general agreement that to enhance the bearing capacity of a system of jointed column; it is required to use a joint infill of limited thickness with compressive strength 'f_m' close to the compressive strength of the adjoining members 'f_p'. However, any variation in f_m between 50-100% of f_p would not affect the ultimate bearing capacity of the system 'f_j' if the joint thickness is taken not greater than 1/15 of the minimum thickness of the adjoining members (see Figure 2.9). The last statement will be examined in Chapter 3, through evaluating the loading-bearing capacity of the column in the beam-column connection investigated in the current study through small-scale tests. The outcome of the small-scale tests will also demonstrate the effects of not using steel plates or steel mats at the ends of the columns.

2.4 Grouted reinforcing bars

In precast concrete connections, as a way to emulate the cast-in-place construction, the ducts (sleeves) and trough serve to house the connectors (steel bars), and they are filled with cement-based grouts. As shown in section 2.2, the grouted reinforcing bars were used in almost all the presented connections, and showed a sufficient capability to transfer tension forces of the connectors. In this trend, for a

proper use of grouted reinforcing bars, it is necessary to take into consideration many aspects regarding the properties of used materials and the construction detailing. The PCI Design Handbook (2004) presents the design provisions for reinforcing bars embedded in grout-filled metallic conduit, as set out below.

1- Having 76 mm as the minimum concrete side cover over the conduit.
2- The conduit should be of 0.6 mm as a minimum thickness.
3- Having 12.5 mm as a minimum annular space around the bar.
4- The minimum grout strength should not be less than 34.5 MPa.
5- The grout should be non-shrink.
6- The embedded length is 381 mm for steel bars of 19 mm, for grouts with a cylinderal compressive strength (*f*c) not less than 34.5 MPa. For higher grout strengths, the embedded length need to be multiplied by $\sqrt{34.5/f\text{c}}$.
7- Confinment steel is required in most applications.
8- Necessary care should be taken to prevent water from entering the ducts before concrete casting, especially in freezing weather.

In the same respect, *fib* (2008) suggests using of corrugated steel sleeves, avoiding forming of air pockets; and using sleeves with a diameter of at least 30 mm greater than the projecting bars to ensure a complete encasing of the bars. Also, it is advised to provide a minimum concrete cover for the duct of not less than the duct diameter, and the clear distance between adjacent ducts also should not be less than the duct diameter. Providing insufficient cover may lead to anchorage failure (splitting of the surrounding concrete) with splitting cracks through the concrete cover. To prevent such failure, *fib* (2008) suggests confining the concrete around the anchorage zone through use of transverse reinforcement.

Brenese (2005) studied the influences of the duct material, number of connectors, bar eccentricity, and transverse reinforcement on the anchorage behaviour of grout vertical duct connections for precast concrete bent cap-to-column connections used in bridge prefabrication (Figure 2.12). This research confirmed what is recommended by *fib* (2008) for using galvanised steel ducts instead of plastic ducts, as using of steel ducts increased the strength and the initial stiffness and prevented pulling out the grout plug. In addition, the galvanised steel ducts provided passive confinement with relatively stable bond-slip behaviour. Also, it has been reported that locating the connectors close to the duct circumferences decreases the bond strength, and providing transverse reinforcement in the connection zone does not improve connection behaviour, and increasing the number of connectors reduces the bond strength.

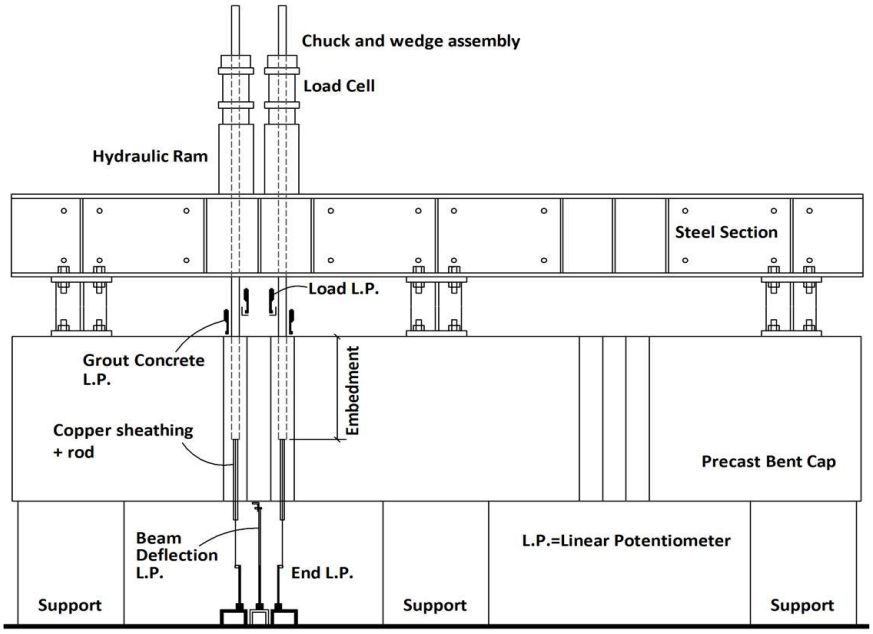

Figure 2.12 Grout bond tests conducted by Brenes (2005)

Raynor et al (2002) tested bars grouted over a short length (50 mm) in ducts and subjected to cyclic load. The reported results showed that the slip of the bars occurs due to crushing of the grout ahead of the bar ribs rather than by splitting, as the steel duct works as a confinement for the grout. In addition, the grout achieved a higher peak bond with the steel bar in comparison with concrete of same compressive strength.

Kuttab and Dougill (1988) conducted experimental tests on grouted and dowelled jointed precast concrete columns subjected to combined bending and axial load (Figure 2.13). The specimens consisted of two 900 mm length column parts in a 200 x 200 mm section with a 25 mm thickness joint. The results were compared with a monolithic column with the same cross-section dimensions and reinforcement. In the precast samples, additional lateral reinforcement was used near the joint and at the loaded ends. The proportion of the grout was a 1:1 sand/cement grout mix with non-shrinkage admixture and a 0.45 water/cement ratio. The grouting was executed by using a pump and maintaining the pressure for at least 1 min after the grout appeared in the outlet.

As can be seen in Figure 2.14, the load capacity achieved in the grouted and dowelled jointed precast concrete columns introduced an axial load-bending moment interaction characteristics which are equal to those of the parent rigid column. In Figure 2.14, the solid lines represent the interaction diagram for the monolithic column, and the broken lines represent the bounds of the precast joint behaviour when the strength is controlled by a different arrangement of corner reinforcement column. The mode of failure in the jointed precast column was localised in the joint with opening or crushing.

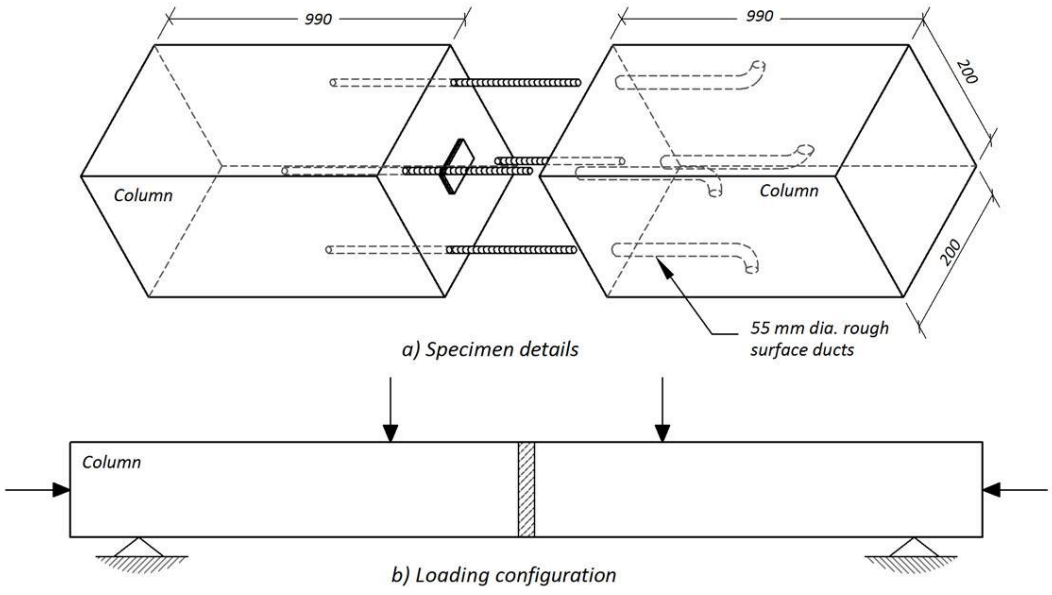

Figure 2.13 Grouted and dowelled column connection tested by Kuttab and Dougill (1988)

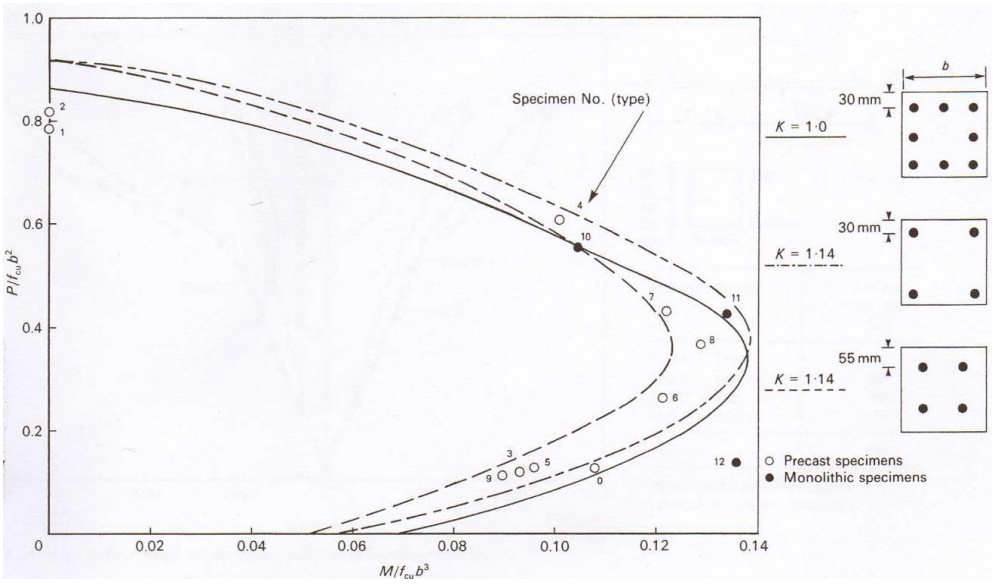

Figure 2.14 Strength envelopes for columns tested by Kuttab and Dougill (1988)

Based on the above review of literature, in the current study, corrugated steel sleeves will be used to house the steel bar connectors taking in consideration the guidance of PCI (2004) presented at the beginning of this section.

2.5 Bond of steel bars

Bond is the interaction between reinforcement and concrete/grout to transfer tensile stresses from the steel to the surrounding concrete along the anchorage length through mechanical interlocking of bar ribs, adhesion and friction. The adhesion effect is small, and the effect of friction is not pronounced until the occurrence of slip; hence, the mechanical interlocking plays the main rule in the bond.

The bond stresses are developed due to the relative displacements between the reinforcing bars and the surrounding concrete/grout, and appear only within a limited length 'l_d' that is shorter than the anchorage length. Figure 2.15 shows the steel stress and bond stress along the bar length at low and high tensile stresses.

The bond mechanism comprises exerting inclined stresses from the steel bar on the concrete which could be analysed into a parallel component (bond stress), which might lead to pull-out failure, and a normal component/radial component (splitting

stress), which in turn might lead to splitting failure in the case of having an insufficient concrete cover (Figure 2.16). To prevent the splitting failure, *fib* (2008) recommended the use of a concrete cover of not less than 3 times the bar diameter 'Ø', while CEP-FIP Model Code 1990 (1993) proposed 5 Ø as the minimum cover for the same purpose, or alternatively to use great amounts of transverse stirrups.

The bond stress is distributed along the anchorage length with a maximum value at the loaded end (active end), as shown in Figure 2.15. This is because the steel strain/stress at the passive end is zero and the bond stress results from the difference in the strain between the steel and the surrounding concrete. For a local bond-slip relation, based on pullout tests of steel bars of short embedded length, CEB-FIP Model Code 1990 (1993) proposed a bond-slip relation over a short length for situations where the local bond slip behaviour is required to be considered (Eqs. (2.3) to (2.5)). The model is illustrated in Figure 2.17 with parameters described in Table 2.2.

$$\tau = \tau_{max} \left(\frac{Sb}{Sb_1}\right)^{\alpha} \quad \text{for } 0 \leq Sb \leq Sb_1 \tag{2.3}$$

$$\tau = \tau_{max} \quad \text{for } Sb_1 \leq Sb \leq Sb_2 \tag{2.4}$$

$$\tau = \tau_{max} - (\tau_{max} - \tau_f) \frac{Sb - Sb_1}{Sb_3 - Sb_2} \quad \text{for } Sb_2 \leq Sb \leq Sb_3 \tag{2.5}$$

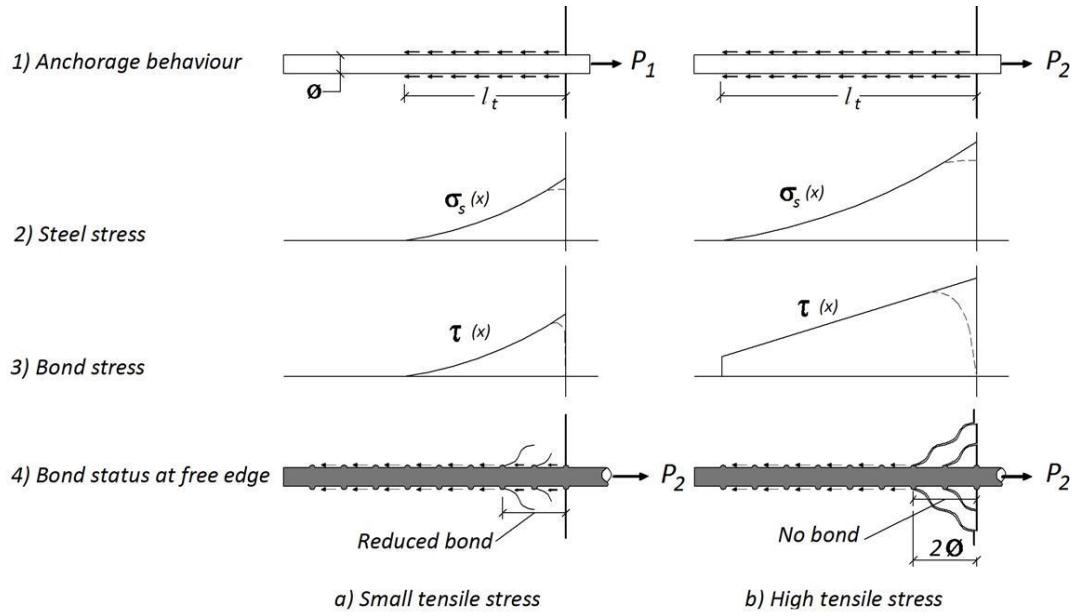

Figure 2.15 Typical anchorage behaviour (*fib*, 2008)

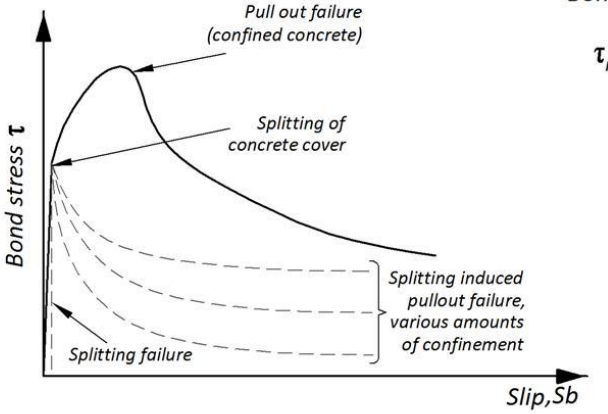

Figure 2.16 Pull-out and splitting failure (*fib*, 2008)

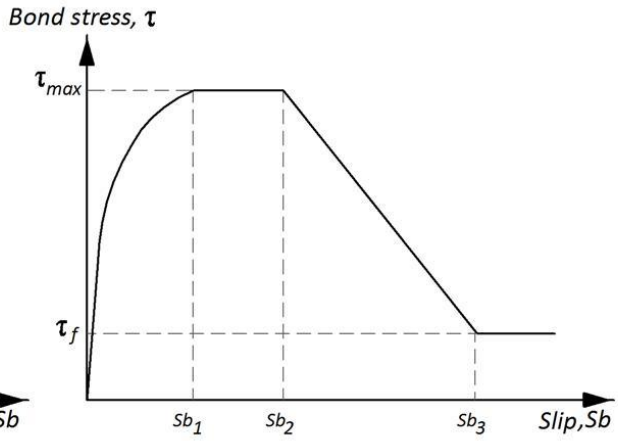

Figure 2.17 Analytical bond stress-slip relationship (CEB-FIP, 1993)

Table 2.2 Parameters for defining the mean bond stress-slip relationship of deformed bars (CEB-FIP, 1993)

	Confined Concrete (pull-out)		Unconfined Concrete (concrete splitting)	
	Good bond cond.	All other bond cond.	Good bond cond.	All other bond cond.
Sb_1	1.0 mm	1.0 mm	0.6 mm	0.6 mm
Sb_2	3.0 mm	3.0 mm	0.6 mm	0.6 mm
Sb_3	C_{clear}*	C_{clear}*	0.6 mm	2.5 mm
α	0.4	0.4	0.4	0.4
τ_{max}	$2.5\sqrt{f_{ck}}$	$1.25\sqrt{f_{ck}}$	$2.0\sqrt{f_{ck}}$	$1.0\sqrt{f_{ck}}$
τ_f	0.4 τ_{max}	0.4 τ_{max}	0.15 τ_{max}	0.15τ_{max}
*c_{clear} is the clear distance between steel bar ribs				

The parameters in Table 2.2 were reported to be valid for concrete of: (i) a clear cover 'C' not less than Ø with a minimum transverse reinforcement 'A_{st}' equal to 0.25 n A_s for the case of unconfined concrete; and (ii) C ≥ 5 Ø with bar clear spacing ≥ 10 Ø and $A_{st} \geq$ n A_s in the case of confined concrete. In which, A_{st} is the stirrup bar area along the anchorage length, n is the number of main bars surrounded by the stirrups, and A_s is the area of one main steel bar.

As shown in Table 2.2, CEB-FIB Model Code 1990 (1993) distinguishes between two bond conditions: confined status, when the steel bar is embedded in concrete either by having sufficient cover or a transverse reinforcement and the failure will be by pulling out the bar; and unconfined status, when the failure is of the splitting type. In addition, both conditions are sub-divided into two subcategories: 'good' and 'all other

cases' bond conditions. The 'good' bond condition occurs when the steel bars have 45-90º with the horizontal during construction, or less than 45º but the bars are either within 250 mm from the bottom or not within 300 mm from the concrete top edge (*fib*, 2008).

As an alternative to this varied bond stress distribution in Figure 2.15, and based on the assumption that the bond stress is constant and not influenced by the stress level in the steel bar (*fib*, 2008), the transmission length 'l_t' could be obtained in the elastic range considering the equilibrium between the external applied load ($\sigma_s \pi \emptyset^2 / 4$) and the average/nominal bond stress 'τ_a' along the transmission length (Eq. (2.6), Eq. (2.7), and Figure 2.18).

$$\sigma_s \frac{\pi \emptyset^2}{4} = \tau_a \pi \emptyset l_{t1} \quad (2.6)$$

$$l_{t1} = l_{t2} + 2\emptyset = \frac{\emptyset \sigma_s}{4 \tau_a} + 2\emptyset \leq l_a \quad (2.7)$$

$$Sb_{end} = \frac{1}{2} \frac{\sigma_s}{E_s} l_{t1} + \frac{\sigma_s}{E_s} 2\emptyset \quad (2.8)$$

$$Sb_{end} = \frac{1}{8} \frac{{\sigma_s}^2 \emptyset}{E_s \tau_a} + \frac{\sigma_s}{E_s} 2\emptyset \quad (2.9)$$

The 2nd term 2Ø in Eq. (2.7) refers to the influence of the concrete cone failure at the active steel bar end, and the 2nd term in Eq. (2.8) is the slip due to this effect. The 1st term in Eq. (2.8) is based on the fact that the steel stress variation along the transmission length is varied linearly. It should be mentioned that Eq. (2.9) is valid for the conditions where the embedded length 'l_a' is greater than the transmission length 'l_t', and for steel stress state less than the yield strength 'f_y'. To relate τ_a with the maximum local bond stress 'τ_{max}', *fib* (2008) proposed a linear relation (Eq. (2.10)) with the α_t values varying according to the steel bar diameter, as shown in Table 2.3.

$$\tau_a = \alpha_t \tau_{max} \quad (2.10)$$

Table 2.3 Recommended values for α_t in Eq. (2.10) (*fib*, 2008)

Bar diameter, Ø (mm)	*6*	*8*	*10*	*12*	*16*	*20*	*24*	*32*
α_t	0.3	0.32	0.34	0.36	0.4	0.42	0.45	0.45

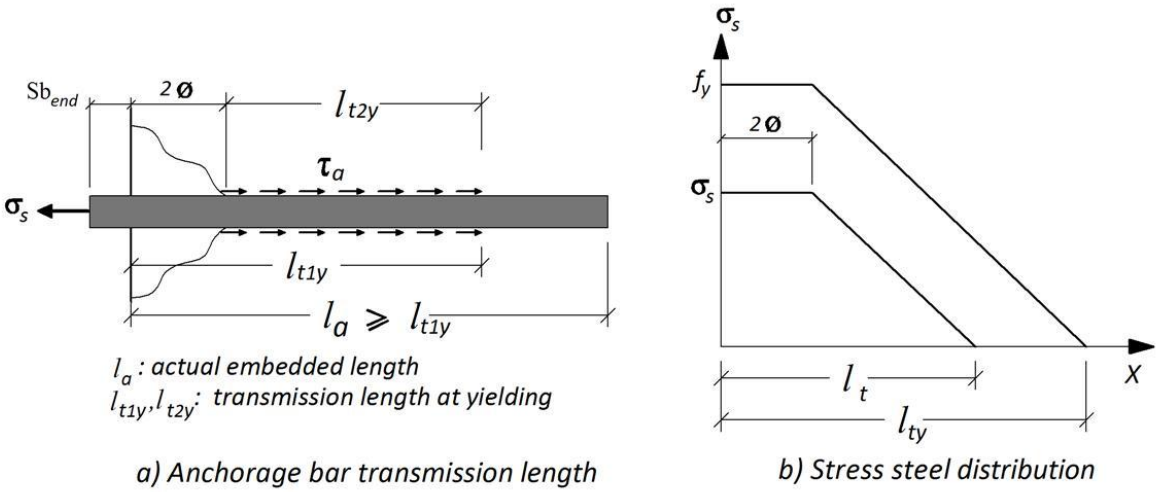

Figure 2.18 Simplified end-slip response prior to yielding (*fib*, 2008)

In the current research, the continuity of the beam top steel bars is provided by embedding them in a narrow trough made at the middle-top of the beam and grouted with cement-based grout, which might require a different bond-slip model from that presented in Table 2.2. From the available literature, no study was found to model the bond-slip relation between steel bars and cement-based grouts. Most of the available studies are dealing with either grouting steel bars into steel ducts (Brenes, 2005; Raynor et al, 2002) or grouting reinforcement into holes drilled in existing concrete (Darwin and Zavaregh, 1996). Based on this fact, for the analytical part in the current study, the CEP-FIP model (1993) will be used in the current research to represent the bond of the reinforcement with cement-based grout, which will be calibrated experimentally through pull-out tests (Appendix F).

2.6 Dowel action

Under large sway loads, the beam-column connection type investigated in the current study experiences sagging moments (Figure 2.19a), which produce tensile forces in the beam bottom bars. As these bars are not continuous across the connection

but are bent around the dowel steel bars extended from the bottom column, the tensile forces are transmitted to the dowel bars as shear forces acting at the joint interface. The shear forces are resisted initially by the adhesion and friction of the joint interface prior to the occurrence of the shear slip. This slip generates tensile stresses in the dowel bars. These stresses result in a compressive force of the same amount and act in the opposite direction on the concrete, which could crush the concrete when a very high shear force is applied. It is advised to not rely on the adhesive due to the fact that the efficiency depends to a large extent on the workmanship and cleaning of the interfaces prior to grouting (*fib*, 2008).

The failure mechanism for the dowel bars in the situation shown in Figure 2.19 occurs by formation of two plastic hinges in the dowel at some distance from the interface accompanied by an uncontrolled large shear displacement. This failure mechanism happens when the dowel bar is embedded in a well confined continuum, which is obtained either by having sufficient concrete cover for the dowel bar or adequate transverse confinement reinforcement around it. The formation of the two plastic hinges happens simultaneously when there is the same strength grade for the concrete/grout at both sides, and the point of inflection appears in the middle of the joint. On the other hand, in case there are two different strength grades, the 1^{st} plastic hinge starts at the weaker side, and the ultimate shear load is reached by the formation of the 2^{nd} plastic hinge.

According to *fib* (2008), for a double-sided dowel action, the ultimate shear capacity would develop at a shear displacement 'Sd_{max}', which is taken as a ratio of the dowel bar diameter '*Ø*' (Eq. (2.11)). The ultimate shear strength 'F_{vR}' is calculated according to Eq. (2.12), where '$f_{c,max}$' is the compressive strength of concrete at the

stronger side, f_y is the strength grade of the dowel bars, and α_0 is a coefficient taken to be 1.15 for double-sided dowels (*fib*, 2008). To calculate the shear load at which the plastic hinge develops at the weaker side could be obtained by applying Eq. (2.12) with using $f_{c,min}$ instead of $f_{c,max}$.

$$Sd_{max} = 0.1\ \emptyset \tag{2.11}$$

$$F_{vR} = \alpha_0\ \emptyset^2 \sqrt{f_{c,max}\ .\ f_y} \tag{2.12}$$

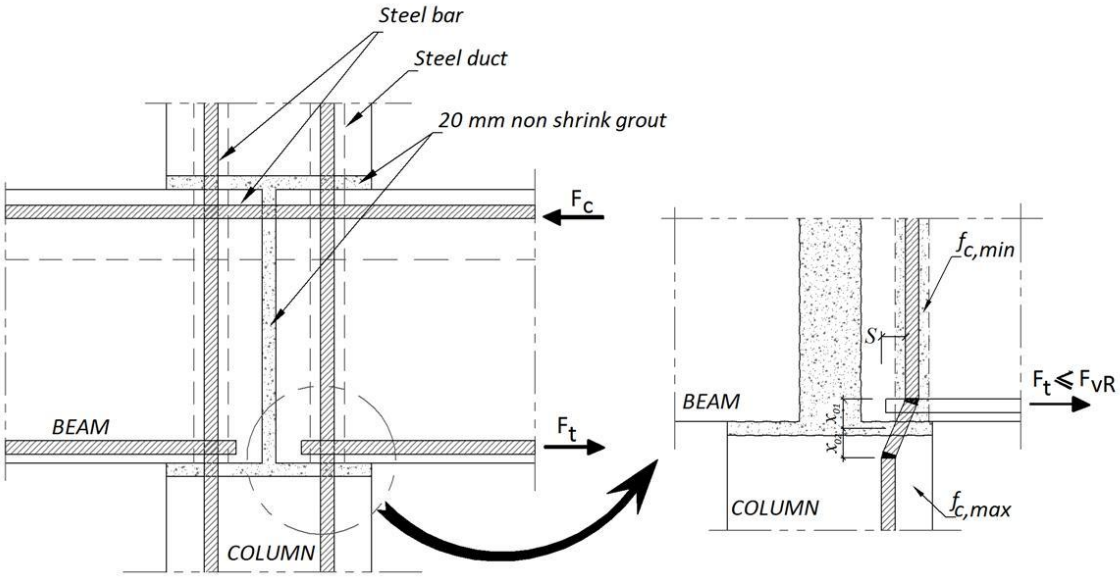

Figure 2.19 Dowel action mechanism in the beam-column connection studied

Although Eq. (2.12) is proposed for the direct dowel action mechanism, it will be used in the current research, to predict the sagging moment capacity of the connection under lateral loads by considering the maximum tensile force in the beam bottom bars F_t to be controlled by F_{VR}. In this model, the contribution of friction between the beam and the mortar bedding in the resisting system is assumed to be negligible, where the friction effect is lost when crack opens (Dulacska, 1972); this is as a result of the opening moments that produce tensile stresses at the interface. When there is no such opening moment, the friction contribution comes from the compressive stress due to external loadings or the steel pull-out (Tsoukantas and Tassios, 1989).

2.7 Semi-rigid response consideration

As mentioned earlier, the assumption of ideally-pinned or fully-rigid connections simplifies the analysis and design approaches. Alternatively, when the behaviour of a connection falls between these two extremes, it needs to be dealt with in a different approach using a semi-rigid frame analysis. In this type of analysis, the effect of the connection flexibility in the frame analysis is modelled through rotational springs, attached at member ends, with specified rotational stiffnesses.

To quantify the connection rotational stiffness 'S' for classification purposes and to include it in the analysis, Monforton and Wu (1963) introduced the end-fixity factor 'γ' as a non-dimensional parameter to associate S with the beam stiffness (3EI/L):

$$\gamma = \frac{\theta_e}{\theta_t} = \frac{\theta_e}{\theta + \theta_e} = \frac{\frac{L}{3EI}}{\frac{1}{S} + \frac{L}{3EI}} = \frac{1}{1 + \frac{3EI}{SL}} \qquad (2.13)$$

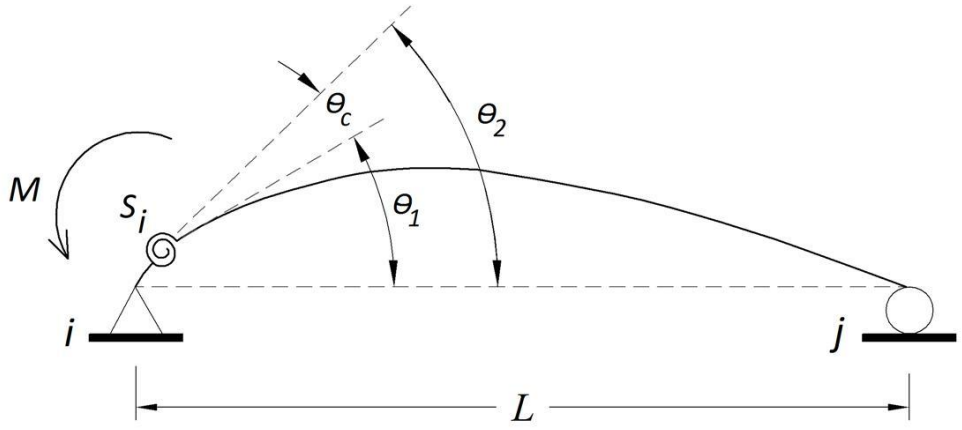

Figure 2.20 Fixity factor rotation components

Where θ_e is the end-rotation due to a unit end-moment, θ is the connection rotation due the semi-rigid behaviour of the connection, and EI/L is the flexural stiffness of the member. S is the rotational spring stiffness, which varies from 0 to ∞ and, by applying Eq. (2.13), γ varies from zero for pinned connections (S = 0) to 1 for fixed connections (S = ∞). Considering both member ends, each member has two fixity factors γ_i and γ_j as shown in Eq. (2.14).

$$\gamma_i = \frac{1}{1 + \frac{3\,E\,I}{S_i\,L}} \quad ; \; \gamma_j = \frac{1}{1 + \frac{3\,E\,I}{S_j\,L}} \tag{2.14}$$

For members with same end rotational stiffness ($\gamma_i = \gamma_j$), the modified beam-end moment 'M_E', modified mid-span moment 'M_S ', mid-span deflection 'δ_s', and the end-rotation 'θ_E' of a single span beam subjected to a uniformly distributed load 'W ' are as given in Eqs. (2.15) to (2.17) and illustrated in Figure 2.21.

$$M_E = M_F \left(\frac{3\,\gamma}{2 + \gamma}\right) \; ; \; M_S = M_F \left(\frac{3 - 1.5\,\gamma}{2 + \gamma}\right) ; \; M_F = \frac{W\,L^2}{12} \tag{2.15}$$

$$\delta_s = \frac{5\,W\,L^4}{384\,EI} \left(\frac{2 - 1.4\,\gamma}{2 + \gamma}\right) \tag{2.16}$$

$$\theta_E = \frac{W\,L^3}{24\,EI} \left(1 - \frac{3\,\gamma}{2 + \gamma}\right) \tag{2.17}$$

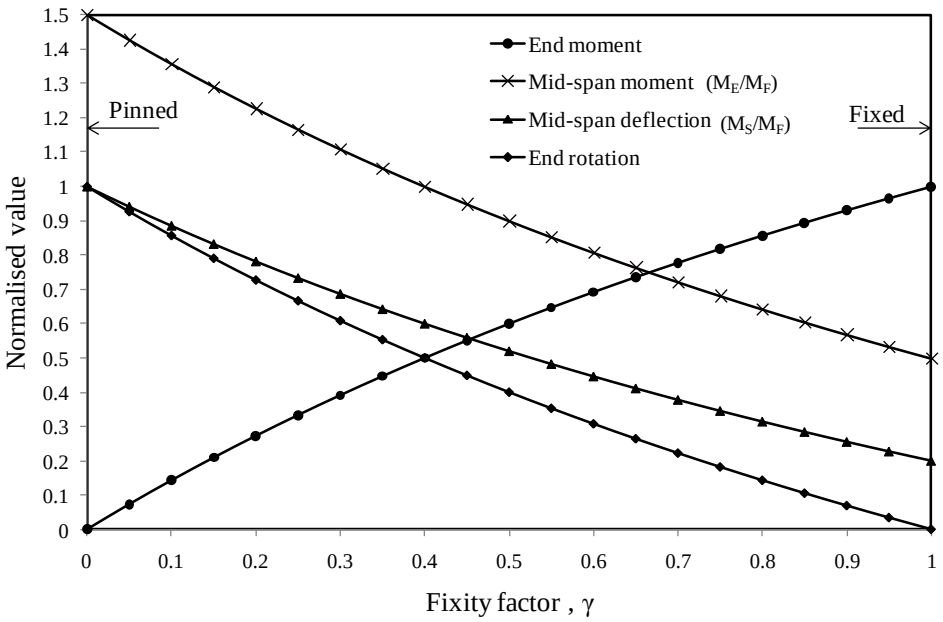

Figure 2.21 Semi-rigid beam moments and deformations versus fixity factor

For instance, Figure 2.22 shows the fixity factor γ for a beam of 6000 mm long, 300 x 400 mm cross-section (second moment of area equal to 1.6E9 m^4) and modulus of elasticity of 38000 N/mm^2 with a beam-column of rotational stiffness 'S' varying from 0 to 600000 kNm/rad. Figure 2.22 reveals that γ is susceptible to the change in S at low stiffness (close to pinned), while the change in S has a very little effect at high stiffness (close to rigid).

Apart from the Brazilian code of practice NBR 9062 (2005), the available concrete codes (EC2 (CEN, 2004b); ACI code, 2008) do not cater for semi-rigid analysis in precast concrete structures, and most of the available classification systems are dealing with steel work, such as the AISC code (2005) and EC3 (CEN, 2005b). Figure 2.22 and Table 2.4 present the limits of four classification systems for defining the boundary of semi-rigid connections based on stiffness. In EC3, the limit between the rigid and semi-rigid zones is based on the Euler instability criterion to ensure that flexibility does not reduce the axial bearing capacity of a member more than 5% (Kishi et al, 1997) and, according to this system; connections could be classified according to their rotational stiffness or their moment resistance.

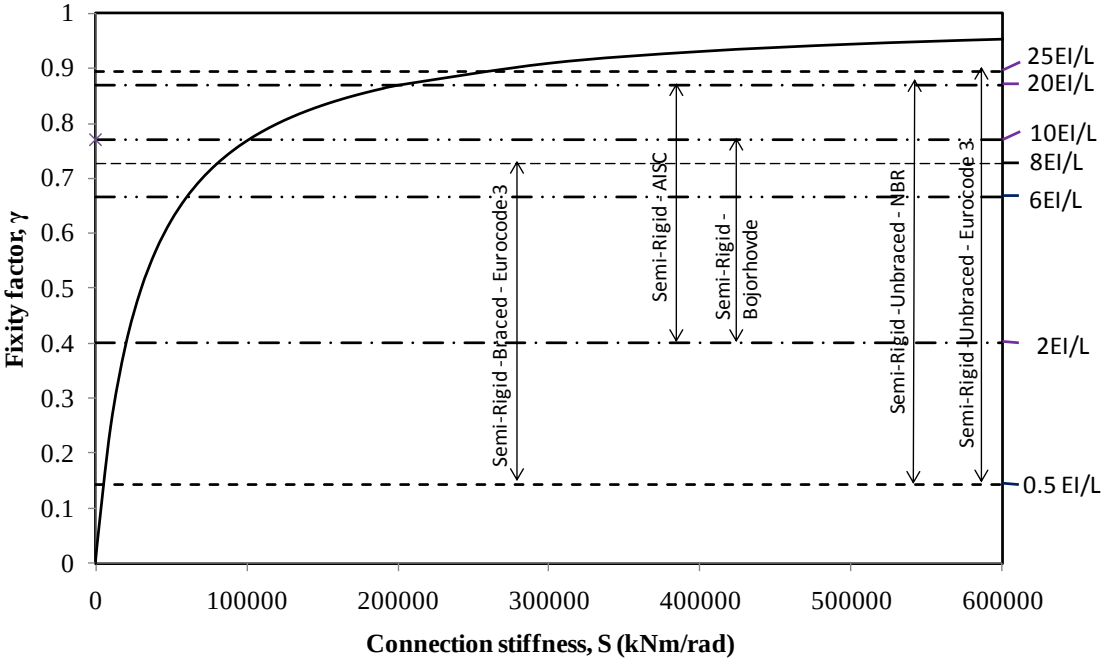

Figure 2.22 Fixity factor versus connection stiffness

Both EC3 and NBR 9062 set 0.5 EI/L, and AISC set 2 EI/L as the rotational stiffness limit for pinned connections. Beyond these limits, connections are considered to be semi-rigid. The limit for considering a connection as rigid is 20 EI/L in both ASCI and NBR 9062, while EC3 distinguishes between braced and unbraced frames by setting 8 EI/L for the first type, and 25 EI/L for the second type. The upper limit for the

semi-rigid behaviour in NBR 9062 (20 EI/L) is lower than that proposed in EC3 (25 EI/L) for unbraced frames, which is possibly due to the fact that NBR 9062 deals with concrete frames where concrete members are stiffer than steel members.

Bjorhovde (1990) suggested a classification system intended for the case where a prior knowledge of the members and structural details are not available. In this system, the connection rotational stiffness is represented by a ratio of the beam rigidity 'EI' divided by a reference beam length 'Lr', which is taken as a multiple of the beam depth 'h'. Lr correlates the connection rotational stiffness 'S' with EI (Lr = EI / S). The connection is classified according to the equivalent reference length Lr; ideally pinned when Lr is less than 2h, semi-rigid when Lr is between 2h and 10h, and as fully rigid when Lr is greater than 10h.

Table 2.4 Connection classification systems

	EC3 (CEN, 2005b)			
	Braced		Unbraced	
	Fixity factor	Rotational Stiffness	Fixity factor	Rotational Stiffness
Rigid	$\gamma < 0.14$	$S < 0.5EI/L$	$\gamma < 0.14$	$S < 0.5EI/L$
Semi-rigid	$0.14 \leq \gamma \leq 0.73$	$0.5EI/L \leq S \leq 8EI/L$	$0.14 \leq \gamma \leq 0.90$	$0.5EI/L \leq S \leq 25EI/L$
Rigid	$0.73 < \gamma$	$8\ EI/L < S$	$0.89 < \gamma$	$25\ EI/L < S$
	NBR 9062 (2005)			
	Fixity factor		Rotational Stiffness	
Rigid	$\gamma < 0.14$		$S < 0.5EI/L$	
Semi-rigid	$0.14 \leq \gamma \leq 0.86$		$0.5EI/L \leq S \leq 20EI/L$	
Rigid	$0.86 < \gamma$		$20\ EI/L < S$	
	AISC (2005)			
	Fixity factor		Rotational Stiffness	
Rigid	$\gamma < 0.40$		$S < 2EI/L$	
Semi-rigid	$0.40 \leq \gamma \leq 0.86$		$2EI/L \leq S \leq 20EI/L$	
Rigid	$0.86 < \gamma$		$20\ EI/L < S$	
	Bjorhovde et al (1990)			
	Fixity factor		Rotational Stiffness	
Rigid	$\gamma < 0.40$		$S < 2EI/L$	
Semi-rigid	$0.40 \leq \gamma \leq 0.77$		$2EI/L \leq S \leq 10EI/L$	
Rigid	$0.77 < \gamma$		$10\ EI/L < S$	

Based on the strength, EC3 classifies a connection as pinned when the design moment resistance of the connection 'M_{con}' is less than or equal to 25% of the design moment resistance of the beam 'M_b'. Besides, the connection is categorised as rigid

when M_c is not less than M_b. Similarly, AISC suggests classifying a connection as pinned when M_{con}/M_b is less than 0.2. Bjorhovde et al (1990) classified a connection as pinned, semi-rigid and rigid when the M_{con} is less than 20% M_b, between 20% M_b and 70% M_b, and greater than 70% M_b, respectively.

Nethercot et al (1998) pointed out that the separate use of the stiffness and strength criteria in the EC3 classification system gives inconsistent results, and might place a connection in two different categories; for instance, a connection could be classified as partial strength and rigid at the same time. Therefore, Nethercot et al suggested that both the strength and stiffness characteristics need to be considered simultaneously in classifying connections. In this trend, Ferreira (2001) suggested a classification system for connections in unbraced frames that works in this direction. In this system (Figure 2.23), in addition to the ideally pinned (zone I) and fully rigid zone (zone V), the semi-rigid zone is divided into three zones: semi-rigid low-strength (zone II), semi-rigid medium-strength (zone III), and semi-rigid high-strength (zone IV).

According to Ferreira (2001), connections of zone II ($0.14 \leq \gamma \leq 0.4$, $0.2 \leq M_E/M_F \leq 0.5$) are not suitable to be used to act in resisting moment; in spite of that, this use would help to reduce the lateral drifts and column base moments. Connection in zone III ($0.4 \leq \gamma \leq 0.67$, $0.5 \leq M_E/M_F \leq 0.75$) can restrain 50% to 75% of the fully-rigid connections and could be used to act in resisting moments. Connections in zone IV ($0.67 \leq \gamma \leq 0.86$, $0.75 \leq M_E/M_F \leq 0.9$), which can restrain 75% to 90% of the fully-rigid connections, are quite suitable to be used in unbraced frames up to 10 storeys. Regarding ductility requirements, connections of zone III are required to be proved experimentally that they offer sufficient ductility to be suitable for stabilisation of sway

frames, while connections of zone IV were proposed to be suitable to be used in a non-seismic zone without the need for verification of ductility.

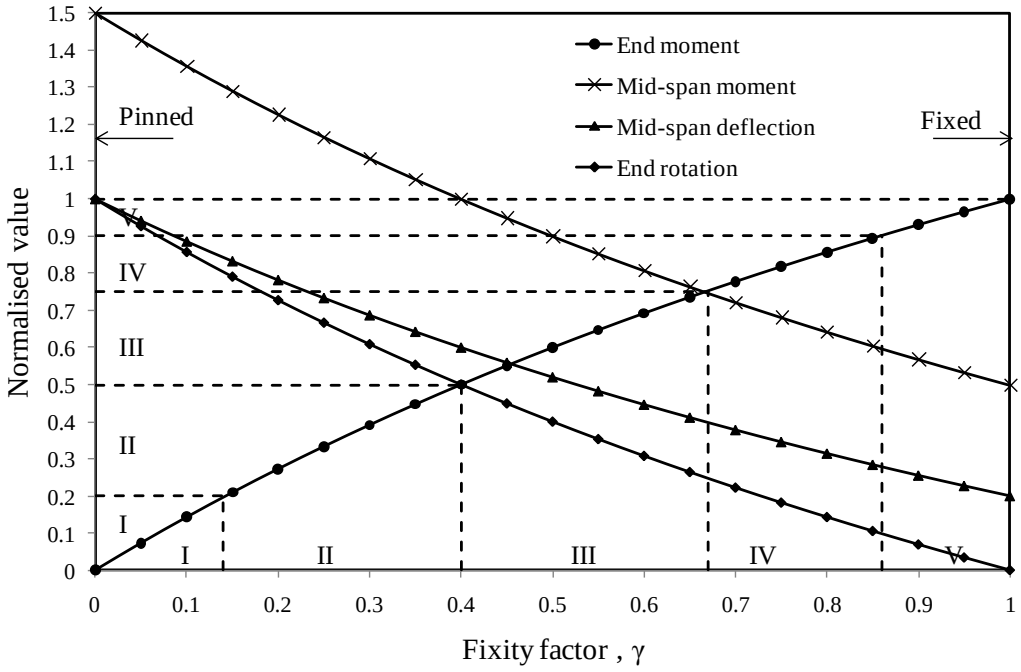

Figure 2.23 Ferreira's classification system (Ferreira, 2001)

2.8 Semi-rigid joint modelling

As has been shown earlier, the connection rotational stiffness 'S' is considered an essential measure for the deformability and for characterising the behaviour of beam-column connections, whether it is pinned, rigid or semi-rigid. In the case of the semi-rigid connections, S is required to be used in the frame analysis, which could be found most effectively by experimental tests. However, for economical reasons, developing theoretical models for characterising connection rotational behaviour is essential and it is a cost-effective alternative tool.

To determine S (M/θ), two connection parameters are required including the moment capacity 'M' and the relative beam-column rotation 'θ'. For a non-linear moment-rotation (M-θ) relation, S could be incorporated in the frame analysis in two different ways:

(i) using an actual non-linear moment-rotation relation (M-θ, curve 1 in Figure 2.24) to characterise connections. For instance, this could be done in ANSYS software (2004) by assigning non-linear rotational springs COMBIN39 at the member ends;

(ii) using a bilinear elastic idealisation for M-θ to characterise the connection behaviour. The initial stiffness 'S_{in}' characterises the uncracked section, but it is too high to be used in frame analyses taking into consideration the stiffness degradation with the increase in the moment. Therefore, as a conservative approximation, the secant rotational stiffness 'S_y' at the onset of yielding of reinforcement (curve 2 in Figure 2.24) could be used in semi-rigid frame analysis; S_y in the current study will be called *yield secant rotational stiffness*, which could be incorporated in ANSYS software (2004) by assigning linear rotational springs COMBIN14 with stiffness equal to S_y at the member ends.

In the 2nd approach, the bilinear relation (curve 2 in Figure 2.24) provides a practical characterising for M-θ relation by providing S_y, which gives an integrated average of how the connection behaved until this point. Also, the true rotational stiffness at the service load stage for a single beam of length 'L' with second moment of area 'I', modulus of elasticity 'E', and subjected to a uniform distributed load 'W' could be found by using the so-called beam-line (Figure 2.24). The beam-line represents the flexural characteristics M-θ of a beam subjected to a certain load in the elastic state. The intersection of the experimental curve (curve 1) with the beam line (curve 3) will give the compatible moment 'M_{se}', rotational deformation 'θ_{se}', and the rotational stiffness 'S_{se}' would be equal to M_{se} / θ_{se}.

Gorgun (1997) and Mahdi (1992) used what was called the ultimate secant rotational stiffness 'S_u' (M_u / θ_u) to characterise the connection behaviour which covers both the elastic and plastic parts behaviour. In the current study, S_y is used to characterise the behaviour of the investigated beam-column connection within the elastic range, and considering S_y as the representative measure for the semi-rigid behaviour under gravity and wind loads.

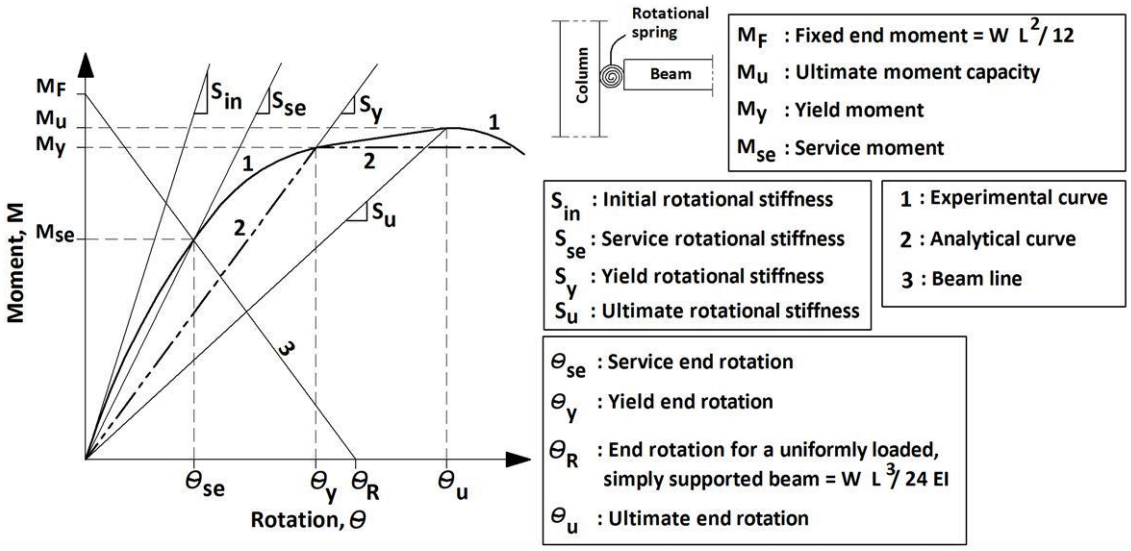

Figure 2.24 Rotational stiffness

Any analytical models should provide a realistic estimation for the two parameters M_y and θ_y. The beam-column connection type investigated in the current study has continuity bars crossing the connection that make it potentially capable to mobilise the full beam hogging moment, and therefore the conventional method for determining M_y could be used, which will be validated experimentally. However, the challenge task is estimating θ_y, which will be determined in the current study through analytical modelling.

As there are many different beam-column connection configurations which imply the need for several models, each one could model a certain type or a range of similar types of beam-column connections. From the literature review, it appeared that there

are very limited calculation methods for modelling the M-θ relation of precast concrete beam-column connection with continuity beam steel bars crossing the connection. For such connection type, Ferreira (2001) proposed that the column and beam relative rotation θ_y at yielding, in beam-column connections with continuity bars crossing the connection, is attributed to joint opening resulting from the elongation of the beam tensile reinforcement within the anchorage length in the column ($f_y\ l_e/E_s\ d$), and to the beam end rotational deformation ($M_y\ l_p/E_c\ I_{eff}$) within a discrete zone at the beam end (Figure 2.25 and Figure 2.26). The moment-rotation response is characterised by the secant rotation stiffness at the first yield of the longitudinal reinforcement.

$$\theta_y = \frac{M_y}{E_c\ I_{eff}}\ l_p + \frac{f_y}{E_s\ d}\ l_e \tag{2.18}$$

$$S_y = \frac{M_y}{\theta_y} \tag{2.19}$$

$$I_{eff} = \left(\frac{M_{cr}}{M}\right)^3 I_I + \left[1 - \left(\frac{M_{cr}}{M}\right)^3\right]\ I_{II} \tag{2.20}$$

In which,

E_s: modulus of elasticity of steel

E_c: modulus of elasticity of concrete

I_{eff}: effective concrete's second moment of area considering crack formation

I_I: second moment of area of uncracked section

I_{II}: second moment of area of cracked section

l_p: plastic hinge length, as it was called by Ferriera (2001) at that time, where there is a concentration of cracks of the connection region, which is associated with the height of the beam section

l_e: available anchorage length within the column

M: bending moment

M_y: yield moment

M_{cr}: cracking moment

S_y : secant rotational stiffness at yielding of reinforcement

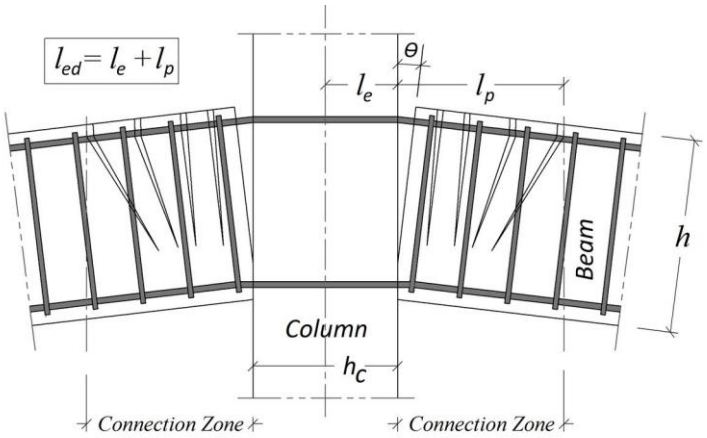

Figure 2.25 Connection zone concept (Ferreira, 2001)

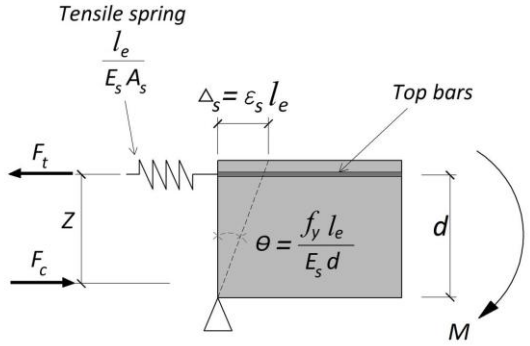

Figure 2.26 Spring model for beam-column rotation due to joint opening at column face (Ferreira, 2001)

2.9 Summary and conclusion

To sum up the literature review presented in this chapter, and to set the required base lines to design the experimental tests in the current study, the points below could be summarised.

1- Regarding discontinuous beam-column connection with continuity bars extended from the bottom column to the top column through grouted sleeves, and beam continuity reinforcement embedded in a trough in the beam, no investigation has been found within the available sources. Therefore, there is scope for investigating this connection type.

2- Regarding the joint infill, below points will be considered in the design of the full-scale tests; however, they will be examined in current research through small-scale tests (Chapter 3).

i) Avoiding the use of soft infill materials as they introduce complicated load-rotation behaviour at large deflections

ii) Using a rigid infill (like cement-based grout) of compressive strength of not less the compressive strength of the precast concrete members (Saleh, 2006; *fib*, 2008)

iii) Using a joint infill of thickness equal to 1/15 of the minimum thickness of the adjoining members to ensure that any possible variation in the grout infill strength in the full-scale tests will have no effect on the bearing capacity of the system

3- Column to column joints made by means of grouted steel bars could achieve a load capacity, and introduce an axial load-bending moment interaction diagram the same as a monolithic column. To achieve this, in the current research, the following points will be taken in consideration in the construction of the full-scale beam-column specimens.

i) A grout mix of 1:1 sand/cement with shrinkage reducing admixture will be used in this study; the water/cement ratio will be determined upon the required fluidity and strength through trial mixes (Appendix D)

ii) Using galvanized steel sleeves (ducts) instead of plastic ducts

iii) Providing a minimum concrete cover for the sleeves of not less than the sleeve diameter

iv) The sleeves should be 0.6 mm as a minmum thickness

v) Using sleeves with a diameter that is at least 30 mm greater than the projecting bars

vi) The minimum grout strength should not be less than 34.5 MPa and close to the joined member strengths

vii) The used grout should be non-shrink

viii) Confinement steel needs to be used around the sleeves

ix) Taking consideration to place the connectors at the sleeve centre

4- Behaviour models: In this chapter, the bond behaviour mechanism between steel bars and concrete/grout and the dowel behaviour mechanism of the column main bars that pass through sleeves in the beam have been presented based on CEB-FIP Model Code 1990 (1993). These models will be used as bases for the theoretical modelling in the current research.

5- Semi-rigid behaviour: It was shown in this chapter that, apart from the Brazilian code of practice NBR 9062 (2005), the available concrete codes (EC2 (CEN, 2004b); ACI Code (2008)) do not cater for semi-rigid analysis in precast concrete structures. However, there is recognition of this kind of behaviour in the steel design codes such as AISC (2005) and EC3 (CEN, 2005b). In the current research, the classification system proposed by EC3 will be used as the base for a classification system for the new precast concrete beam-column connections.

6- Theoretical modelling: a lack of modelling tools for connections with continuity beam top bars crossing the connection was observed. In the current research, Ferreira's model (2001) will be extended and calibrated against the experimental results obtained from this study.

CHAPTER 3

BIAXIAL LOADING TEST RESULTS AND DISCUSSION

3.1 Introduction

One of the key components in the precast concrete beam-column connection investigated in the current study is the joint infill, which exists in two forms: horizontal and vertical (Figure 3.1). The horizontal joints are filled using solid infill (concrete or grouts) or soft infill (Neoprene), while the vertical joint is either left as a gap (see Figure 1.1) or filled with solid infill (concrete or grout) or soft infill (Polystyrene sheet). The geometric shape and surface characteristics of the joints and physical properties of the used infill material are the major factors in the load transfer mechanism.

In Chapter 2, it has been shown that using soft infill introduced a complicated load-rotation curve as a result of the thrust between beams at large deflections (Comair and Dardare (1992); de Chefdbien and Dardare (1994)); therefore, this alternative was not considered as a potential infill option to be used in the beam-column type investigated in this study.

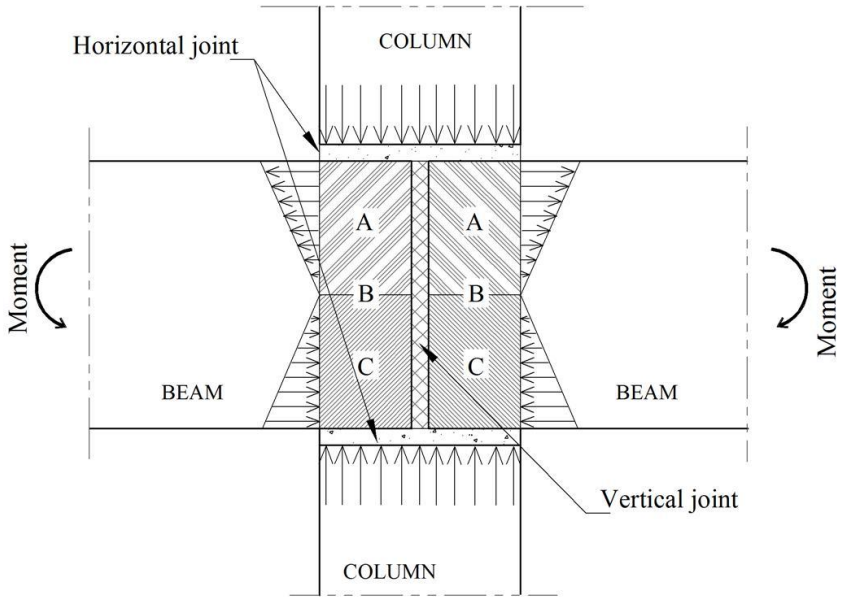

Figure 3.1 Stress distribution around beam-column joint under gravity loads

In this chapter, the experimental programme and the results of small-scale beam-column connection specimens tested under biaxial loading are presented. This preliminary investigation is essential for the design of the full-scale tests to set the status and thickness of the joints. To serve in this direction, the following variables were tested.

i) The status of the horizontal joints; direct contact or 10 mm cement-based grout.

ii) The status of the vertical joint; 10 mm gap or 10 mm cement-based grout.

iii) Beam axial load to column axial load ratio; 0%, 20%, 50%, 75%.

The used 10 mm joint thickness was based on the literature review; it was reported that a joint of a thickness less than 1/15 of the minimum dimension and of strength grade not less than 50% of the adjoining members does not decrease the ultimate bearing capacity (Dragosavic, 1978). The intention from this thickness was to investigate the validity of this suggestion in beam-column configuration, keeping in mind that Dragosavic's statement was based on tests of joints in axially loaded members.

The concrete in the beam-column connection is under a biaxial state of stress (Figure 3.1); under gravity loads, the vertical stress in the column is mainly compression, while the horizontal stresses in the beams vary along the depth due to hogging moment. From Figure 3.1, it is clear that the beam part within the connection is subjected to three types of stress states. At zone A, there is a biaxial compression-tension state, while at zone C there is a biaxial compression-compression state. At the line between zones A and B, the concrete is only subjected to a uniaxial vertical compression stress. As the joint infill is only active under compression stress, the main focus in this research part was towards zone A (biaxial compressive stress status). This

is because, in order to resist tensile stresses across the connection, steel ties are required. However, in spite of that, two tests were conducted to show the connection response under direct tensile force applied to the beam.

3.2 Test Programme

3.2.1 Description of test series

The experimental programme consisted of seven series: CC1 to CC5 tested under biaxial compression loading, CT tested under biaxial compression-tension loading, and C tested for a uniaxial compression load. The geometry, loading, and main variables in the series are shown in Table 3.1 and Figure 3.2. Figure 3.3 shows the test rig for series CC1 to CC5, while Figure 3.4 shows the test rig for series CT. The aims of the tests were as below.

i) Series CC1, CC2 and CC3: to investigate the effects of three different statuses for the joints on the ultimate bearing capacity under different load ratios. Also, series CC1 and CC2 were compared to investigate the effects of the vertical joint status on the strain distribution in the column and beam.

ii) Series CC4 and CC5: to investigate the effects of the horizontal joint status on the stress distribution in the column under different load ratios.

iii) Series CT: to examine the weak point in a plain discontinuous precast concrete beam-column connection for transferring beam tensile forces.

It should be mentioned that, in each of series CC4 and CC5, three tests were conducted using only one specimen. It was important to examine the effects of the load ratio on the stress distribution while keeping the same contact status for the grout with the column and beam. For each series (CC4 and CC5), in the first loading ratio (20%), the loads were applied up to 50% of the predicted ultimate bearing capacity, followed by

unloading. Then, the same specimen was used for the other two loading ratios (50% and 75%) up to the same loading level.

Table 3.1 Details of biaxial loading test specimens

Series	Test No.	Loading ratio (P1/P2) *	Vertical joint status	Horizontal joint status
C	C1	-------	-------	-------
CC1	CC10	1 / 0.00	Gap	Direct contact
	CC1a	1 / 0.20	Gap	Direct contact
	CC1aa	1 / 0.35	Gap	Direct contact
CC2	CC20	1 / 00.0	Grout	Direct contact
	CC2a	1 / 0.20	Grout	Direct contact
	CC2b	1 / 0.50	Grout	Direct contact
	CC3c	1 / 0.75	Grout	Direct contact
CC3	CC3a	1 / 0.20	Grout	Grout
	CC3b	1 / 0.50	Grout	Grout
	CC3c	1 / 0.75	Grout	Grout
CC4#	CC4a	1 / 0.20	Grout	Direct contact
	CC4b	1 / 0.50	Grout	Direct contact
	CC4c	1 / 0.75	Grout	Direct contact
CC5#	CC5a	1 / 0.20	Grout	Grout
	CC5b	1 / 0.50	Grout	Grout
	CC5c	1 / 0.75	Grout	Grout
CT	CT1	-1 / + 0.15	Gap	Direct contact
Notes	* [P1: column vertical load, P2: beam horizontal load] # Three tests were performed using one specimen for the three column load/beam load ratios. The applied loads in series CC1 to CC5 were compressive loads, while in series CT, the +ve sign refers to tensile loads and the –ve sign refers to compressive loads.			

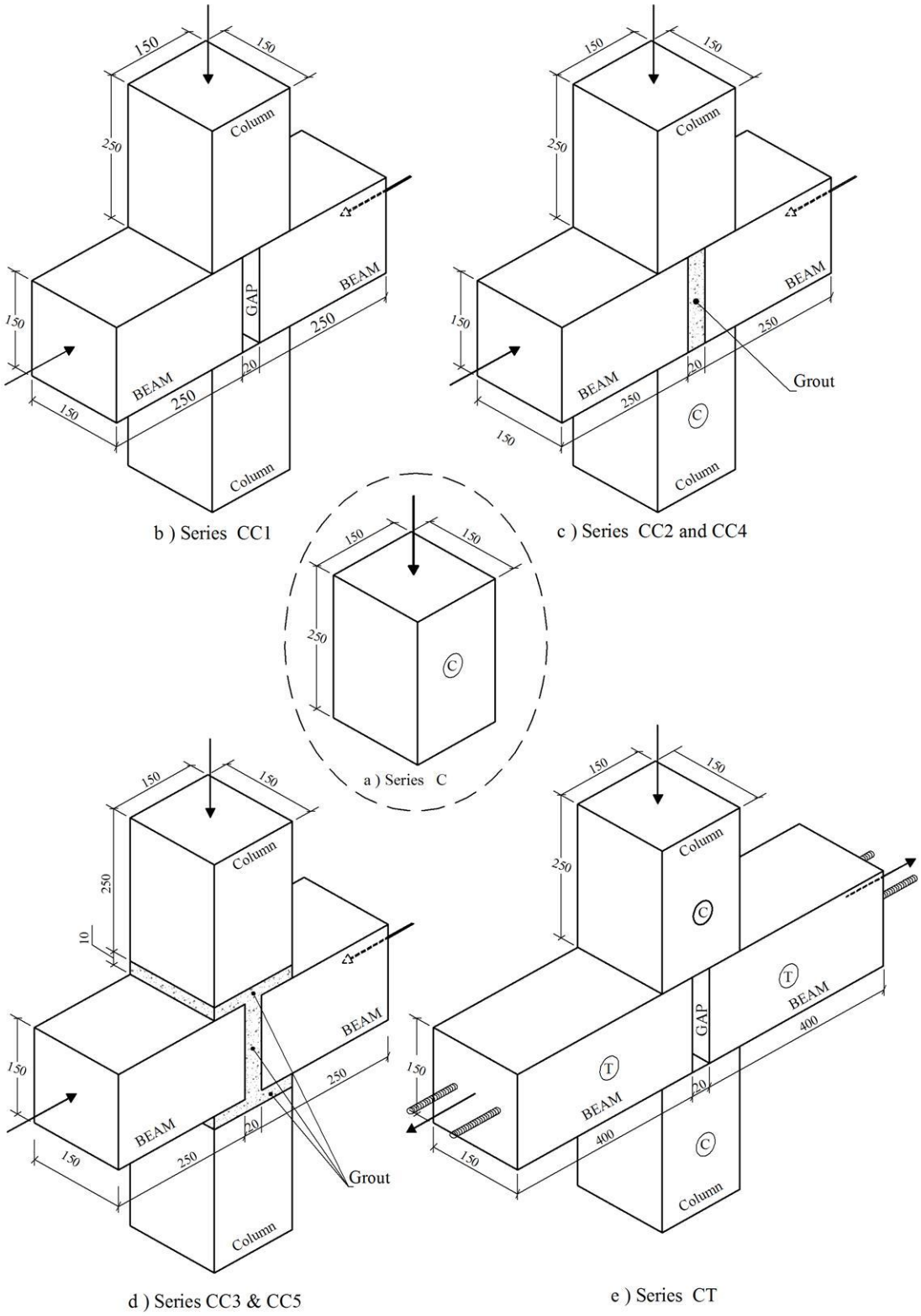

Figure 3.2 Geometry and configuration of series tested (C, CC1 to CC5 and CT)

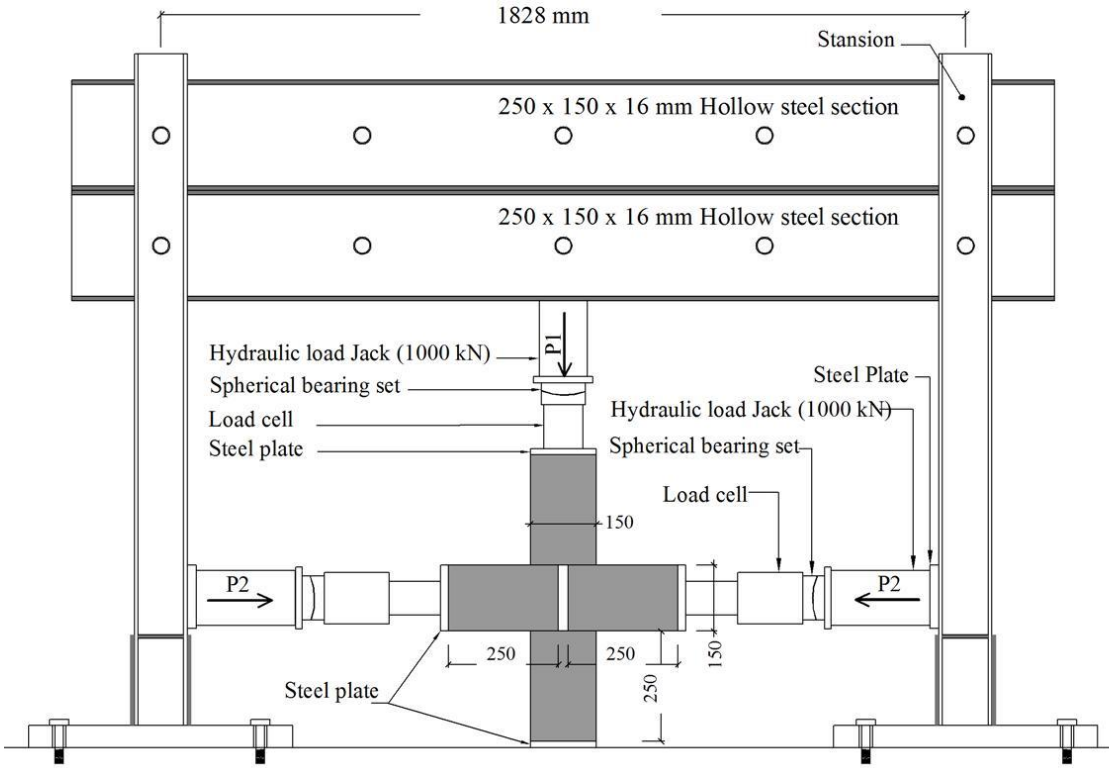

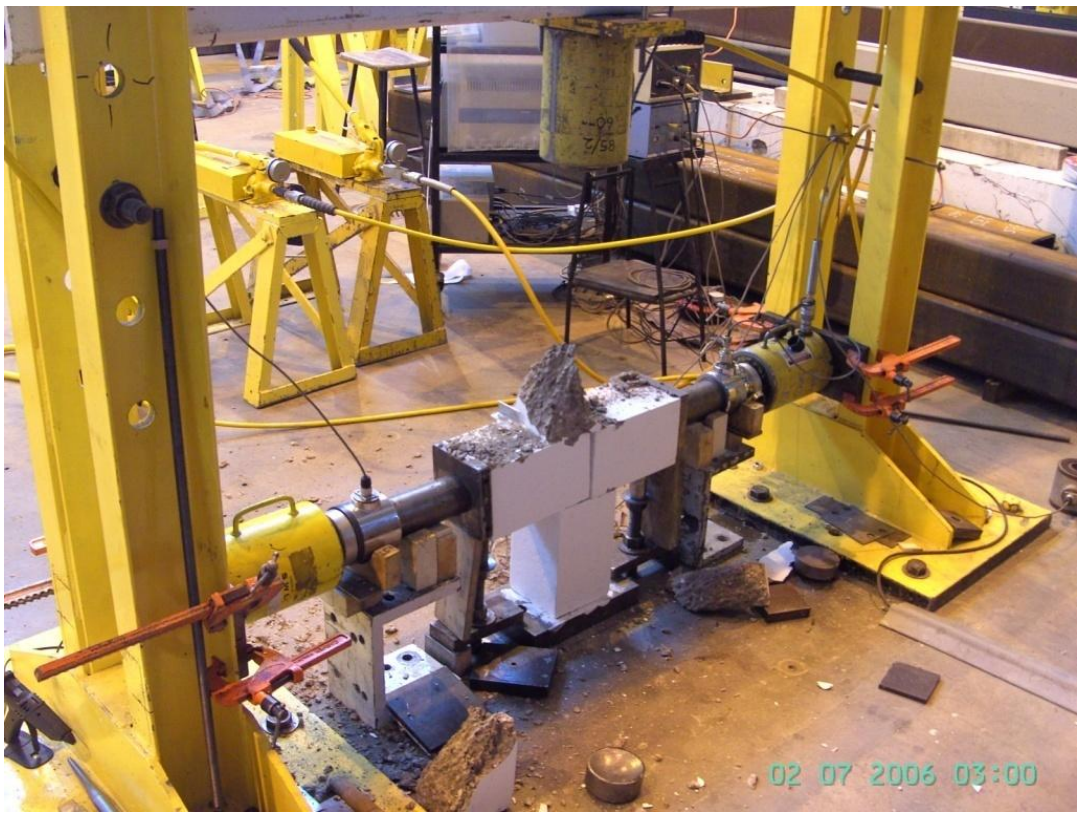

Figure 3.3 Test rig for series CC1 to CC5

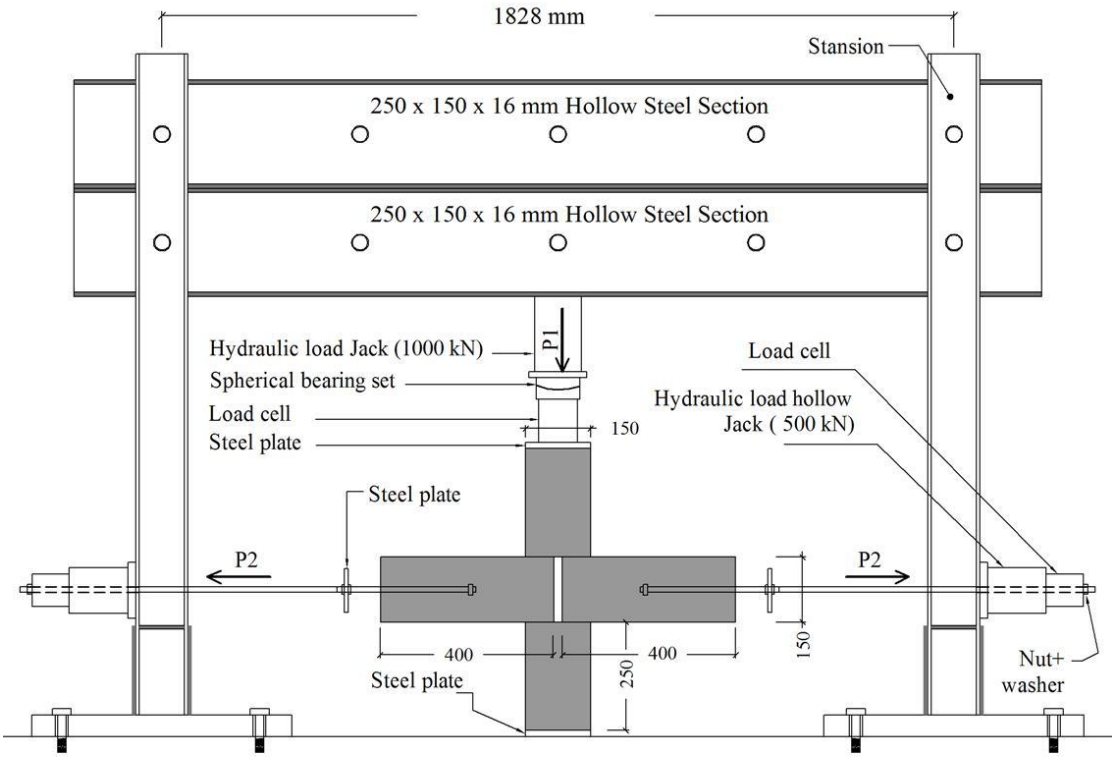

Figure 3.4 Test rig for series CT

3.2.2 Strain measurement

The strain distribution around joint interfaces is mainly affected by the joint conditions (status) within the connections. The vertical joint between the beam-ends could be filled with grout or left as a gap, while the two horizontal joints between the column and the beam could be filled with grout or be in direct contact status. Figure 3.5 shows the ideal load path under biaxial compressive-compressive loading for series CC1 and CC2 assuming that all the adjoining members at region A are in full contact without any possibilities for movement. In practice, this situation is difficult to guarantee, especially in the case where there is no horizontal joint infill. The condition might lead to a strain distribution differing from the proposed one. In this respect, to investigate the strain distribution, it was essential to provide strain gauges within adjoining members' minimum dimensions (D Zone).

This principle was applied in series CC4 and CC5 as shown in Figure 3.6, where 10 strain gauges were provided in the top column within 172.5 mm distance (1.15 h; h: member depth) from the joint interface. The intention was to investigate the effect of the horizontal joint infill on the stress distribution in the column. From the results, it appeared that these effects could be captured within the first row of strain gauges; therefore, fewer strain gauges were provided in series CC1 to CC3 to examine the effects of the vertical infill on the stress distribution in the column and beam.

Electrical resistance strain gauges of 30 mm length (triple the size of the maximum coarse aggregate) of PFL-30-11 type were used. A multi-channel computer-operated data acquisition system was used to record the data.

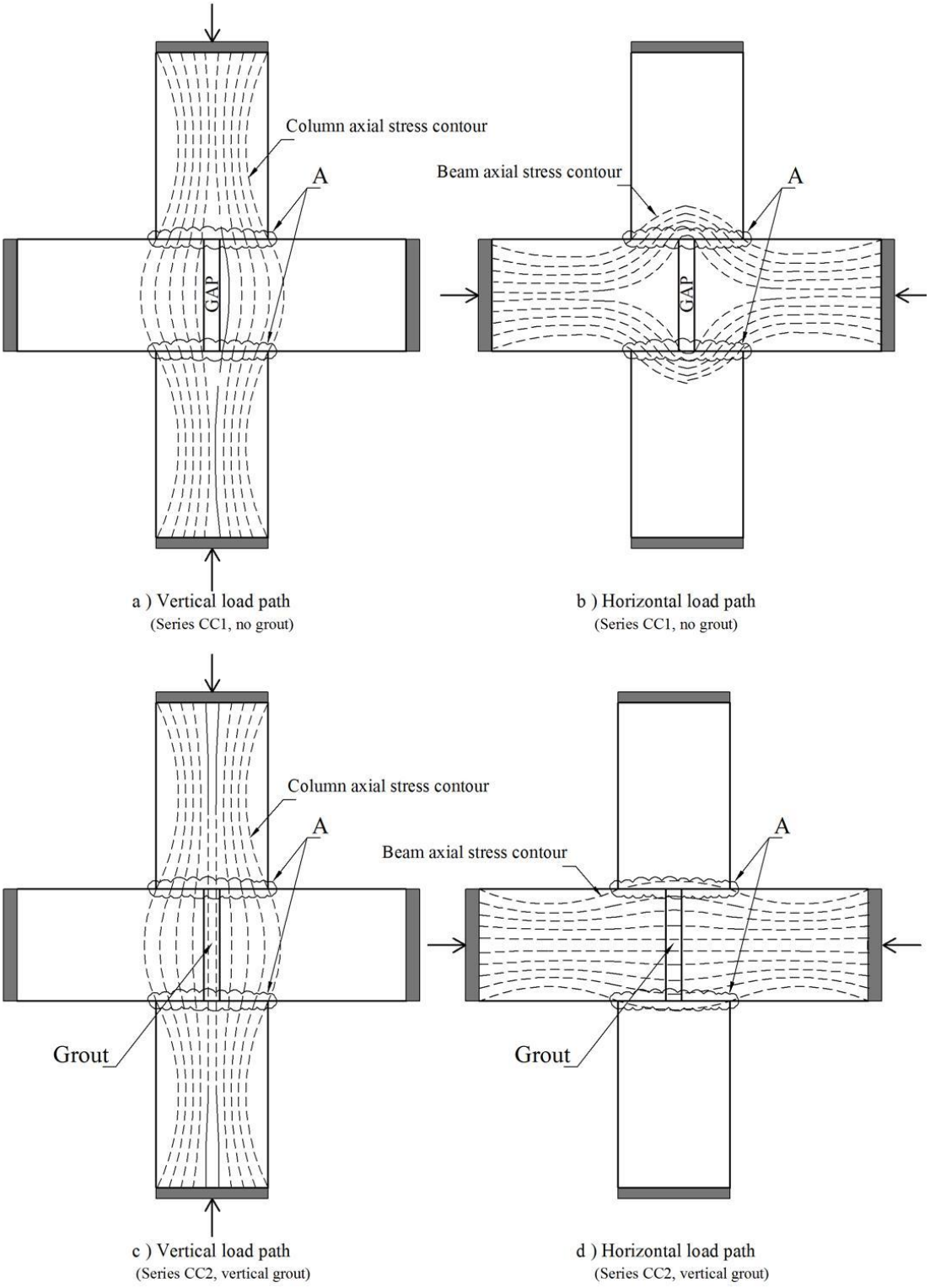

Figure 3.5 Load path through the joint

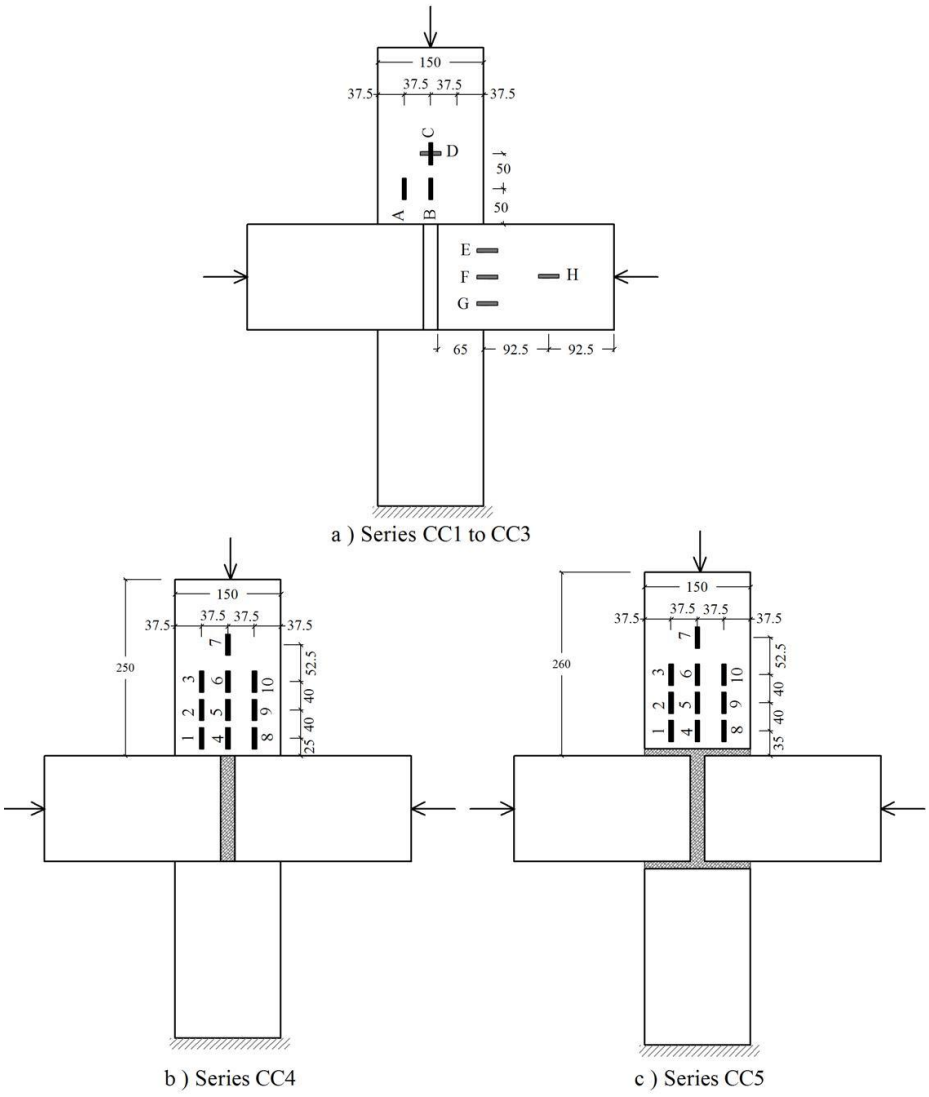

Figure 3.6 Strain gauge layout in series CC1 to CC5

3.2.3 Material properties

Cement of type CEM II/A-L 32.5 R and river sand were used in the concrete and cement-based grout, while 10 mm crushed stone was used as a coarse aggregate in the concrete. The sieve analysis for the sand is shown in Appendix E. The concrete and grout mixes and properties are summarised in Table 3.2. The concrete was moist cured for seven days and then preserved in air until the day of the test, while the grout was only cured in the laboratory temperature.

As can been seen in Table 3.2, the mix proportion for series CC3 was changed due to running out of the used original cement. Although the new used cement was of

the same type as the original type, it had a higher compressive strength. Therefore, the mix proportion was changed to obtain the same strength. However, the mix proportion for the grout was kept the same as for the original mix, but it was tested at two days age rather than four days age as shown in Table 3.2.

For each concrete mix, four 100 mm control cubes were taken and cured in conditions the same as the tested specimens. Two cubes were tested at seven day age, and the other two were tested on the day of testing the corresponding specimen. For the grout, two 100 mm control cubes were taken and were tested on the day of testing the corresponding specimen.

Table 3.2 Mix proportions for biaxial loading tests

Series	Mix	Targeted strength		Mix proportion per m^3				
		Strength (N/mm^2)	Age (days)	Cement (kg)	Gravel (kg)	Sand (kg)	Water (litres)	Super plasticiser (ml)
C CC1,CC2, CC4, CC5, CT	Concrete	35	12	360	1015	800	215	900
	Grout	35	4	535	1515	----	210	2000
CC3	Concrete	35	8	335	1015	800	191	900
	Grout	40	2	535	1515	-----	210	2000

3.3 Test results and discussion

The results of the specimens tested within the seven series are presented in Table 3.3, including the actual compressive strength of the concrete and grout, applied load ratio, joint status, ultimate stress and the mode of failure. The repeated tests are labelled with an asterisk. The result of series C is the average of seven tests with standard deviation of 1.13 N/mm^2 for the tested specimen, and 1.9 N/mm^2 for the control cube strength. For the other series, the standard deviation for the concrete strength was 1.64 N/mm^2 (excluding series CT), and for the grout it was 3 N/mm^2.

Table 3.3 Biaxial loading test results

No.	Series	Test reference	Cube compressive strength of concrete, f_{cu} (N/mm^2)	Loading ratio (P_1 / P_2)	Vertical joint status	Horizontal joint status	Cube compressive strength of grout, f_{cu} (N/mm^2)	Vertical direction			Failure mode
								Ultimate load (kN)	Nominal stress, σ_u (N/mm^2)	σ_u / f_{cu} (%)	
1	C	C1	35.3	------	------	------	------	599.4	26.6	74.4 %	Crushing
2	CC1	CC1-0	33.5	-1 / 0.00	Gap	D.C	------	450.2	20.0	59.7 %	Cracking
3		CC1-0*	35.5	-1 / 0.00	Gap	D.C	------	428.8	19.0	53.7 %	Cracking
4		CC1-a	35.0	-1 / -0.20	Gap	D.C	------	455.7	20.3	57.9 %	Crushing
5		CC1-a*	37.0	-1 / -0.20	Gap	D.C	------	452.2	20.1	54.3 %	Crushing
6		CC1-aa	34.2	-1 / -0.35	Gap	D.C	------	469.2	20.9	61.0 %	Crushing
7	CC2	CC2-0	33.7	-1 / 0.00	Grout	D.C	32.0	505.3	22.5	66.6 %	Cracking
8		CC2-a	37.7	-1 / 0.20	Grout	D.C	20.8	518.7	23.0	61.1 %	Crushing
9		CC2-a*	32.5	-1 / 0.20	Grout	D.C	36.8	532.3	23.7	72.8 %	Crushing
10		CC2b	34.2	-1 / -0.50	Grout	D.C	34.5	549.4	24.4	71.4 %	Crushing
11		CC2-c	36.2	-1 / -0.75	Grout	D.C	36.3	581.2	25.8	71.4 %	Crushing
12	CC3	CC3-a	38.0	-1 / -0.20	Grout	Grout	45.2	609.9	27.1	71.3 %	Crushing
13		CC3-b	38.0	-1 / -0.50	Grout	Grout	40.0	569.1	25.3	66.6 %	Crushing
14		CC3-b*	34.7	-1 / -0.50	Grout	Grout	33.0	603.2	26.8	77.3%	Crushing
15		CC3-c	38.7	-1 / -0.75	Grout	Grout	43.0	659.0	29.3	75.7 %	Crushing
16	CC4	CC4-a	38.2	-1/ -0.20	Grout	D.C	The load was applied up to 50% of the ultimate load				
17		CC4-b	38.2	-1/ -0.50	Grout	D.C	The load was applied up to 50% of the ultimate load				
18		CC4-c	38.2	-1/ -0.75	Grout	D.C	The load was applied up to 50% of the ultimate load				
19	CC5	CC5-a	39.3	-1/ -0.20	Grout	Grout	The load was applied up to 50% of the ultimate load				
20		CC5-b	39.3	-1/ -0.50	Grout	Grout	The load was applied up to 50% of the ultimate load				
21		CC5-c	39.3	-1/ -0.75	Grout	Grout	The load was applied up to 50% of the ultimate load				
22	CT	CT1	31.0	-1/ +0.15	Gap	D.C	------	100.0	4.4	14.3 %	Cracking
23		CT1*	31.0	-1/ +0.15	Gap	D.C	------	120.0	5.3	17.2%	Cracking
* Repeated tests.						D.C : Direct Contact					

3.3.1 Biaxial compression-compression

3.3.1.1 Ultimate strength and failure modes

In series CC1, it was not possible to apply beam loads greater than 35% of the column load owing to sliding of the beams at higher load ratios as a result of the existence of the vertical gap between the beams. In series CC2 to CC5, beam loads up to 75% of the column loads were applied after providing the vertical infill. Figure 3.7 shows the ultimate bearing capacity versus the beam load/column load ratio for specimens of series CC1 to CC3. From this graph, it could be noticed that:

i) there is a clear boost in the column ultimate bearing strength by providing grout for the vertical infill;

ii) there is no significant effect for the horizontal joint infill on the column ultimate bearing strength;

iii) there is a slight tendency to increase the column ultimate bearing strength by increasing the axial beam load, which works as a confinement for the column; however, due to the scattering of the data, no decisive conclusion could be made.

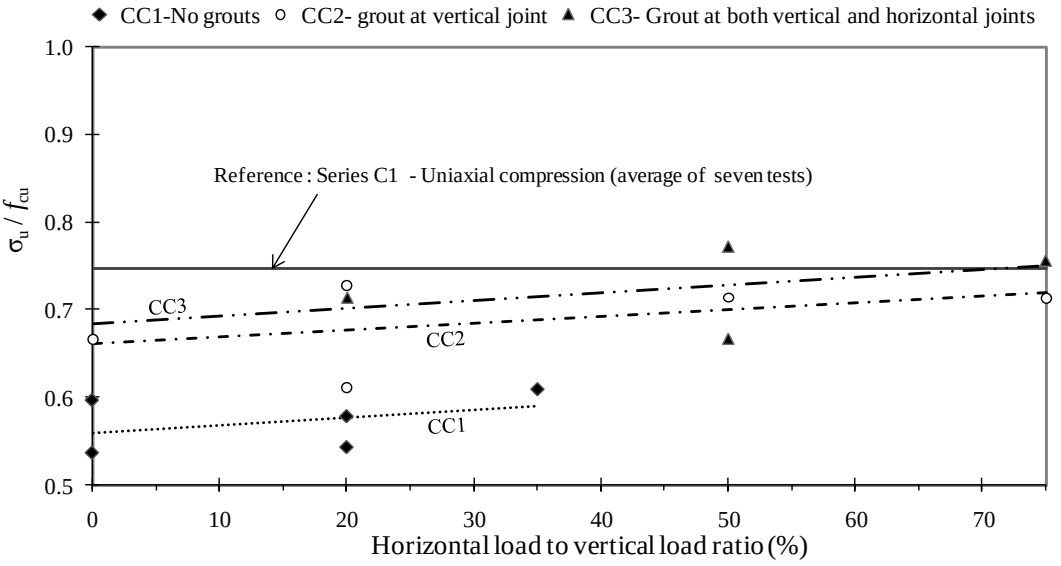

Figure 3.7 Ultimate strength to horizontal/vertical load ratio relation for series CC1 to CC3

In test series CC3, where grout infills are provided at all three joints, the achieved load bearing capacity ranged between 89% and 103% of that obtained in the single block test (C1) without a decisive conclusion for the beam axial load effect. This might suggest that the connection with grouts at all the three joints could be used in the proposed full-scale tests, and the above-mentioned load capacities could be achieved without the need to provide steel plates or horizontal steel nets at the column-ends. The use of steel plates at the joint was recommended by Minnert (1997) and Saleh (2000) to develop a full bearing capacity for the joint. The benefits behind the use of these steel plates in Minnert's test were: (i) increasing the load bearing capacity from 90% to 100% of the calculated bearing capacity, and (ii) transferring the stresses in the steel bars which were welded to the steel plates more effectively. In the current test, the steel bars are crossing the joints to be received by sleeves; therefore, there is already an adequate stress transfer in the column bars. According to the design requirement for the prototype frame (Appendix A), the applied column load (500 kN) in the full scale tests produces a stress in the column equal to only 9 % of the ultimate strength of concrete 'f_{cu}'. The ratio is well below the minimum load bearing capacity of 89%, as a ratio of the single block specimen C1, and 66%, as a ratio of f_{cu}.

As mentioned in the literature review, there is far less agreement regarding the effects of using the horizontal infill (bedding) on the ultimate bearing capacity. Barboza et al (2006) found that it increases the strength up to a limited thickness; however, Saleh (2000) and Gorgun (1997) mentioned that it decreases the strength**.** Theoretically**,** the second point of view is correct if a perfect contact condition is ensured between the adjoining elements without using a joint infill. However, due to practical reasons, it is

not possible to ensure this perfect contact; therefore, the first point of view might be acceptable.

To justify this argument, the results of the current research have shown that use of horizontal cement grout of a thickness equal to 1/15 of the adjoining members' minimum dimension and strength equal to the concrete strength of the precast concrete members did not decrease the strength. In addition, it enhanced the ultimate strength due to the improvement in the strain distribution by reducing local contact regions between the beam and column

With respect to the failure modes experienced in series C1, CC1, CC2 and CC3 (Figure 3.8), the failure mode was crushing in the top column in specimens with beam loads. Though, the failure mode was splitting cracking in the column in the other cases, where no beam loads were applied, due to the absence of confinement forces.

3.3.1.2 Effects of vertical joint status on strain distribution

To investigate the effect of the vertical joint status on the strain distribution, specimens of series CC1 and CC2 are compared. Figure 3.9 shows the effect on the axial strain distribution in the column, while Figure 3.10 shows the effect on the axial strain distribution in the beam, for specimens with 20% beam to column load ratio (specimens CC1-a*, CC2-a*). As can be seen, providing the vertical grout improved the consistency of the strain distribution towards being more uniform. A similar behaviour was observed in the other beam/column load ratios (0%, 50% and 75%) by comparing the corresponding specimens in series CC1 and CC2.

Figure 3.9a shows the inconsistency in the strain distribution that is pronounced through the strain readings at locations B, C and D after a stress level of 0.45 (σ/f_{cu}), where there was a change in the stress development direction.

3.3.1.3 Effects of horizontal joint status on strain distribution

For the effect of using the grout in the horizontal joint on the strain distribution in the column, specimens of series CC4 and CC5 are compared. Figure 3.11shows the effect in specimens with 50% beam to column load ratio (specimens CC4-b and CC5-b). As shown, providing the horizontal grouts helped in producing a consistency in strain distribution in specimen CC5-b. A similar behaviour was observed under the other beam/column loading ratios of 20% and 75%.

To justify the use of one sample for three tests in each of series CC4 and CC5, positioning of the top column was investigated in series CC4 (direct contact between the column and beam). In each specimen of series CC4, an additional test was carried out using a different position for the top column. The new position was made by rotating the top column 180° with respect to its original position. It was noticed that there was a significant difference in the strain distribution as a result of having different local contact statuses. This led to the conclusion that it is difficult to assure a perfect contact condition between the column and beam without using a horizontal grout infill. Apparently, in spite of the fact that using the horizontal grout did affect the ultimate strength significantly, its effect in producing a uniform strain distribution was very clear.

Figure 3.8 Failure modes of series C1, CC1 to CC3

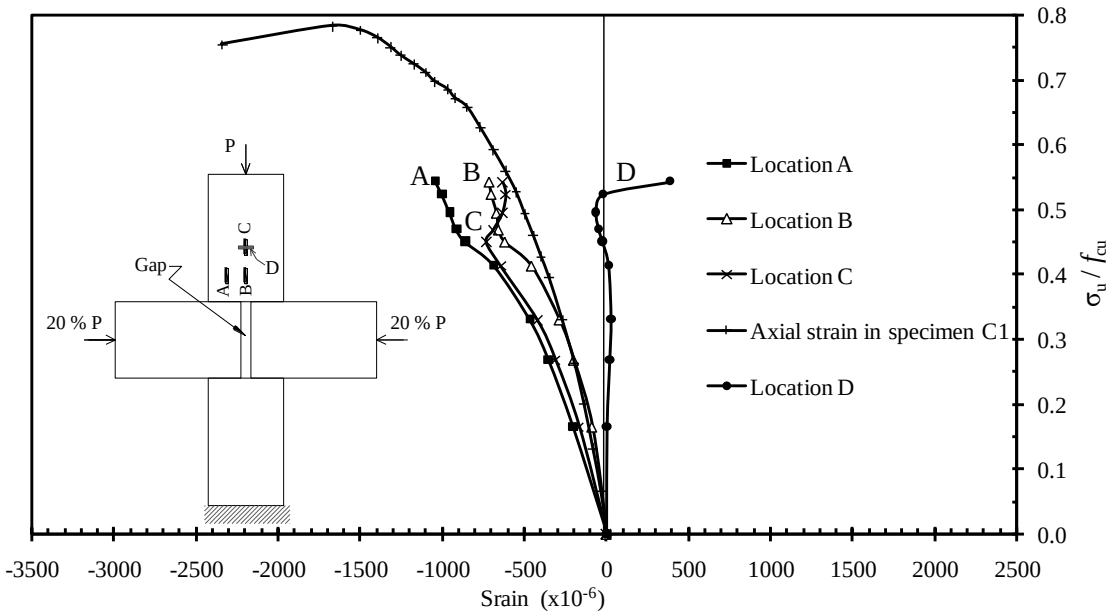

a) Specimen CC1-a* (no vertical joint infill)

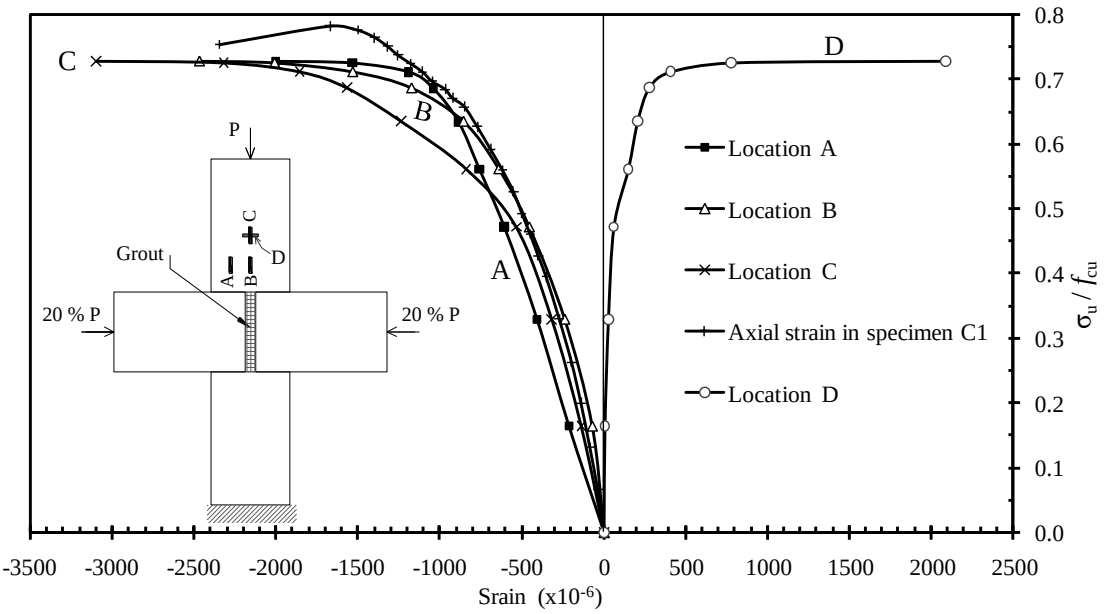

b) Specimen CC2-a* (with vertical joint infill)

Figure 3.9 Effect of vertical joint status on column axial strain distribution

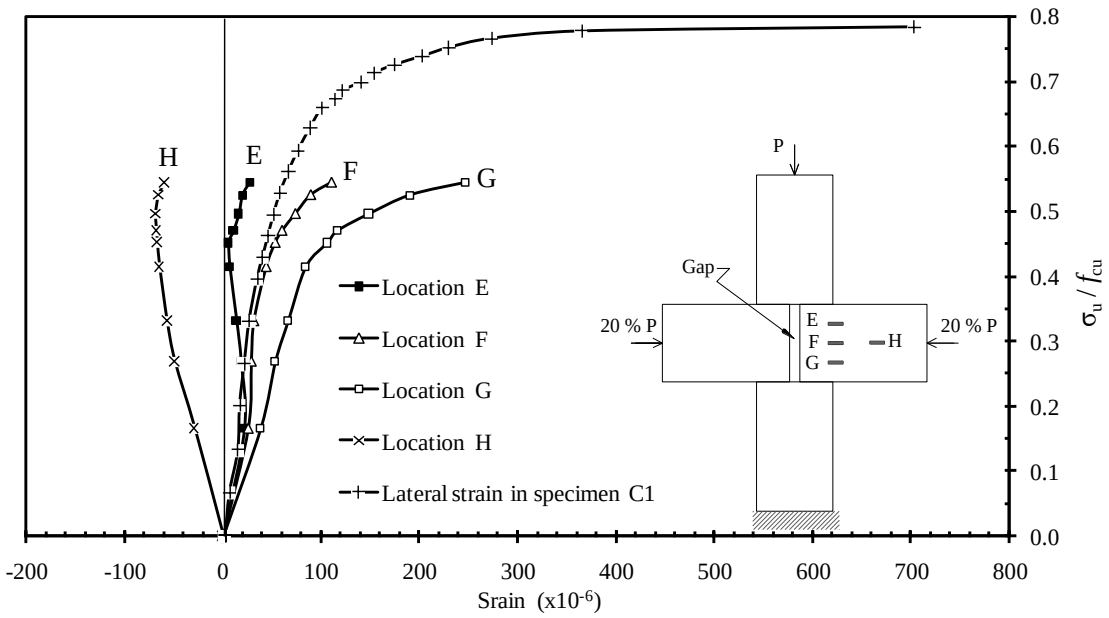

a) Specimen CC1-a* (no vertical joint infill)

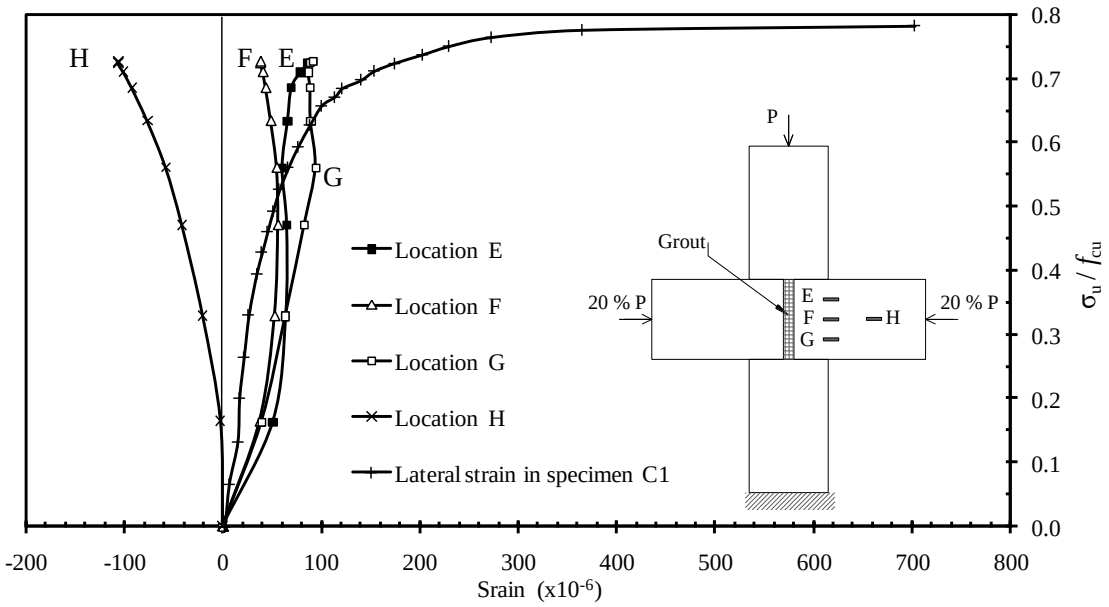

b) Specimen CC2-a* (with vertical joint infill)

Figure 3.10 Effect of vertical joint status on beam axial strain distribution

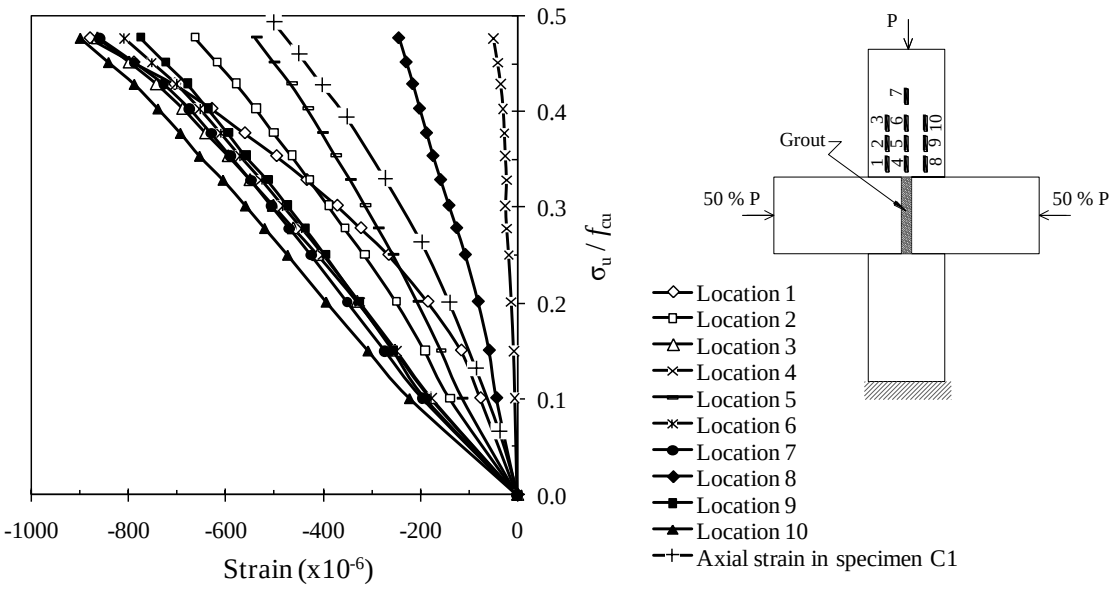

a) Specimen CC4-b (beam-column direct)

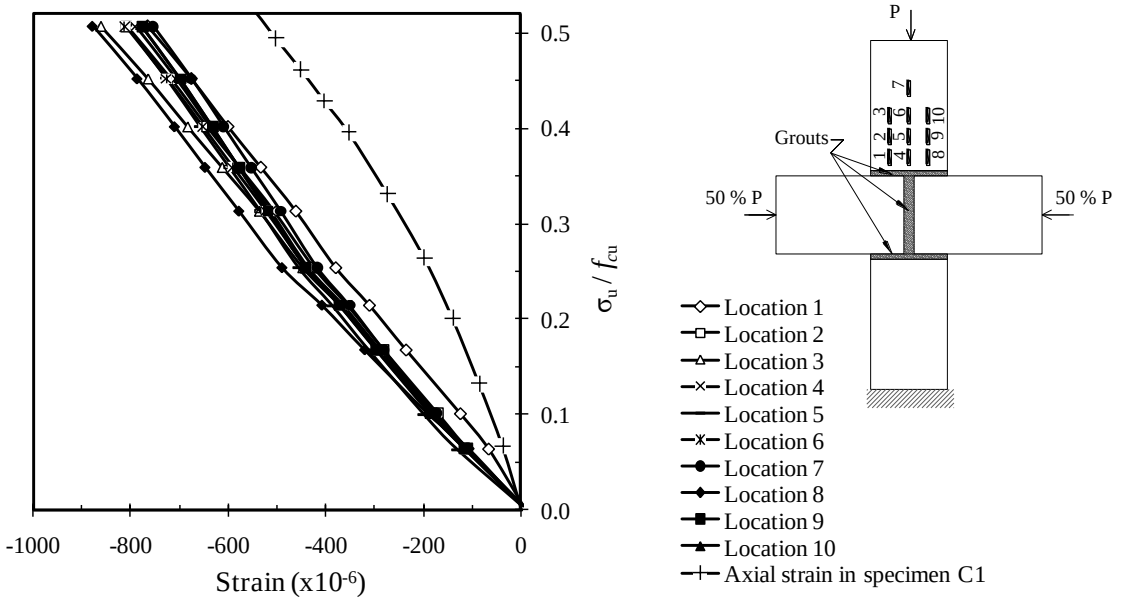

b) Specimen CC5-b (with horizontal joint infill)

Figure 3.11 Effect of horizontal joint status on column axial strain distribution

3.3.2 Biaxial compression-tension

Series CT consisted of two specimens without any joint infill material (CT1 and CT1*) with a beam axial tensile load to column axial compressive load ratio of +0.15/-1.0. The aim was examining the weak point in the system of plain concrete beam and column in transferring beam tensile forces. In specimen CT1, at 100 kN compressive column load (14% of f_{cu}) and 15 kN tensile beam load (25% of f_{ctm}), longitudinal cracks initiated at the middle of the column. The test was repeated by examining specimen CT1*; the same failure mechanism happened at 120 kN column load (17% of f_{cu}) and 18 kN tensile beam load (30% of f_{ctm}). The reason behind this basic behaviour is related to a high intensity of splitting tensile stresses at the middle part of the column adjacent to the gap.

Based on these two results, it could be stated that plain concrete columns are not able to transfer beam tensile forces as it was expected. This emphasised the need for extending the beam bars across the vertical joint to transfer the beam tensile force in a direct way; in addition, column links with small spacings have to be provided near the connection to prevent the occurrence of splitting cracks in the column.

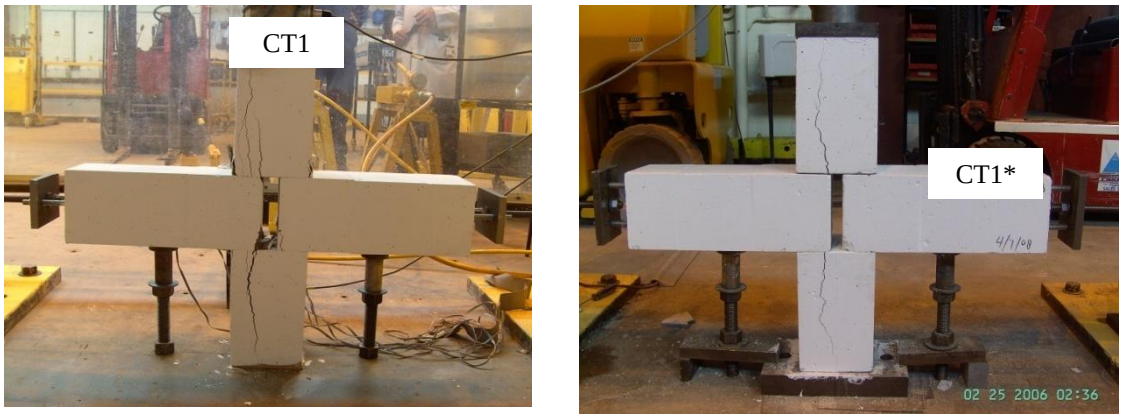

Figure 3.12 Failure modes in series CT

3.4 Summary and conclusion

Upon completion of the preliminary tests on the discontinuous concrete blocks simulating precast concrete beam-column connections under biaxial loads, the following conclusions could be drawn.

1- The connection was able to transmit axial loads and present strength not less than 89% of the uniaxial compressive strength of the single block specimen, and not less than 66% of f_{cu}. This was achieved by using cement grouts at all joints with a thickness of 1/15 of the adjoining members' minimum dimension and strength close to the strength of adjoining members.

2- The vertical gap in the connection should be filled with a structural infill to prevent sliding of the beam.

3- The vertical grout infill provided a sufficient stratum to transfer the loads and achieve a uniform strain distribution in both the column and beam.

4- The existence of the vertical grout infill increased the ultimate bearing capacity of the column.

5- Providing of cement-based grout at the horizontal joints had no significant effects on the ultimate strength. However, it had a marked effect in achieving a uniform strain distribution in the column.

6- The connection is required to be designed to transfer beam tensile forces through steel ties crossing the connection with sufficient column links near the connection.

CHAPTER 4
FULL-SCALE TEST PROGRAMME

4.1 Introduction

This chapter introduces the experimental work setup used for testing full-scale precast concrete beam-column connections subjected to individual gravity (three tests) and sway loads (two tests). The main variable in the test programme was the connection reinforcement detail in order to identify the most effective detail under both gravity and sway loads. The results from the small-scale bearing tests were used to specify the interface joint status and thickness. The thickness was chosen to be 1/15 of the least dimension of the adjoining members, and target strength not less than the strength of the adjoining members based on the results presented in Chapter 3. In this chapter, the test specimens, test rig, and instrumentation, and the studied parameters are presented, while the results and discussion are presented in Chapters 5 and 6. Also, an error analysis is performed to quantify the potential errors in the results reported in the current study.

4.2 Design of experiments

The experiments were designed to test a representative sample that characterise the connection behaviour of an internal beam-column intersection in a prototype building consisting of three spans and four storeys (Appendix A). The number of storeys normally affects the moments generated under sway loads, but without a significant effect on the moments generated under gravity loads. The selected number of storeys was based on counterbalancing the beam-end sagging moment due to wind loads by the hogging moment due to permanent dead and live loads.

The member dimensions, reinforcement, and the column loading (500 kN) used in the specimens are based on a rigid frame analysis and design for the prototype building. The research interested in studying the effects of the proposed modifications

in the conventional connection configuration (see Figure 1.1), which included the following.

i) Providing the continuity bars at the beam-top within the beam itself to be active to work under dead loads.

ii) Grouting the vertical joint between the beams.

iii) The effects of using three reinforcement details for the connection in reducing the crack width and forcing the final failure to occur outside the connection zone. Connection reinforcement type T1 is considered as the reference modification, while the other two types T2 and T3 were compared to it.

The full-scale experimental programme intended to examine if the above modifications (independent variables) make a difference in the behaviour.

4.3 Details of test specimens

4.3.1 Geometry and reinforcement details

The experimental programme consisted of five full-scale beam-column connection specimens, representing an internal connection in a lower floor of a three-bay four-storey building. As shown in Table 4.1 and Figure 4.1, the test specimens were divided into two series: (i) GR, consisted of three specimens subjected to gravity loading (Figure 4.1a), and (ii) SW, consisted of two specimens subjected to sway loading (Figure 4.1b).

The beams and the columns were cast at the SCC Company in Manchester, and assembled at the University's laboratory to form sub-frame specimens. In all tests, the beam had a rectangular cross section with a width of 300 mm and a total depth of 400 mm, whereas the columns had a 300 mm square section. The longitudinal reinforcement of the beams included 2H20 mm diameter deformed bars as the bottom reinforcement,

while the top reinforcement was variable. The longitudinal reinforcement of the columns consisted of 4H20 mm diameter deformed bars. In all tests, over the lengths of the beams and columns, transverse reinforcement of 10 mm diameter deformed bars was used at spacing as shown in Figure 4.3 to Figure 4.5.

Table 4.1 Description of the full-scale beam-column connection tests

Series	Loading type	Test reference (specimen)	Sub-frame detail figures	Connection reinforcement type	Testing situation
GR	Gravity	GR1	Figure 4.1a	T1	Horizontal
		GR2*	Figure 4.1a	T2	Vertical
		GR3	Figure 4.1a	T3	Horizontal
SW	Sway	SW1	Figure 4.1b	T1	Horizontal
		SW2	Figure 4.1b	T3	Horizontal

* Test GR2 is a joint test designed by the researcher, tested by the researcher and Chang, and it has been already published in a Master dissertation (Chang, 2009).

The continuity of the column main bars was provided through corrugated steel sleeves in the beam and in the top column, wherein the continuity of the beam-top bars was provided through a grouted trough in the middle-top of the beam. The precast beam and column were connected using cement-based grout in the sleeves and the trough. To ensure a surface free from laitance at the construction joints, a layer of concrete retarder was applied to the formwork at required locations. The retarder was brushed off after concrete hardening and dismantling of the formwork (Figure 4.2a and Figure 4.2b).

As the main variable in the test, three types of connection reinforcement details were used: T1, T2, and T3, as illustrated in Figure 4.3 and Figure 4.4. The improvement in the connection reinforcement details was towards decreasing the crack widths at the connection zones prior to failure by using type T2, and ultimately forcing the final damage to occur outside the connection zone by using type T3.

The connection reinforcement of type T1 is the reference type, while type T2 was obtained by using additional U-shaped horizontal links at the beam-ends, bending the beam-bottom bars around the column bars, and using of steel links with closer spacing at the column-ends next to the connection side , as shown in Figure 4.4a. For type T3, besides what were provided in type T2, three further links were added at the column ends close to the connection with additional 2H20 mm beam-top steel bars of 1100 mm length that crossed the connection. The justification for the use of the connection reinforcement of types T2 and T3 will be apparent within the presentations of the results in Chapters 5 and 6.

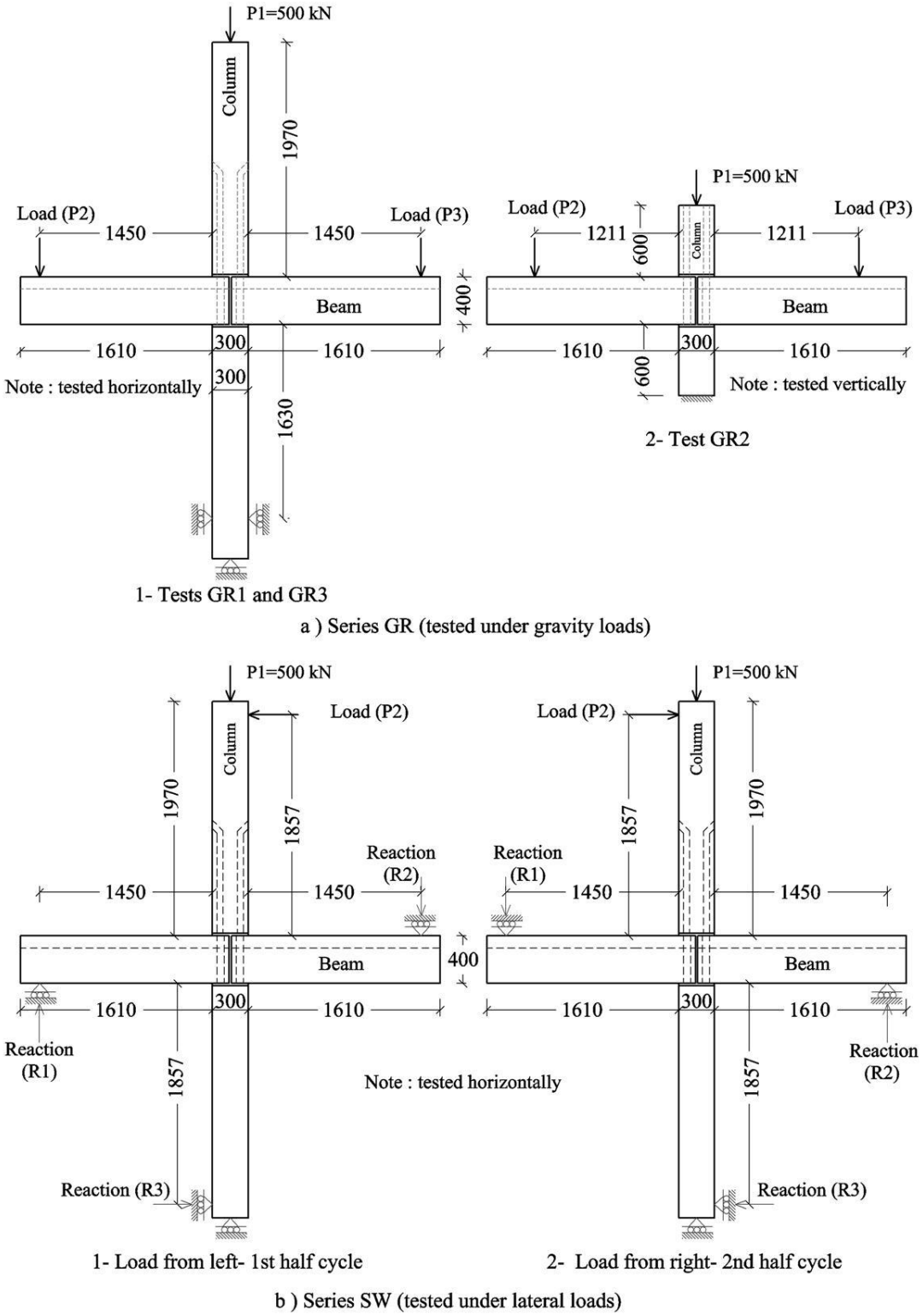

Figure 4.1 Full-scale test geometry

a) Top column, showing corrugated sleeves to receive bottom column bars

b) Beam, showing the end at the connection side where sleeves are installed to bypass bottom column dowel bars

c) Bottom column with 4H20 mm protruding bars

d) Beam form work and beam-end reinforcement details of type T1 (specimens GR1 and SW1)

e) Top column form work at the end that connected to the connection

Figure 4.2 Specimen components

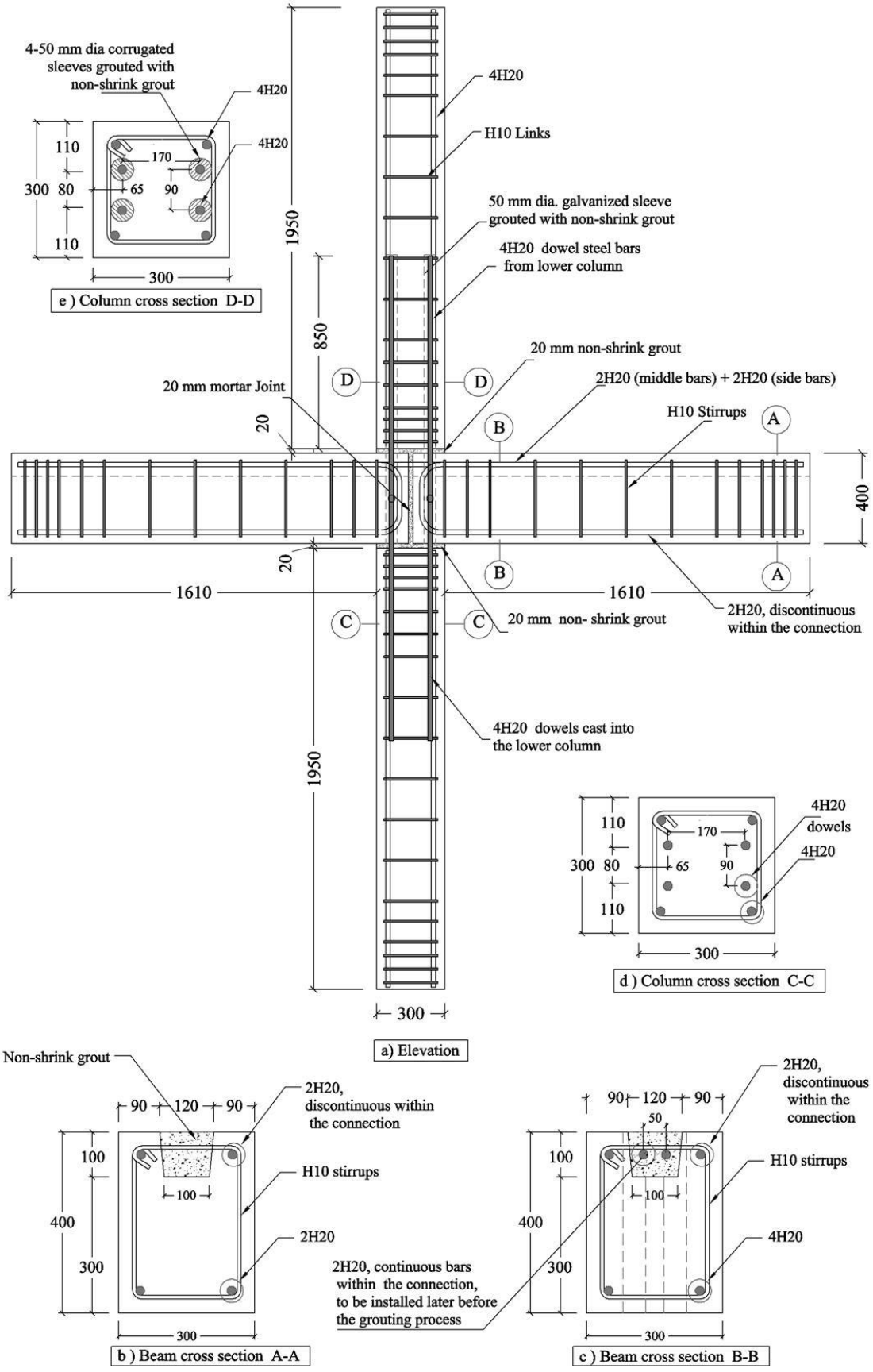

Figure 4.3 Details of specimens GR1 and SW1 (connection reinforcement type T1)

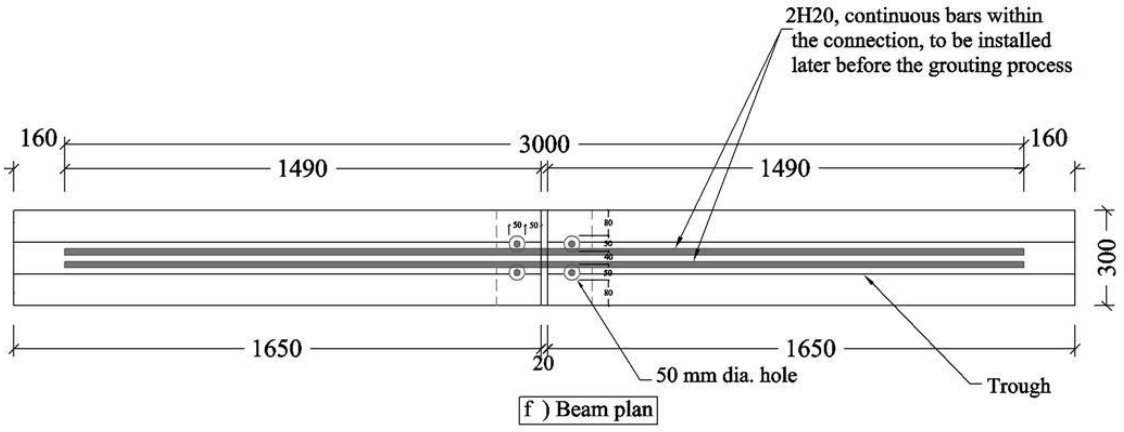

f) Beam plan

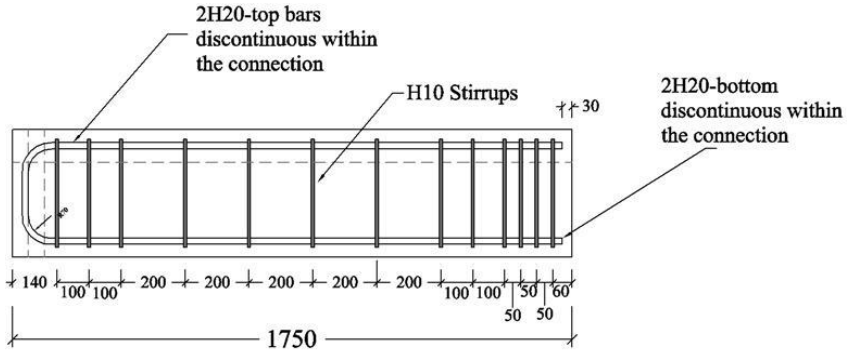

g) Beam reinforcement details (elevation)

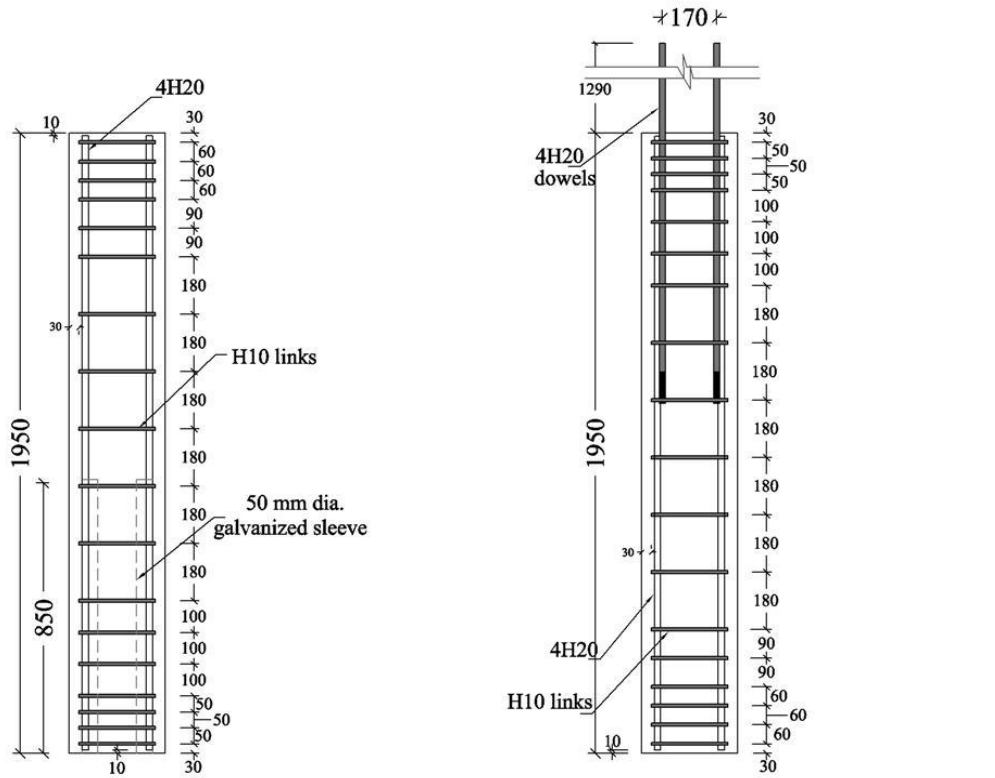

h) Top column reinforcement details (elevation)

i) Bottom column reinforcement details (elevation)

Figure 4.3 (Cont.) Details of specimen GR1 and SW1 (connection reinforcement of type T1)

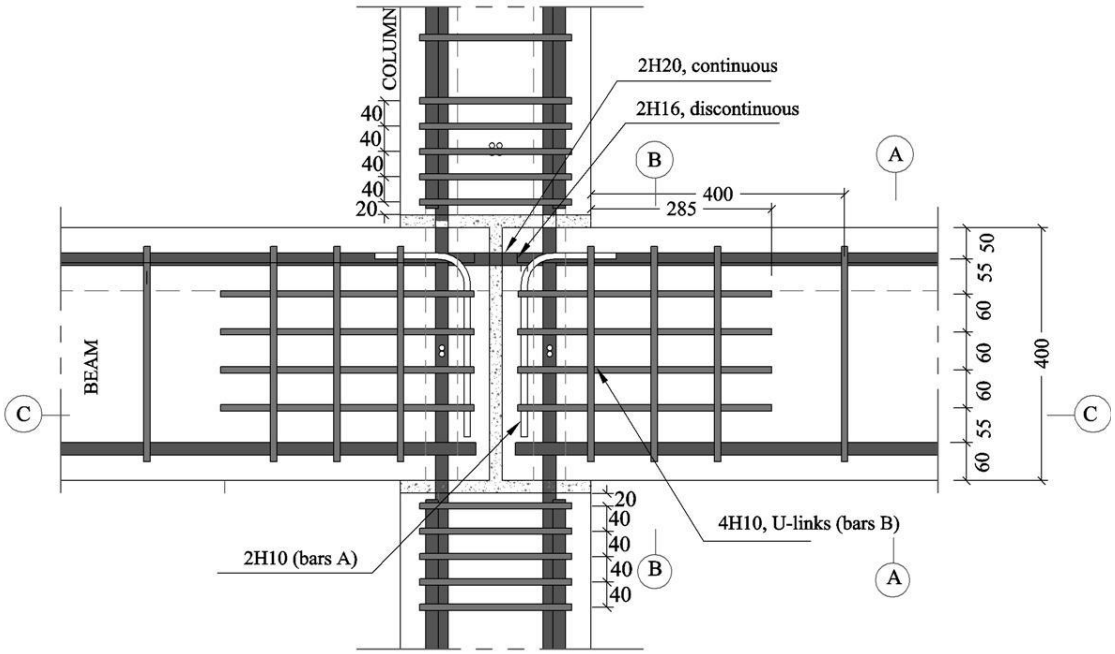

a) Connection reinforcement detail of type T2 (specimen GR2)

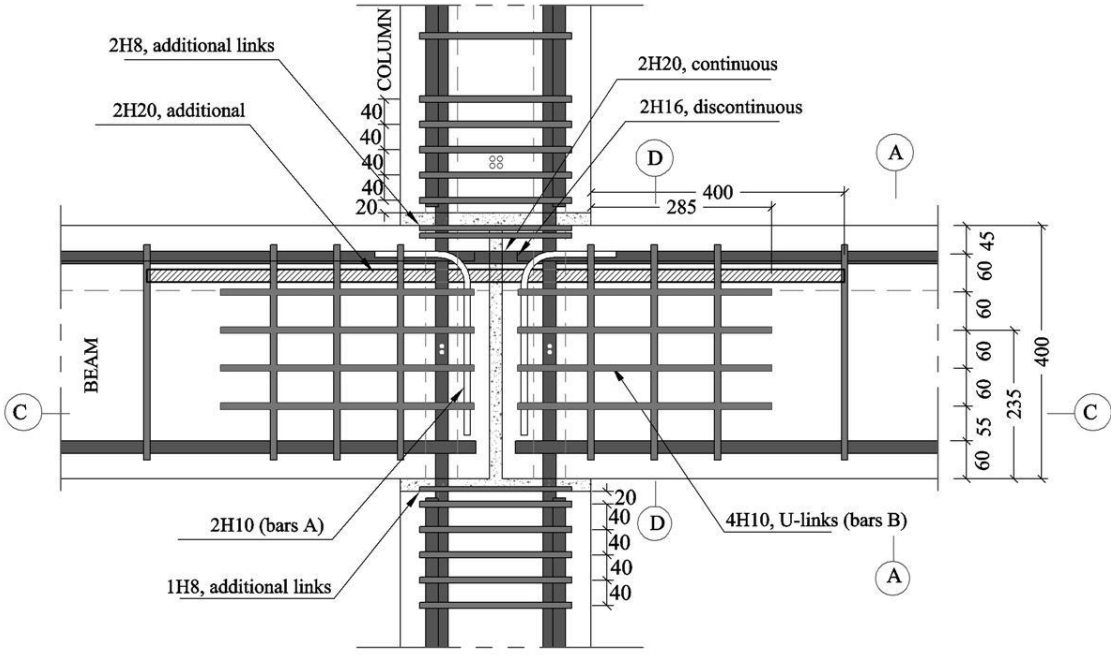

b) Connection reinforcement detail of type T3 (specimens GR3 and SW2)

Figure 4.4 Modifications T2 and T3 in the connection reinforcement detail

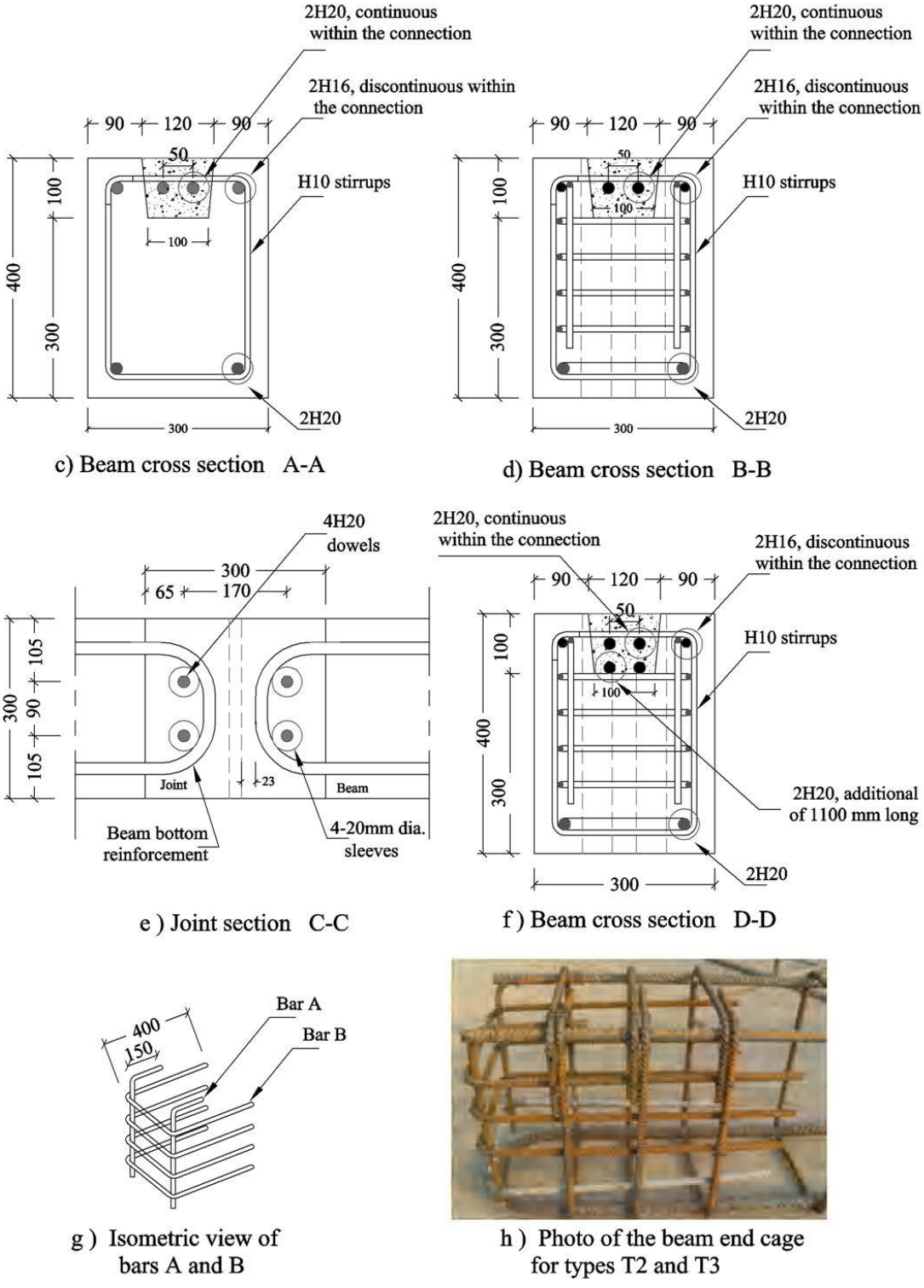

Figure 4.4 (Cont.) Modifications T2 and T3 in the connection reinforcement detail

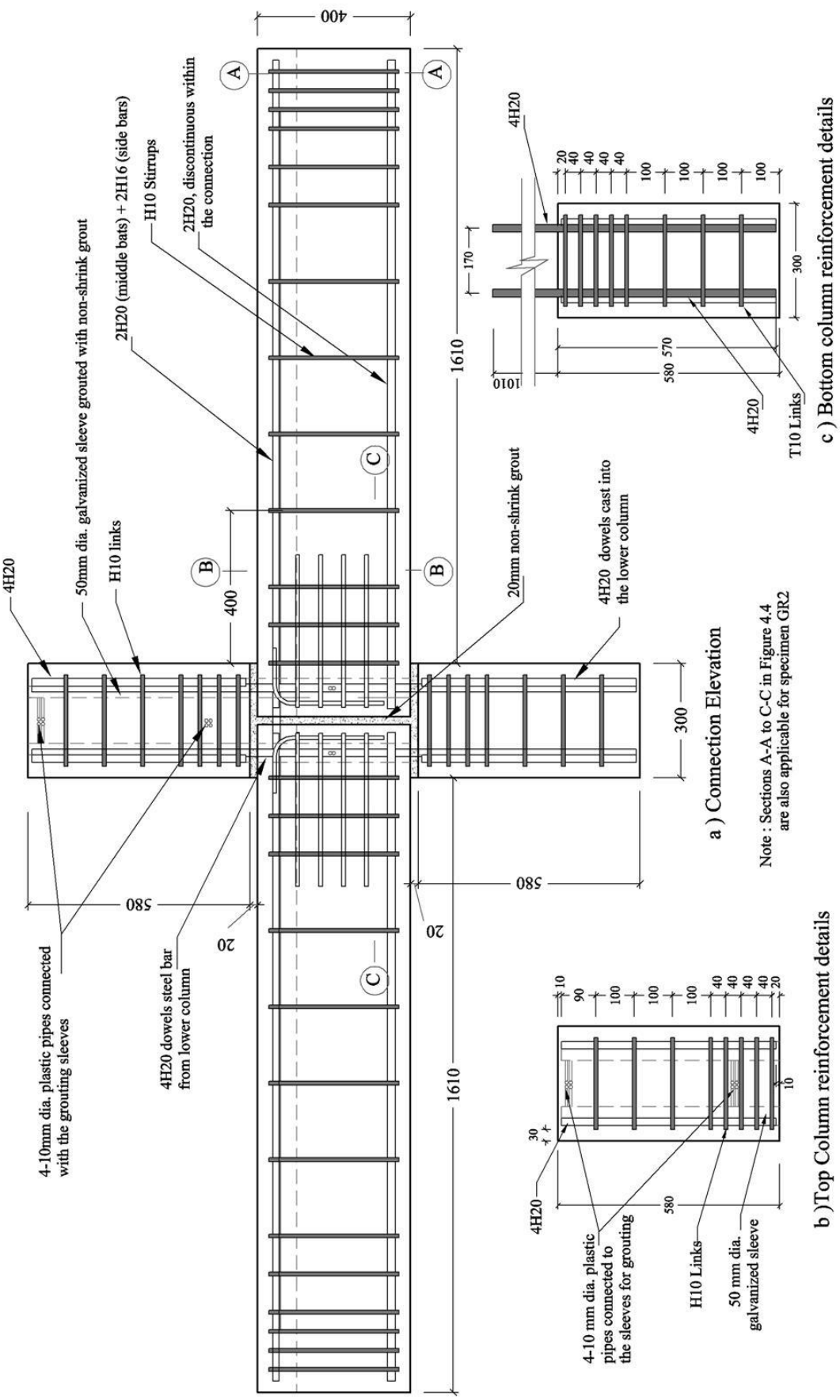

Figure 4.5 Specimen GR2 details (connection reinforcement type T2)

4.3.2 Instrumentation

The full list and layout of the instrumentation used in the full-scale tests (series GR and SW) are presented in Appendix C. The functions of the measurements are presented in Table 4.2 and Figures 4.6 and 4.7.

Table 4.2 Instrumentation functions

Sensor function	Location		Note
	Series GR	Series SW	
Load cells			
Applied column axial load	P1	P1	
Applied column lateral load	--------	P2*	
Applied beam load	P2,P3	--------	
Beam-end reaction	--------	R1*,R2*	
Bottom column reaction	--------	R3*	
Potentiometers			
Beam deflection	d1,d2	--------	
Beam mid-height sway	--------	d1*	
Column sway	--------	d2*	
Beam-column rotation (M1)	d3,d4	d3,d4,d5,d6	Rot M1 = measurement / L2
Beam-column rotation (M2)	d5,d6,d7,d8	--------	Rot M2 = (d5+d6)/L1 (d7+d8)/L1
Strain gauges			
Top axial column - strain	S1,S2,S3	S1,S2,S3	Investigate the strain concentration in the column
Bottom axial column - strain	S4,S5,S6	S4,S5,S6	
Top beam steel bar - strain	S7,S8,S9,S10,S11	S7,S8,S9,S10,S11	Investigate the strain distribution in the bars
Beam- compressive strain	S12,S13,S14,S15	--------	Investigate the strain concentration in the beam
Column dowel bar - strain	--------	S12,S13	Investigate the strain concentration in the bar
Additional column link - strain	--------	S14,S15	Investigate the strain state in the links

* The direction of measurement in Figure 4.7 is related to the 1st half-cycle loading (Figure 4.1b(1)); for the half-loading cycle ((Figure 4.1b(2)), the measurements were taken at the opposite direction

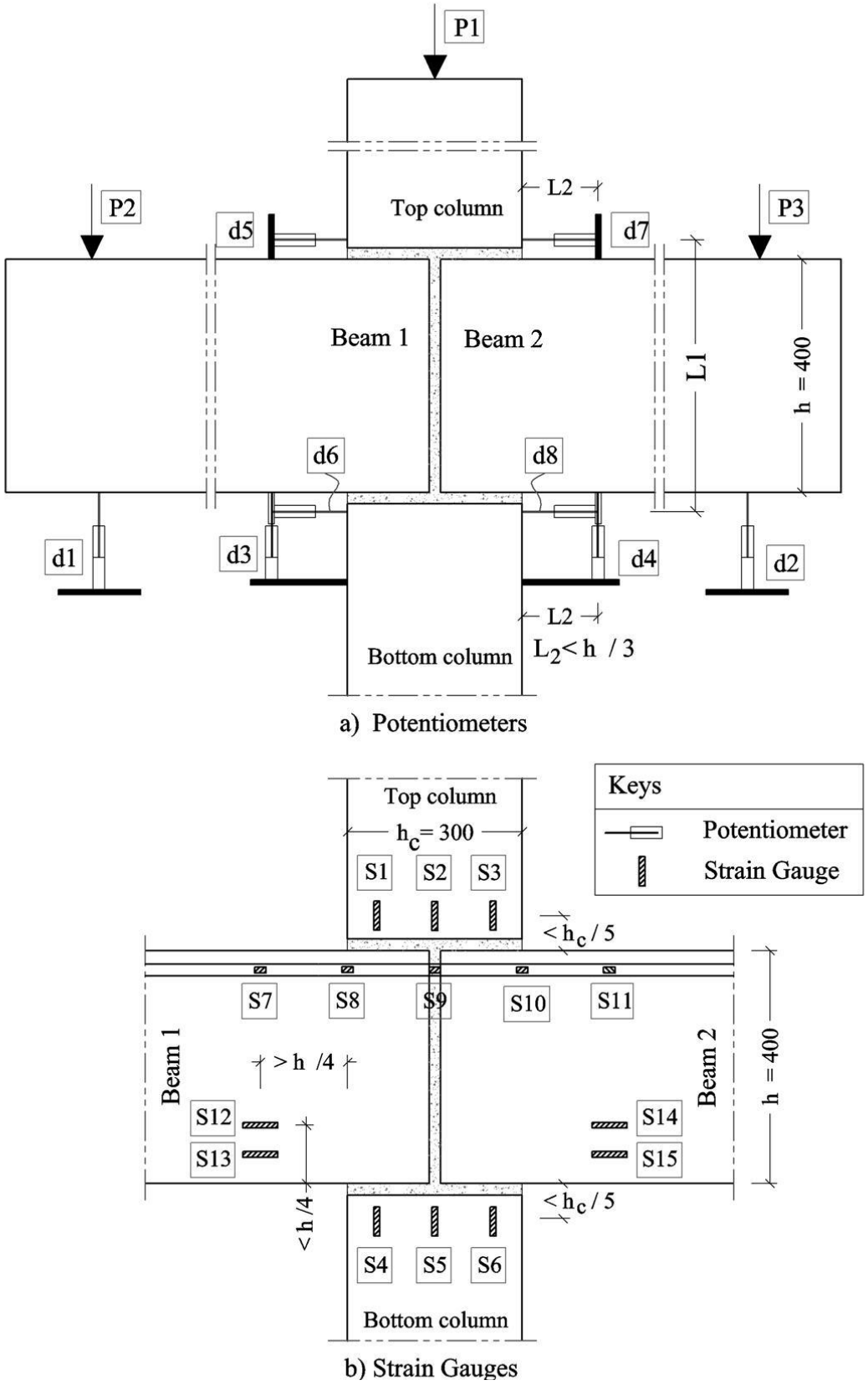

Figure 4.6 Instrumentation layout for specimens of series GR

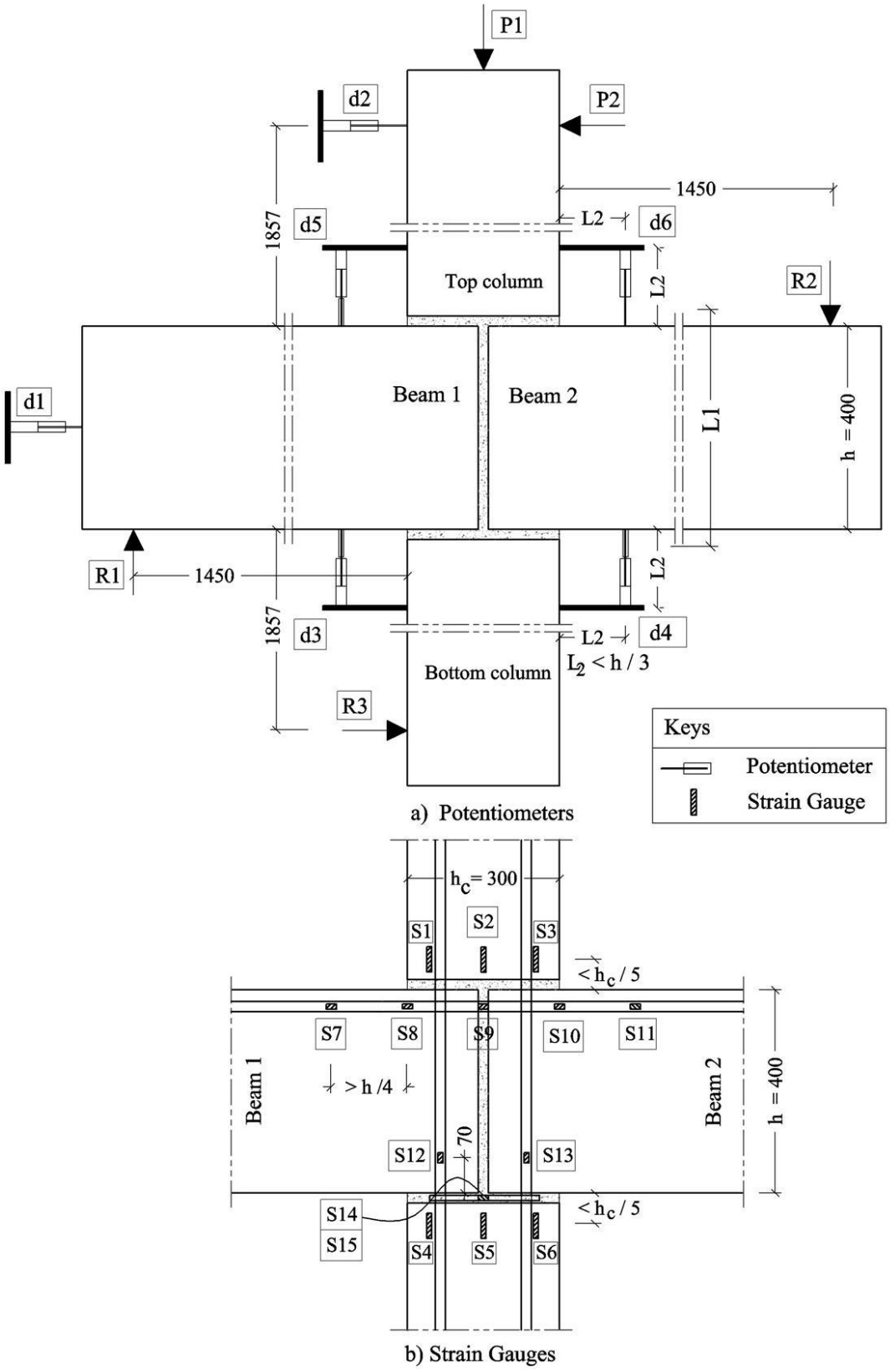

Figure 4.7 Instrumentation layout for specimens of series SW

4.3.3 Loading procedure

To simulate the upper storey loading in the prototype frame (Appendix A), a compressive force of 500 kN, representing 5.6 N/mm^2 compressive stress in the column, was first applied to the column and kept constant during the subsequent load stages in all tests. The column load was applied manually using a hydraulic pump connected to a load jack within a self-equilibrating system (all specimens except GR2) or within a reaction frame in the case of specimen GR2 (Appendix B).

In series 1 (GR), the hogging moment was applied to the connection through eccentric beam loads both acting at 1,450 mm (specimens GR1 and GR3) and 1,221 mm (GR2) from the face of the column, i.e. 4.14 and 3.45 times the beam effective depth 'd', respectively. In order to study the effect of repeated loading on the recovery of the strain, in specimen GR2, 30% (in average) of the applied beam load was unloaded and reloaded again in four cycles. This cyclic loading procedure was conducted when the beam load was at 25%, 50%, 75% and 100% of the expected yield moment. Loading and unloading increments were 5 kN and 10 kN, respectively. The applied beam loads induced reactions at the end of the bottom column catered for a pinned jointed restraint.

In series 2 (SW), a sway load was applied manually using a hydraulic pump connected to a load jack at the far end of the top column in approximately 5 kN intervals with unloading at about 10 kN increments. This load induced reactions at the far beam-ends, and a reaction at the far lower column-end as shown in Figure 4.1b. By reversing the direction of the applied lateral load to the column, the effects of repeated wind loading were simulated. The column sway load was applied in two directions (left and right) through different load cycles (Figure 4.8); each cycle represents loading and

unloading in one direction up to the first cracking moment in the case of specimen SW1 and up to 50% of the yield moment capacity in the case of specimen SW2. The cyclic loading stage followed by applying monotonic sway load to failure to the left direction.

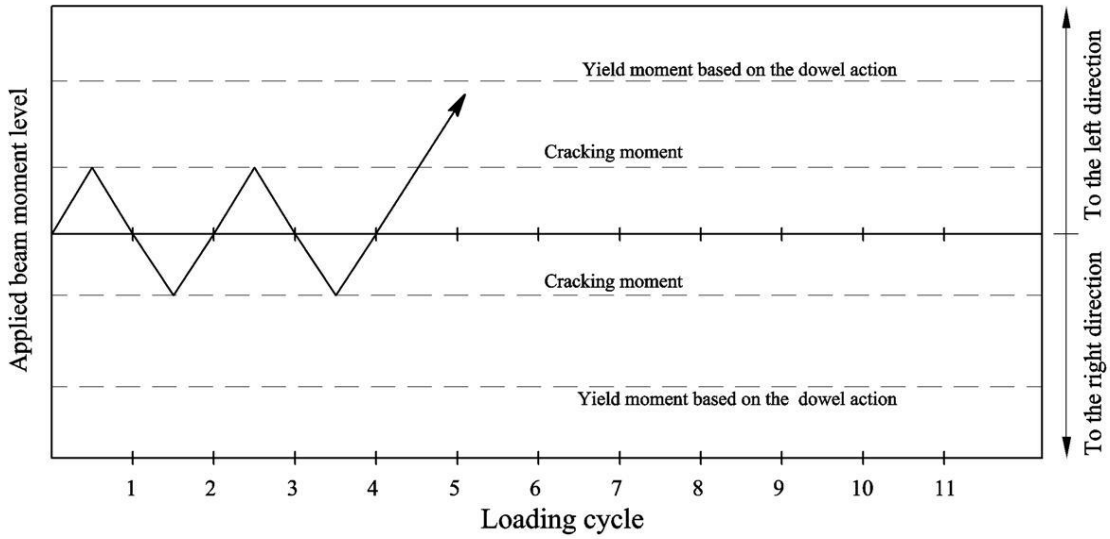

a) Loading procedure for specimen SW1

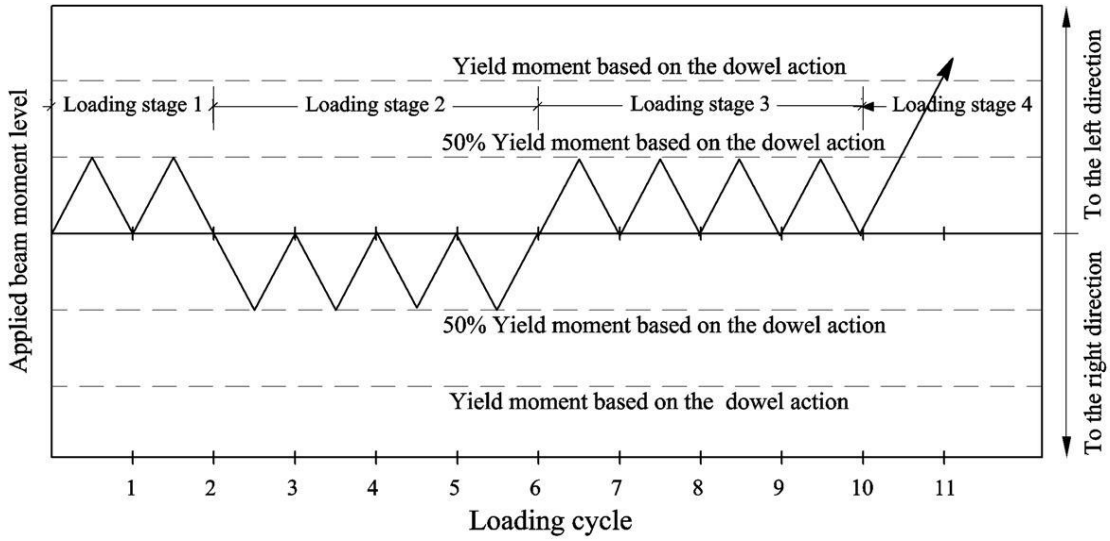

b) Loading procedure for specimen SW2

Figure 4.8 Loading procedures in series SW

4.4 Material

4.4.1 Concrete

The beam and column concrete were cast at the SCC Company in Manchester using ready-mix concrete, which was used throughout the whole investigation. The concrete contained CEM I cement with a mix proportion of 1:2.25:3.1 ((cement: sand: gravel) based on dry weights) with 20 mm maximum aggregate size. The mix contained 45% water, and 1.8% super-plasticizer agent as weight ratio to the cement. The cast concrete was only cured in the laboratory air until the day of testing. The actual concrete properties for the test series are summarised in Table 4.3, and the calculated properties are listed in Table 4.4.

Table 4.3 Experimental strength characteristics of concrete

Specimen and location		Age (days) at day of testing	Cube compressive strength, f_{cu} (N/mm^2)						
			28 days			**Test day**			
			1	2	Ave.	1	2	3	**Ave.**
GR1	Beams + Columns	121	----	-----	-----	62.0	64.0	64.0	**63.3**
GR2	Beams + Columns	67	72.0	72.5	72.3	75.5	76.5	-----	**76.0**
GR3	Beams	118	77.7	-----	77.7	81.0	84.5	-----	**82.8**
	Columns	113	63.5	68.0	65.8	67.0	74.0	-----	**70.5**
SW1	Beams + Columns	54, 55	----	-----	-----	68.5	68.5	67.5	**68.2**
SW2	Beams	152, 153	73.5	68.0	70.8	79.5	80.0	-----	**79.8**
	Columns	148, 149	68.0	63.5	65.8	70.0	68.5	-----	**69.3**

Table 4.4 Calculated properties of concrete

Specimen and location		Cylinder compressive strength, f_c (kN/mm^2)	E_c (kN/mm^2)	f_{ct} (N/mm^2)	$f_{ct,fl}$ (N/mm^2)
GR1	Beams + Columns	52.4	36.2	3.9	4.7
GR2	Beams + Columns	61.0	37.9	4.2	5.0
GR3	Beams	67.8	39.1	4.4	5.2
	Columns	57.2	37.1	4.0	4.9
SW1	Beams + Columns	55.6	36.8	4.0	4.8
SW2	Beams	64.8	38.5	4.3	5.1
	Columns	56.4	37.0	4.0	4.8

f_c : is the equivalent compressive cylinder strength (Table 3.1 in EC2 (CEN, 2004b)).
E_c : is the short-term value for modulus of elasticity of concrete = 22 $(f_c / 10)^{0.3}$.
f_{ct} : is axial tensile strength of concrete = 2.12 ln $(f_c/10)$ for concrete grade > C50/60.
$f_{ct,fl}$: is the flexural tensile strength = max {(1,6 - h/1000) f_{ct}; f_{ct} }, where h is the total member depth.
* All above equations are according to EC2 (CEN, 2004b), but with replacing f_{cm} by f_c, and f_{ctm} by f_{ct}, where f_{cm} and f_{ctm} are the mean values

4.4.2 Grout

The grout was cast at the university's laboratory, and the mix proportion was chosen based on many trial mixes (details of which are shown in Appendix D) to ensure a strength close to the concrete strength and flow-ability enough to pass easily through the beam trough and the corrugated sleeves.

The grout contained CEM II/B-V 32.5 N cement and river sand passing through 2.8 mm sieve with a targeted grade of C60 (f_{cu}) at the day of testing. A mix proportion of 1:1 ((cement : sand) based on dry weights) was used with 28% water, 1.7% super-plasticizer agent, and 0.8% shrinkage reducing admixture as weight ratio to the cement. The sieve analysis of the sand is shown in Appendix E. The grout was only cured in the laboratory air until the day of testing. The actual material properties of the cement-based grouts are summarised in Table 4.5. For each grout mixture, 100x100x100 mm control cubes were taken and cured in similar conditions to the test series. Three cubes were tested at the same day of the series testing. The target strength of the mortar grout was C60 (f_{cu}) at 12 days age.

Table 4.5 Strength characteristics of grout

Specimen	Age (days) at day of testing	Cube compressive strength, f_{cu} (N/mm^2)						
		Test day				28 days		
		1	2	3	**Ave.**	1	2	Ave.
GR1	14	65.5	66.0	65.5	**65.7**	75.5	75.0	75.3
GR2	12	53.0	54.5	58.0	**55.2**	-----	-----	-----
GR3	14	60.0	59.5	59.5	**59.7**	68.0	70.0	69.0
SW1	13, 14	65.0	63.5	63.5	**64.0**	-----	-----	-----
SW2	13, 14	62.0	64.5	64.5	**64.5**	72.0	72.5	72.3

4.4.3 Steel

The main reinforcement of the column and beam consisted of deformed steel bars of 16 and 20 mm diameter, while the web reinforcement was 10 mm diameter deformed steel bars. In specimens with connection reinforcement details of type T3, additional column links of deformed steel bars of 8 mm diameter were used within the lower beam-column joint and top beam-column joints. The strength and modulus of elasticity of the reinforcing bars used in each test are listed in Table 4.6.

Table 4.6 Strength characteristics of reinforcement

Bar diameter	Specimen	Yield strength, f_y (N/mm^2)				Modulus of elasticity, E_s (kN/mm^2)			
		1	2	3	Ave.	1	2	3	Ave.
8 mm	All	520.3	534.8	513.3	522.8	191.8	194.1	197.7	194.5
10 mm	All	598.5	600.2	596.4	598.4	196.9	201.1	196.8	198.3
16 mm	All	549.3	552.8	550.1	550.7	189.6	189.4	192.6	190.5
20 mm	GR1, SW1	568.3	572.4	-------	570.4	208.6	198.7	-------	202.7
20 mm	GR2, GR3, SW2	531.3	533.2	-------	532.3	204.9	196.1	-------	200.5

4.5 Error analysis

It should be mentioned that, in spite of giving every attention to prevention of errors in the reported results, there is still a margin of error due to many aspects in the measurement process that caused the results to deviate from the 'true' values. To estimate the reliability of the experimental tests, the potential errors in the experimental measurements are presented, identified and quantified in the next sub-sections.

4.5.1 Random errors

Random errors are related to the natural limitation in the measurement instruments, such as the fluctuation in the instrument readings, and to the operator's way of observing, recording and interpreting the readings (operator errors). This type of error cannot be identified but it is susceptible to mathematical treatments such as

averaging several measurements, and estimating errors using statistical means such as the standard deviation. A measurement is considered to be precise when the random errors are relatively small.

In the current research, the readings of the measurements (loads, strains, and deflections) were recorded using a computer-operated data acquisition system, meaning that there were no operator errors. For the other source of random errors, the limit of error and the sensitivity in the measured inputs using potentiometers, load cells, and strain gauges are tabulated in Table 4.7. As shown, the errors are of small amounts and they have a negligible effect on the results in comparison to the systematic errors, as will be shown later. Therefore, it could be stated that the precision of the measurements is within an acceptable range.

Table 4.7 Sensitivity and limit of error in the data acquisition system at 20 ± 3º C

A - Potentiometers	Measuring behaviour				
	Deflections for determining rotation	Crack width, concrete deformation	Beam deflection -GR-	Beam sway –SW-	Column sway -SW-
Maximum measuring range	15 mm	20 mm	50 mm	100 mm	200 mm
Maximum measuring Volts	2	2	2	2	2
1μ Volt equals to	7.5E-6 mm	10E-6 mm	25E-6 mm	50E-6 mm	100E-6 mm
Sensitivity	10 μV				
Limit of error in the potentiometers	±0.005% + 1μV				
B - Load cells	Measuring behaviour				
	Column axial load		Beam, column loads and reactions		
Maximum measuring range	1000 kN		250 kN		
Maximum measuring Volts	24 V		24 V		
1μ Volt equals to	41.66E-6 kN		10.42 E-6 kN		
Sensitivity	100 μV				
Limit of error in the load cells	± 0.005% + 1μV				
C- Strain gauges	Sensitivity = 0.1 με		Limit of error = ± 15 με		
Sensitivity: is the smallest measurable input change that the instrument can detect					

4.5.2 Systematic errors

Systematic errors make the mean values of the results depart from the accurate value in one specific direction when repeating the tests; such errors cannot be removed by repeating measurements or averaging large numbers of results. The effects of the systematic errors need to be estimated in order to make the required corrections. A test is considered to be accurate when the systematic errors are relatively small.

This type of error is produced due to a bias in the measurement process, such as using imperfect calibrated apparatuses, or in the physical configuration including the presence of physical effects that have not been taken into account. The possible systematic errors in the current research are identified, quantified and corrected if applicable in the next sub-sections.

4.5.2.1 Physical effects

In the experimental tests, there were deviations in the cross-section dimensions, members' alignment due to construction reasons, and in the strength grade of the concrete and steel due to taking the average of individual tests for each material (refer to Table 4.3 and Table 4.6). The maximum deviations observed in the beam-column tests conducted under gravity tests (taking series GR as a case study) are listed below, with the effects of the deviation in b, h, d, f_c, and f_y being quantified in Section 4.5.2.3.

- Alignment $< \pm 0.1\%$
- Mortar thickness $< \pm 2$ mm
- Beam breadth dimension, b $< \pm 2$ mm ($\pm 0.67\%$)
- Beam depth dimension, h $< \pm 2$ mm ($\pm 0.50\%$)
- Beam effective depth dimension, d $< \pm 4$ mm ($\pm 1.14\%$)
- Concrete compressive strength, f_c $< \pm 2.05\%$
- Main steel bar grade (H20), f_y $< \pm 0.37\%$

On the other hand, some other physical effects that have been identified and quantified, and the required corrections were carried out accordingly. These effects included the undesired test system displacement and the inclusion of the column axial deformation in the measured beam deflection in the tests under gravity loads.

In addition to the above physical effects, the error in the results due the friction between the ground and the specimens (GR1, GR3, SW1 and SW2) was minimised to the lowest possible level. This was done by supporting the beam and column at their far ends on a relatively small area (300 x 100 mm) and using oiled hard wooden pieces to separate them from the support (see Figures B.2 and B.8 in Appendix B). These small contact areas had an effect only at the beginning of the tests (2-3 kN load that represents 2-3% of the applied load) where no displacement was recorded at this loading stage. However, when the specimens started to move, a normal displacement occurred. By neglecting the zero reading at the 2-3 kN load, a linear displacement-load relation was established at this elastic loading stage.

4.5.2.2 Calibration of instruments

Imperfectly calibrated instruments have a significant effect on the reliability of the results; therefore, all the instruments were calibrated, including the load cells and potentiometers. In addition, the calibration of the strain gauges was provided by the manufacturer. However, there was an error in the readings of the potentiometers and load cells, which are still included in the results. The error had two fractions: (i) the fraction that occurred due to neglecting the constant term in the linear input-volt equation (term ‘a’ in Figure 4.9); and (ii) the fraction that occurred due to the assumed linear input-volt relation.

In the current study, the maximum combined error due to both fractions was ± 1.05% in the potentiometer readings (deflections and rotations), and ± 2.18% in the load cells (moments).

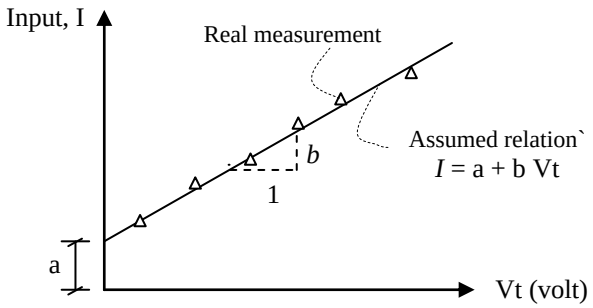

Figure 4.9 Typical calibration curve

4.5.2.3 Total systematic errors

Figure 4.10 shows the effects of an individual error amount of ± 2% in each of *b*, *h*, *d*, f_c and f_y on the moment capacity, strain and deflection of the beam in series GR. As shown, the beam moment capacity is mostly affected by d and f_y, while b and f_c have a very little effect; on the other hand, the beam strains and deflections are mostly affected by h, but b and f_c still have a noticeable effect.

For the beam-column connections tested under gravity loads (series GR), the maximum anticipated error in the presented results with respect to the strains, deflections and moment capacity are presented in Table 4.8. The effects of the deviations in the beam cross-section dimensions and in the material grades are calculated by substituting the deviations listed in Section 4.5.2.1 in Figure 4.10, while the effects of the errors in the instrumentation are taken directly from Section 4.5.2.2.

Table 4.8 shows that there is a maximum potential margin of errors of ± 2.77%, ± 3.82%, ± 3.78% within the reported strains, deflections and moment capacity, respectively. It should be emphasised that this amount of errors would happen only

when all sources of errors have the same error sign (+ or -) and they are in their extreme level, which is unlikely to happen, as the errors may cancel each other when they have different signs of effects. However, the shown error percentages in Table 4.8 express the reliability of the results and to what extent the results could be trusted.

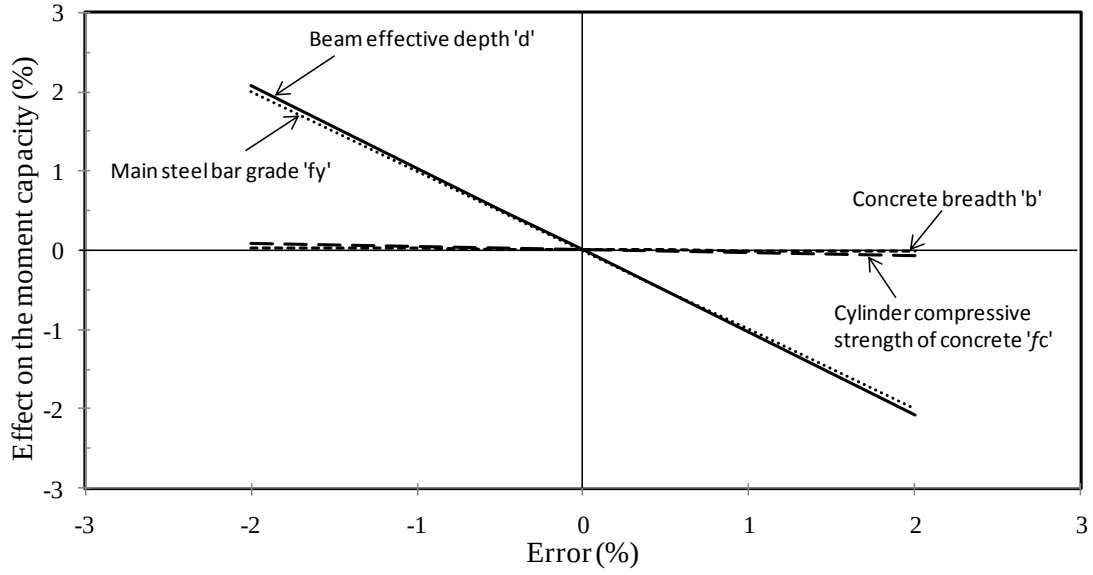

a) Beam moment capacity

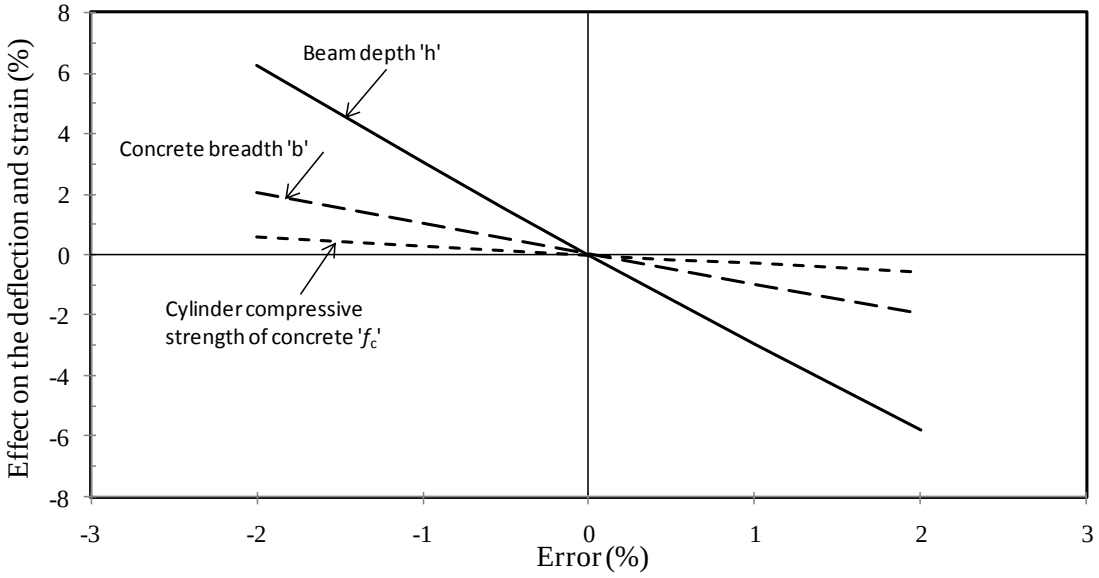

b) Beam deflection and strain

Figure 4.10 Effects of beam cross-section properties on the results of series GR

Table 4.8 Summary of potential systematic errors in the results of series GR

Maximum error		Effect on the results (%)		
Source	Amount (%)	Strain	Deflection	Moment capacity
Calibration of potentiometers	± 1.05	------	± 1.05	------
Calibration of load cells	± 2.18	------	------	± 2.18
Beam breadth, b	± 0.67	± 0.67	± 0.67	± 0.02
Beam depth, h	± 0.50	± 1.49	± 1.49	------
Beam effective depth, d	± 1.14	------	------	± 1.18
Main steel bar grade, f_y	± 0.37	------	------	± 0.37
Cylinder compressive concrete strength, f_c	± 2.05	± 0.61	± 0.61	± 0.03
Total maximum error		± 2.77	± 3.82	± 3.78

4.5.3 Significance of error in relative beam-column rotation

The key measurement in the beam-column specimens is the relative beam-column rotation 'θ' that is used to characterise the flexibility of the connection through the rotational stiffness 'S_y' ($S_y = M/\theta$). The error in θ is related directly to the error in the potentiometers used to calculate the deflection of the beam with respect to the column; the maximum anticipated error in these deflections is ± 3.82% as shown in Table 4.8, which will affect S_y by - 3.97% [100(1-(1/(1-0.0382))] to + 3.68% [100(1-(1/(1+0.0382))]. However, in semi-rigid frame analyses, the change in S_y does not reflect exactly the amount of change in the moments generated in the beams. To clarify this feature, the prototype building frame considered in this study (Appendix A) was analysed under UDL gravity loads using S_y values varying from - 100% to + 100% as ratio to the experimental rotational stiffness value of S_y obtained from test GR1.

Figure 4.11 shows the effect of this variation (± 100%) on the hogging moment generated at the beam-end A in comparison to the situation where the experimental S_y of GR1 is used. To demonstrate the insignificance of errors within the experimental S_y

range, within a 40% error (± 20%), the effect on the hogging moment at location A is only 6.9%. This shows that the error in measuring rotations is not decisive for the beam-column connection type investigated in the current study. For specimen GR1, with the potential error in the measured S_y (- 3.97% to + 3.68%), the effect on the beam-end moment generated at location A is only - 0.75% to + 0.55% based on Figure 4.11.

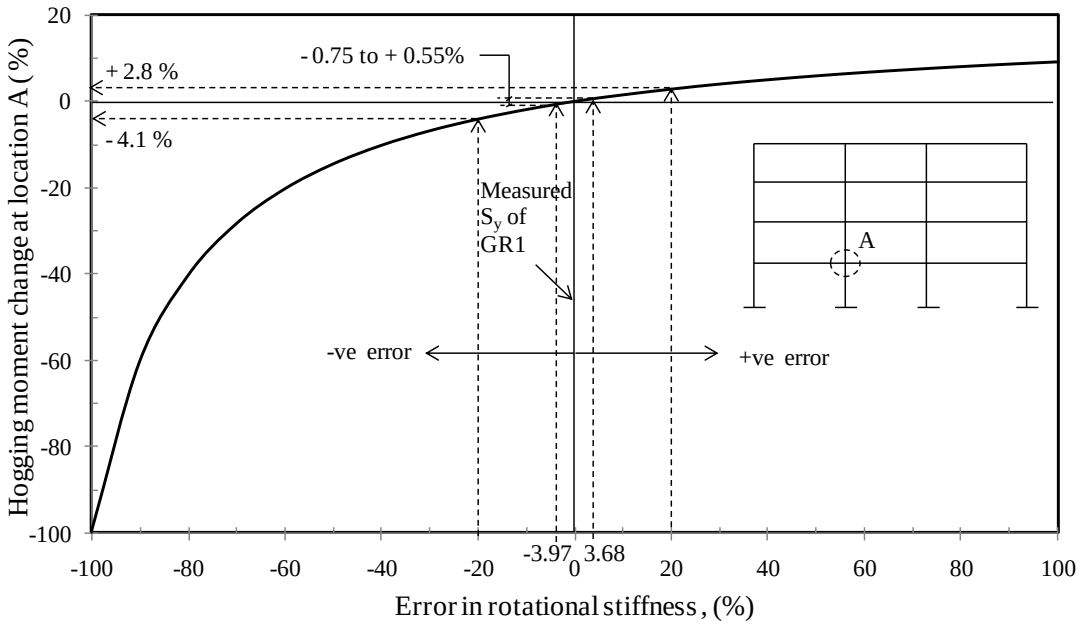

Figure 4.11 Significance of error in beam-column rotational stiffness

4.6 Summary

In this chapter, the test programme of the full-scale beam-column connection tests were presented, including the details of the geometry, reinforcement, instrumentation, and material properties. In addition, the way of designing the specimens was given, with a reference to Appendix A for further information. Moreover, an error analysis has been performed to quantify the errors in the reported results taking series GR as the case study.

CHAPTER 5

FULL-SCALE TEST RESULTS AND DISCUSSION: GRAVITY LOADS

5.1 Introduction

The results and discussion of the 1st part of the full-scale beam-column connection tests (series 1 – GR) are presented in this chapter. The series consisted of three specimens subjected to gravity loads with the connection reinforcement detail taken as the main variable through using three different reinforcement detail types (T1, T2 and T3). The aim of this variable was to enhance the connection serviceability, limiting the damage within the connection, shifting the beam rotation concentration away from the connection to increase the rotational stiffness and eventually producing an equivalent monolithic connection.

The results are shown and compared with each other in terms of beam-end deflections, relative beam-column rotation, cracking pattern, crack openings, compressive deformation in the compression zone and the concrete and steel bar strains, which are confronted against predicted ones.

Furthermore, a theoretical model was calibrated to categorise the moment-rotation behaviour of specimens GR1 and GR2, while specimen GR3 will be shown to behave as a monolithically cast-in-place connection.

5.2 Calculation techniques

5.2.1 Experimental moment calculation

The experimental beam moments were calculated at the column faces by multiplying the load recorded by load cells at the far member ends by the corresponding distance to the column face.

5.2.2 Experimental relative beam-column rotation

So far, there is no standard method to experimentally measure the relative beam-to-column rotations 'θ'; however, in the absence of such guidance, a variety of techniques has been used by various researchers.

Mahdi (1992), Gorgun (1997), and Ferreira (1999) determined the rotation through relative vertical deflections of the compression face of the beam with reference to the bottom column without deducting the rotation due to beam-end flexural curvature. Elliott et al (2003a) pointed out that the measured rotation should not include such rotation; otherwise it will be counted twice in the frame analysis. To accommodate this aspect in the current study, the rotation was calculated by dividing the deflection at location 1 by the distance from the column face 'L1', and deducting the rotation along the length L1 due to bending curvature (see Figure 5.1).

$$\theta_1 = \frac{POT_1}{L_1} - \frac{M\ L_1}{E_c\ I_{eff}} \qquad (5.1)$$

In which M is the applied moment, E is the concrete modulus of elasticity and I_{eff} is the effective second moment of area based on the Branson's model (ACI, 2008a). The measured deflection (POT1) is taken with reference to the column, using POTs mounted on a steel rod fixed with the column. The rotation in the other side was calculated using the same approach. This method of measuring rotations will be called M1.

The second method (M2) for calculating θ has been used by Pillai and Kirk (1981), Bhatt and Kirk (1985), Stanton et al (1986), Dolan and Pessik (1989), Mahdi (1992), Gorgun (1997), Korkmaz and Tankut (2005), and Alva et al (2009), which is based on measuring the relative beam-column displacement at the top and bottom of the beam (locations 2 and 3 in Figure 5.1), where the POTs are mounted on steel rods fixed with the top and bottom surfaces of the beam. The measurement at the top (location 2)

measures the beam crack opening 'w', and at the bottom (location 3) measures the beam compressive deformation 'δ_c'. These two measurements determine θ according to Eq. (5.2). The 2nd term in Eq. (5.2) is similar to the 2nd term in Eq. (5.1) but using L4 instead of L1. It is worth mentioning that method M2 is susceptible to the crack relative location with respect to the location of mounting the POTs.

$$\theta_2 = \frac{POT_2 + POT_3}{L2} - \frac{M\ L_4}{E_c\ I_{eff}} \tag{5.2}$$

In addition to the above-mentioned methods, Stanton et al (1986) and de Chefdebien and Dardare (1994) determined the rotation from the difference between the measured and calculated deflection, under the applied load, divided by the load span (method M3).

$$\theta_3 = \frac{\Delta_e - \Delta_c}{L3} \tag{5.3}$$

In which Δ_e (POT_4, POT_5) is the experimentally measured deflection of the beam under the load point, Δ_c is the calculated deflection using conventional models at the same location, and L3 is the distance from the applied load to the column face. This method assumes that Branson's model (ACI, 2008a) of calculating deflections is able to capture all the non-linear behaviour of concrete under all loading types.

In the current research, methods M1 and M2 were used to determine the relative beam-column rotation.

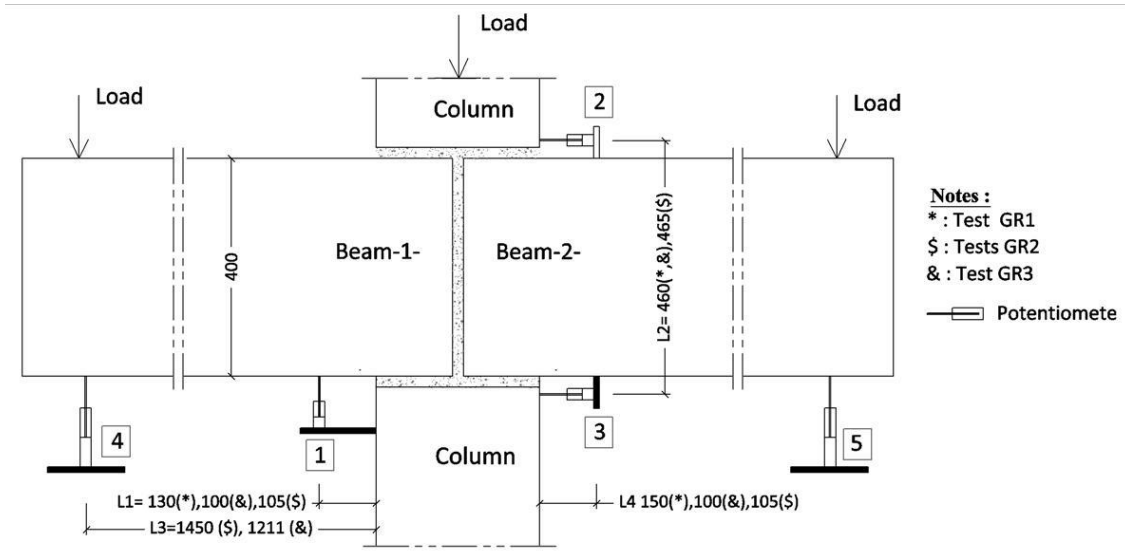

Figure 5.1 Measurement locations for calculating relative beam-column rotation in series 1

5.2.3 Experimental rotational stiffness calculation

Two types of experimental rotational stiffness were calculated: uncracked secant rotational stiffness 'S_{cr}' calculated before the appearance of the first crack, and yield secant rotational stiffness 'S_y' calculated at the onset of yielding of reinforcement (Figure 5.2). S_y represents a conservative approach for representing the elastic range of behaviour, which could be easily incorporated in semi-rigid frame analyses. S_y is the slope of the M-θ curve considering the chord connecting the point of yielding of reinforcement with the origin point, while S_{cr} is the slope of the chord prior to crack.

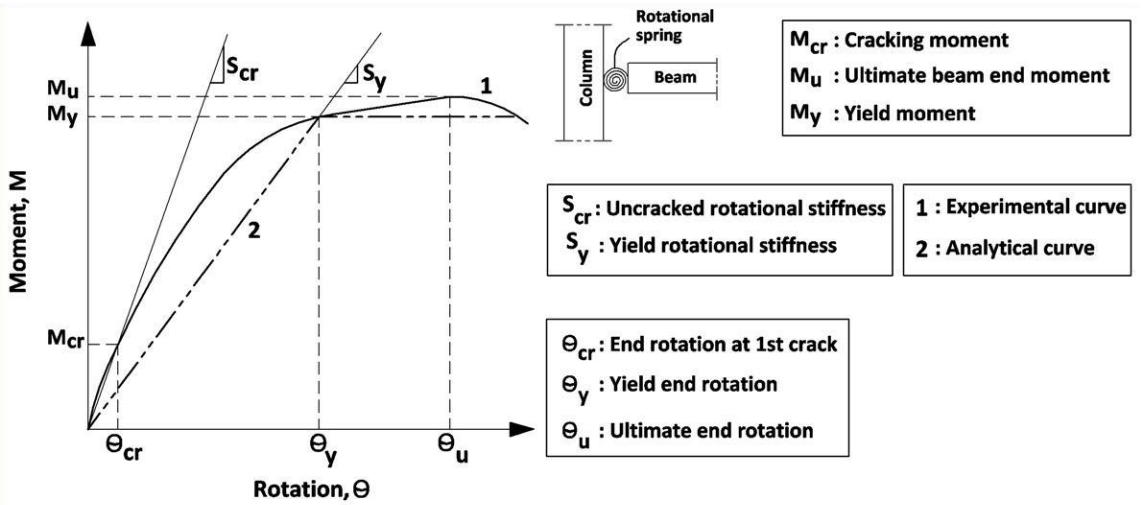

Figure 5.2 Connection rotational stiffness modelling

5.2.4 Predicted moment capacity calculation

The predicted cracking moment 'M_{cr}', yielding moment 'M_y' and the ultimate moment capacity 'M_u' of the beam were found based on EC2 (CEN, 2004b) as shown below, to be compared against the experimental values.

$$M_{cr} = \frac{f_{ct,fl} \; I_I}{y_t} \tag{5.4}$$

$$M_y = A_s \, f_y \, Z_{II} \tag{5.5}$$

$$M_u = A_s \, f_y \, Z_{III} \tag{5.6}$$

$$Z_I = d - \frac{1}{3} x_I \; ; \; Z_{II} = d - \frac{1}{3} x_{II} \; ; Z_{III} = d - 0.4 \; x_{III} \tag{5.7}$$

Where I_I is the second moment of area of gross uncracked section, y_t is the distance from the neutral axis to the extreme fibre in the tension side of the beam, A_s is the tension steel bar area, f_y is the actual yield strength of the reinforcing bars, d is the effective depth of the beam cross section, x_I, x_{II}, x_{III} are the neutral axis depths from the compression side of the beam for uncracked section, fully cracked section, and at the ultimate state, respectively, and $f_{ct,fl}$ is the flexural tensile strength of concrete.

The f_y grades were obtained experimentally, while $f_{ct,fl}$ was calculated according to Eq. (5.8a) according to EC2 (CEN, 2004b). In the equation, f_c is the concrete cylinder compressive strength, which was obtained by converting experimentally determined f_{cu} values to equivalent f_c values using Table 3.1 in EC2:

$$f_{ct} = 0.3 \, f_c^{\,2/3} \qquad \text{for } f_c \leq C50/60 \tag{5.8a}$$

$$f_{ct} = 2.12 \ln \left(1 + \frac{f_c}{10}\right) \qquad \text{for } f_c > C50/60 \tag{5.8b}$$

$$f_{ct,fl} = \max\left\{\left(1.6 - \frac{h}{1000}\right) \; f_{ct} \; ; \; f_{ct}\right\} \quad : \text{h is the member depth} \tag{5.8c}$$

5.2.5 Predicted deflection calculation

In calculating beam deflection, the key factor is the sufficiency in the estimation of the effective second moment of area 'I_{eff}'. Branson's model (ACI, 2008a) was used for this estimation for beams with monolithic connection at the ends, as shown below:

$$I_{eff} = I_I \qquad for\ M \leq M_{cr} \tag{5.9}$$

$$I_{eff} = \left(\frac{M_{cr}}{M}\right)^3 I_I + \left[1 - \left(\frac{M_{cr}}{M}\right)^3\right] I_{II} \leq I_{eff} \qquad for\ M > M_{cr} \tag{5.10}$$

$$M_{cr} = \frac{f_{ct,fl} \quad I_{eff}}{y_t} \tag{5.11}$$

in which M is the applied bending moment, M_{cr} is the cracking moment, I_I is the second moment of area of gross uncracked transformed section, I_{II} is the second moment of area of fully cracked section, $f_{ct,fl}$ is the flexural tensile strength of concrete, y_t is the distance from the neutral axis of the member to the extreme fibre in the tension face.

Al-Shaikh et al (1993) showed that the above model underestimated I_{eff} by 30% in the case of heavily reinforced beams (ρ = 2%), and 12% in the case of lightly reinforced beams (ρ = 0.8%). Also, according to Al-Zaid et al (1991), the model was found to underestimate I_{eff} by 20% for beams under concentrated loads; this discrepancy was attributed to having different lengths over which a beam cracks to specific load conditions. In this respect, in order to consider the higher I value at the less cracked sections under concentrated loads, the beam deflection 'δ' was recommended by Ghali (1993) to be calculated through integrating the curvature (M/EI) over the beam's length based on the moment-area theorem.

$$\delta = \int \frac{M}{E_c\ I_{eff}}\ xr\ dx \tag{5.12}$$

Where M is the applied moment, I_{eff} is the effective second moment of area according to Eqs. (5.9) and (5.10) which is varied along the beam's length, and E_c is the

modulus of elasticity of concrete. In the current study, deflections were calculated according to Eq. (5.12) by dividing the beam into 100 mm-long segments and calculating a different I_{eff} value for each segment; xr in Eq (5.12) is the distance from these segments to the location of calculating deflection. However, the actual deflections for beam with semi-rigid end connections would be higher than that obtained using the above procedure due to additional deflections resulting from relative beam-column rotations. This difference will be investigated within the presentation of the measured deflections in the next sections.

5.2.6 Predicted strain calculation

The predicted strain 'ε' in the beam for both concrete and steel bars was calculated using the elastic flexure formula:

$$\varepsilon = \frac{M\ y}{E\ I_{eff}} \tag{5.13}$$

Where E is the modulus of elasticity of considered material (steel/concrete), I_{eff} is taken as I_I when calculating the strain at cracking moment 'ε_{cr}', and calculated according to Eq. (5.11) to determine the strain at yield moment 'ε_y' in both concrete and steel (Figure 5.3). The values of y (distance to the neutral axis) were calculated considering an uncracked section at M_{cr}, and considering a fully cracked section at M_y.

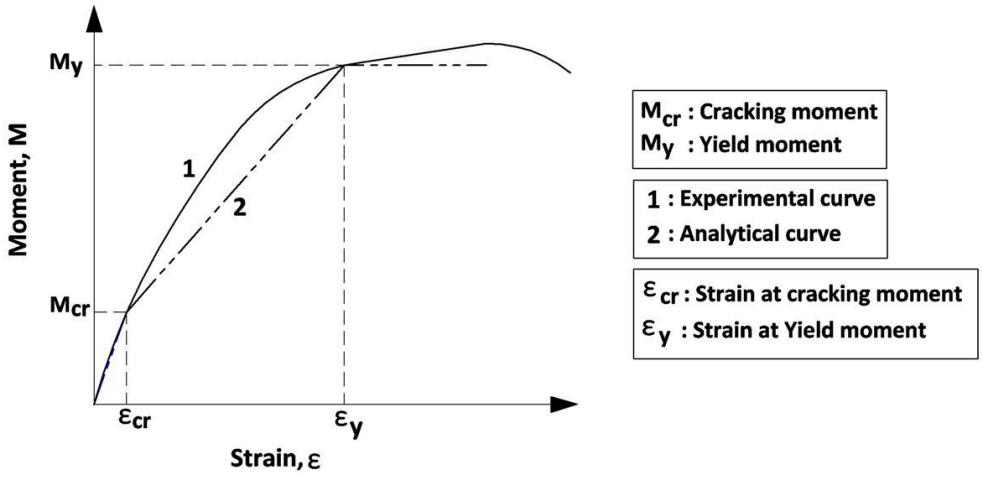

Figure 5.3 Moment-strain relation modelling

5.3 Series 1 test results

The load configuration and the details of the connection reinforcement types (T1, T2 and T3) could be found in Figures 4.1 to 4.5. The results of the tested specimens are presented in Table 5.1 and the characteristics of the materials were presented in Section 4.4. The relative beam-column rotations used to compute the rotational stiffness reported in Table 5.1 were determined using method M1 mentioned in Section 5.2.2.

Table 5.1 Summary of test results of series 1 (GR)

Test	Connection side	Yield moment, M_y (kNm)			Ultimate moment, M_u (kNm)			Rotational Stiffness# (kNm/rad)	
		Cal.	Exp.	Ratio %	Cal.	Exp.	Ratio %	S_{cr}	S_y
GR1*	Beam-1-	115.8	131.1	113.2	121.3	137.3	113.3	133493	30160
	Beam-2-		132.0	114.0		139.2	114.8	---------	---------
GR2&	Beam-1-	143.4	135.5	94.5	151.1	155.3	102.8	137197	29910
	Beam-2-		134.8	94.0		149.4	98.9	105806	28950
GR3$	Beam-1-	149.8	-----	-----	157.8	159.4	101.0	---------	106905
	Beam-2-		-----	-----		159.7	101.2	222846	100857

Test Ref.	Cracking moment, M_{cr} (kNm)		
	Cal.	Exp.	Ratio %
GR1	39.4	43.5	110.4
GR2	41.3	29.3	71.0
GR3	44.4	46.4	104.5

* : the critical section is at column face

& : the critical section is at 300 mm from column face, and the reported moments include 3.7 kNm self-weight moment

$: the critical section is at 400 mm from column face

: The reported rotational stiffnesses under S_y are the yield stiffness for specimens GR1 and GR2, while for GR3, it is the stiffness at 159.4 kNm in the ascending part of the moment-rotation curve.

In Table 5.1, both the experimental and calculated beam moments are at the column face; the calculated beam moment capacities are based on different critical beam sections according to the reinforcement details (notes *, & and $ in Table 5.1) without considering the two discontinuous beam side bars (refer to Figure 4.3).

5.3.1 Specimen GR1

This specimen represents the reference for the other two specimens. In GR1, usual reinforcement details (detail T1, Figure 4.3) were provided at the connection with bending the beam main steel bars at the bottom to the top to form beam top reinforcement. The continuity of the beam top reinforcement across the connection was provided through using 2H20 steel bars embedded in grout within the trough.

5.3.1.1 Strength, rotational stiffness capacity and deflection of GR1

Specimen GR1 (Table 5.1) achieved a beam moment capacity not less than the predicted one, and exhibited an adequate stiffness. The predicted yield moment was 115.8 kNm ($M/bd^2 f_c = 0.06$), while the experimental one was 131.1 kNm for beam 1 ($M/bd^2 f_c = 0.068$), with the yield secant rotational stiffness 'S_y' of 30160 kNm/rad (see Figure 5.4). The moment at 0.3 mm crack width was 108 kNm ($M/bd^2 f_c = 0.056$).

Figure 5.4 shows the beam-column relative rotations 'θ' using two different methods, where method M1 gives higher θ values in comparison with method M2. This is because method M2 is susceptible to the crack locations and, at many loading stages, the POTs (at location C in Figure 5.4, for example) did not capture main cracks that happened within the connection. This is clear from the curve of method M2, where there is a setback in the curve around the yielding due to large cracks that occurred within the connection. This recommends the use of method M1 as a reliable way to measure the relative beam-column rotation.

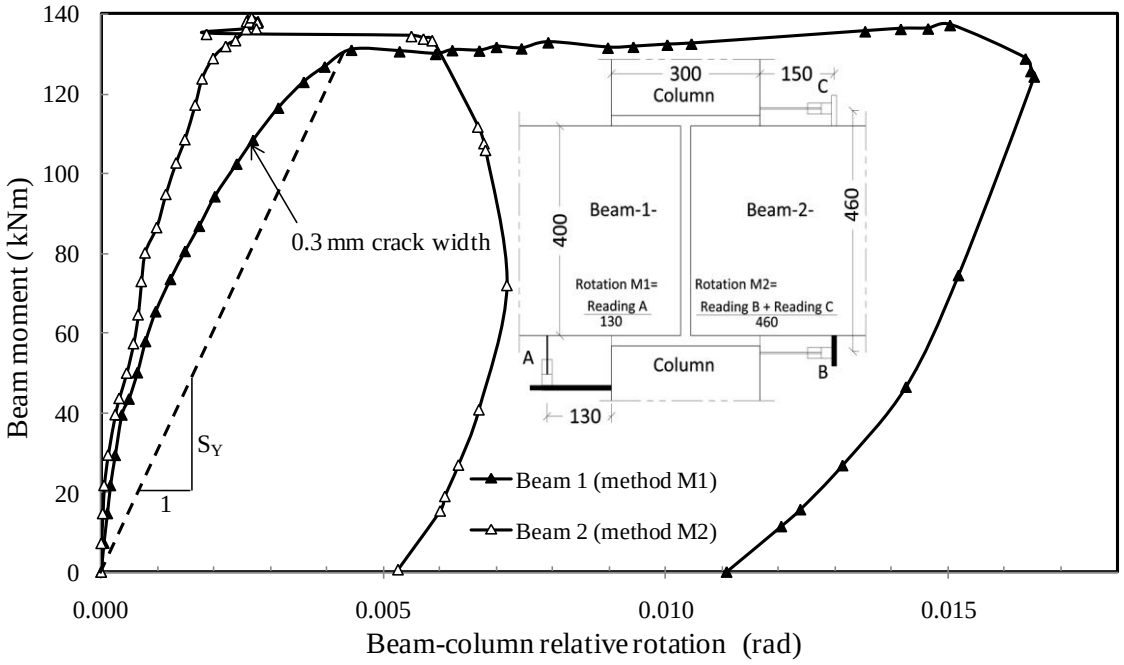

Figure 5.4 Beam moment vs. relative beam-column rotation in specimen GR1

Figure 5.5 shows the experimental beam deflections compared with predicted ones. In order to differentiate the additional deflection due to the relative beam-column rotation, the beam deflection is presented in two forms: (i) the elastic deformation 'Δ_1' considering the concrete's effective second moment of area I_{eff} as it was described in Section 5.2.4, and (ii) the elastic deformation due to the release of the rotation in the connection zone 'Δ_2' ($\Delta_2 = \theta$ L, where L is the lever arm of the load).

It is clear from Figure 5.5 that there is a match between $\Delta_1 + \Delta_2$ curve and the experimental deflection curve at the early loading stage, but there is some discrepancy afterwards. To some extent, this could be attributed to the model of calculating I_{eff}, where Al-Shaikh et al (1993) pointed out that the Branson model (ACI, 2008a) for calculating I_{eff} underestimated its value by 12% in the case of a lightly reinforced member (ρ = 0.8%), compared to the 0.6% reinforcement ratio used in specimen GR1.

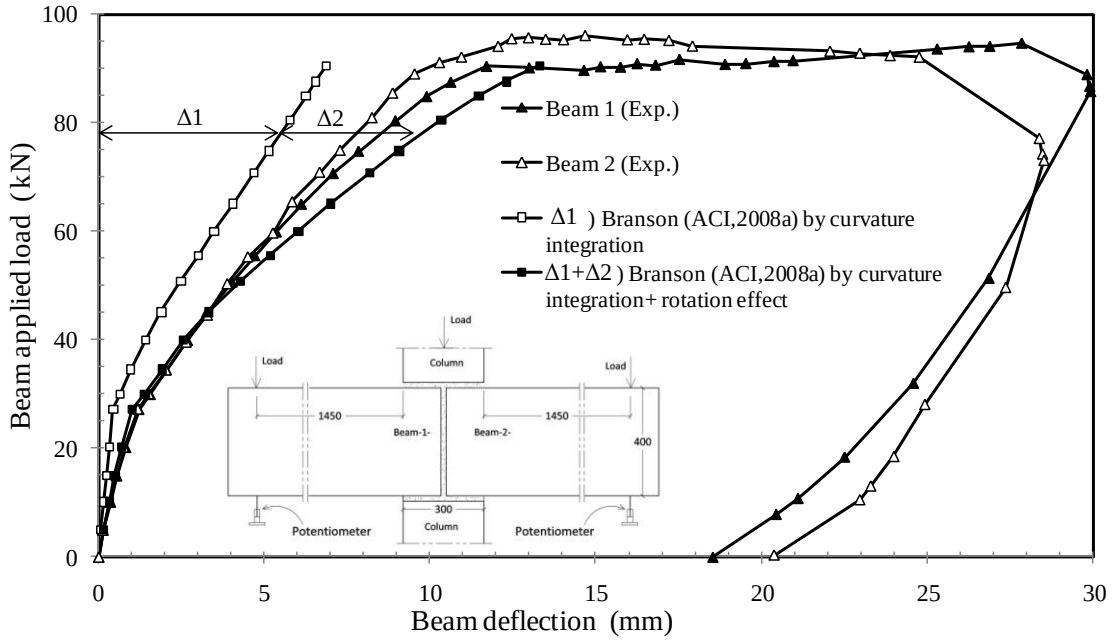

Figure 5.5 Beam load vs. deflection in specimen GR1

5.3.1.2 Crack pattern and failure mode of GR1

The failure mode of specimen GR1 was ductile with crack distribution along the beam length (Figure 5.6); however, there was concentration of cracks within the connection at the late stages of loading. The failure type was a combined flexure-bond with a ductility index of 3.5.

The bond loss partially developed in beam 1 (left beam) as shown in Figure 5.7c and Figure 5.7g, and fully developed in beam 2 (right beam) as shown in Figure 5.7d and Figure 5.7h. This difference was due to stopping the test upon noticing the bond loss at beam 2 without allowing the full bond loss to happen in beam 1. In beam 1, the bond loss appeared through splitting cracks and the pull-out of the beam grout.

In was beneficial to have beam 2 in the partial bond loss condition. This is to examine the initial state of the bond loss. By examining Figure 5.7g, it is clear that the bond loss started between the active 2H20 top steel bars embedded in the grout through

horizontal splitting cracks accompanied by losing the bond between the grout and the concrete at one side.

The first crack appeared at the interface between the beam and vertical grout within the connection at a beam load of 30 kN, followed by cracks at both sides accompanied by an extension of the first crack within the connection to the top and the bottom. After that, usual crack propagation similar to rigid beam-column connection was observed in the beam at both sides.

At load 55 kN (60% of the yield load) in beam 1 and load 60 kN (66% of the yield load) in beam 2, cracks appeared at the end of the 2H20 (discontinuous bent bars) within the connection signalling an improper bond state of these bars. At this stage, it could be stated that another behaviour mechanism started by locating the weak beam section at the end of these bent bars within the connection rather than the beam section at the column face.

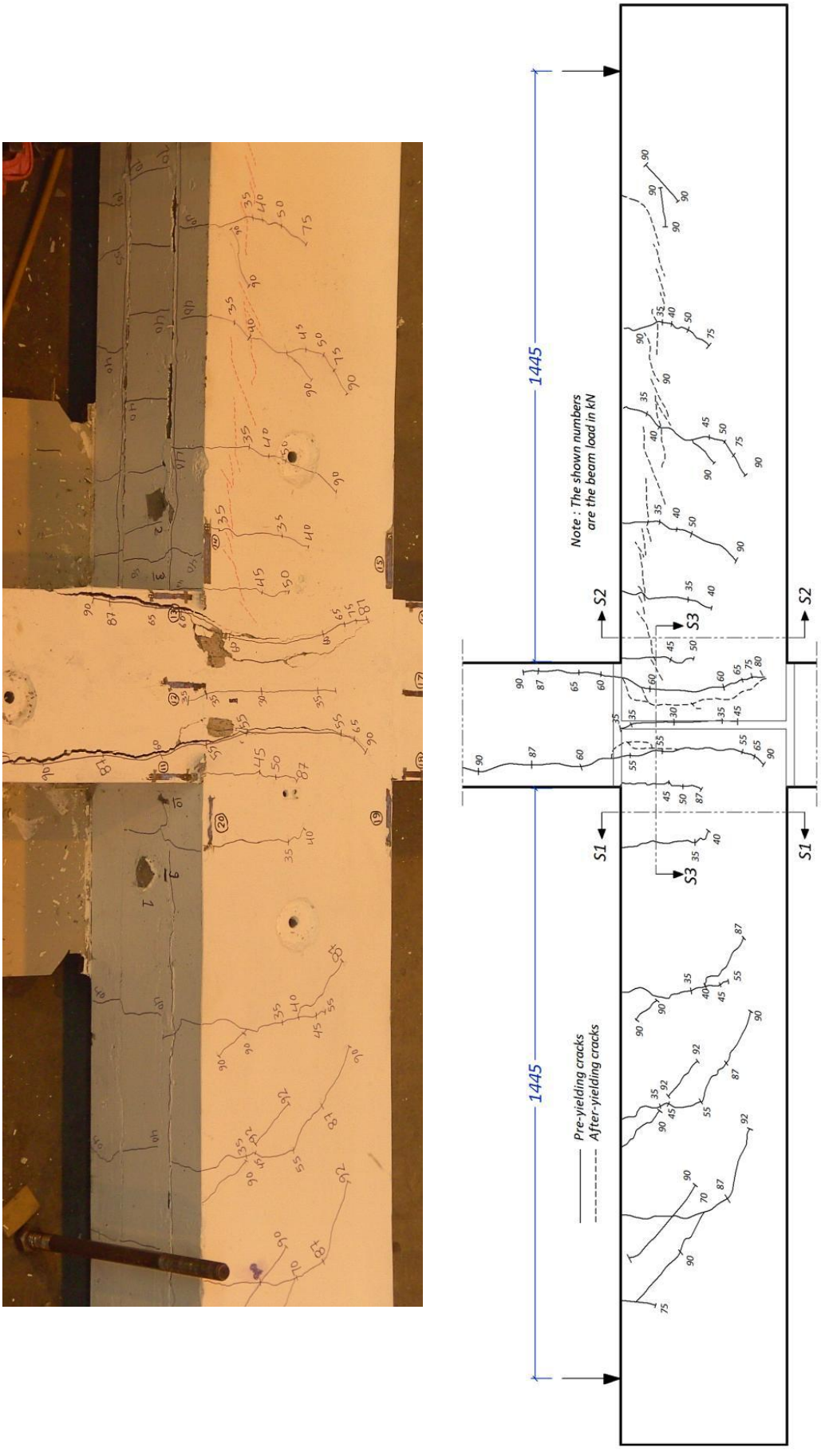

Figure 5.6 Cracking pattern at failure in specimen GR1

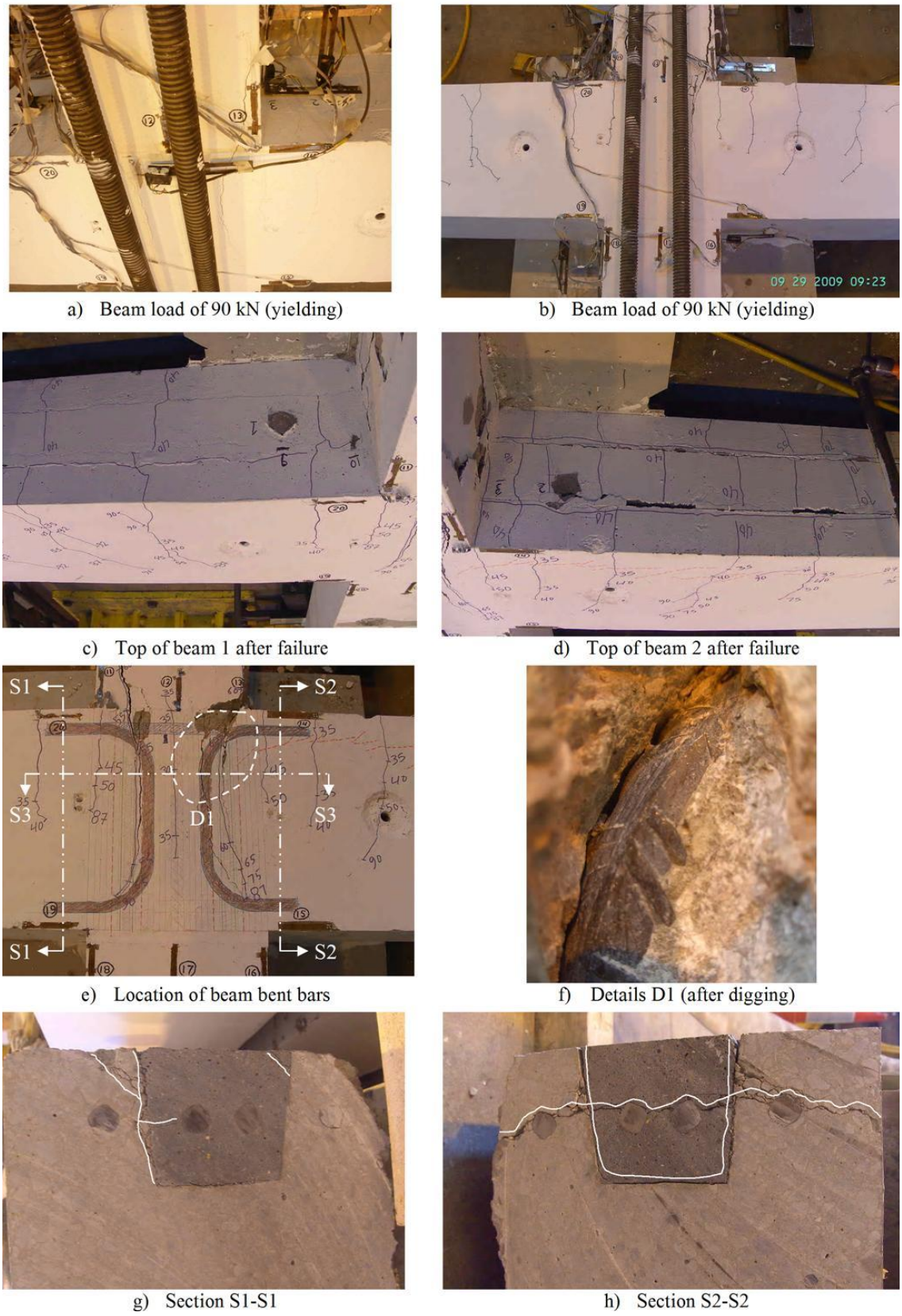

a) Beam load of 90 kN (yielding)

b) Beam load of 90 kN (yielding)

c) Top of beam 1 after failure

d) Top of beam 2 after failure

e) Location of beam bent bars

f) Details D1 (after digging)

g) Section S1-S1

h) Section S2-S2

Figure 5.7 Details of propagation, distribution and spacing of cracks in specimen GR1

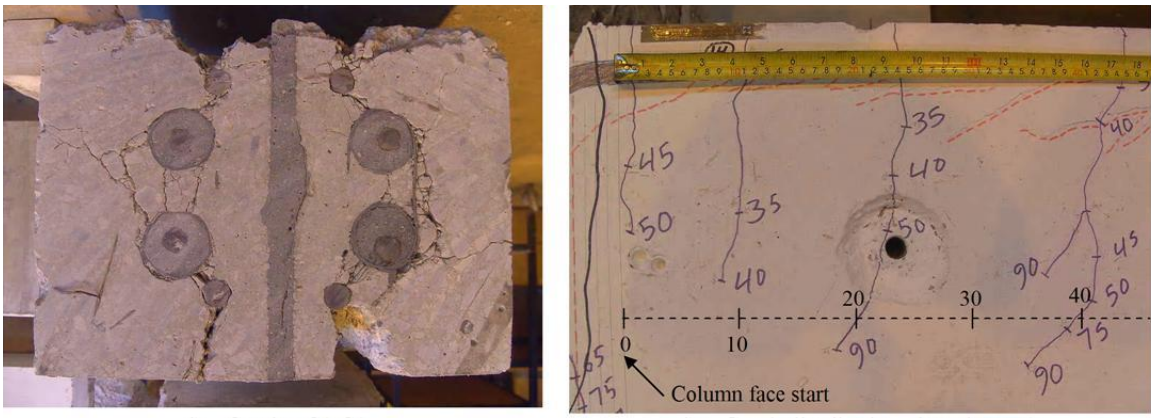

i) Section S3-S3 j) Crack distribution along beam 2

Figure 5.7 (Cont.) Details of propagation, distribution and spacing of cracks in specimen GR1

5.3.1.3 Beam steel and concrete strains and deformations of GR1

Figure 5.8 and Figure 5.9 show the moment 'M' versus crack opening '*w*' at the top of the beam, and M against the compressive deformation 'δ_c' at the bottom face of the beam, respectively. These two readings (*w* and δ_c) gave the relative beam-column rotation using method M2. In both graphs, by comparing the experimental relation with predicted relation assuming rigid connection behaviour, it is obvious that there is an additional tension crack opening at the top of the connection and additional compressive deformation at the bottom of the connection. These are the cause of the occurrence of the relative beam-column rotation and consequently the semi-rigid behaviour of the connection.

The crack opening represents the crack widths within the measured zone only, and does not include the cracks outside it. This is especially true for not including the cracks within the connection, where fine cracks appeared at the early loading stage with a concentration of large cracks at the ultimate limit state. This might explain the set back of the crack width of beam 2 after the yielding before continuing to follow beam 1. This might suggest that using these readings to calculate the relative beam-column rotation would not give the correct relative rotation and overestimate the rotational stiffness.

Figure 5.10 and Figure 5.11 show the strain recorded in the beam for both the concrete and steel bars, respectively. The experimental values are compared with predicted ones obtained using the procedure presented in Section 5.2.6, where point P1 represents the cracking moment and point P2 represents the yield moment. The contribution of the non-continuous 2H20 side bars was not considered in the calculation of the predicted strains.

According to Figure 5.10 and Figure 5.11, the experimental curve follows the predicted behaviour, and the only exception is location D in the steel bars. The discrepancy in this bar started prior to the yielding, which is attributed to a different bond status at location D. In Figure 5.11, it is noticeable that there is a difference in the behaviour between the predicted curve and the tested one between moments 21.7 (15 kN beam load) and 39.5 kNm (27.25 kN beam load). The difference is attributed to cracks at the precast component interfaces within the connection that did not extend to the external surface of the concrete to be seen, which are not considered in the predicted curve.

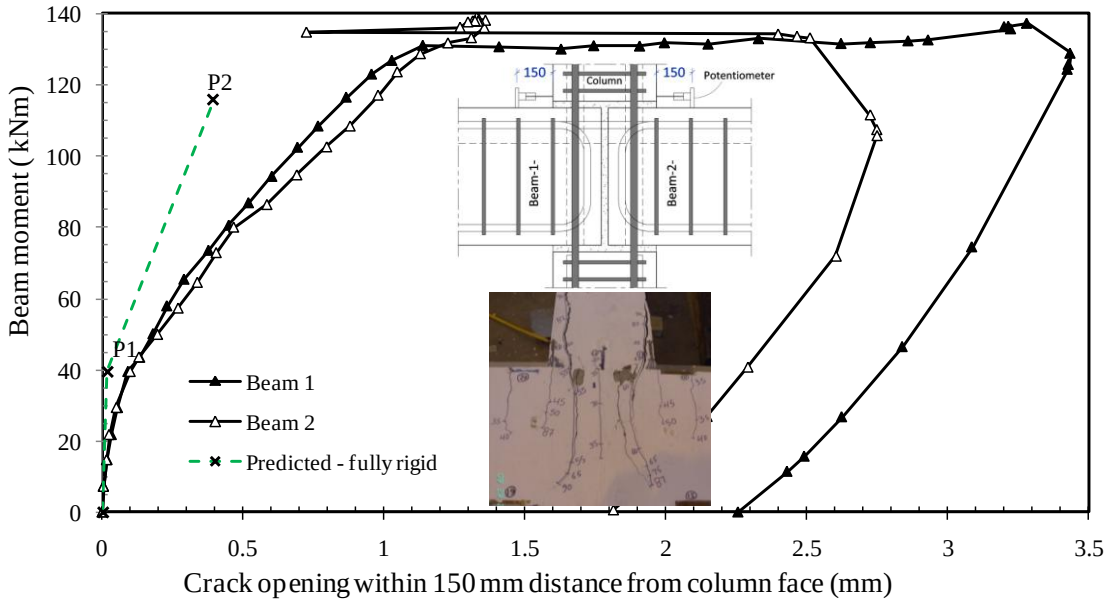

Figure 5.8 Beam moment vs. crack opening at beam-column top boundary in specimen GR1

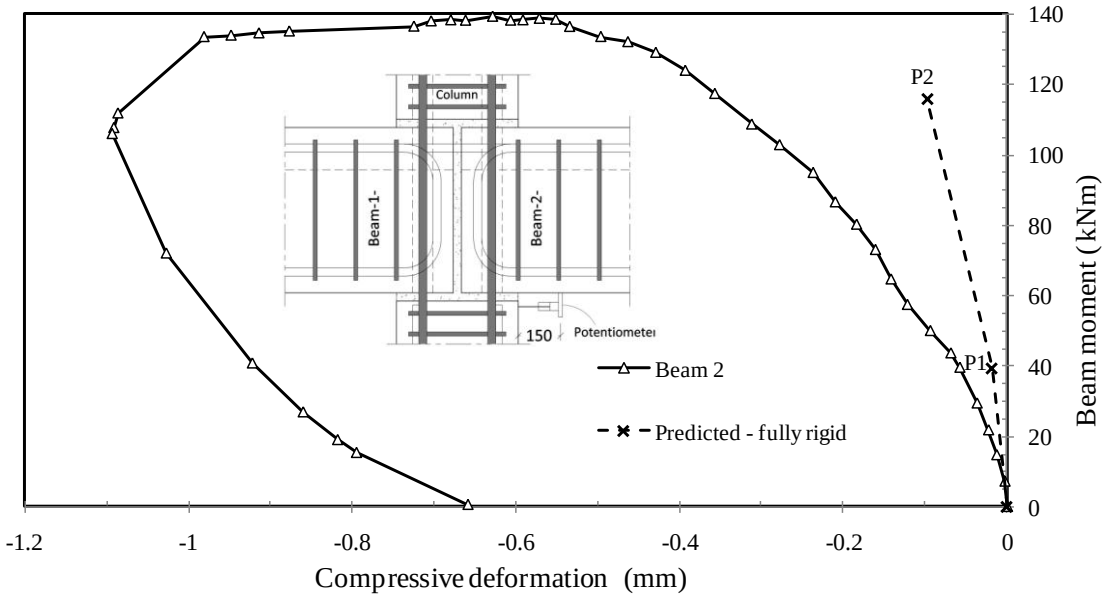

Figure 5.9 Beam moment vs. concrete compressive deformation at bottom beam-column interface in specimen GR1

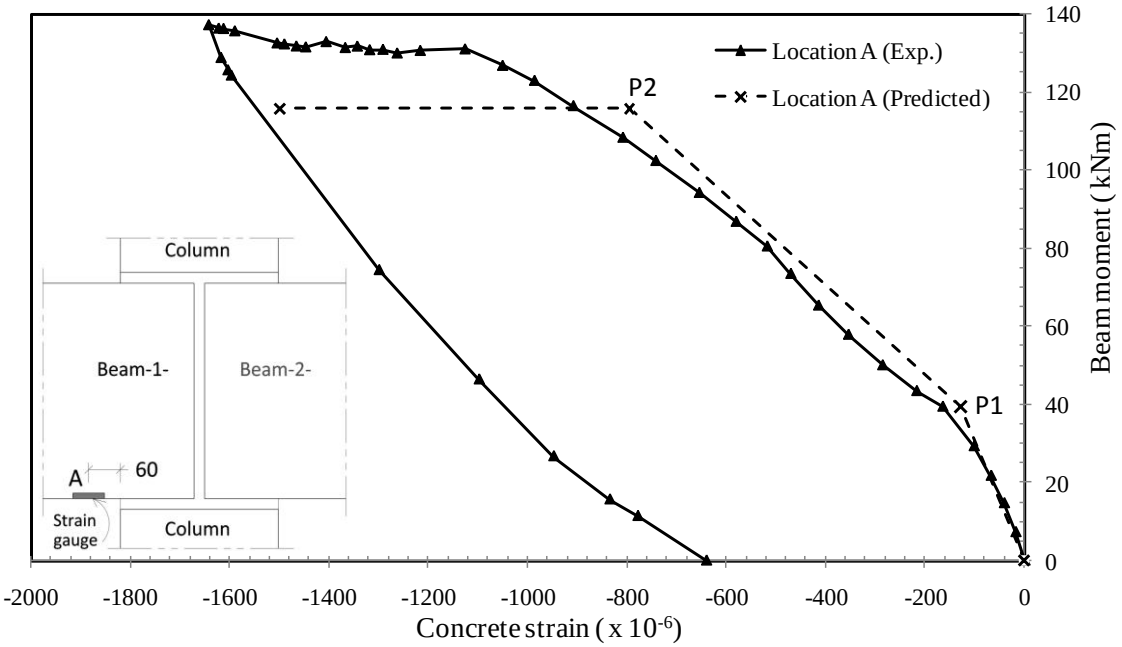

Figure 5.10 Beam moment vs. concrete compressive strain at the bottom of beam 1 in specimen GR1

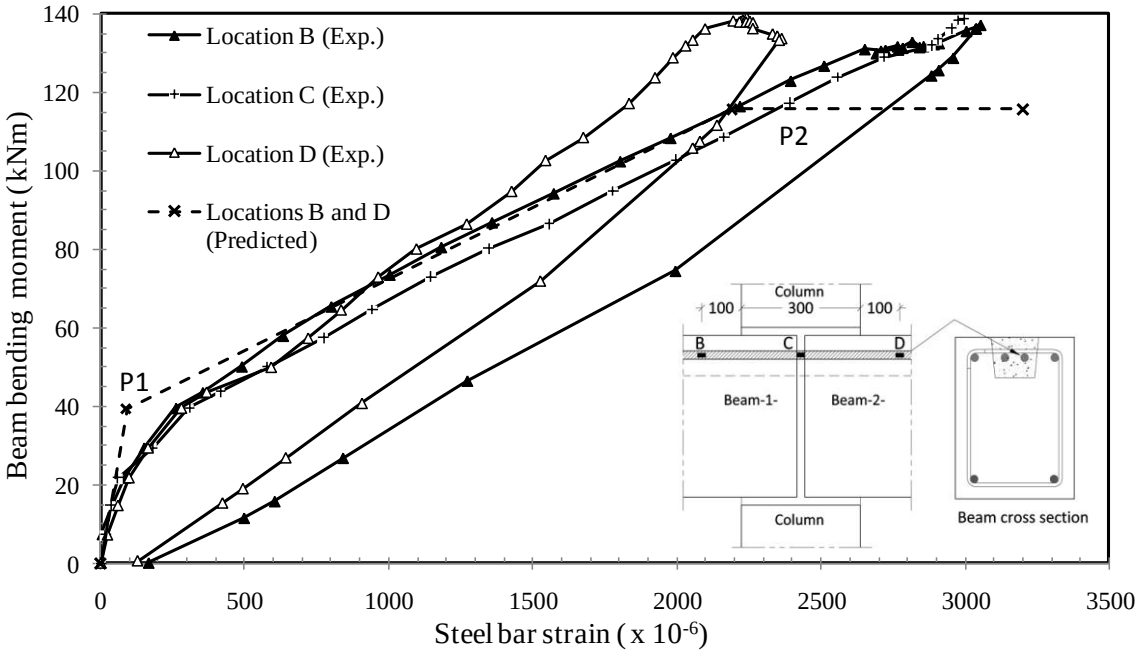

Figure 5.11 Beam moment vs. beam steel bar strain in specimen GR1

5.3.1.4 Column vertical strain distribution of GR1

The axial strain distributions in the top column are shown in Figure 5.12; as shown, there is an eccentricity in the column axial load, which is the reason for not having a uniform constant strain distribution even before applying the beam load.

The dashed lines in Figure 5.12 are connecting the readings of the middle strain gauge 'SG' with those at the right side, which does not represent the actual strain status starting from a 65.4 kN beam load. This is because, at this loading stage, the cracks extended to the top of the SG at the right side, and started to separate the location, where the SG was attached, from the column. The strain in the top column (apart from the initial column load eccentricity) was almost uniform up to a 59.6 kN beam load, before the extension of cracks to the top column.

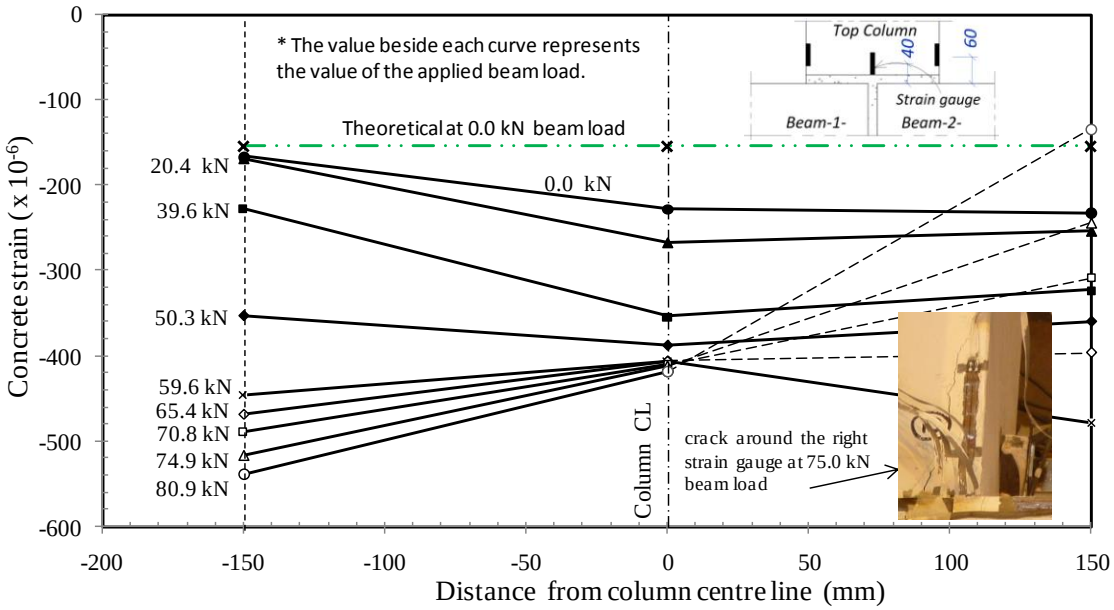

Figure 5.12 Strain distribution at top column in specimen GR1

5.3.2 Specimen GR2

Based on the results of specimen GR1, the design of specimen GR2 aimed to modify the behaviour by decreasing the crack widths within the connection zone, which comprises the interfaces and parts of the adjoining elements, and shifting the concentration of cracks to the outside of this zone. The modifications included the use of 2H16 mm diameter straight steel bars as the beam discontinuous top bars, horizontal U-shaped links at the beam ends, and closer column link spacing at the connection side (Figure 4.4a). In addition, in order to investigate the effect of repeated loading on the strain recovery, the specimen was tested under repeated loading schemes (Section 4.3.3). It should be mentioned that the moments reported in Table 5.1 regarding specimen GR2 include a moment of 3.7 kNm due to the beam self-weight, which represents 2.8% to 2.4% of the reported moments; despite that, the loads and moments reported for GR2 are those due to only the applied beam load as no measurements were taken for the deflection or the rotation under the self-weight.

5.3.2.1 Strength, rotational stiffness capacity and deflection of GR2

Specimen GR2 achieved a beam moment capacity close to the one predicted according to EC2 (CEN, 2004b) (Table 5.1). The predicted yield moment was 143.7 kNm ($M/bd^2 f_c$ =0.064), while the experimental value was 136.7 kNm ($M/bd^2 f_c$ = 0.061), with yield secant rotational stiffness 'S_y' ranging from 29910 kNm/rad for beam 1 and 28950 kNm/rad for beam 2 (see Figure 5.13). This range of S_y is close to that obtained in specimen GR1, meaning that the connection reinforcement of type T2 had no significant effect on S_y.

Figure 5.13 shows the beam-column relative rotations 'θ' of specimen GR1 using method M1 (refer to Section 5.2.2). As shown in the specimen GR1 results, this method would give a more representative value for θ to be used in determining the rotational stiffness of the connection.

Figure 5.14 shows the experimental beam deflections compared with the predicted ones. Similar to specimen GR1, the beam deflection is attributed to the elastic deformation (Δ_1), and the release of the rotation in the connection zone ($\Delta_2 = \theta L$). As shown, there is almost a perfect match between the predicted curve ($\Delta_1+\Delta_2$) and the experimental curve at the early loading stage; however, at the later loading stages, there is some discrepancy due to the same reason presented for specimen GR2 (the underestimation of I_{eff}, refer to page 5-10).

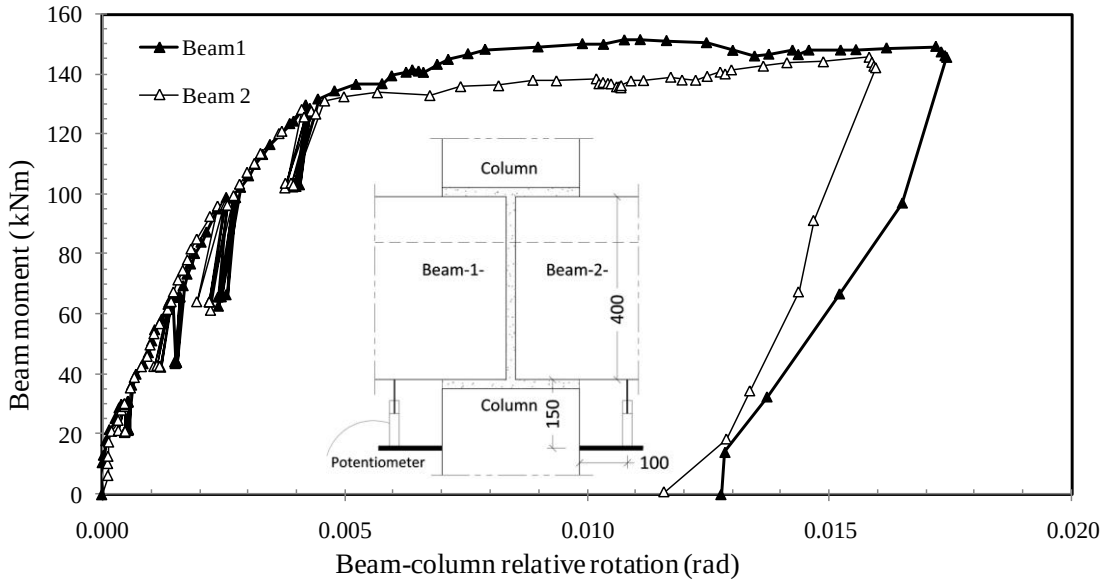

Figure 5.13 Beam moment vs. relative beam- column rotation in specimen GR2

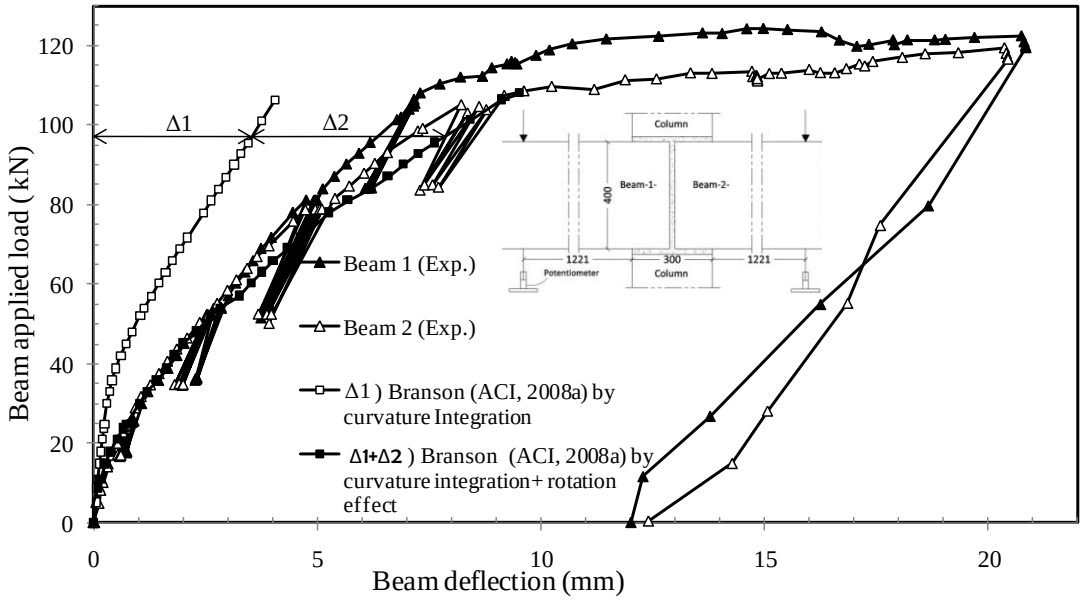

Figure 5.14 Beam load vs. deflection in specimen GR2

5.3.2.2 Crack pattern and failure mode of GR2

The failure mode of specimen GR2 was ductile (Figure 5.15 and Figure 5.16) with a distribution of cracks along the beam length. The new connection reinforcement detail (type T2) was successful in shifting the location of the large cracks to be 380 mm from column face (location E in Figure 5.15b, and Figure 5.17), where the additional horizontal links are terminated. Up to 72 kN beam load (88 kNm moment = 65% of the

yield moment), the cracks observed within the connection were hair cracks, and there was a controlled crack width zone at the beam-ends. Starting from that load (72 kN beam load), the crack width at location A started to widen and reached 0.3 mm width at 102 kN beam load (124 kNm moment = 95% of the yield moment), followed by a concentration of cracks within the connection at both sides. The final failure type was a flexure failure without bond loss.

From above, it is apparent that the new connection reinforcement detail (T2) was able to control the crack width within the connection zone up to 95% of the yield moment. However, detail T2 failed to prevent the final concentration of cracks from happening within the connection. This shows that the final weak section along the beam length is still around the middle of the connection where only the 2H20 beam steel bars are continuous. This feature was addressed and aimed to be solved in the following specimen (GR3).

Table 5.1 shows that the new reinforcement detail T2 had no significant effect on M_y or S_y; however, there was a marked decrease in the crack width at the beam-ends close to the column face where the additional horizontal links were provided.

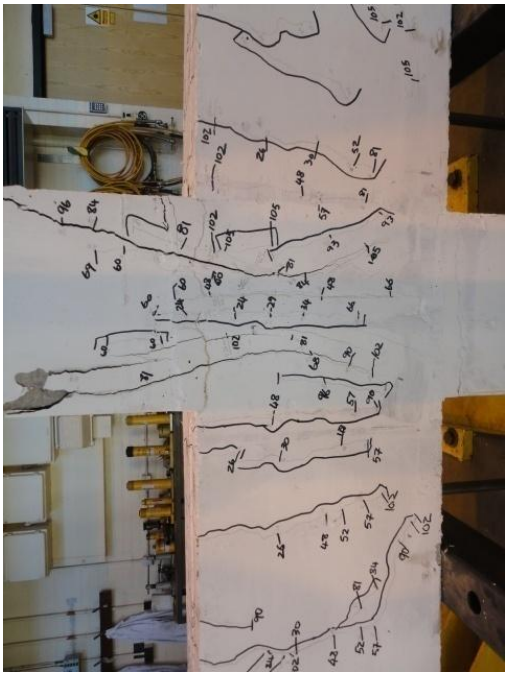

a) Photo

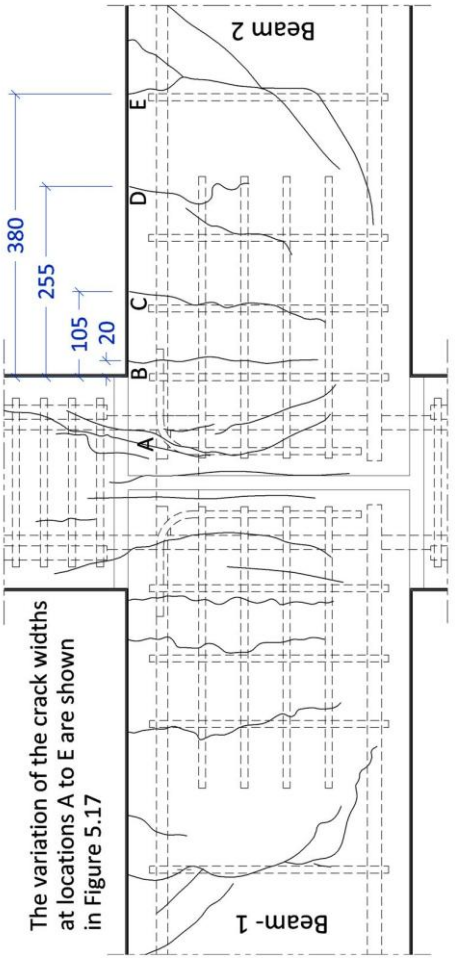

b) Approximate crack-reinforcement relative location

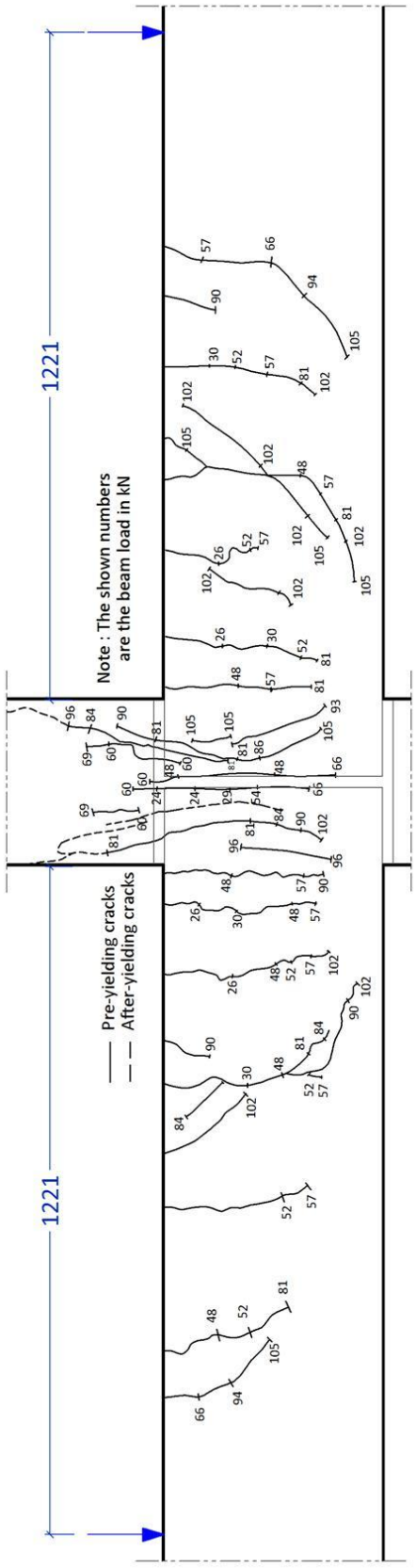

c) Sketch

Figure 5.15 Cracking pattern at failure in specimen GR2

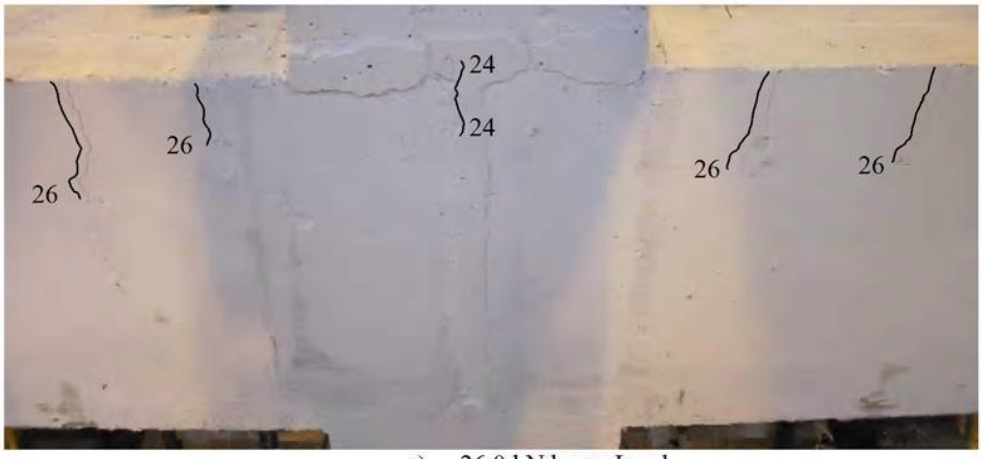

a) 26.0 kN beam Load

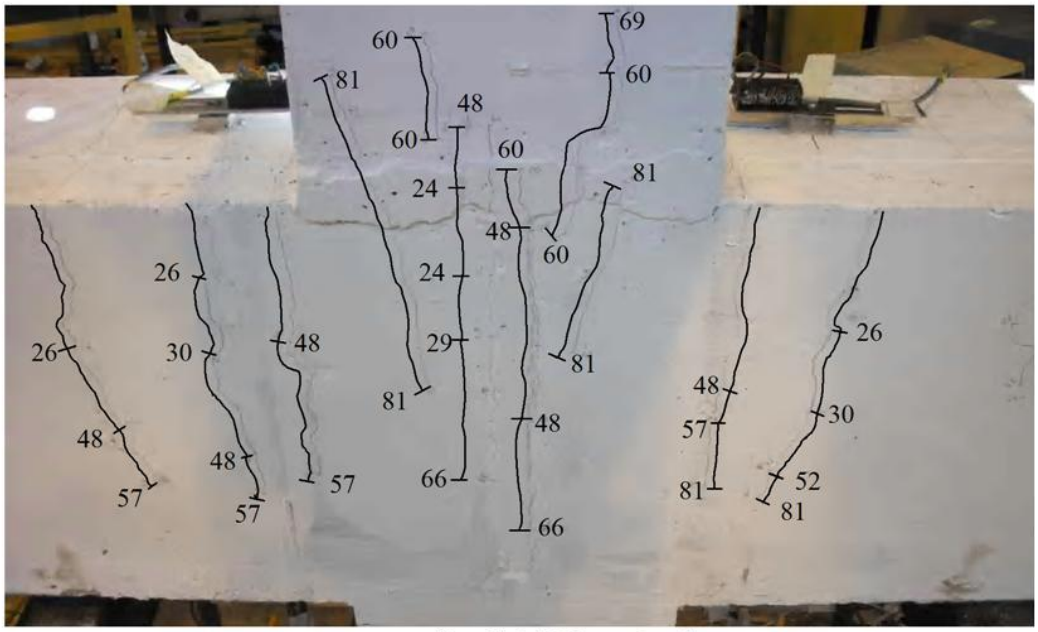

b) 81.0 kN beam Load

c) 105kN beam Load (prior to yielding)

d) At failure

Figure 5.16 Details of crack propagation at different beam load levels in specimen GR2

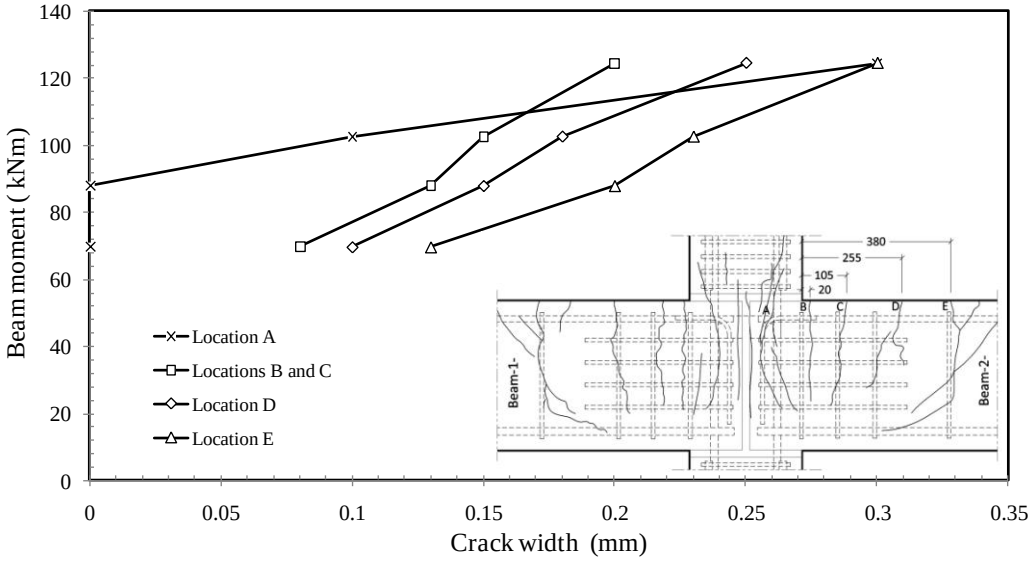

Figure 5.17 Crack width vs. beam load in specimen GR2

5.3.2.3 Beam steel and concrete strains and deformations of GR2

Figure 5.18 shows the beam moment 'M' versus crack opening 'w' at the top of the beam within the measured zone (100 mm); there was a continuous development in the crack width up to some stage after the yield moment 'M_y'. However, this development stopped in the middle of the plastification stage and there was even a decrease in the crack width in beam 1. This is attributed to the extension of large cracks from the connection to the top column, which was outside the zone of crack width measurement. On the other hand, the variation of the compressive deformation 'δ_c' at the bottom face of the beam against M within the measured zone (100 mm) was consistent even after the yielding as shown in Figure 5.19, which demonstrates the ductility of the connection. However, as shown in Figure 5.18 and Figure 5.19, the experimental behaviour of the beam-column connection is still not close to the rigid behaviour.

Figure 5.20 and Figure 5.21 show the strains recorded in both the concrete and steel bars, respectively, which are compared with relations predicted using the procedure presented in Section 5.2.6 and considering the horizontal H10 links used at

the beam-ends in the calculation of I_{eff}. As seen, the experimental curves follow the predicted relations, except for the steel bar strain around the 41.3 kNm predicted cracking moment (29.3 kN beam load). This behaviour is similar to what have been observed in specimen GR1.

Figure 5.21 shows that there was a change in the experimental behaviour at 18 kN beam moment (15 kN beam load) indicating the occurrence of cracks within the connection that did extend to the surfaces. Through the visual inspection, no crack was observed at this loading stage, and the first crack initiated in the vertical interface between the beam and the vertical grout within the connection at a moment of 29.3 kNm (24 kN beam load), followed by a crack at the column face at a moment of 32 kNm (26 kN beam load)

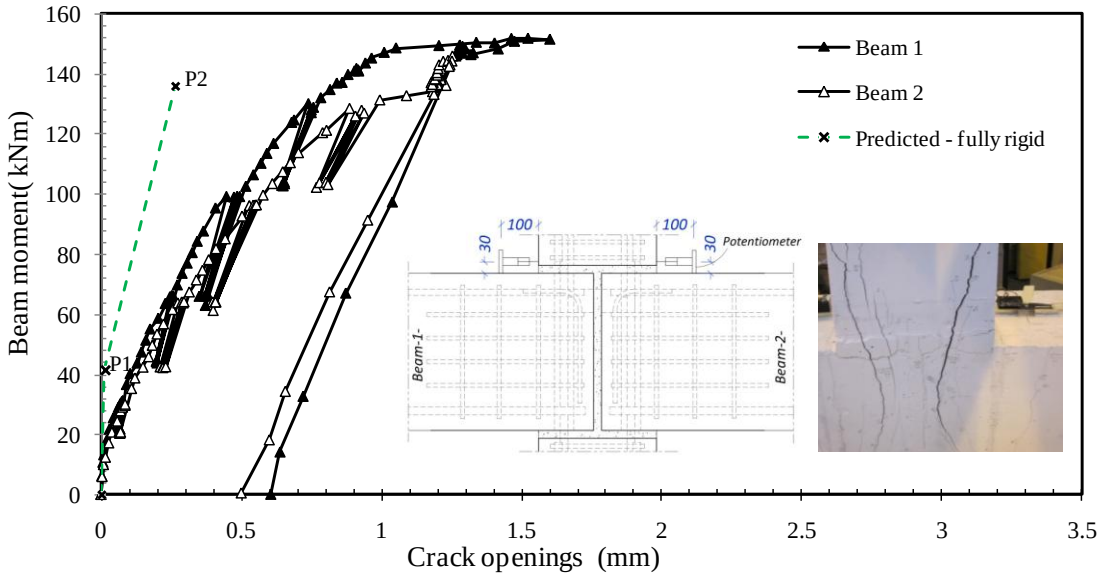

Figure 5.18 Moment vs. crack opening at beam-column top boundary in specimen GR2

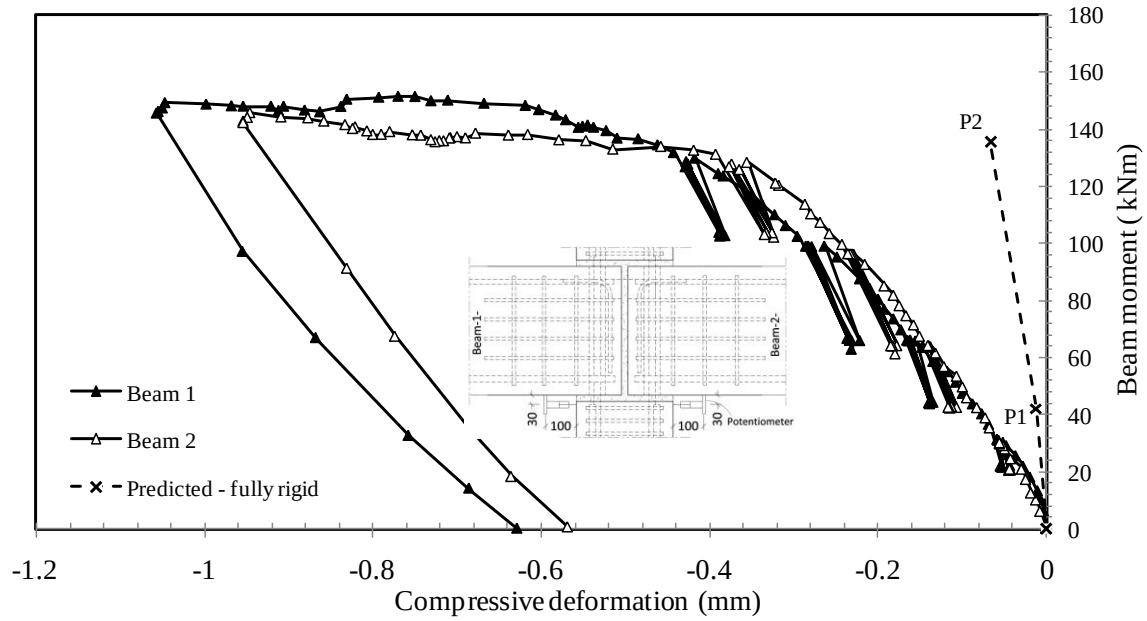

Figure 5.19 Moment vs. concrete compressive deformation
at bottom beam-column interface in specimen GR2

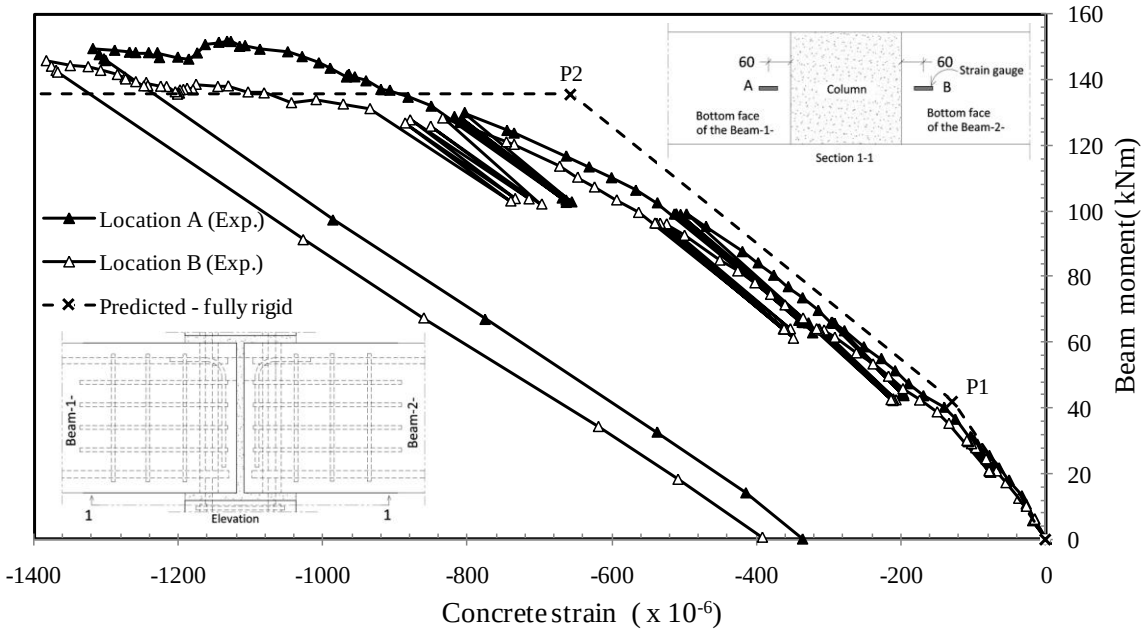

Figure 5.20 Moment vs. concrete compressive strain
at bottom of beam in specimen GR2

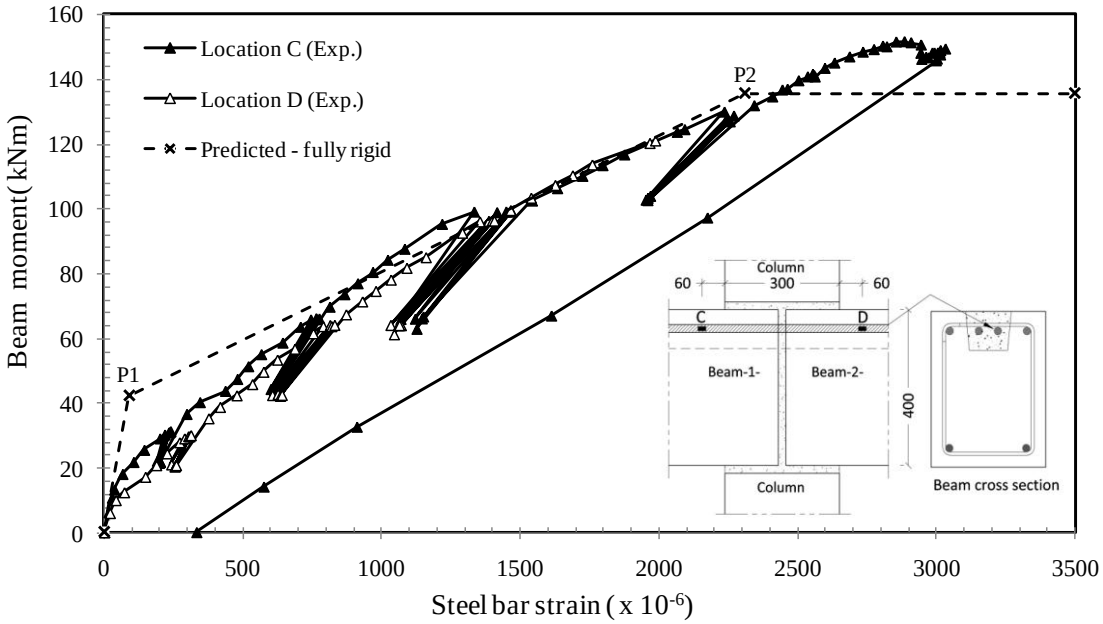

Figure 5.21 Moment vs. beam steel bar strain in specimen GR2

5.3.3 Specimen GR3

To prevent the plane of weakness that appeared in the previous specimen (GR2) prior to yielding (refer to page 5-22), in the current specimen (GR3) 2H20 short steel bars of length equal to the column width plus two times the beam depth (300 + 2 x 400 = 1100 mm) were added in the beam trough to work as an active beam top reinforcement within the connection zone. In addition, 2H8 mm additional links were added around the column main bars at the beam top level (detail T3, Figure 4.4b).

5.3.3.1 Strength, rotational stiffness capacity and deflection of GR3

The achieved maximum moment (M = 210.1 kNm for beam 1) of specimen GR3 increased by 60% with respect to M_y of GR1; however, there was a sudden drop in the moment at that stage due to a bond loss at approximately 300-400 mm from column face. The beam moment dropped to approximately the moment of resistance of the 3 m long continuous 2H20 mm steel bars at 400 mm from column face (115.4 kNm), giving a final stable M = 159.4 kNm at the column face, which could be considered as the safe

ultimate moment capacity (M_u). For the beam at the other side (beam 2), the maximum achieved moment was 217 kNm and reduced to 159.7 kNm at the loss of bond.

It is believed that, before the moment drop, the stress in the two H20 shorts bars was transmitting to the 2H16 side bars through a 520 mm indirect overlapped length (refer to Figure 4.4b). Up to 210 kNm moment (beam 1) and 217 kNm moment (beam 2), it seems that there was a contribution from the 2H16 non-continuous side bars; beyond this moment, only the 2H20 mm continuous steel bars were active. In spite of this, the critical section remained at 300-400 mm from column face, where the continuous 2H20 bars remained active. This gave a final M_u = 159.4 kNm (beam 1), which is still 16% greater than the M_u in the reference test GR1.

There was a very significant increase in the rotational stiffness (245%) in GR3. This is true if S of GR3 is calculated at a moment equal to 159.4 kNm for beam 1 in the ascending part, which is considered as the ultimate moment capacity of beam 1, neglecting the contribution of the 2H16 mm discontinuous side bars.

The ductility of GR3 could not be captured through the measured rotations (Figure 5.22) due to the concentration of the rotation (at the plastification stage) away from the column face, where the rotation measurements were taken; however, the ductility is apparent through the measured deflections (Figure 5.23).

In Figure 5.23, similar to what has been done for specimens GR1 and GR2, a comparison is made between the experimental beam deflections and the predicted values. The comparison shows that the difference between the experimental and predicted deflection values is small in specimen GR3 compared with the other two specimens (GR1 and GR2), which is an indication of behaviour close to a monolithic one.

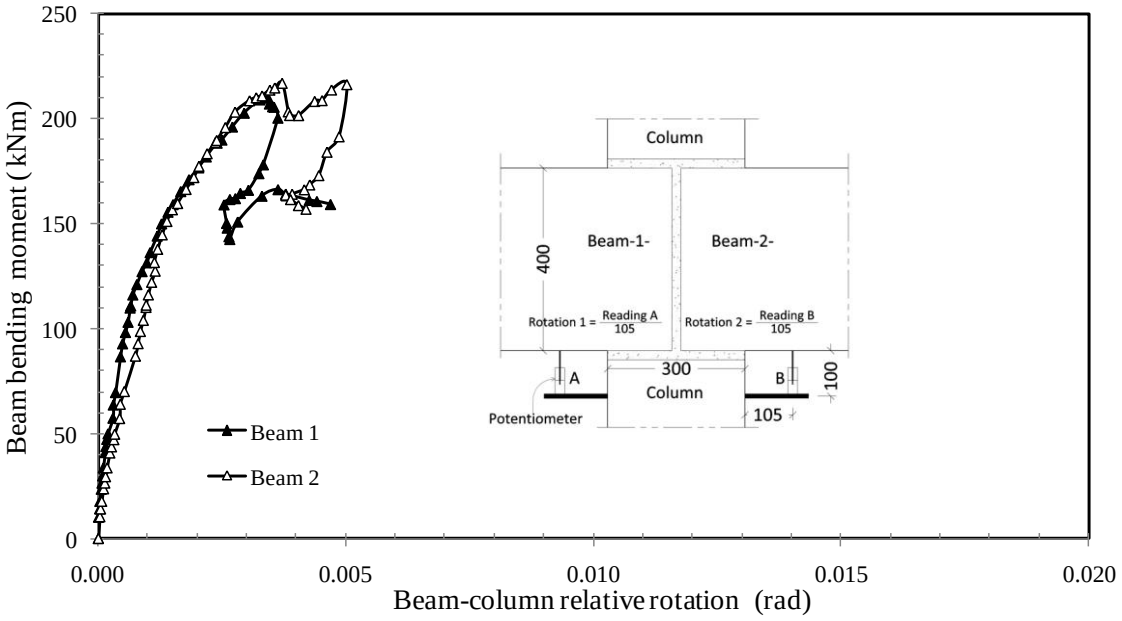

Figure 5.22 Beam moment vs. relative beam-column rotation in specimen GR3

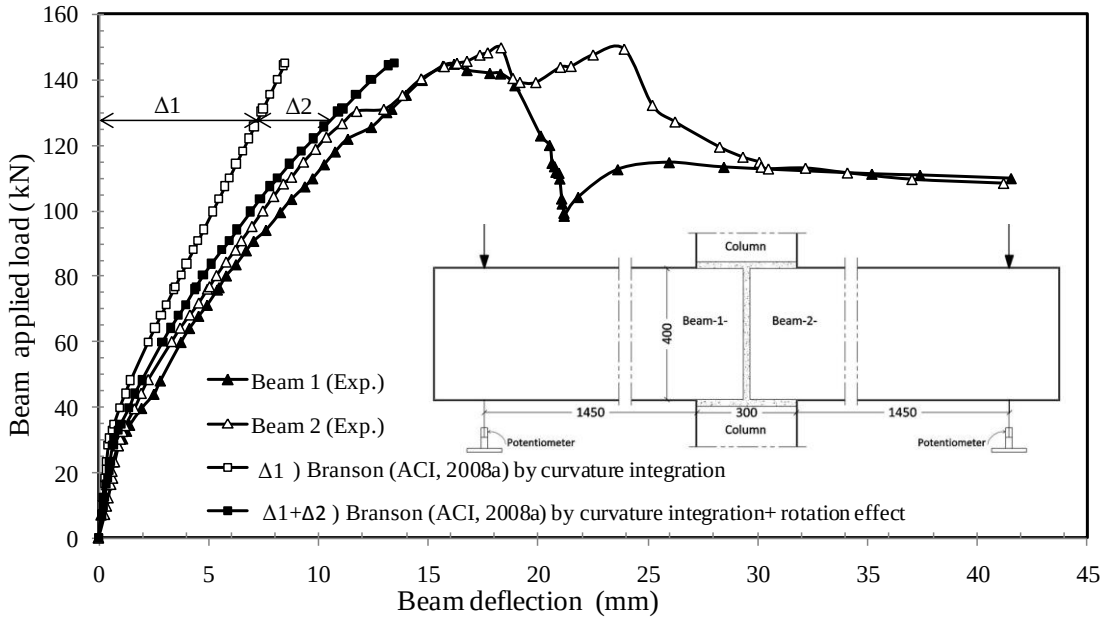

Figure 5.23 Beam load vs. deflection in specimen GR3

5.3.3.2 Crack pattern and failure mode of GR3

Specimen GR3 showed a ductile behaviour with a controlled crack width within the connection zone, similar to specimen GR2. The significant feature observed in specimen GR3 is being able to prevent the crack concentration at the connection (prior to steel yielding and in the plastification stage) and enforce it to be located within 300 to

400 mm (75% to 100% of the beam depth) from the column face (see Figures 5.24 and 5.25).

In contrast to the other two specimens (GR1 and GR2), the first cracks initiated in the beams at a distance of 120 to 400 mm from the column face (not within the connection) at a beam load of 32 kN due to the use of the 2H20 additional short steel bars in the trough which crossed the connection. At a beam load of 40 kN (58 kNm moment), cracks appeared at the column faces accompanied by a vertical crack within the connection at the interface between the beam and the grout.

At the following loading stages, there was a propagation of cracks in the beam from the column faces towards the location of the applied beam loads, with less crack propagation within the connection in comparison with specimens GR1 and GR2. There was limited crack width zone at the region close to the column face; for example, the crack width did not exceed 0.1 mm at location A (see Figure 5.26). The concentration of cracks was at location B (300-400 mm from column face), where the crack width was 0.15, 0.2 and 0.3 mm at beam loads of 68, 94 kN and 114 kN, respectively.

The closest crack to the applied beam loads happened at a load of 126 kN and 130 kN for beam 1 and beam 2, respectively. These cracks propagated vertically and diagonally indicating a flexure-shear mechanise resulting from a large shear force to moment ratio.

The connection ductility is clear through sustaining a constant beam load after the bond loss; however, the test was stopped when the beam deflection reached 2.2 and 2.6 (ductility index) times the deflection recorded at the maximum load. This stop was due to the damage appeared in the beam within 300-400 mm from column faces, where the final failure type could be classified as a flexure-bond loss failure.

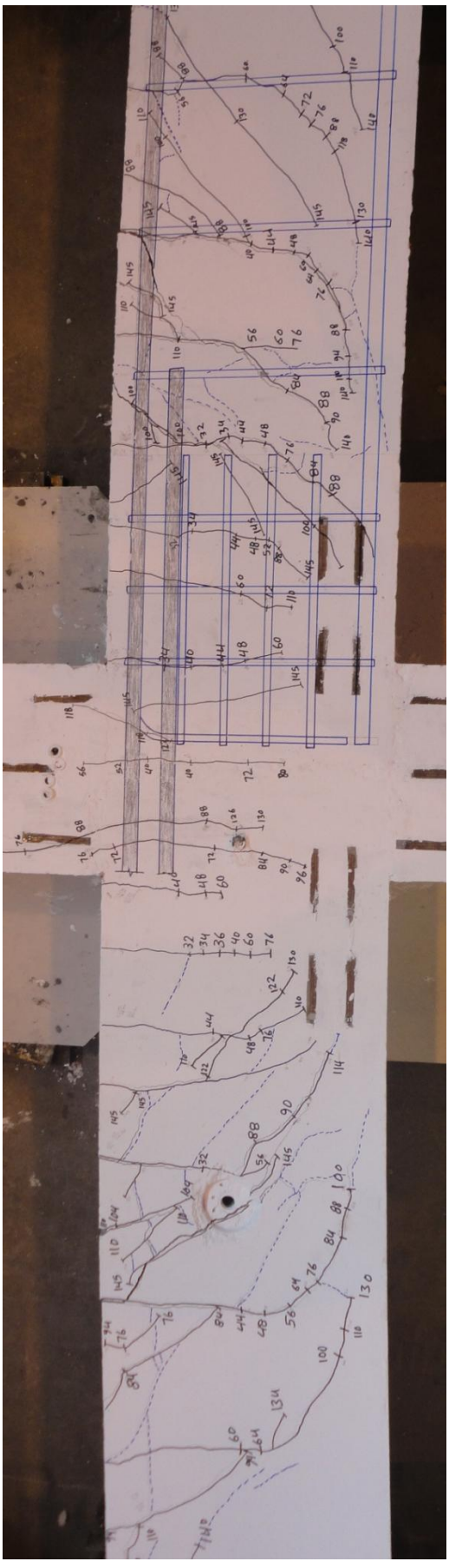

a) Photo

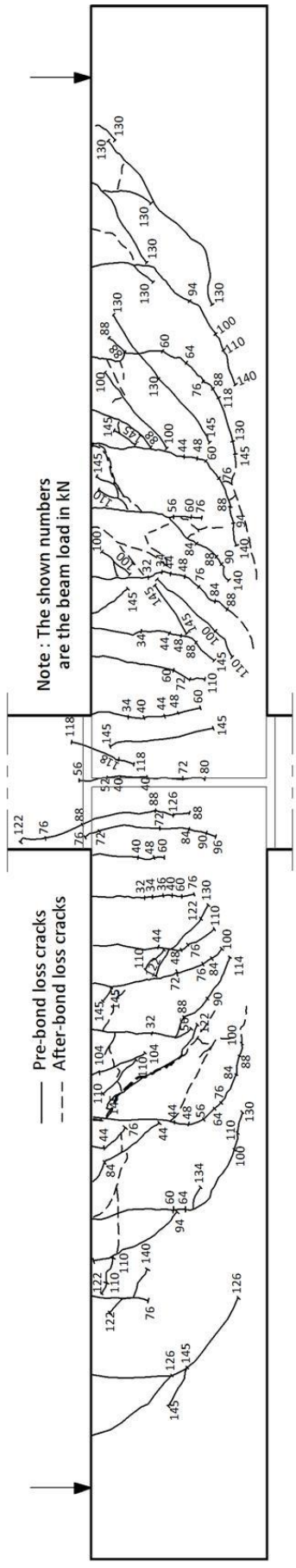

b) Sketch

Figure 5.24 Cracking pattern at failure in specimen GR3

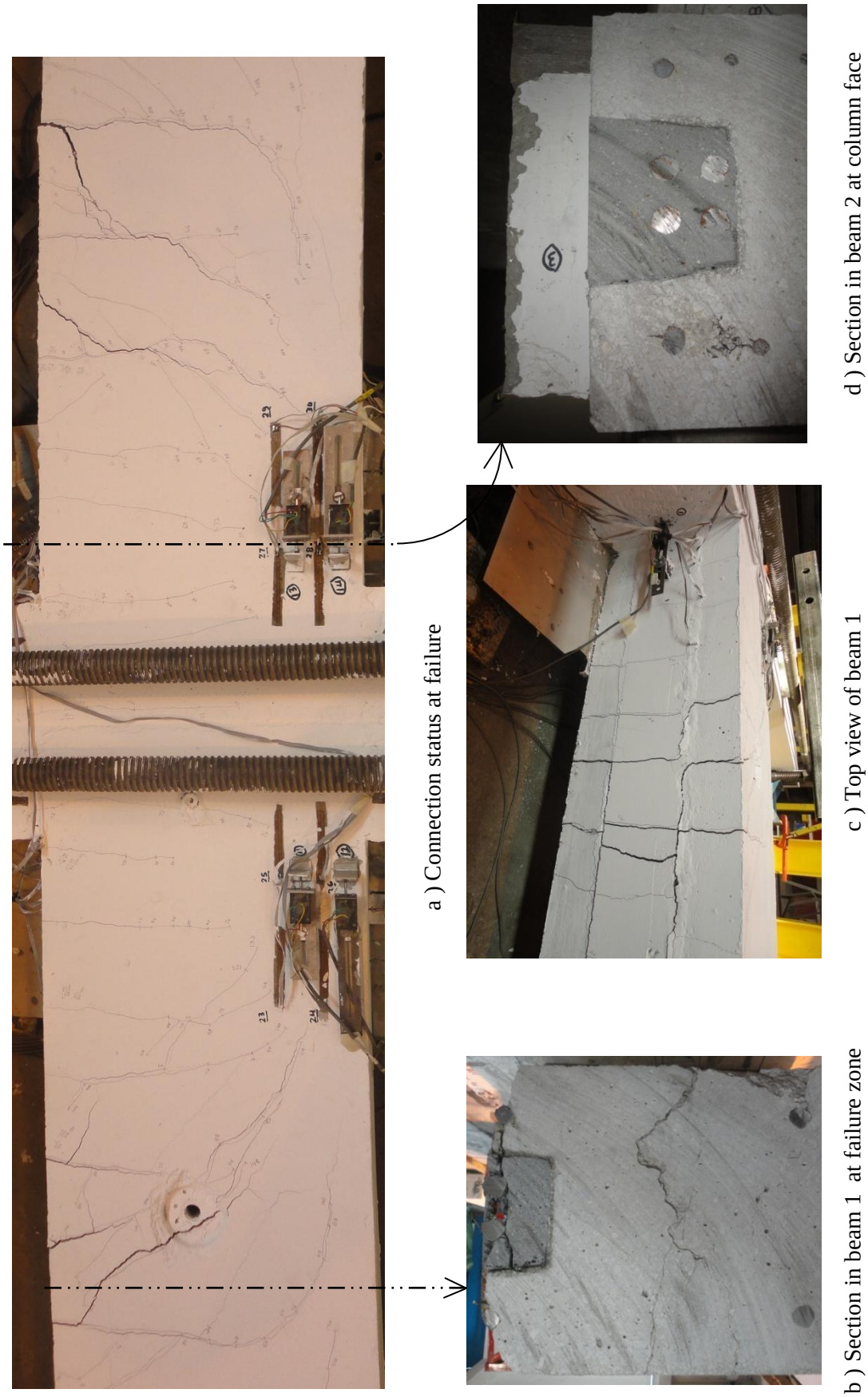

a) Connection status at failure

b) Section in beam 1 at failure zone

c) Top view of beam 1

d) Section in beam 2 at column face

Figure 5.25 Inspection of failure locations in specimen GR3

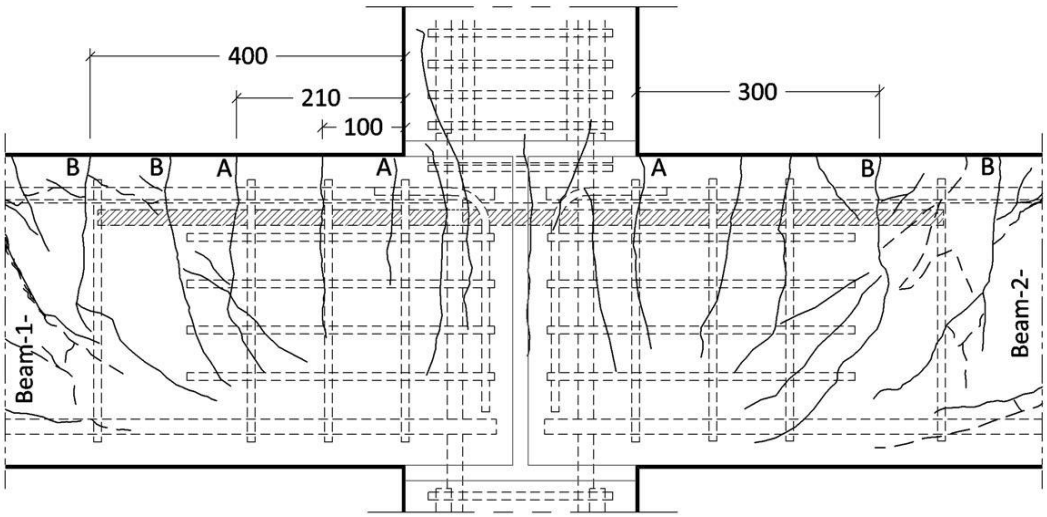

Figure 5.26 Crack width measurement locations in specimen GR3

5.3.3.3 Beam steel and concrete strains and deformations of GR3

The variation of the crack opening '*w*' (tensile deformation) at the top of the beam within the measured zone (105 mm) against the beam moment '*M*' is shown in Figure 5.27. A continuous increase in the crack width was observed at both beam sides up to the maximum moment capacity (210 kNm in beam 1), when a sudden drop occurred in the crack width at these regions due to the bond loss and intensifying the cracks within 300-400 mm away from the column faces. From the graph, it could be noticed that the drop in the crack opening is almost proportional to the amount of the dropped moment; this suggests that the stress in the steel bars at the column face was still in the elastic range.

On the other hand, the deformation δ_c at the compression zone of the beam against *M* within the measured zone (105 mm) was increasing even after the bond loss (Figure 5.28), indicating an increase in the concrete strain due to the crack propagation to location A from the region at 300-400 mm from the column face.

The variation of beam compressive strain recorded at two elevations (50 mm and 100 mm from the bottom) at 150 mm away from the column face is shown Figure 5.29. The behaviour is compared with the predicted relation for a rigid connection using the effective second moment of area as has been presented in Section 5.2.6. The predicted curves were based on calculating the strain at two points: (i) cracking moment using the uncracked second moment of area (point P1); and (ii) yield moment using the effective second moment of area at yielding (point P2) using Branson's model (ACI, 2008a). It should be mentioned that the calculations considered the full contribution of the 4H20 continuous beam top steel bars and the horizontal steel links at the beam ends. The comparison shows that the experimental results are corresponding to the relation predicted for three locations out of four, where there is some discrepancy at location B.

According to the predicted relation, locations A to BB are in compression state for the whole loading stage, and the neutral axis was predicted to be not less than 100 mm (above locations A and AA) up to the fully cracked stage (stage II). However, at the moment of 145 kNm (100 kN beam load) for beam 1 and the moment of 160 kNm (110 kN beam load) for beam 2, cracks extended diagonally from adjacent sections to reach the strain gauges at these locations. It seems that, in spite of being able to predict the strains to some extent, the predicted relation failed to expect the occurrence of a tension zone at these locations, especially at locations A and AA. Furthermore, this behaviour could be noticed in the variation of the neutral axis level along the beam depth at 150 mm from the column face (section 1-1), as shown in Figure 5.30. At the moment of 145 kNm in beam 1, the strain at location A turned out to be tensile due to a diagonal extension of cracks from the beam section at 300-400 mm away from the column face.

It should be stated that the predicted relation in Figure 5.29 is based on the assumption that the crack at 150 mm from the column face, where the strains are calculated, is vertical and no crack would extend to this location from other locations. It appears that, due to the concentration of cracks at 300 to 400 mm away from the column faces (region 1), the behaviour at section 150 mm from the column face (region 2) was affected, and there was extension of cracks from region 1 to region 2.

The strain in the top steel bar at locations D to G within the beam trough versus the beam moment is shown in Figure 5.31 in two forms: (i) the strain variation at locations D to G up to the maximum ultimate moment before the bond loss, and (ii) the strain variation at locations E and G for the whole loading history. Figure 5.31 shows that there is a reasonable agreement between the experimental and the strains predicted at location E. In contrast to specimens GR1 and GR2, there was less disagreement between the predicted steel strains and the experimental ones around the cracking moment. This is attributed to the additional 2H20 short steel bars across the connection (reinforcement detail of type T3) that delayed the hair cracks at the vertical interfaces within the connection.

The strain variation of the top steel bar along the beam length starting from the connection centre to 300 mm from the column face (locations D to G) is shown in Figure 5.32 in two forms: (i) stage 1 (Figure 5.32a) that shows the variation up to the maximum achieved moment (210 kNm in beam 1); and (ii) stage 2 (Figure 5.32b) that shows the decline in the steel bar strains after the loss of bond. At stage 1, the maximum strain was at location G, where the horizontal links are terminated and the 2H20 short bars are about to reach the passive end; this confirms that the section of strain (stress) concentration was away from the column face, which fulfils the aim behind the design

of specimen GR3. At stage 2, the strain decline at location G was steeper than other locations; this reflects the fact that the bond loss happened at location G (Figure 5.32b). From above, it is clear that the yielding happened at location G, followed by the loss of bond that resulted in the drop in the moment capacity.

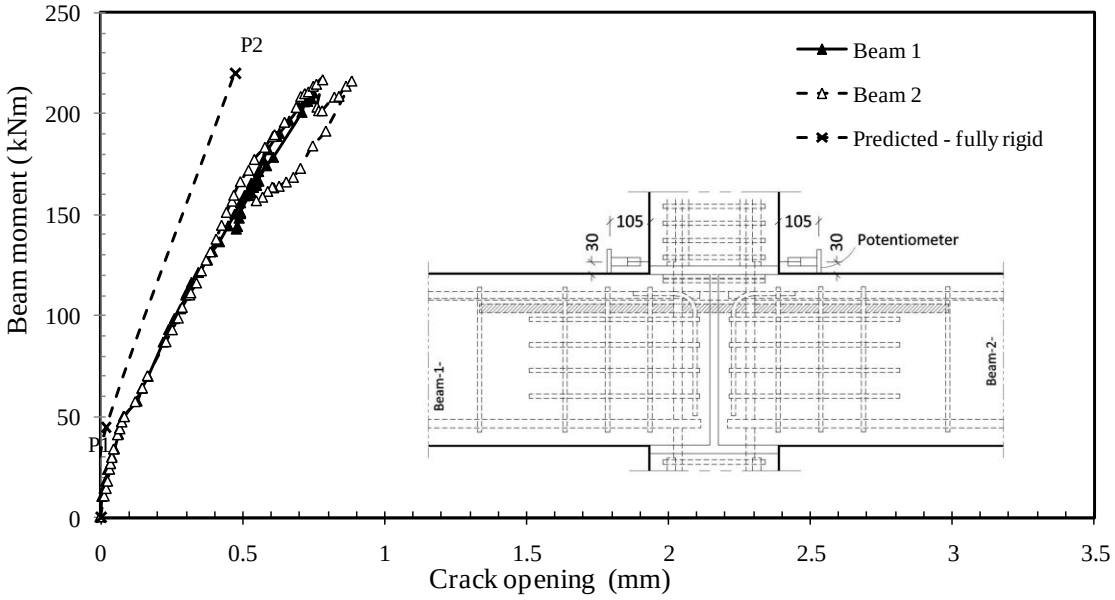

Figure 5.27 Moment vs. crack opening at beam-column top boundary in specimen GR3

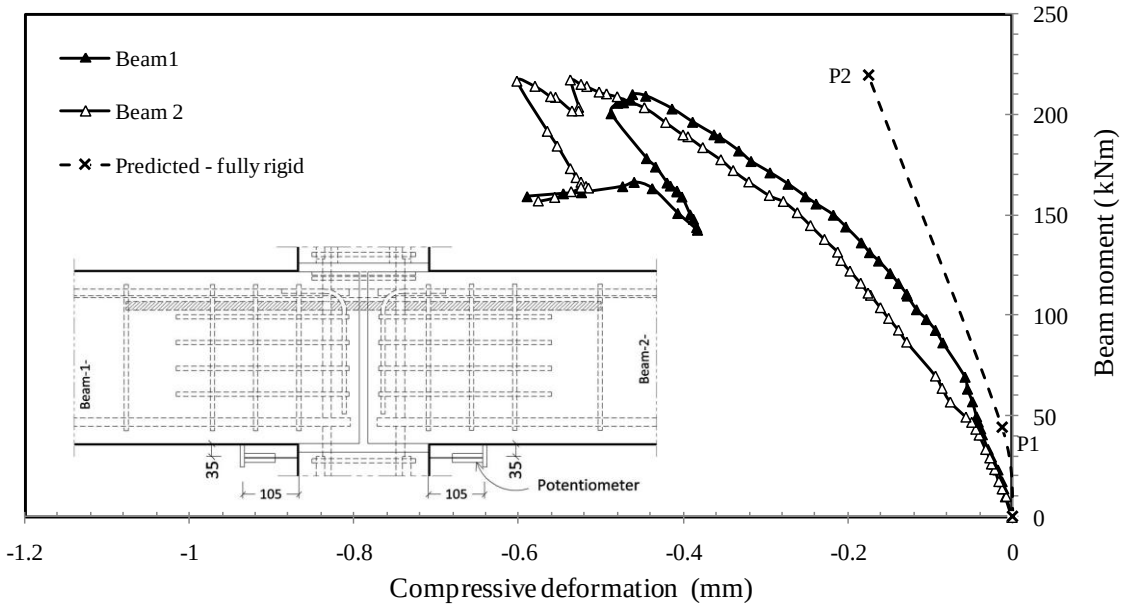

Figure 5.28 Moment vs. concrete compressive deformation at bottom beam-column interface in specimen GR3

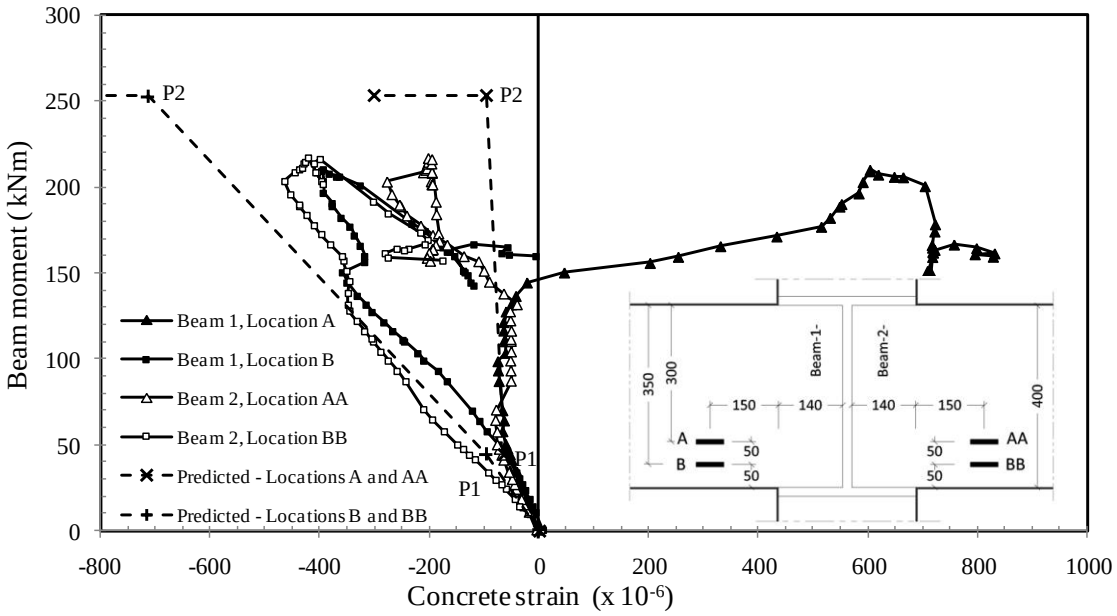

Figure 5.29 Moment vs. concrete compressive strain
at the bottom of beam in specimen GR3

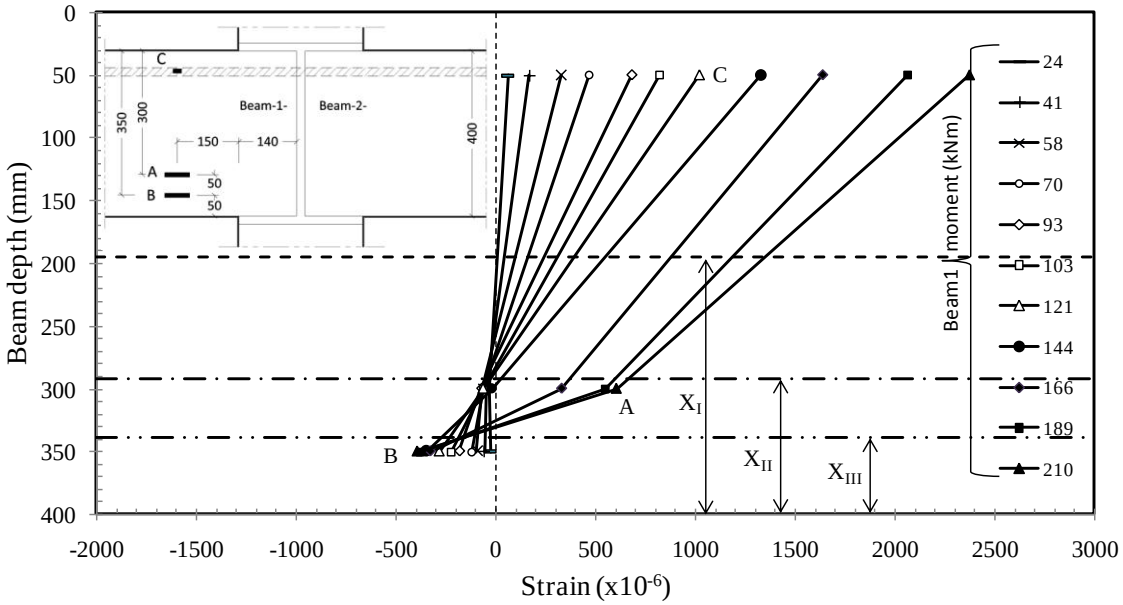

Figure 5.30 Neutral axis variation in beam 1 (specimen GR3)

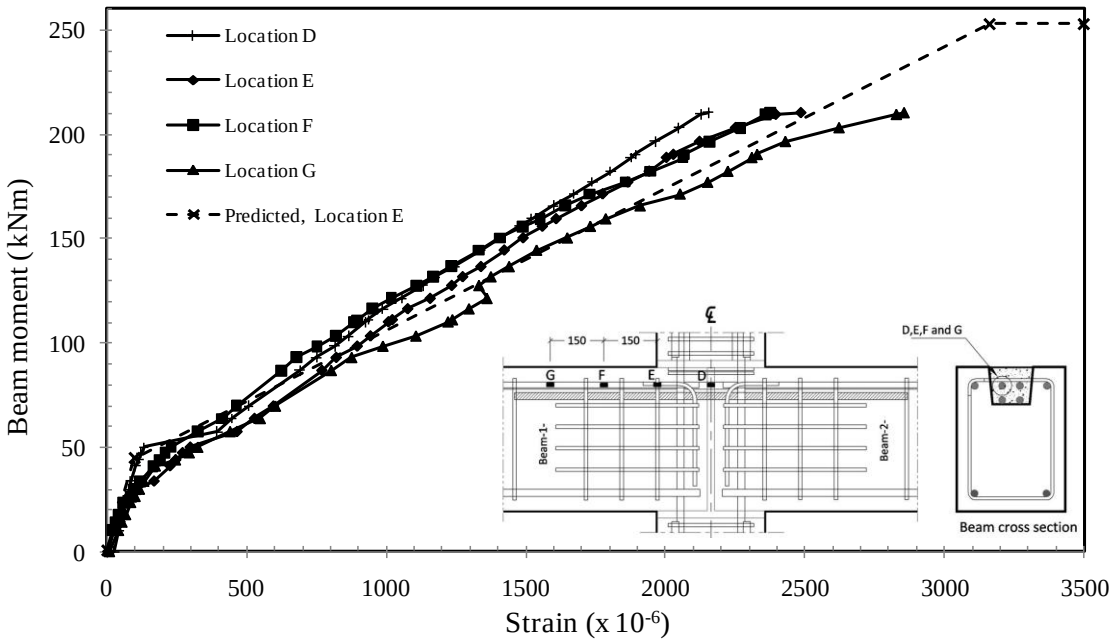

a) Up to the loss of bond (210.1 kNm beam 1 moment) at locations D to G

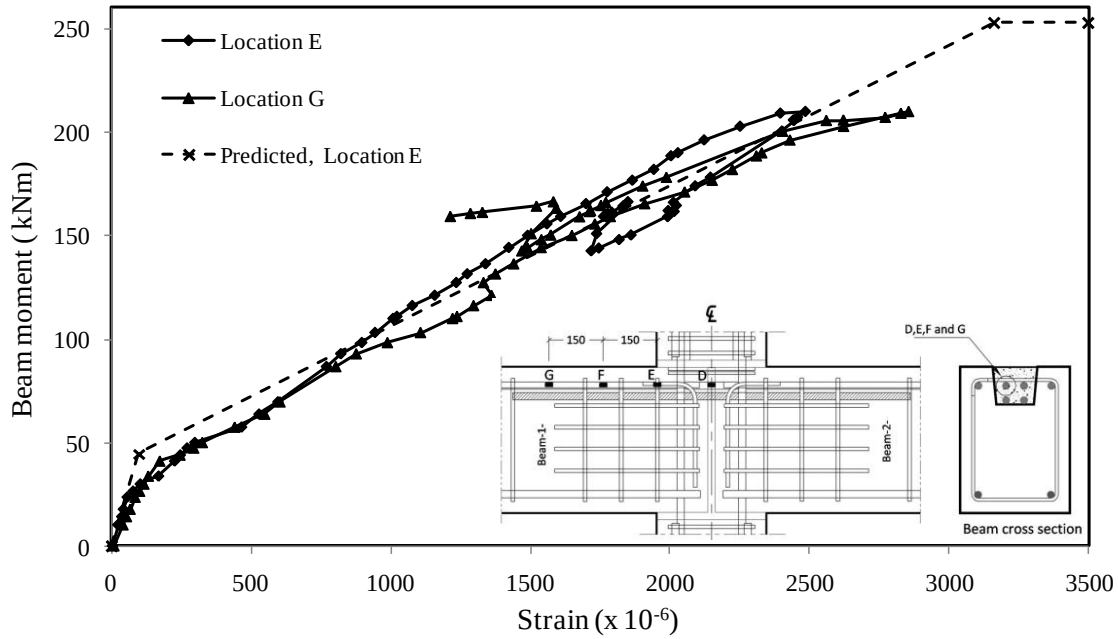

b) For the whole loading history at locations E and G

Figure 5.31 Moment vs. beam steel bar strain in specimen GR3

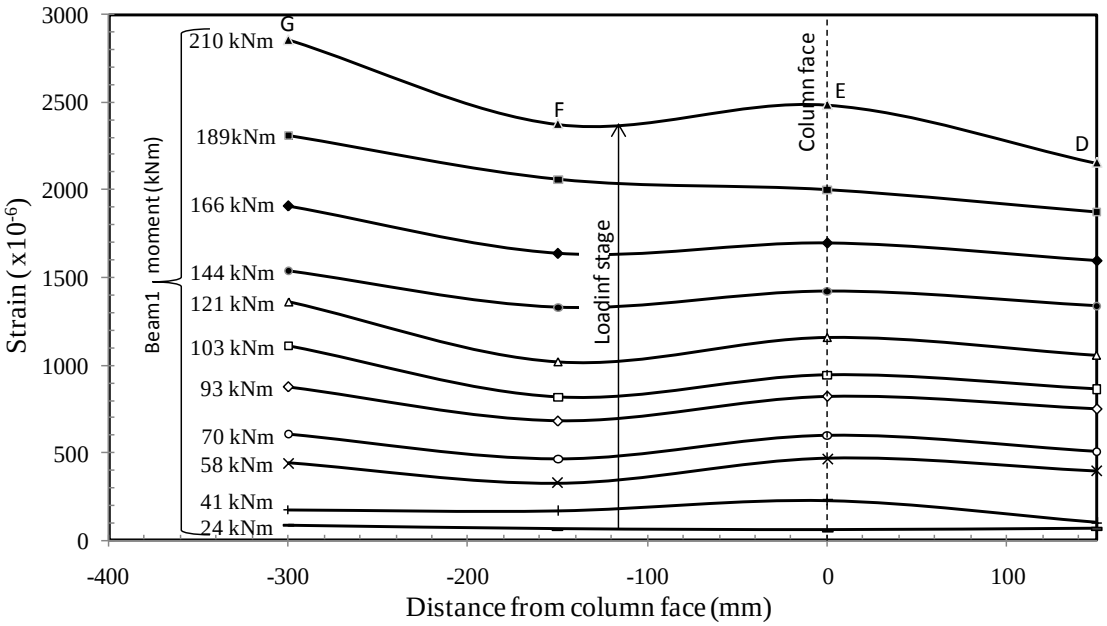

a) Up to the ultimate moment 210.1 kNm (beam 1)

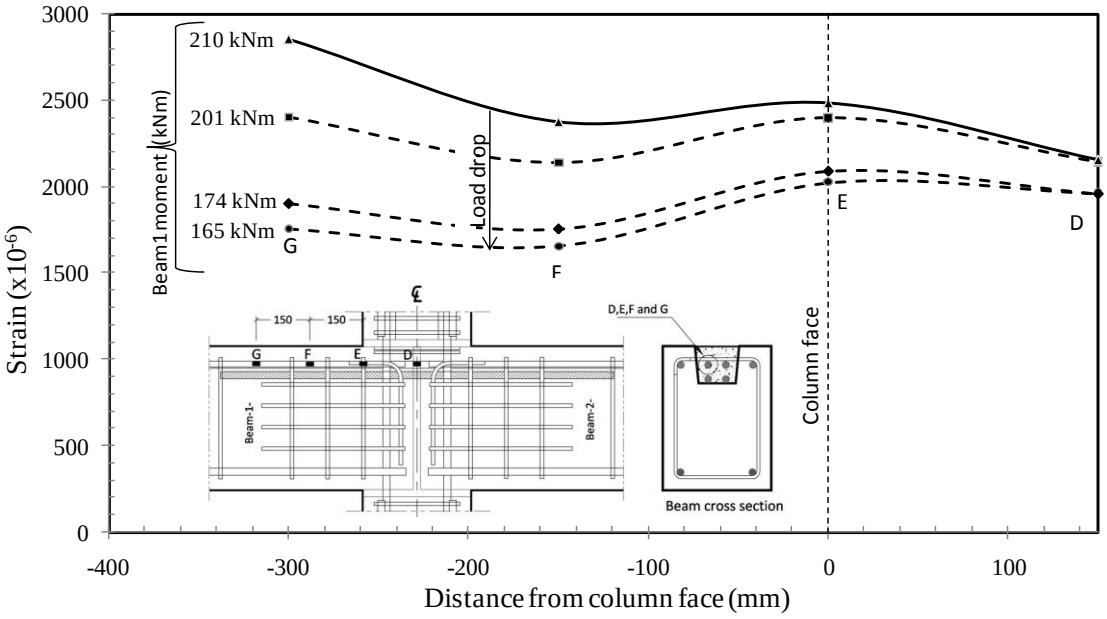

b) Descending part after the bond loss

Figure 5.32 Steel strain variation of beam top steel bar in specimen GR3

5.3.3.4 Column vertical strain distribution of GR3

The overall column axial strain variation with the beam load is shown in Figure 5.33; the strains remained compressive at all loading stages except at locations X and Z,

where the strain turned out to be tension at the edge due to extension of the cracks from the beam-ends to the locations X and Z.

The details of axial strain variation along the column width at the top and bottom is presented in Figure 5.34 and Figure 5.35. In contrast to specimen GR1, it is clear from both figures that there was only a slight eccentricity in the column axial load (500 kN) leading to almost a uniform constant strain (stress) distribution at zero beam load, and to be very close to the predicted ones.

As shown in Figure 5.34, at the early loading stages, there was almost no increase in column axial strain in the top column; this would suggest that there was limited relative beam-end rotation at that loading stage in specimen GR3. This is true for the loading states prior to a beam load of 94 kN for location X and to a beam load of 110 kN for location Z. Starting from these loads, the strain at X and Z began to decrease (from negative values towards zero) and turned out later to be positive (tensile strains). When the strains reached the ultimate tensile strain of concrete, cracks occurred at locations X and Z, and when the cracks crossed the SGs, the readings were no longer valid; therefore, the strains are not reported for the higher loads.

In Figure 5.35, the axial stain distribution in the bottom column under the 500 kN axial column load and zero beam load is close to the predicted one. By applying the beam load, the strain intensified at the edges (location XX and ZZ) indicating locating the reactions for the beam loads away from the column centre line. The same trend of strain distribution continued through the subsequent beam loading stages. As seen, there was a prying action exerted by the beam rotation on the column edge.

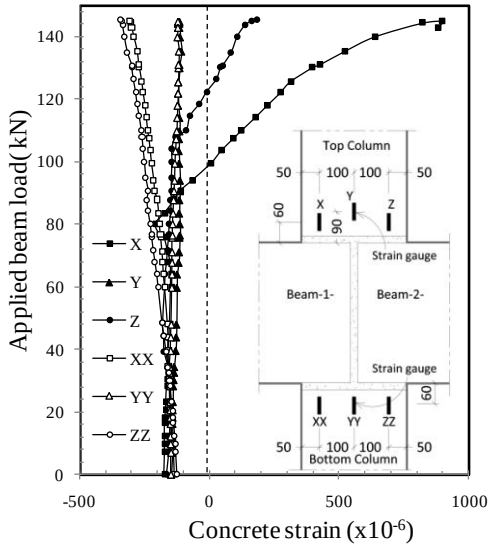

Figure 5.33 Column axial strain vs. beam load in specimen GR3

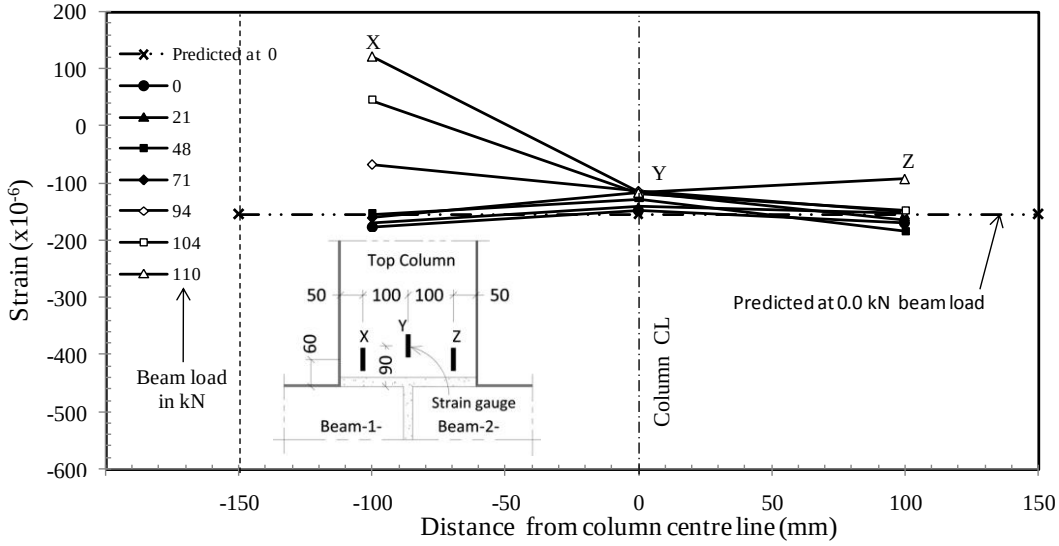

Figure 5.34 Axial strain distribution in top column in specimen GR3

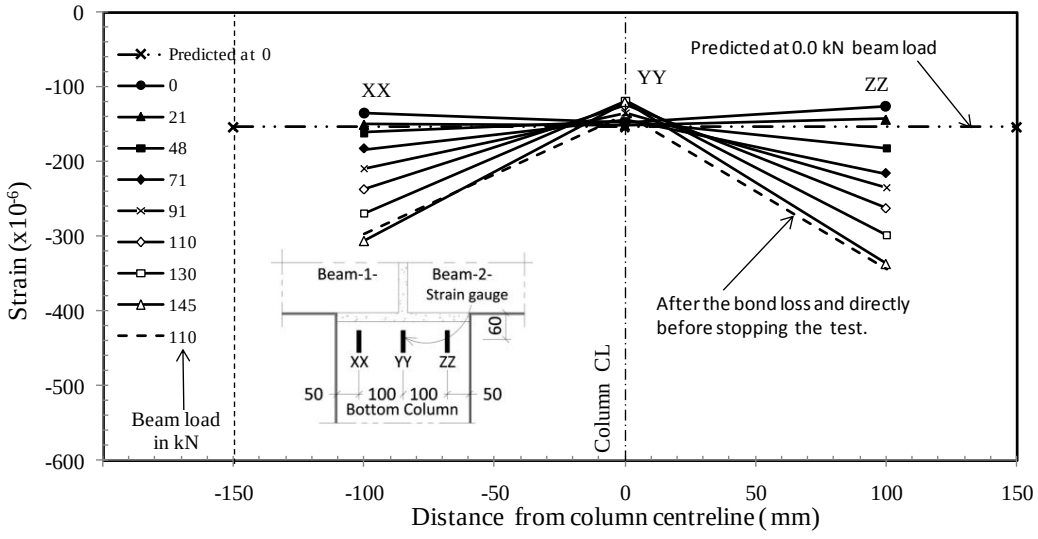

Figure 5.35 Axial strain distribution in bottom column in specimen GR3

5.3.4 Comparison of results

5.3.4.1 Moment capacity and rotational stiffness

In specimen GR1, in spite of achieving the full moment capacity, there was a concentration of cracks within the connection prior to yielding, which is unfavourable for satisfactory connection behaviour. Hence, specimens GR2 and GR3 were designed with improved connection reinforcement details of T2 and T3, respectively (Figure 4.4).

Figures 5.37 and 5.38 show that the detail T2 had no significant effect on the rotational stiffness; however, there was a marked decrease in the crack width at the beam-ends close to the column face (Figure 5.17). Also, using T2 enhanced the beam strength, to some extent, due to the contribution of additional horizontal links. This behaviour is more pronounced in beam 1.

For reinforcement type T3 (specimen GR3), the maximum achieved moment (M=210 kNm) increased by 60% compared to M_y of GR1 (Figure 5.36), and the rotational stiffness increased by 245% considering the stiffness at 159.4 kNm for GR3 (Figure 5.37).

All the specimens showed a ductile behaviour; however, in specimen GR3, the ductility is noticeable through the measured deflections (Figure 5.36) rather than the measured rotations (Figures 5.37 and 5.38). This is due to the concentration of the rotation after the loss of bond away from the column face, where the rotation measurements were taken.

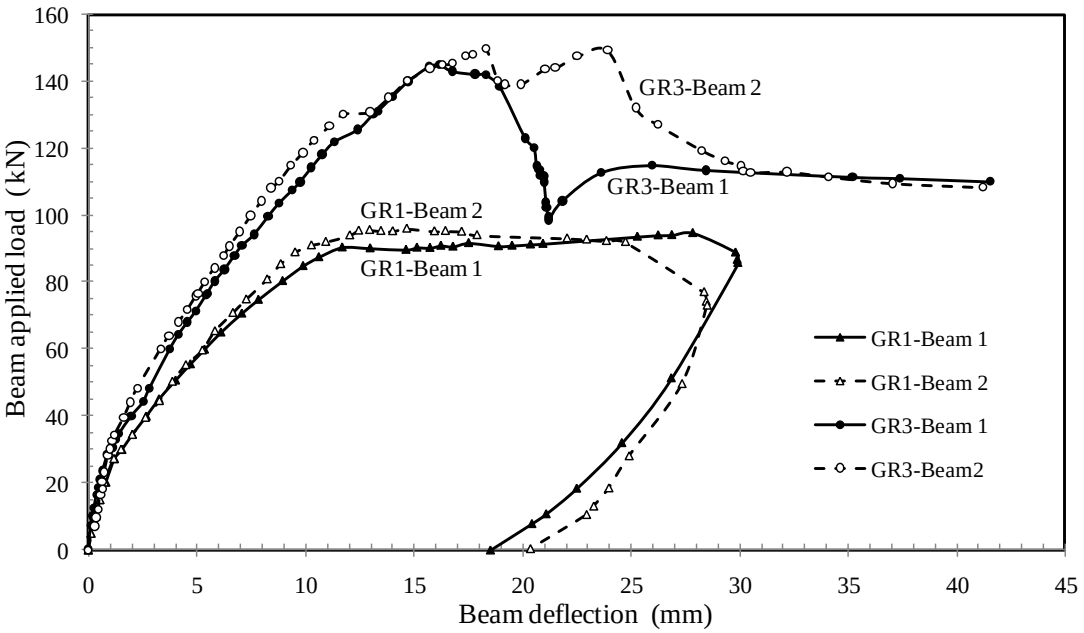

Figure 5.36 Beam deflection vs. load in specimens GR1 and GR3

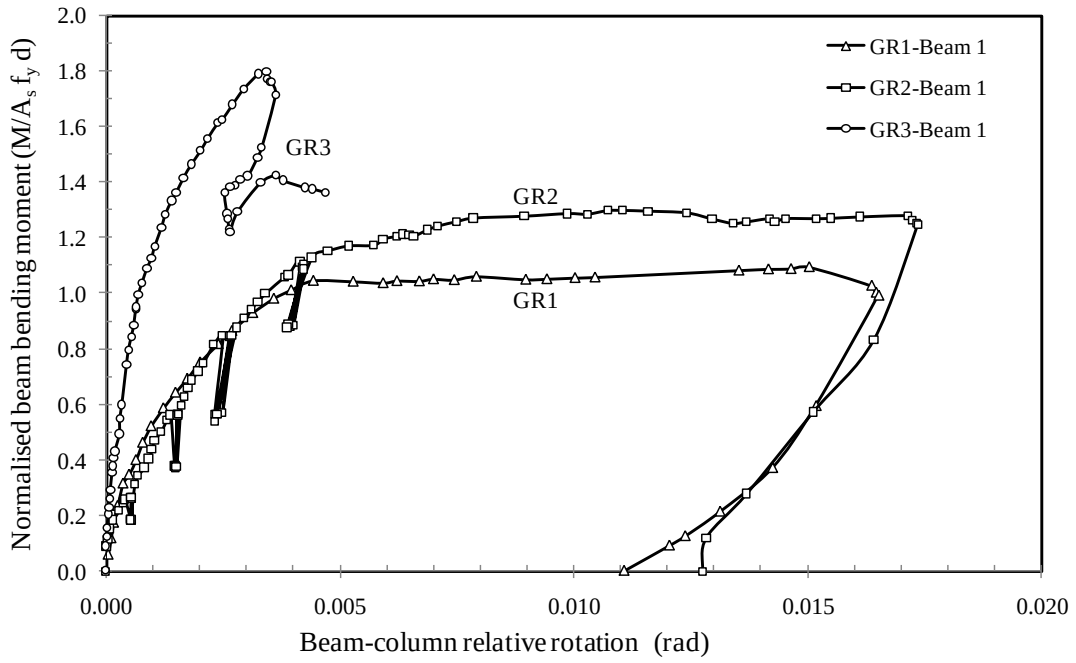

Figure 5.37 Beam-column rotation vs. normalised moment in series GR

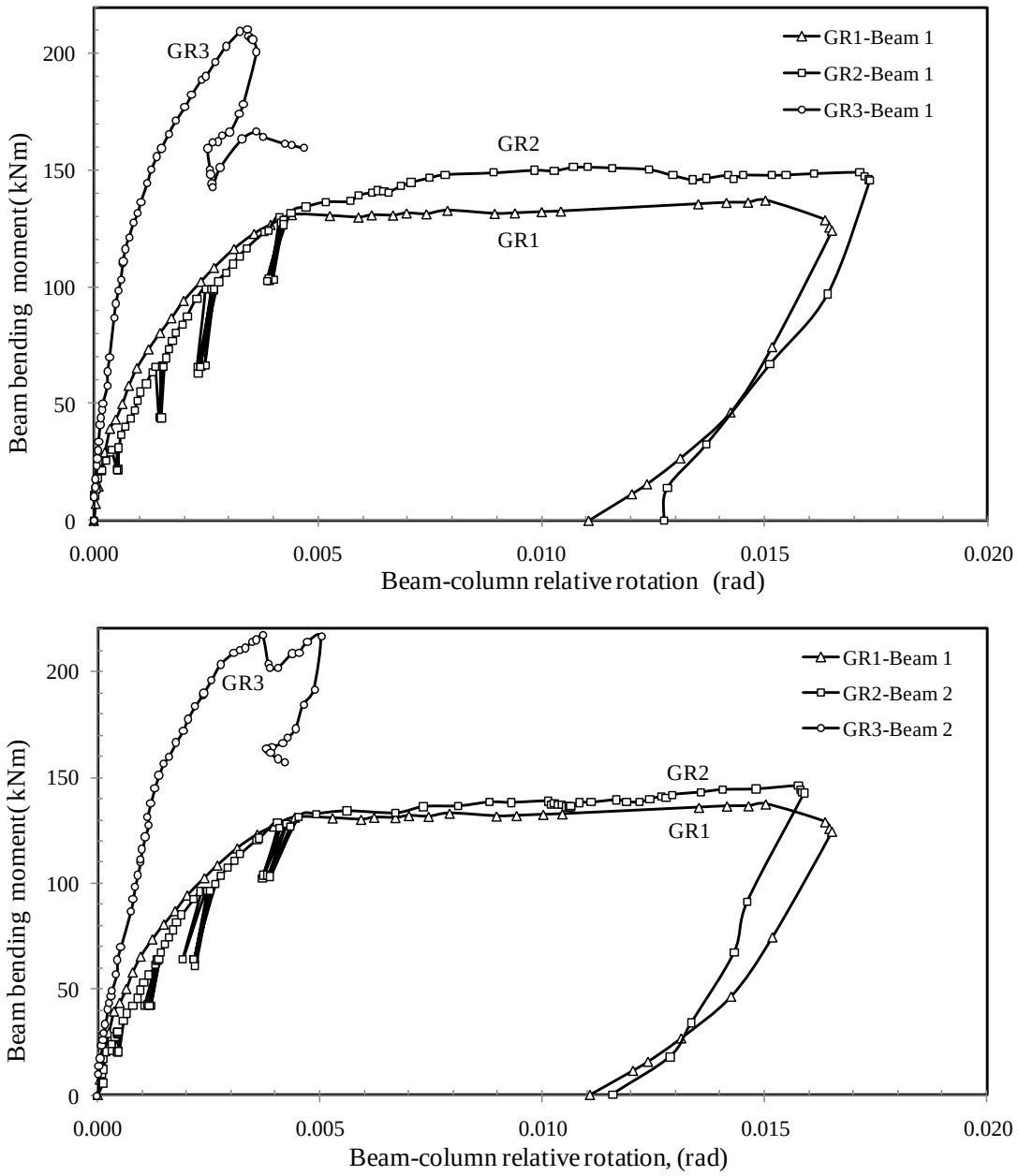

Figure 5.38 Beam-column rotation vs. moment in series GR

5.3.4.2 Crack pattern and failure mode

Compared to GR1, specimen GR2 achieved a better crack distribution with a controlled crack width region within 300 mm from the column face, and enforced the maximum crack width to be located beyond this region up to 88% of the yield moment, followed by large cracks (3 mm width and more) within the connection (Figure 5.39).

This shows that specimen GR2 (connection detail of type T2) was able to delay the concentration of cracks within the connection, but failed to prevent it.

In GR3, thanks to the additional horizontal links and 2H20 short bars (connection detail of type T3), the concentration of the final damage did not happen in the connection zone; rather, it happened at 400 mm from the column face, coincidentally where the additional 2H20 bars and the horizontal links are terminated. In addition, GR3 provided a controlled crack width region within 300 mm from the column face, the same as in specimen GR2.

To show the relation between the experimental secant rotational stiffness 'S' and the crack width, the variation of S in specimens GR2 and GR3 versus the applied beam moment are shown in Figure 5.40. In the graph, the maximum crack width recorded at certain loading stages is indicated. From the graph, it is clear that specimen GR2 experienced a typical service crack width 0.3 mm at around 76% of the yield moment; in contrast, the 0.3 mm crack width did not appear in specimen GR3 until late loading stages due to the use of the additional 2H20 short bars at the connection.

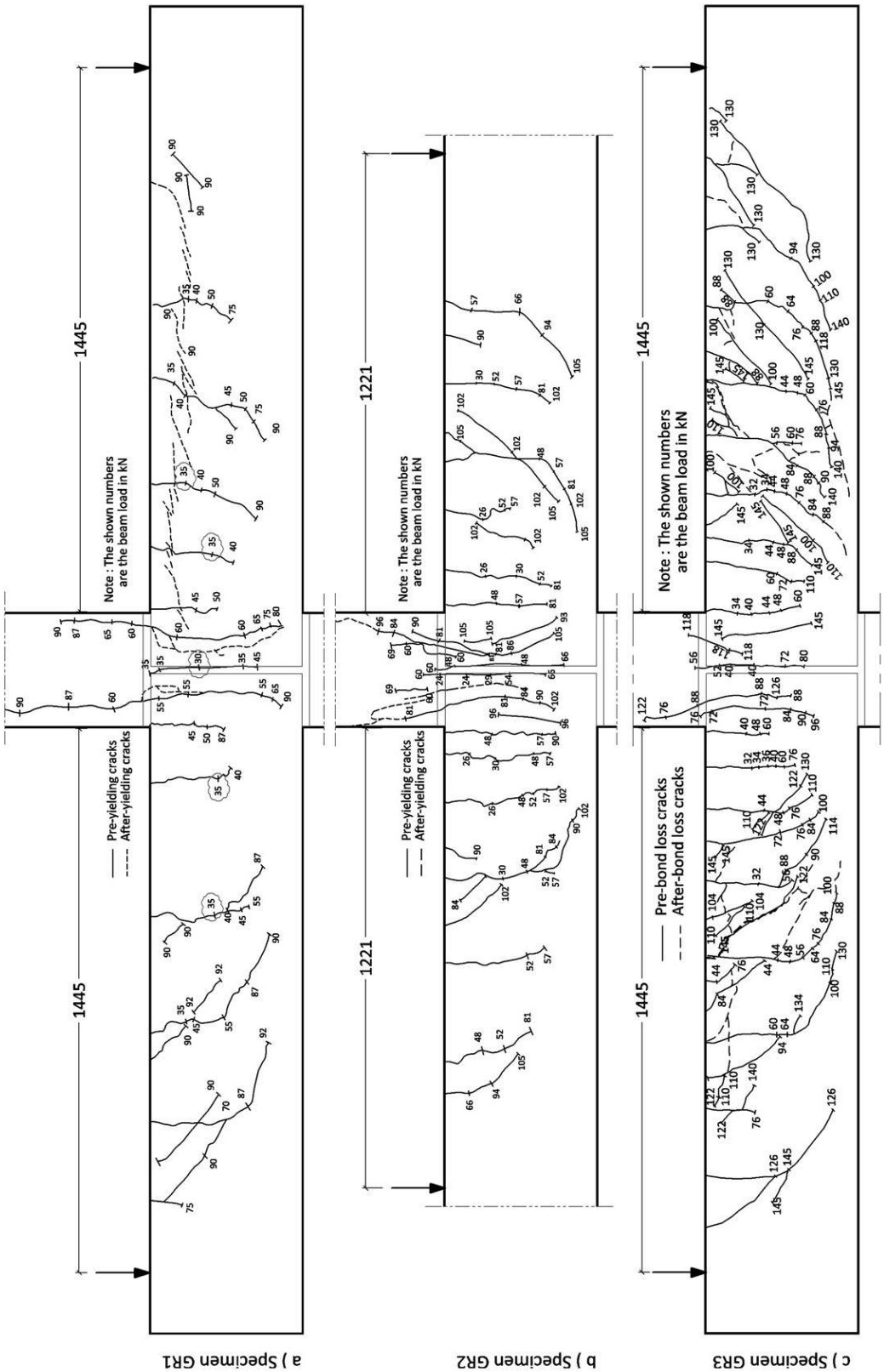

Figure 5.39 Cracking pattern at failure in specimens of series GR

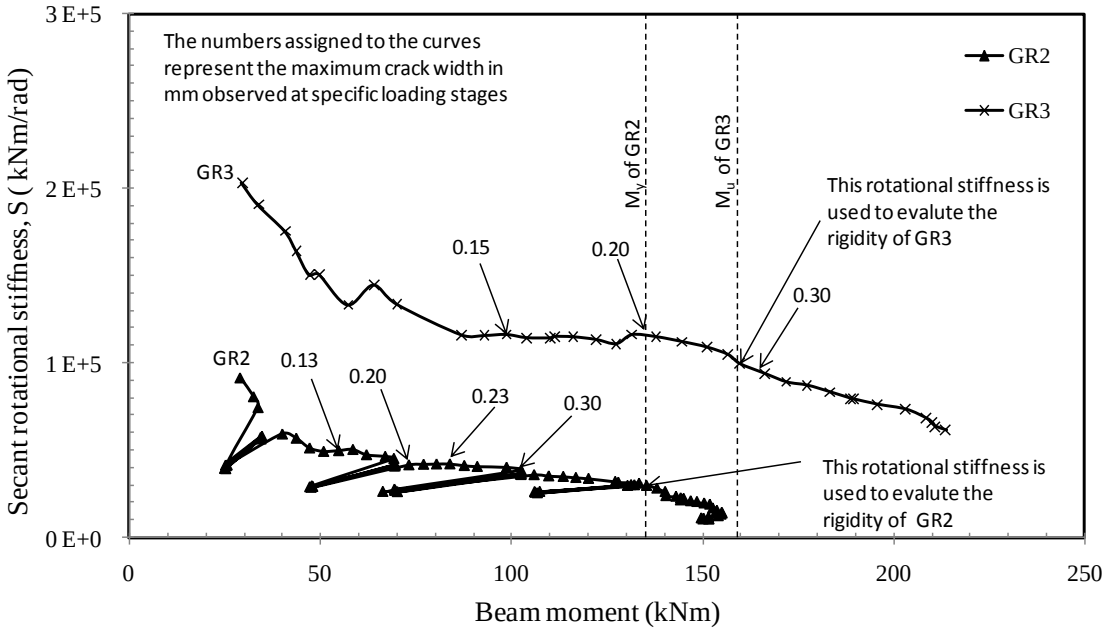

Figure 5.40 Rotational stiffness deterioration in specimens GR2 and GR3

5.3.4.3 Preliminary connection evaluation

For a rigorous evaluation of the effects of the beam-column flexibility on the internal distribution of moments within frame structures, the rotational stiffnesses need to be incorporated in a full semi-rigid analysis, which will be performed in Chapter 8.

However, as a preliminary step, connections could be classified as pinned, semi-rigid or rigid considering a single span and based on classification systems stated earlier in Section 2.8. In this respect, the yield secant rotational stiffness 'S_y' was evaluated against the classification system proposed by EC3 (CEN, 2005b), which is a classification system for structural steelwork to define the boundaries for connection behaviour based on stiffness. As stated in Chapter 2 (Section 2.8), for a better recognition of the connection flexibility, Monforton's (1963) end-fixity factor could be calculated based on the flexural rigidity (EI/L) of the connected member, which would vary from zero for pinned connections ($S_y = 0$) to 1 for fixed connections ($S_y = \infty$) as below:

$$\gamma = \frac{1}{1 + \frac{3\,E_c\,I}{S_y\,L}} \tag{5.14}$$

In which E_c is the modulus of elasticity of concrete, I is the second moment of area of the beam, S_y is the yield secant rotational stiffness of the connection, and L is the effective span of the beam.

Figure 5.41 shows the variation in γ (using Eq. (5.14)) for a single span of different span lengths using the yield secant rotational stiffness of GR1 (S_y = 30160 kNm/rad), GR2 (S_y = 29910 kNm/rad) and GR3 (S_y = 106905 kNm/rad) using two different values of E_cI for the beam, namely full E_cI (curves a, b and c) and 0.5 E_cI (curves d, e and f). According to the ACI Code of Practice (2008a), these values are proposed to be suitable for analysis of structures subjected to gravity loads. However, the comparison showed that using full E_cI for the connected members affects enormously the classification of the connection, as shown in Figure 5.41.

Also seen in Figure 5.41, the GR1 specimen is classified as semi-rigid for span lengths between 0.94 m and 15.59 m using full E_cI (curve b), and for span lengths between 0.47 m and 7.79 m using 0.5 E_cI (curve e). On the other hand, by considering the much greater S = 106,905 kNm/rad from specimen GR3, the connection is classified as rigid for L greater than 2.37 m (using 0.5 E_cI, curve f). In practice of small spans, the beam section and negative reinforcement are kept the same as the adjacent long spans, in spite of having low negative moment there. This guarantees having uncracked sections and a very large rotational stiffness, which was found to be 222 846 kNm/rad prior to onset of cracks in the case of using connection reinforcement of type T3 (GR3).

As shown in Figure 5.41, connection specimens GR1 and GR2 (as the rotational stiffness of specimen GR2 is almost as same as that of GR1) are classified as semi-rigid

for most of the practical spans, while connection specimen GR3 is classified as a rigid connection (equivalent to a monolithic beam-column connection) considering that achieving 80% rigid hogging moment is sufficient.

For a single span beam with equal end-rotational stiffnesses, the semi-rigid hogging moment 'M_E' at supports could be found as a ratio of the fixed-end moment (M_F= $wL^2/12$) using Eq. (5.15), and the semi-rigid mid-span sagging moment 'M_S' could be found as a ratio of the mid-span moment ($wL^2/24$) of a fixed-end beam using Eq. (5.16). The variations of the semi-rigid end moments achieved in a single span of varied span lengths are shown in Figure 5.42 for all tested specimens. The validity of use of Eq. (5.15) and Eq. (5.16) for beams in full frames subjected to gravity loading will be examined in Chapter 8.

$$\frac{M_E}{M_F} = \frac{3\,\gamma}{2+\gamma} \quad ; \quad M_E = \frac{W\,L^2}{12} \cdot \frac{3\,\gamma}{2+\gamma} \tag{5.15}$$

$$M_S = \frac{W\,L^2}{24} \cdot \frac{2\,(3-1.5\,\gamma)}{2+\gamma} \tag{5.16}$$

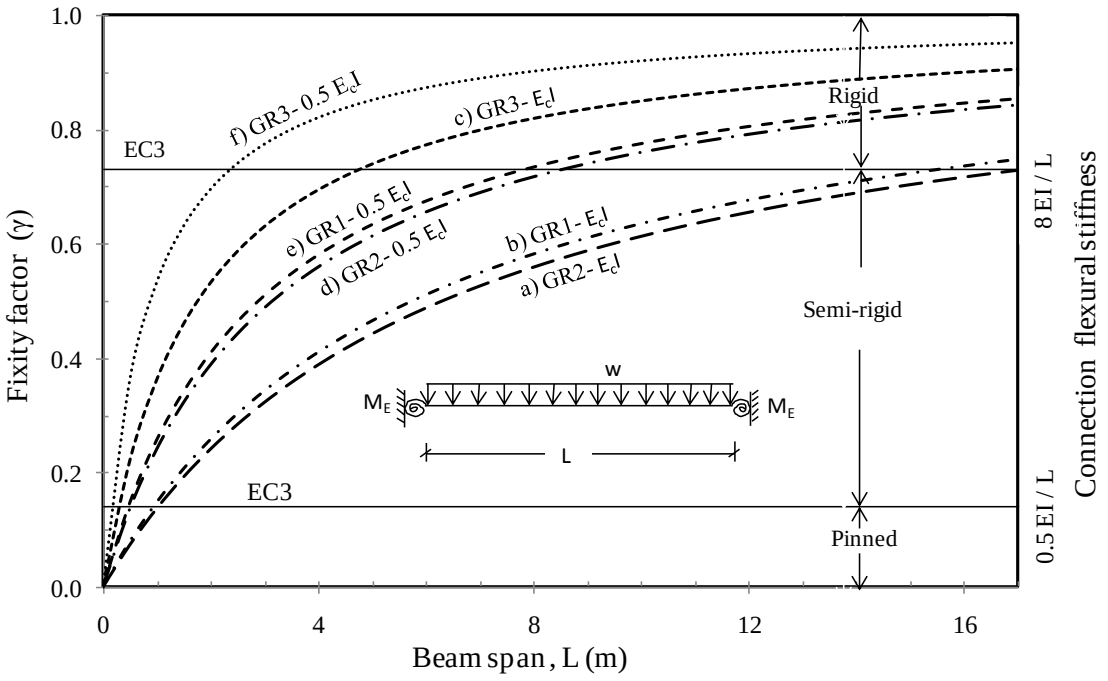

Figure 5.41 Classification of specimens in series GR

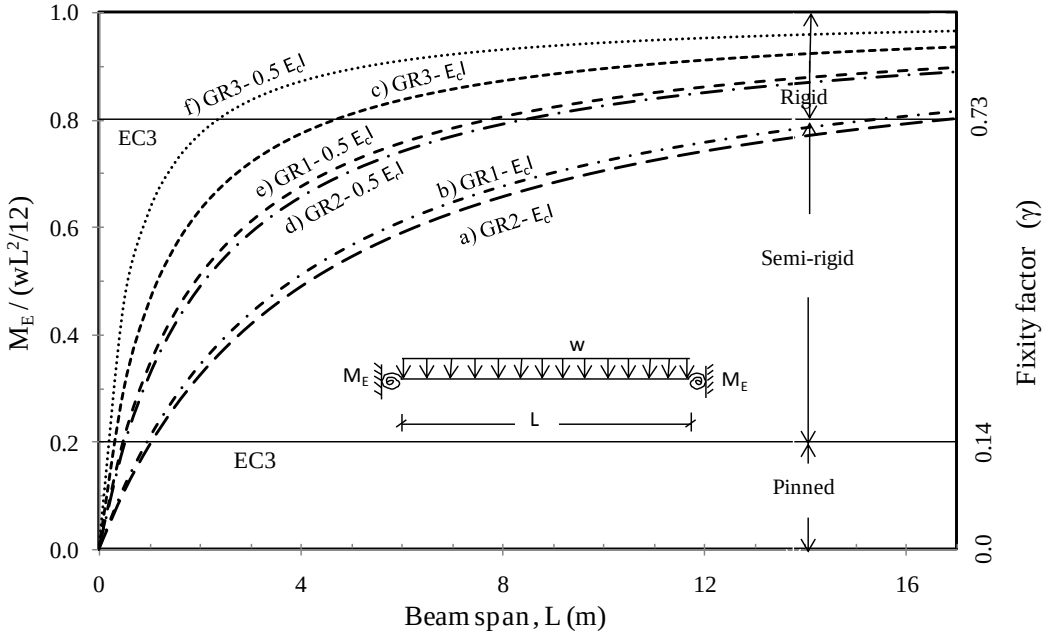

Figure 5.42 Semi-rigid hogging moments achieved in a single span beam using S_y of specimens in series GR

5.4 Analytical modelling

Specimens GR1 and GR2 exhibited semi-rigid behaviour under gravity loads, meaning that for an accurate analysis of frames comprising such connections, the rotational stiffness of the beam-column connections needs to be incorporated in the analysis. To characterise the behaviour of semi-rigid connections, the yield moment of resistance 'M_y' and the beam-column relative rotation at yielding 'θ_y' could be known most effectively from full-scale experimental testing. However, due to the cost of such experiments, this approach is limited for research purposes and for preliminary evaluation of new connection types. Therefore, simplified analytical models are essential as a cost-effective alternative tool.

As part of this research, an analytical model (Ferreira, Elliot and Hasan, 2010) was proposed to predict the rotational stiffness for a precast beam-column connection with continuity steel bars crossing the connection at the top of the beam. In this kind of connection, the relative beam-column rotation arises mainly due to the elongation of the steel bars within the connection zone, which is highly affected by the crack propagation

and the bond-slip status. The yield secant rotational stiffness 'S_y' represents the stiffness at the onset of the first yield of longitudinal reinforcement, as below:

$$S_y = \frac{M_y}{\theta_y} \tag{5.17}$$

In beam-column connections with fully anchored beam top bars, the yielding moment was taken to be equal to (refer to Section 5.2.4):

$$M_y = A_s \ f_y \ \left(d - \frac{x_{II}}{3}\right) \tag{5.18}$$

In the model, θ_y is attributed to two behaviour mechanisms: (i) steel bar elongation with the column (l_e), where the bond status is considered as "good"; and (i) steel bar elongation at the beam end (l_d) close to the column face, where the bond status is considered as "reduced bond" due to the concentration of deformations. θ_y is calculated just before the first yield occurrence at the continuity bars ($\varepsilon_s=\varepsilon_{sy}$). In beam-column connections without corbels, the rotation could be obtained (Eq. (5.19)) by dividing ε_{sy} by the difference between the effective section depth '*d*' and the fully cracked section neutral axis 'x_{II}' (see Figure 5.43).

$$\theta_y = \left(\frac{\epsilon_{sy}}{d - x_{II}}\right) l_{ed} \tag{5.19}$$

$$\epsilon_{sy} = \frac{\sigma_y}{E_s} \tag{5.20}$$

$$l_{ed} = l_e + l_d \tag{5.21}$$

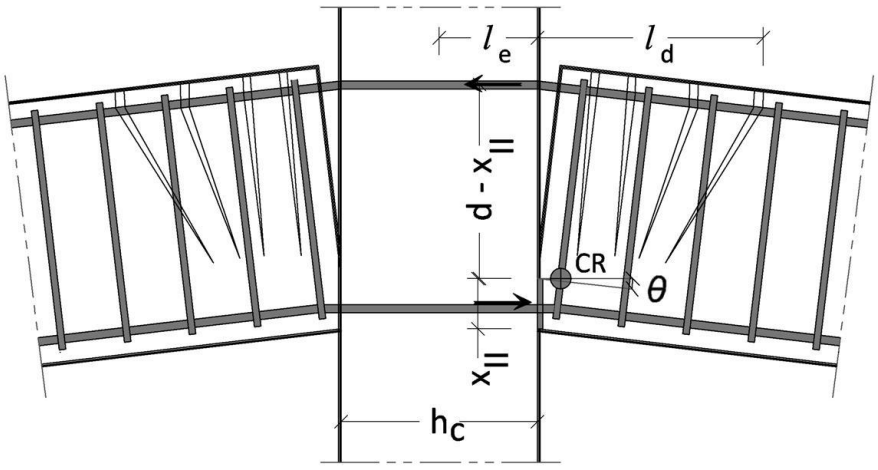

Figure 5.43 Deformation configuration in the beam-column connection studied

As shown in Section 2.5 (Chapter 2), the transmission bond length 'l_{t2}' is influenced by the steel bar diameter 'Ø', stress level in the steel bars 'σ_s', and the average/nominal bond stress 'τ_a', which is taken as half of the maximum local bond stress 'τ_{max}':

$$l_{t1} = \frac{\emptyset\, \sigma_s}{4\ \tau_a} + 2\ \emptyset \tag{5.22}$$

$$\tau_a = \frac{1}{2}\ \tau_{max} \tag{5.23}$$

$$l_{t1} = \frac{\emptyset\, \sigma_s}{8\ \tau_{max}} + 2\ \emptyset \tag{5.24}$$

CEB-FIP 1990 model Code (1993) suggests two values for τ_{max} for a concrete-steel bar bond:

$$\tau_{max} = 2.5\sqrt{f_c} \quad ; \quad \text{for 'good bond condition'} \tag{5.25}$$

$$\tau_{max} = 1.25\sqrt{f_c} \quad ; \quad \text{for 'other bond conditions'} \tag{5.26}$$

In the beam-column connections type investigated in the current study, the active bond is between the grout and the steel bars; therefore, the above two equations cannot be used directly in the model. To determine the maximum local bond stress for grout-steel bar contact, two pull-out tests of H20 mm steel bars embedded in grout have been conducted in this study (see Appendix F). The results showed that τ_{max} for a steel bar-grout bond in 'good' condition could be taken as $2.0\sqrt{f_c}$ to characterise the behaviour; bearing in mind that this equation might be valid only for the grout mix and the H20 steel bar used in the current study. Accordingly, for the maximum local bond stress for steel bars embedded cement-based grout, Eq. (5.25) and Eq. (5.26) could be re-written as below:

$$\tau_{max} = 2.0\sqrt{f_c} \quad ; \text{ for 'good bond condition' ; } le \tag{5.27}$$

$$\tau_{max} = 1.0\sqrt{f_c} \quad ; \text{ for 'other bond conditions' } ld \tag{5.28}$$

It was suggested (Ferreira, Elliot and Hasan, 2010) to consider the bond condition within the column as '*good bond condition*', and that at the beam end as '*other bond conditions*'. Accordingly, Eq. (5.29c) is obtained by substituting Eq. (5.27) and Eq. (5.28) into Eq. (5.24) for both l_e and l_d to obtain l_{ed} eventually.

$$l_e = \left(\frac{\emptyset f_y}{16\sqrt{f_c}} + 2\emptyset\right) \leq \frac{h_c}{2} \tag{5.29a}$$

$$l_d = \left(\frac{\emptyset f_y}{8\sqrt{f_c}} + 2\emptyset\right) \leq d - \frac{x_{II}}{3} \tag{5.29b}$$

$$l_{ed} = \left(\frac{3 f_y \emptyset}{16\sqrt{f_c}} + 4\emptyset\right) \tag{5.29c}$$

Table 5.2 shows both the experimental and analytical results for the yield moment 'M_y', relative beam-column rotation at yielding 'θ_y', and the yield secant rotational stiffness 'S_y' in specimens GR1 and GR2. The same results are shown graphically in Figure 5.44 and Figure 5.45. As can be seen, the analytical model could characterise the connection behaviour for design purposes. In specimen GR2, the difference between the analytical yield moment and the experimental one is due to the fact that the contribution of the horizontal links is neglected in the model. Providing of these links works in the direction of guaranteeing a strong connection by additional moment capacity (refer to Section 1.7.3).

Table 5.2 Comparison between experimental and analytical results

Measurement	Specimen GR1		Specimen GR2	
	Exp.	Analytical	Exp.	Analytical[&]
M_y (kNm)	131.1	115.8	131.1[$]+3.7[*]	108.35
θ_y (rad)	0.0044	0.0039	0.0044	0.0037
S_y (kNm/rad)	30160	29692	29910	29284
$: Moment due to concentrated applied load			*: Calculated self-weight moment	
& The contribution of the horizontal 8H10 U-shaped links at the beam end in GR2 is not considered.				

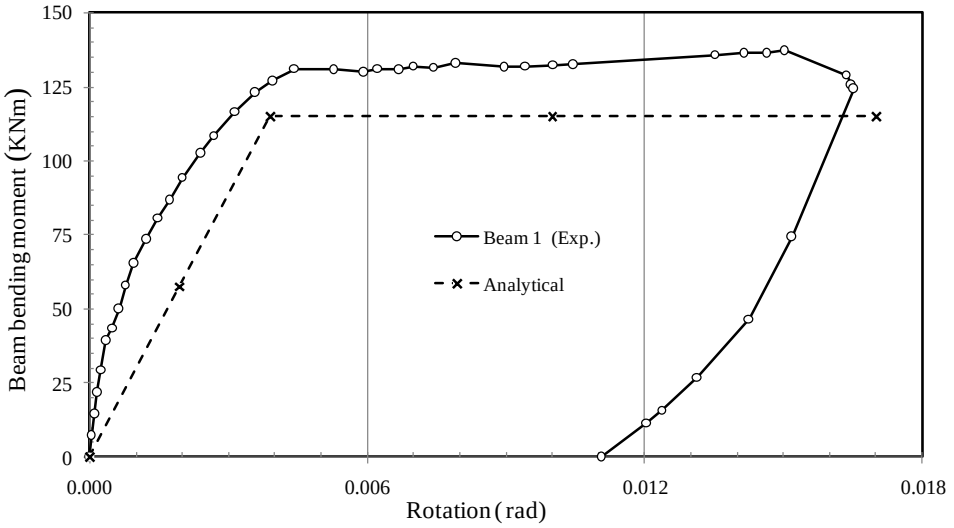

Figure 5.44 Analytical and experimental moment-rotation relations of specimen GR1

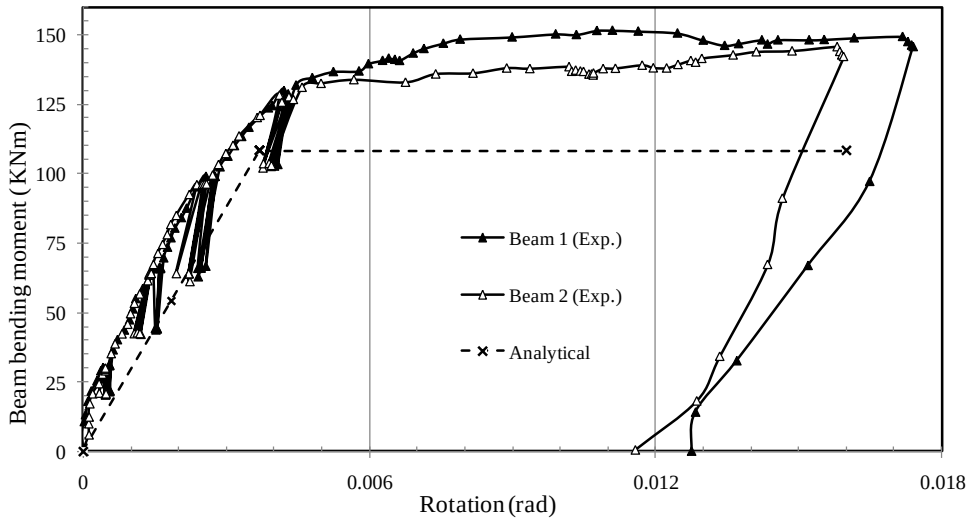

Figure 5.45 Analytical and experimental moment-rotation relations of specimen GR2

5.5 Summary and conclusion

In this chapter, the results of three full-scale discontinuous beam-column connections subjected to gravity loads have been presented; the main variable in the specimens was the reinforcement detail of the connection. Also, a theoretical model to characterise the rotation-moment relation of the semi-rigid specimens (GR1 and GR2) has been validated against the experimental relations. Based on the experimental evidence obtained from this study and the theoretical model, the following conclusions could be drawn.

1- The proposed discontinuous precast concrete beam-column connection is capable to mobilise the full hogging moment capacity of the beam (GR1, GR2 and GR3) with enhanced rotational stiffness (GR3).

2- The proposed discontinuous precast concrete beam-column connection provided a hogging moment capacity exceeded the calculated values by between 1% and 13%.

3- The measured rotational stiffness was found to be between 28950 (reinforcement detail T1) and 106905 (reinforcement detail T3) kNm/rad, compared to a datum value of 34253 kNm/rad (4EI/L based on uncracked second moment of area I_I=0.0016 m^4, and E=39070 N/mm^2 of specimen GR3) for a fully rigid beam of 7.3 m length (L/h = 18.25, where h is the beam depth).

4- As a preliminary classification, specimens GR1 and GR2 are classified as semi-rigid, and specimen GR3 is classified as rigid for the span length that they were designed for (L=7.3 m).

5- Providing horizontal links at the beam ends close to the connection (reinforcement detail T2) ensured a controlled crack width within the transition zone up to 95% of the yield moment.

6- The concentration of cracks was shifted away from the column face by providing additional short steel bars crossing the connection at the top of the beam (reinforcement detail T3).

7- For an accurate deflection calculation for beams comprising such connections, in addition to the elastic deflection calculated by Branson's model (ACI, 2008a), there is a need to consider the additional deflection resulting from the relative beam column connection rotation.

8- For connection reinforcement details T1 and T2, a semi-rigid frame analysis is required to be performed for frames comprising such connections up to a certain beam span depending on the beam geometry and main steel bars. Beyond this limit, the connection could be dealt with as conventional cast-in-situ connections.

9- Through using connection reinforcement detail T3, specimen GR3 could be considered equivalent to a monolithic beam-column connection in terms of strength, rotational stiffness and ductility under gravity loads, where the transition zone at the beam was shifted away from the column.

10- In the semi-rigid frame analysis, for structural analyses, the yield secant rotational stiffness could be used as a conservative approach, which represents an average integrated characteristic for the behaviour regardless of the loading history.

11- An analytical model to characterise the rotation-moment relation of the semi-rigid precast beam-column specimens (GR1 and GR2) has been validated against the experimental results. The model provided good approximations for the yield secant rotational stiffnesses obtained experimentally.

12- For a realistic relative beam-column rotation measurement, the measurements need to be taken at the compression side of the beam within a distance equal to half of the beam depth, and deducting the rotation resulting from the elastic flexure behaviour.

CHAPTER 6

FULL-SCALE TEST RESULTS AND DISCUSSION: SWAY LOADING

6.1 Introduction

In this chapter, the experimental results of testing two full-scale discontinuous precast concrete beam-column connections subjected to sway loading (series 2 – SW) are presented. The primary objective was to identify the moment-rotation characteristic of the connection; in particular, examining the way of mobilising the beam-end sagging moment through column dowels. In this respect, the capacity of the specimens was designed to be governed by yielding of the column dowel bars. In the experimental testing, a horizontal sway load was applied to the top column to simulate the pattern of wind loading, with reactions developing at the beam-ends and bottom end of the column in accordance to the inherent structural response of the frame (Figure 4.1.b).

The geometry of the specimens, loading arrangement, and reinforcement details have been given in Chapter 4. The main variable in series SW was the connection reinforcement detail; the change required in the connection detail emerged after testing the 1st specimen (SW1) and observing unfavourable failure mechanism due to using the connection reinforcement detail T1 (Figure 4.3). The design of the 2nd connection reinforcement detail T3 (specimen SW2, Figure 4.4b) aimed to mobilise the beam sagging moment with ductile behaviour.

The behaviour of the connection is categorised based on the load-sway relation, moment-relative rotation and the failure mode; in addition, supplementary measurements are presented including crack widths and strains in concrete and steel bars within the connection zone.

6.2 Calculation techniques

6.2.1 Experimental moment calculation

The experimental beam moments (M_{b1} and M_{b2}) were calculated at the column faces by multiplying the loads recorded at the beam ends by the corresponding lever arm (the distance from the line of action of the load to the column face). This distance was initially taken as 1.45 m, but in the subsequent loading stages the distance was adjusted to reflect the sway measured at the beam mid-height (Figure 6.1).

Figure 6.2 shows the sign convention for the moments (M_{b1} and M_{b2}), where the beam sagging moments are considered as positive, while beam hogging moments are considered as negative. Also, the figure shows the sign convention for the sway and rotation.

6.2.2 Experimental relative beam-column rotation

As mentioned in Chapter 5, there is no standard method to experimentally measure the relative beam-column rotations 'θ'. Three methods were presented and it was shown that method M1 (measuring the rotation at the compression beam side) is the most representative one (refer to Section 5.2.2).

However, Mahdi (1992) determined θ under sway loading through measuring relative vertical deflections of the beam bottom face with reference to the column. This means that the rotations were measured at the compression side in one beam side and at the tension side in the other beam side. In this approach, Mahdi (1992) assumed that the relative rotation at the top and bottom of the connection was equal.

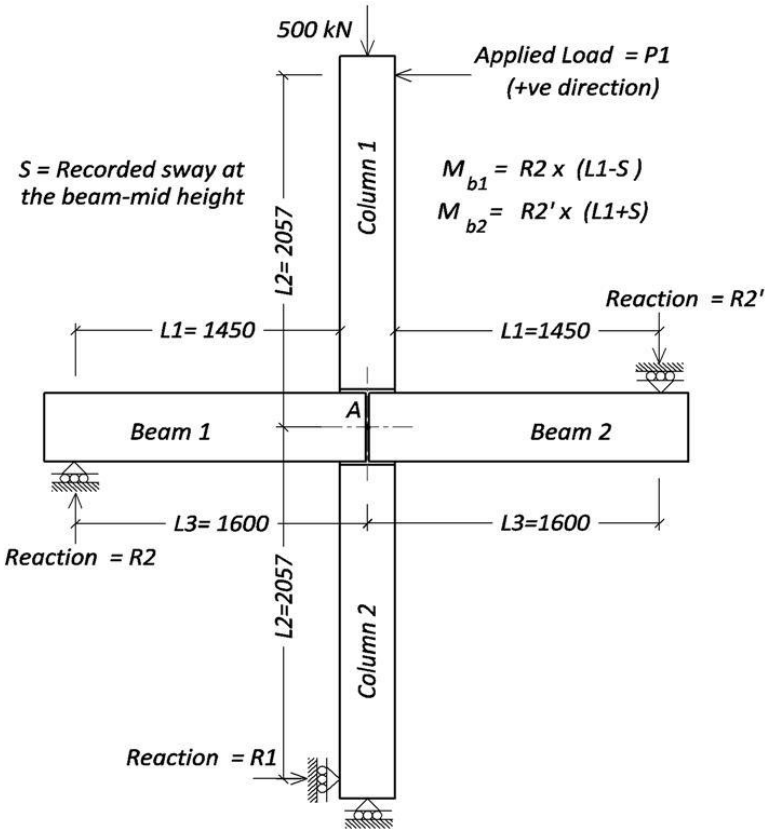

a) Loading configuration in cycles with the top column load being applied to the left (+ve direction)

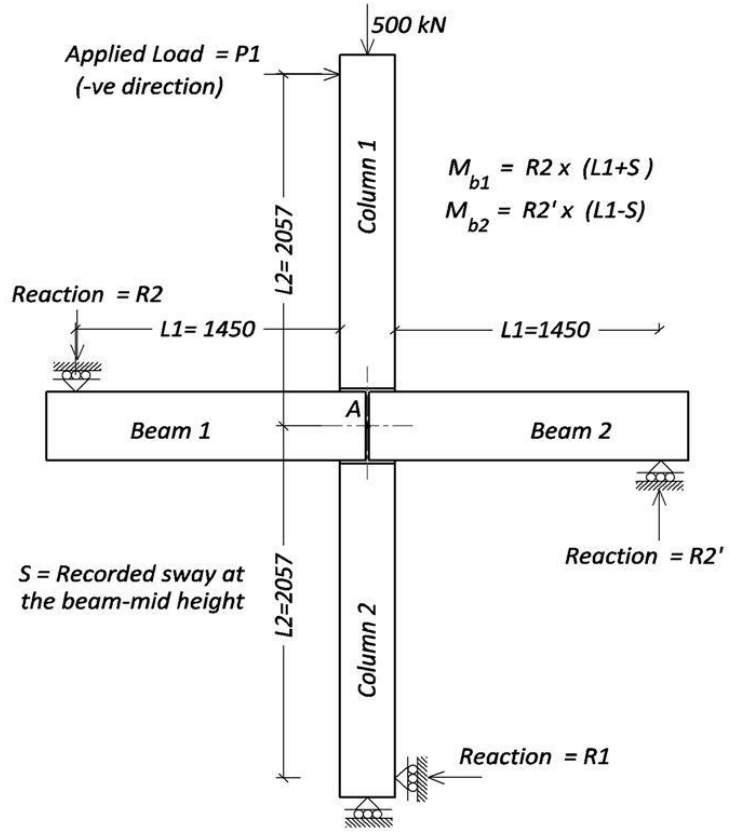

b) Loading configuration in cycles with the top column load being applied to the right (-ve direction)

Figure 6.1 Loading configuration and derived experimental moments in series SW

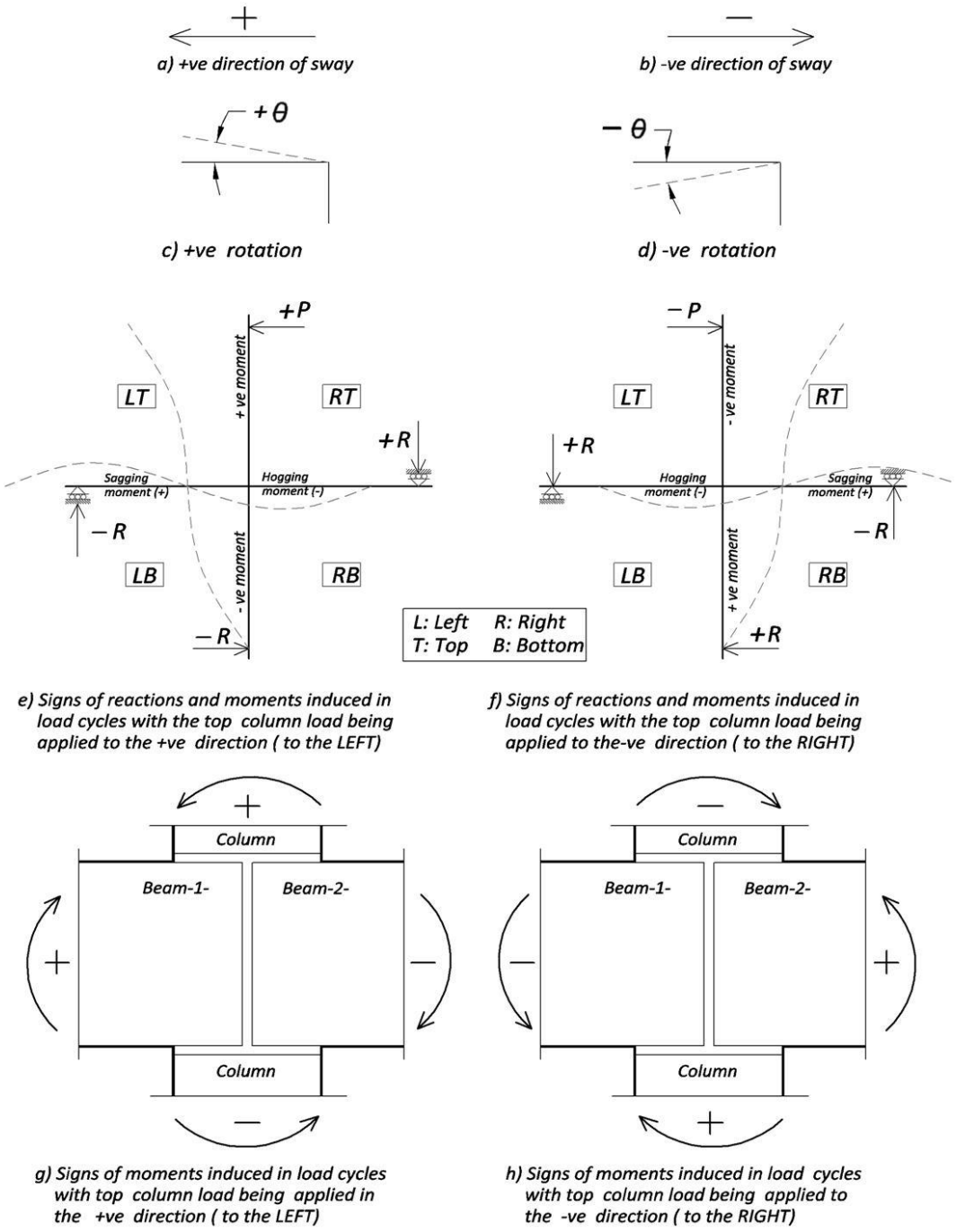

Figure 6.2 Sign convention used in presentation of the experimental results of series SW

In this study, for specimens of series SW, the rotations were measured at all four beam-column interfaces to check for differences. This is essential due to the fact that the column is not one unit and there are two different mechanisms that mobilise the beam hogging and sagging moments at the top and bottom of the connection, respectively.

For instance, at the left top beam-column interface (LT), the rotation was obtained by dividing the deflections at location 1 by the offset distance from the column face L_4. It is worth mentioning that the rotation along L_4 resulting from bending curvature has not been deducted from the measured rotation θ_{LT}; this is because it represented a very small percentage of the total rotation (around 1%) in comparison to 13% to 23.7% in series GR. Therefore:

$$\theta_{LT} = \frac{POT_1}{L_4} \qquad (6.1)$$

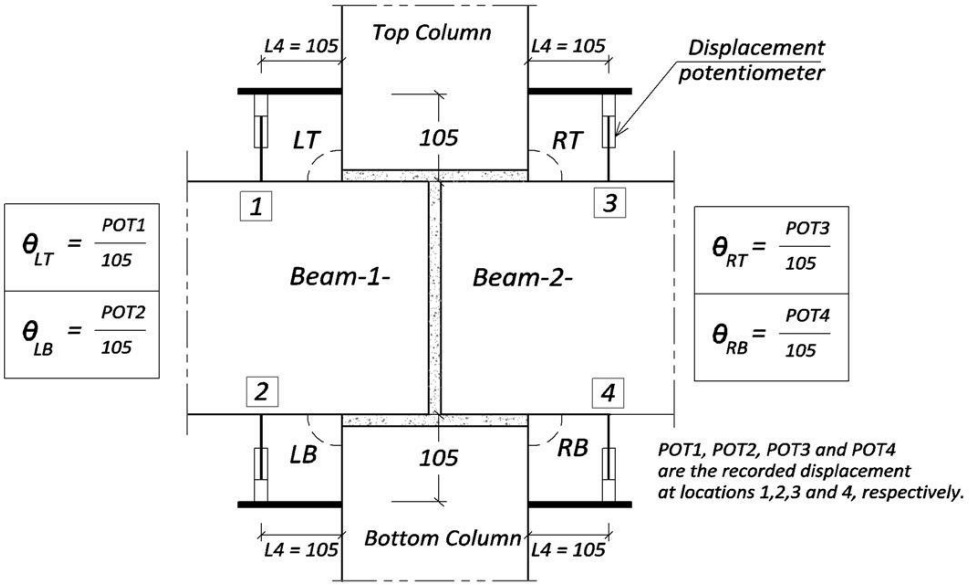

Figure 6.3 Instrumentation layout for measuring relative beam-column rotations in series SW

6.2.3 Experimental rotational stiffness calculation

The experimental rotational stiffness of the connection was derived at two stages: (i) uncracked secant stiffness 'S_{cr}' prior to cracking moment 'M_{cr}'; and (ii) yield secant rotational stiffness 'S_y' at the yield moment 'M_y'. Referring to Figure 5.2 in the previous chapter, $S_{cr} = M_{cr} / \theta_{cr}$ and $S_y = M_y / \theta_y$, where θ_{cr} and θ_y are the relative beam-column rotation prior to cracking and at the yielding of reinforcement, respectively.

6.2.4 Predicted moment capacity calculation

The predicted cracking moment 'M_{cr}' and yield moment 'M_y' of the beam were calculated based on EC2 (CEN, 2004b), as shown below:

$$M_{cr} = \frac{f_{ct,fl} \; I_I}{y_t} \tag{6.2}$$

$$M_y = A_s \, f_y \, Z_{II} \tag{6.3}$$

$$Z_{II} = d - \frac{1}{3} X_{II} \tag{6.4}$$

The above procedure was applied to estimate the moment capacity of the beam when subjected to hogging moment. In the current series SW, under sway loading, when one side of the beam is subjected to hogging moment, the other side is subjected to sagging moment. For calculating M_y at the sagging moment side, the term $A_s \, f_y$ in Eq.(6.3) was required to be checked against the dowel capacity of the column bars ($F_{VR} = \alpha_o \, Ø^2 \sqrt{f_{c,max} \;\; f_y}$, Eq. 2.12 and Figure 2.19) (*fib*, 2008). If $A_S \, f_y$ in Eq. (6.3) was found to be greater than F_{VR},, then moment capacity of the connection 'M_{yd}' will be controlled by the capacity of column dowel bars 'F_{VR}'.

$$M_{yd} = F_{vR} \; Z_d \tag{6.5}$$

$$Z_d = d - \frac{1}{3} x_d \tag{6.6}$$

$$x_d = \frac{2 \, F_{vR}}{f_c \; b} \tag{6.7}$$

6.2.5 Predicted sway calculation

For comparison purposes, the 1st order sway at the top column was calculated for a reference rigid beam-column connection with a geometry the same as that used in series SW. In the sway calculation, the full modulus of elasticity of concrete 'E_c' was used for all loading history, while for the second moment of area, two values were used:

(i) full uncracked I_I for loading stages up to the cracking moment; and (ii) 0.35 I_I for beams, and 0.75 I_I for columns for cracked sections (ACI, 2008a).

6.2.6 Predicted strain calculation

The theoretical concrete and steel strain 'ε' in the beam was calculated using the elastic flexure formula in the same way as has been shown in Section 5.2.6:

$$\varepsilon = \frac{M\ y}{E\ I_{eff}} \tag{6.8}$$

6.3 Series 2 test results

The results of the two specimens (SW1 and SW2) are presented in Table 6.1 and the characteristics of the materials have been presented in Chapter 4. As shown, specimen SW1 did not develop the predicted yield moment due to the insufficiency in the connection detail, while specimen SW2 exceeded the predicated moment by 15.8% but with a low yield secant rotational stiffness.

Table 6.1 Summary of test results of series 2 (SW)

Test Ref.	Connection side	Yield moment, M_y (kNm)			Rotational Stiffness# (kNm/rad)	
		Calculated	Experimental	Ratio %	S_{cr}	S_y
SW1	Beam 1	56.3	45.0	79.9	---	---
SW2	Beam 1	58.8	68.1	115.8	9052 (LB)	1278
	Beam 2	---	78.4	---	10743 (RT)	1610

The rotational stiffnesses are those produced under opening moments (sagging moment at beam 1 in the case of the LB interface, and hogging moment at beam 2 in the case of the RT interface).

6.3.1 Specimen SW1

The aim of testing specimen SW1 was to verify whether the dowel action at the bottom of the connection would mobilise the beam sagging moment by bending the beam bottom bars to the top (Figure 4.2d) forming the beam top reinforcement

(connection reinforcement detail T1). At this stage of the study, it was believed that the 500 kN column load would play a role, to some extent, in developing the dowel action mechanism. The loading was applied in four loading cycles followed by monotonic loading to failure (refer to Figure 4.8).

6.3.1.1 Strength, rotational stiffness capacity and sway of SW1

The predicted moment capacity of the connection at the bottom of the beam was 56.3 kNm based on the dowel action capacity of the column main bars, while the achieved experimental moment capacity was 45.0 kNm.

The sway of the top column (location A) and of the beam mid-height (location B) are shown in Figure 6.4, and the relative beam-column rotation 'θ' at the LB interface is shown Figure 6.5. As shown, during the cyclic reversed loading stages, the connection showed a stable behaviour. However, in the monotonic loading stage, there was a limited increase in the beam moment (32 to 45 kNm) beyond the cracking moment. The behaviour was accompanied by a large sway, large relative beam-column rotation and concentration of cracks within the column-beam interface. This shows that there was no development of the dowel action mechanism, suggesting that the current connection detail T1 was not successful in mobilising the beam-end sagging moment.

Between 32 kNm and 45 kNm beam moments, the increase in the moment was due to two mechanisms: (i) intact bond between the beam bottom bars and concrete as a result of bending these bars to the top to form the beam side bars; and (ii) the friction between connection components. Beyond 45 kNm beam moment, despite losing the bond with the concrete, the beam bottom steel bars were able to withstand some

moments due the anchorage with the beam top bars, which was the reason for not having a brittle failure.

For a detailed examination of what happened at the left bottom beam-column interface (LB), Figure 6.5 presents 'θ' at this location for both the entire loading history and the initial two reversed load cycles. From the graph, it is clear that the connection exhibited a large initial rotational stiffness before the occurrence of cracks; afterwards, in the repeated loading cycles, the active stiffness was lower but remained stationary. In the monotonic loading stage, at 30 kN sway load (45 kNm beam 1 moment), an abrupt increase occurred in θ followed by a decrease in the beam moment.

Regarding the different behaviour mechanisms at the LB interface under sagging moment (opening moment, resulting dowel action mechanism) and hogging moment (closing moment), Figure 6.5b shows that θ under the opening moment was almost twice as θ under the opening moment, indicating a very significant difference in the response.`

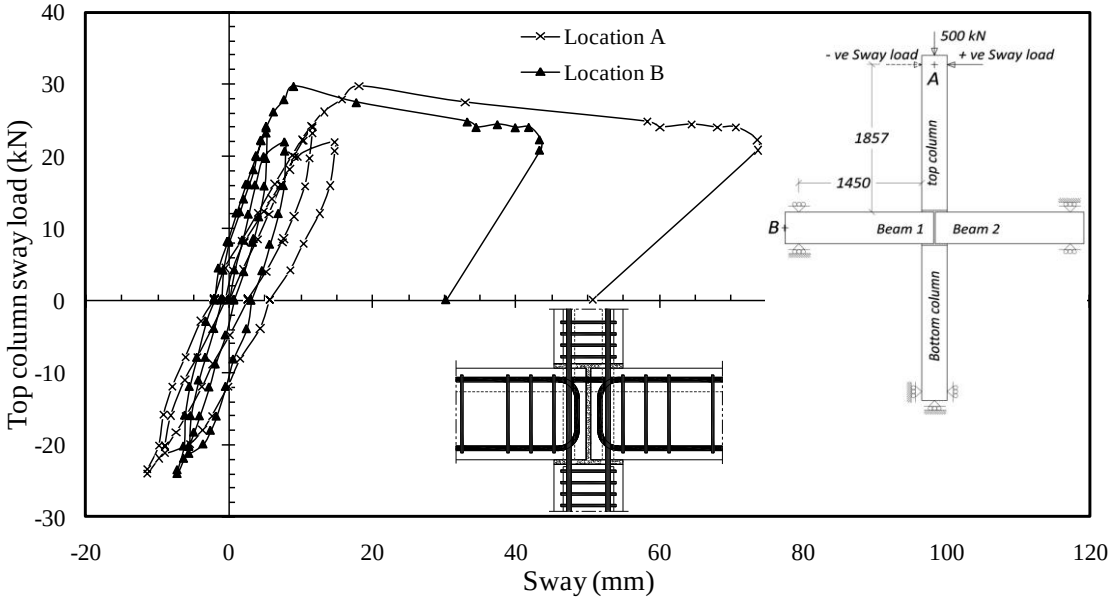

Figure 6.4 Applied column sway load vs. sway at locations A and B in specimen SW1

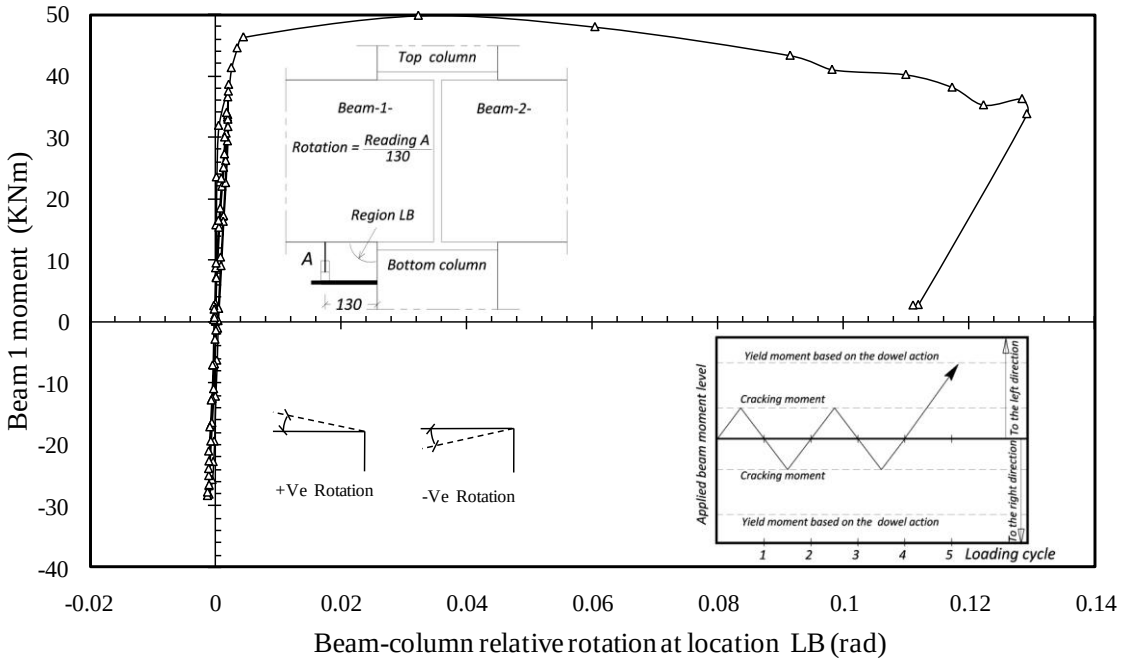

a) The whole loading history

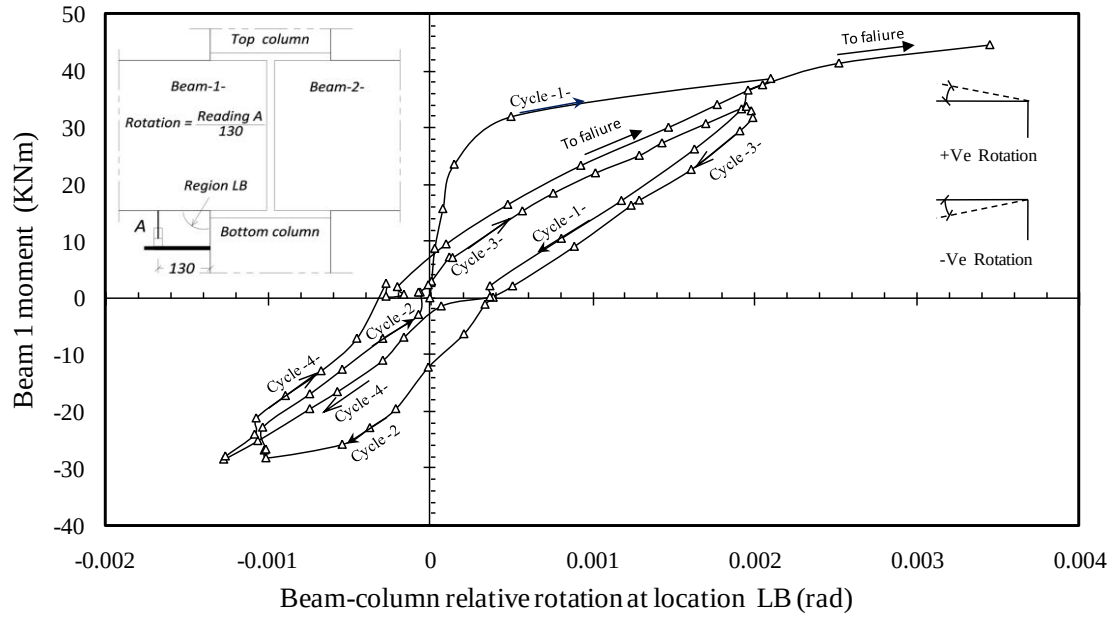

b) Enlargement of cyclic loading stage

Figure 6.5 Beam 1 moment vs. relative beam-column rotation in specimen SW1

6.3.1.2 Crack pattern and failure mode of SW1

Figure 6.6 shows the crack distribution in specimen SW1 at the end of the 1st and 2nd load cycles and at failure. In the 1st load cycle, the cracks initiated simultaneously at the vertical interface between the grout and the beam within the connection, and in the beam at the column face at a beam moment equal to 32 kNm. In the 2nd load cycle, similar cracks happened at the opposite beam sides. These cracks remained without propagation in the 3rd and 4th load cycles.

In the monotonic loading stage, there was no further crack propagation under the monotonic load up to the cracking moment. After that, there was very limited crack propagation in the beam between 32 kNm to 45 kNm beam moment. Afterwards, the cracks started to concentrate at the beam-column interface, at the LB beam-column interface. The concentration of cracks remained at that location with a continuous increase in the crack width.

As stated above, in specimen SW1, there was a concentration of cracks at the column face with very limited cracks along the beam length due to the insufficient bond of the beam bottom bars. From this, it is clear that the column bars did not develop the dowel action required to mobilise beam-end sagging moments. In this trend, to modify the behaviour and to develop the full dowel action capacity of the column bars, connection detail T3 was designed to be examined in specimen SW2, as will be presented in the next section.

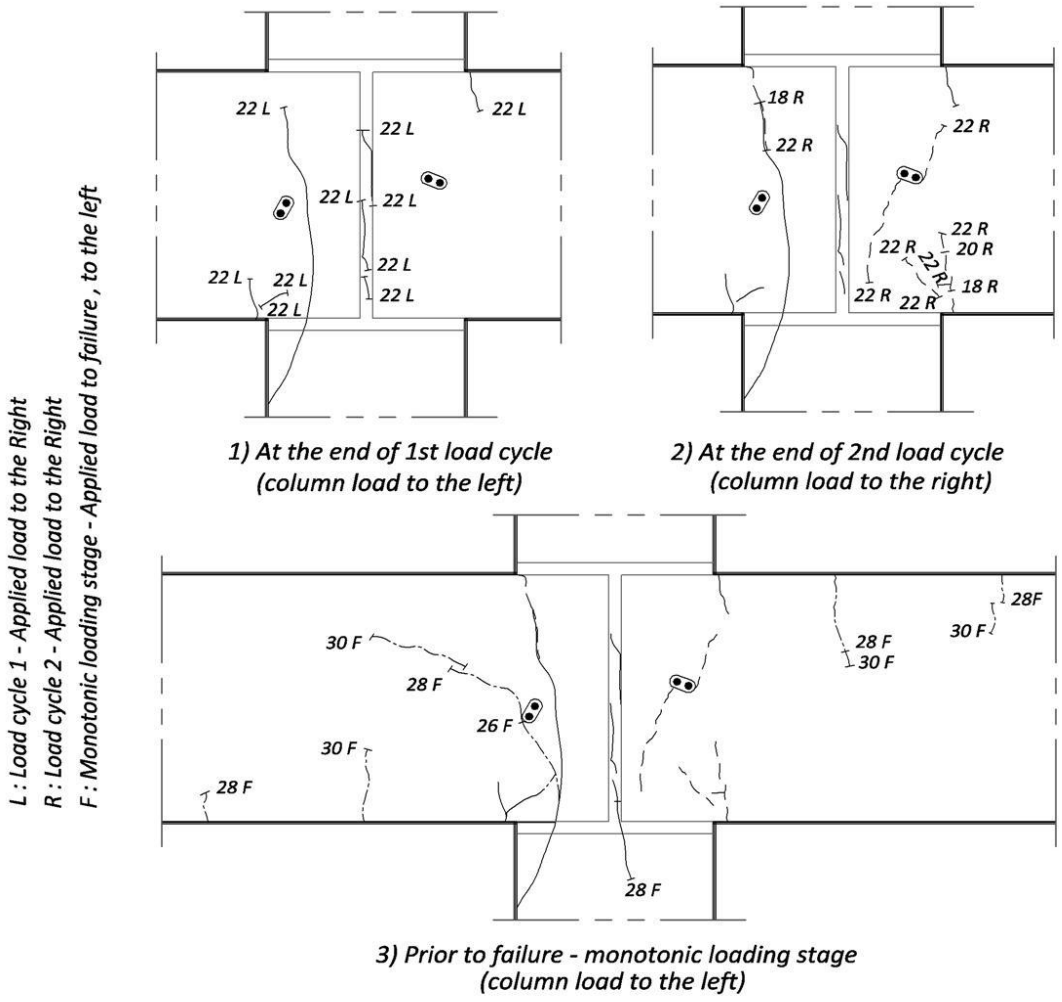

a) Crack distribution at different loading stages

b) Failure mode

c) Left-bottom beam-column interface status at failure

Figure 6.6 Crack propagation and failure mode in specimen SW1

6.3.2 Specimen SW2

The design of specimen SW2 aimed to prevent the failure type that occurred in specimen SW1, by implementing the connection reinforcement detail type T3 (Figure 4.4b). This was done by: (i) bending the beam bottom bars in a horizontal plane around the column bars; (ii) providing horizontal links at the beam-ends to confine the region, and (iii) using additional links around the column dowel bars at the bottom of the connection (Figure 4.4b). The column sway load was applied in four loading stages (Figure 4.8b), as listed below.

(i) Stage 1: two cycles including applying column sway load to the left

(ii) Stage 2: four cycles including applying column sway load to the right

(iii) Stage 3: four cycles including applying column sway load to the left

(iv) Stage 4: applying monotonic column sway load to failure.

Each cycle included applying column sway load up to 50% of the predicted connection capacity in mobilising the beam-end sagging moment.

6.3.2.1 Strength, rotational stiffness capacity and sway of SW2

The moment reported in Table 6.1 is beam 1 moment 'M_{b1}' measured at the column face, where the dowel action mechanism was active in the 4th loading stage. The achieved moment capacity at beam 1 'M_{b1}' was 68.1 kNm, in comparison with a predicted 58.8 kNm moment. The additional capacity is attributed to the additional 1H8 link around column dowel bars at the bottom of the connection (Figure 4.4b); however, this capacity was accompanied by large crack widths (1.7 mm to 3.5 mm), suggesting that the predicted sagging moment capacity of the connection (58.8 kNm) gives a reasonable estimation for the sagging moment capacity of the connection in the practice.

In beam 1, at location LB, the maximum crack width was 0.3 mm in the 1st, 2nd and 3rd cyclic loading stages, which increased to 3.5 mm at the yielding stage of the column dowel bars. At this stage, the test was stopped due to limitations in test configuration, which rose from losing the verticality in the way of applying the sway load against the top column and from 100 mm maximum beam sway allowed by the test rig. The main intentions from testing specimens SW2 were:

(i) developing full dowel action in the column bars;

(ii) producing a satisfactory distribution of cracks.

These aims were achieved when the connection behaviour reached the plateau in the measured sway, rotation and strains; therefore, at the yielding stage and due to the above-mentioned limitations, the test was stopped.

The sway measured at the top column (location A) and at the mid-height of beam (location B) is shown in Figure 6.7. As could be noticed, the sway at location A was almost twice the sway at location B, indicating the occurrence of almost the same sway mechanism at the bottom and top sides of the beam-column connection in spite of having two different moment transmitting mechanisms. At sway load of 60.7 kN (68.1 kNm beam moment), the load-sway relation reached a plateau demonstrating the yielding of the column bars that were transmitting the beam sagging moment through the dowel action mechanism. This will be shown in detail in Section 6.3.2.3, where the column steel strains are reported.

To compare specimen SW2 with a parent rigid cruciform, Figure 6.7 shows the 1st order sway calculated at location A for both cases. The comparison shows that the sway in specimen SW2 is higher than the parent rigid one by 328%; this sway would produce significant 2nd order moments in the columns.

In the 4th loading stage, the largest relative beam-column rotation 'θ' occurred at the left-bottom beam-column interface (LB) as it was under opening sagging moment without having direct continuity in the beam bottom reinforcement (Figure 6.8a). For this reason, the rotational stiffness at this location will be used to characterise the connection response for both sagging and hogging beam moment under sway loads in Chapter 8. To support this selection, by comparing the M-θ relation at locations LB and RT, it is clear that there was no significant difference in the measured rotations up to the yielding of the column dowel bars.

However, after yielding, the larger increase in θ occurred at location LB, where the yielding in the column dowel bars happened. The yield secant rotational stiffness at beam 1's side 'S_{y1}', which was under an opening sagging moment at yielding, was found to be 1278 kNm/rad (68.1 kNm / 0.0533 rad). At beam 2's side, which was under an opening hogging moment at yielding, S_{y2} was found to be 1610 kNm/rad (78.4 kNm / 0.0487 rad). In spite of the higher rotational stiffness at beam 2 (26% higher than S_{y1}), it will be shown in Section 6.4 that this difference has no significant effect on the response. The assessment of the effects of S_{y1}=1278 kNm/rad on frame responses under sway loads will be carried out in Chapter 8.

For a detailed examination of the connection rotational stiffness at the cyclic loading stages, Figure 6.8b shows the M-θ relation of beam 1 at LB interface at those stages. In the 1st loading cycle in the 1st loading stage, the connection showed a large rotational stiffness prior to the occurrence of cracks. In the following loading cycles within the same loading stage, the connection showed a stable but lower rotational stiffness as the cracking stiffness was active and the applied load did not exceed those applied in the first load cycle.

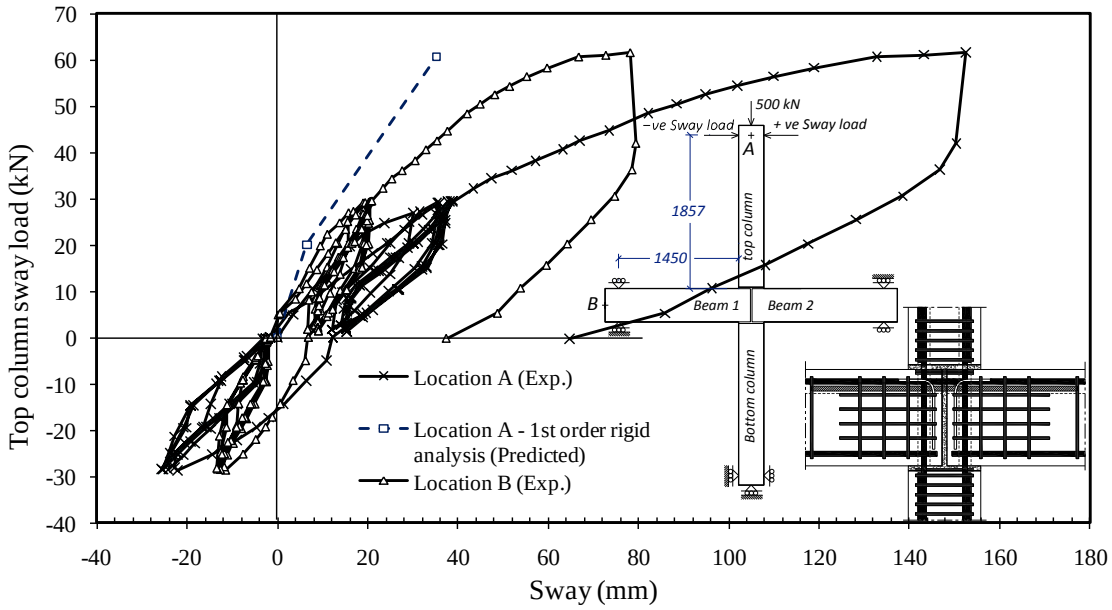

a) The whole loading stages (locations A & B)

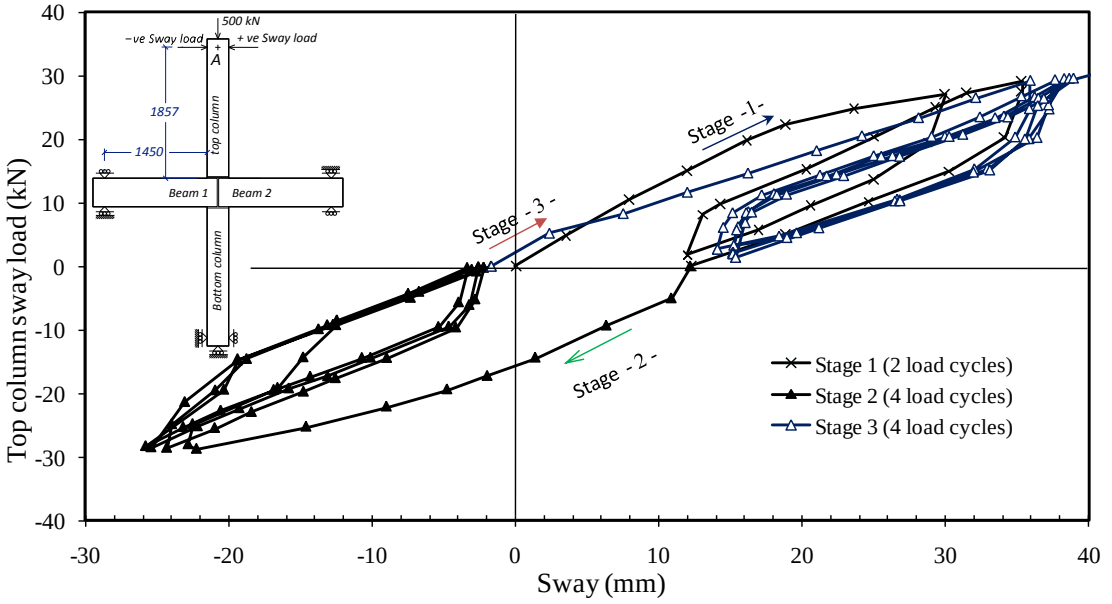

b) Enlargement of the early loading stage (location A)

Figure 6.7 Applied column sway load vs. sway at locations A and B in specimen SW2

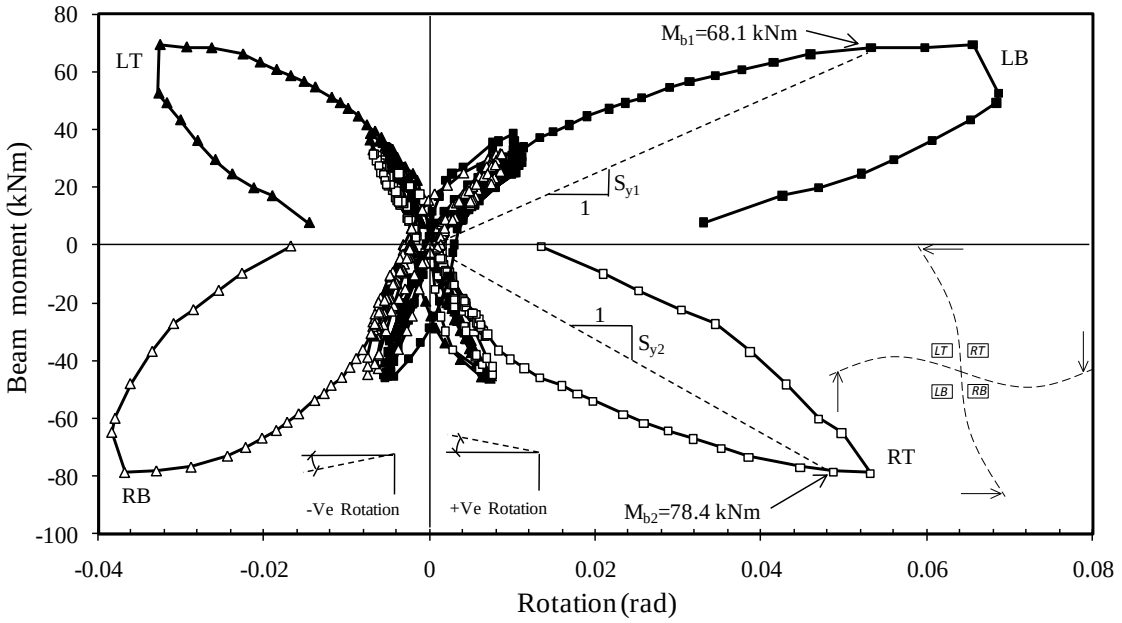

a) The whole loading stages (at all four beam-column interfaces)

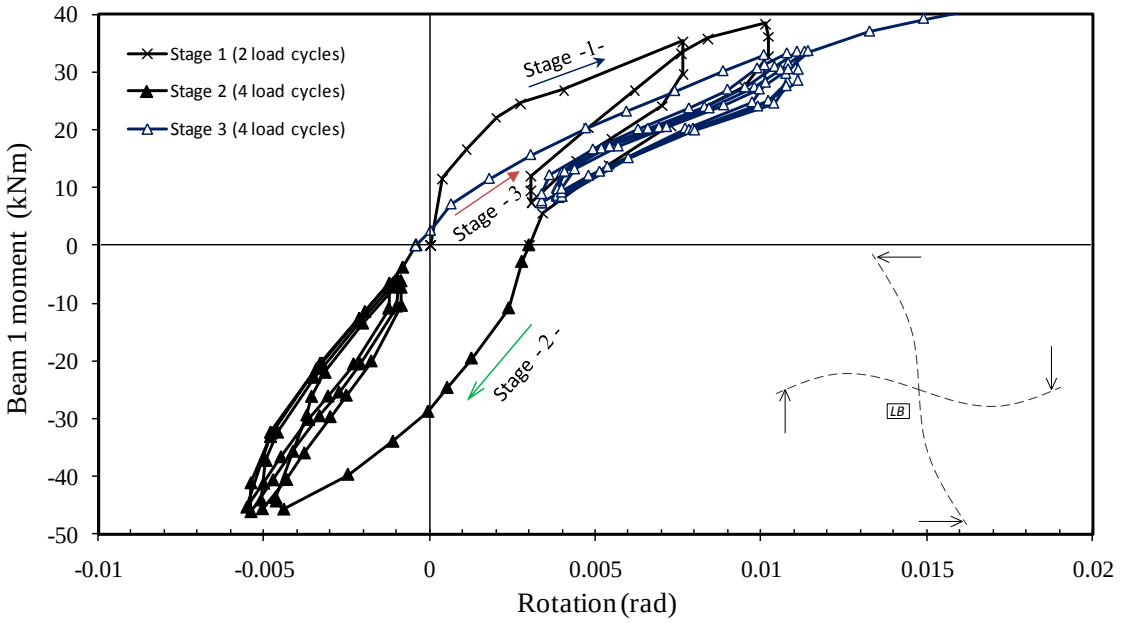

b) Enlargement of 1st, 2nd and 3rd loading stages at LB interface

Figure 6.8 Beam moment vs. relative beam-column rotation in specimen SW2

6.3.2.2 Crack pattern and failure mode of SW2

The crack patterns at the end of the 1st, 2nd and 4th loading stages are shown in Figure 6.9. In the 1st loading stage (Figure 6.9a), the first cracks appeared at the column faces at 22 kN sway load (M_{b1} = 25 kNm), followed by cracks within the connection at

the vertical interface between the grout and the beam with a propagation of cracks along the beam length. In the same way, in the 2nd loading stage (Figure 6.9b), the first cracks initiated at the column faces at 18 kN sway load (M_{b1} = 25 kNm) with a very similar crack propagation but at the opposite beam sides. At the end of loading stages 1 and 2, the maximum applied cyclic load produced 50% of the predicted sagging moment capacity of the connection. At the end of this loading stage, the maximum crack width was 0.3 mm at location D2 (Figure 6.11a and Figure 6.12), at which the dowel action mechanism was active. From a serviceability point of view, this moment level would determine the service limit state for the connection under sway loads, meaning that it is recommended to keep the sagging moment within the 50% of the predicted capacity at the service loading stage.

In the 3rd loading stage, four load cycles were applied without occurrence of any further cracks. At the 4th loading stage, where the load was applied to failure, the cracks propagated along the beam length towards the beam reactions without cracks in the column apart from those occurred within the connection (Figure 6.9c). This situation continued up to 52 kN sway load (M_{b1} = 58 kNm), which corresponds to 97 kNm column moment (M_{c1}), where the first cracks occurred simultaneously in the top and bottom columns followed by further cracks during the subsequent loading. This confirms the contribution of the column axial loads in delaying the occurrence of cracks in the column.

The largest cracks occurred at the column faces (locations D1 and D2) and at the middle of the connection (location D3) as shown in Figure 6.11, which shows the sizes and locations of these cracks at failure. To trace the crack development, Figure 6.12 shows the crack width at locations D1 and D2 versus beam moment. As shown, the

crack width at location D2 was always higher than that at location D1. This is because there was no direct continuity in the beam bottom reinforcement at location D2.

Figure 6.11c might give misleading information about the location of failure; however, by cutting the connection at location A-A (see Figure 6.11a and Figure 6.11e), it is obvious that the failure was due to yielding of the column bars, where the cracks turned around the dowel bars.

The exploration of the crack path within the connection in specimen SW2 demonstrates the capability of the connection reinforcement type T3 in developing the full dowel action capacity of the column bars and spreading the cracks along the beam length before reaching the column. This behaviour is essential in prevention of brittle failure under sway loads and ensures a robustness of the connection. However, this behaviour was accompanied by low rotational stiffness and large crack widths.

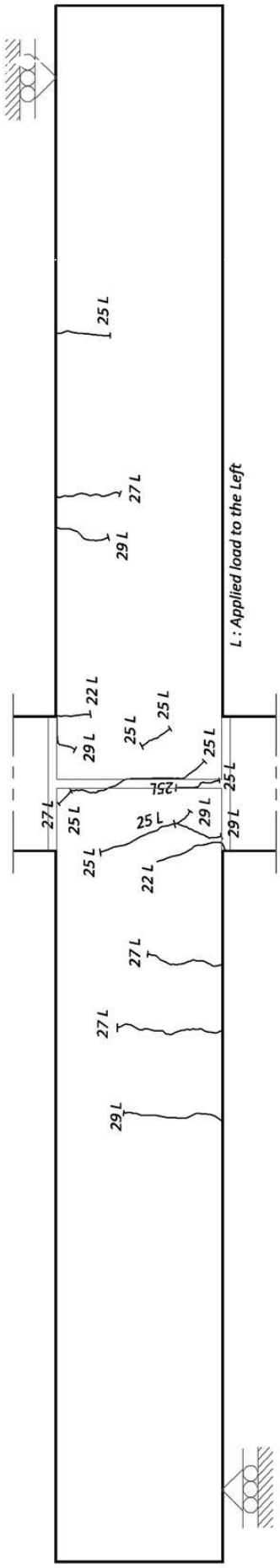

a) End of loading stage 1

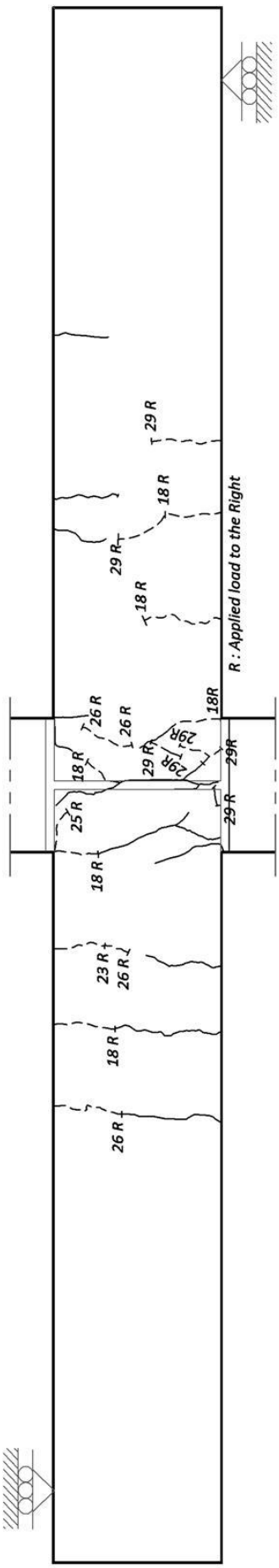

b) End of loading stage 2

Figure 6.9 Crack propagation in specimen SW2 at the end of loading stages

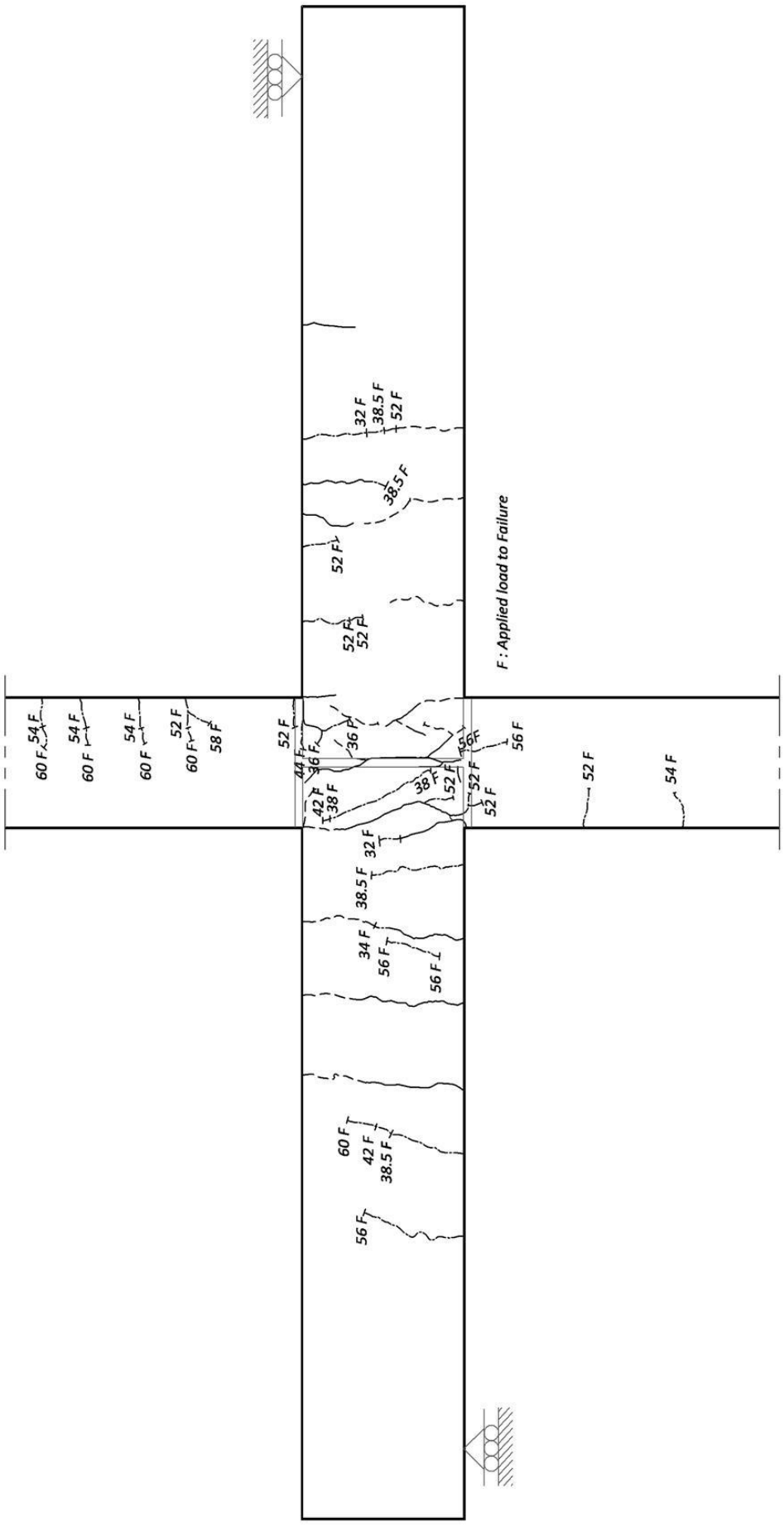

c) At failure (end of load stage 4)

Figure 6.9 (Cont.) Crack propagation in specimen SW2 at the end of the loading stages

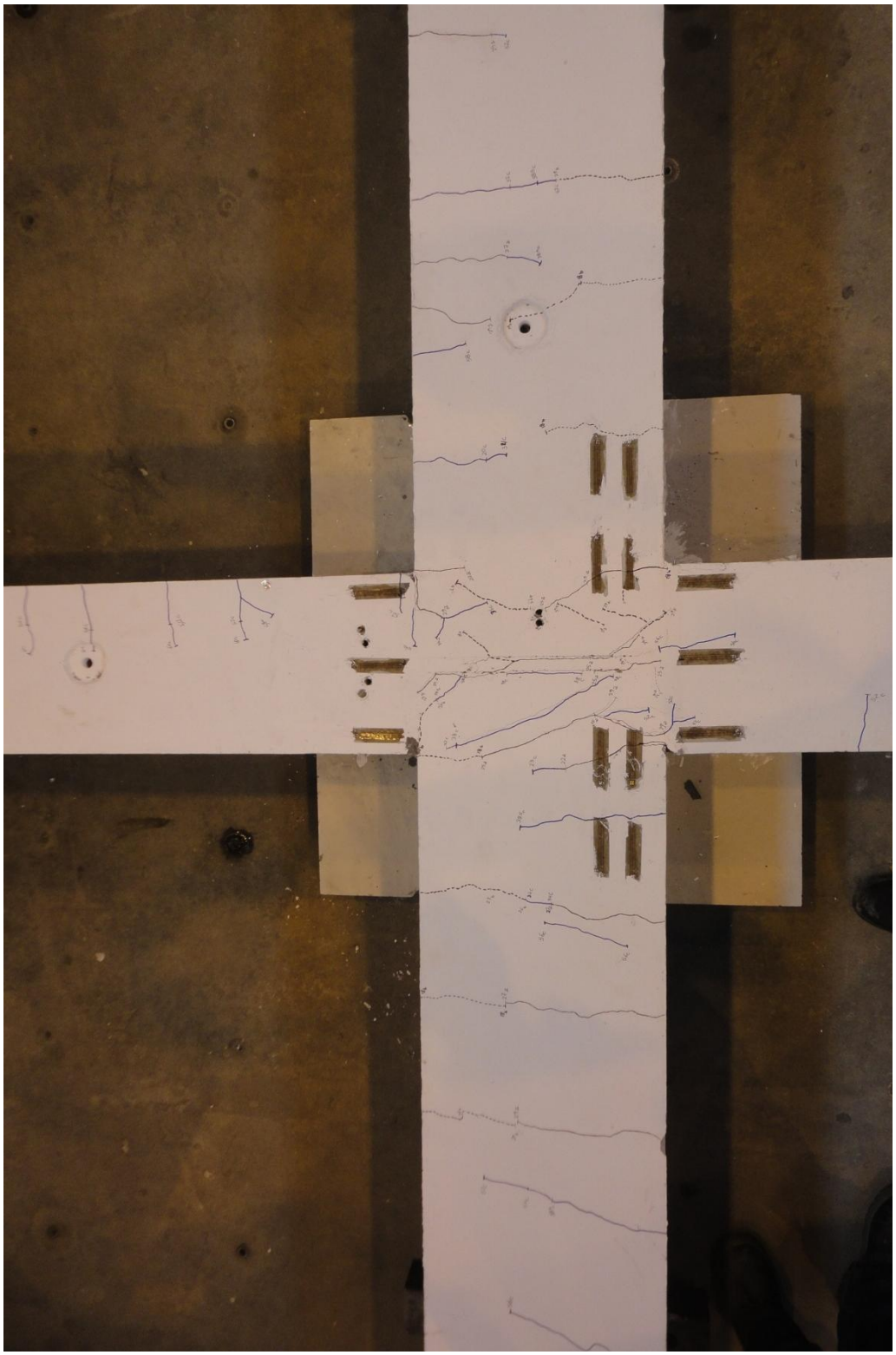

Figure 6.10 Failure mode in specimen SW2 (at the end of loading stage 4)

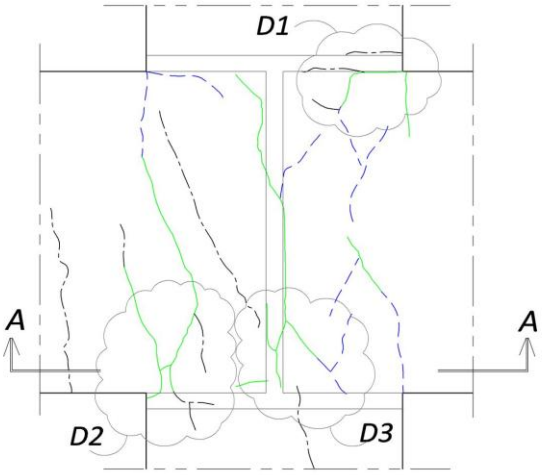

a) Detail locations

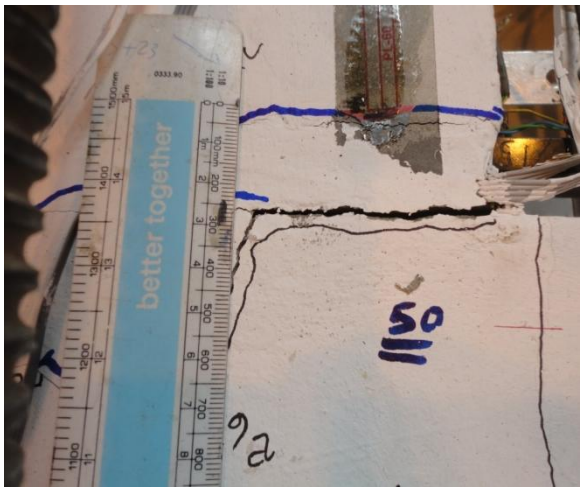

b) Location D1 prior to stopping the test

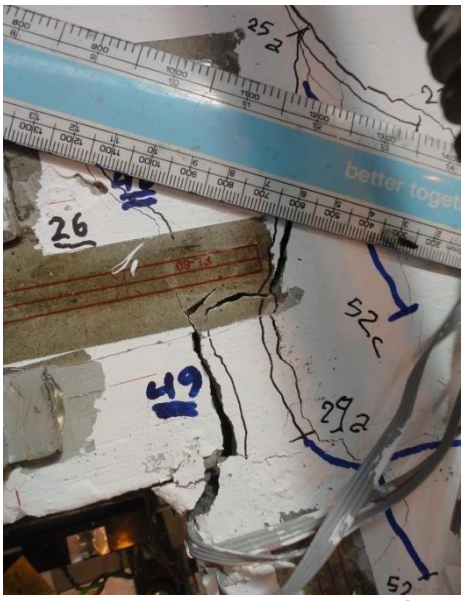

c) Location D2 prior to stopping the test

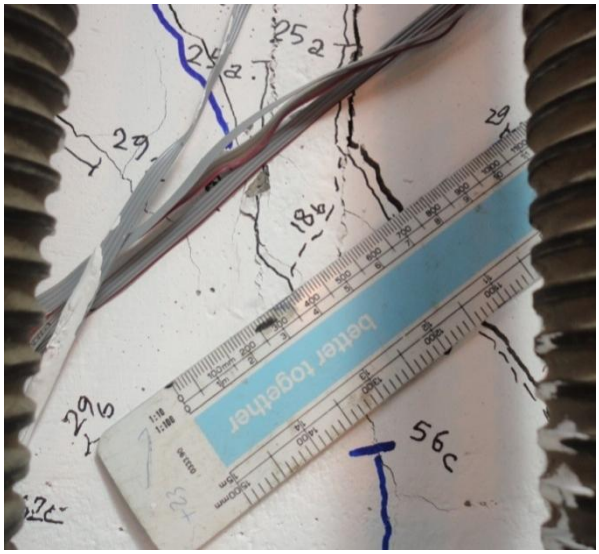

d) Location D3 prior to stopping the test

e) Section A-A

Figure 6.11 Crack width and path within connection in specimen SW2

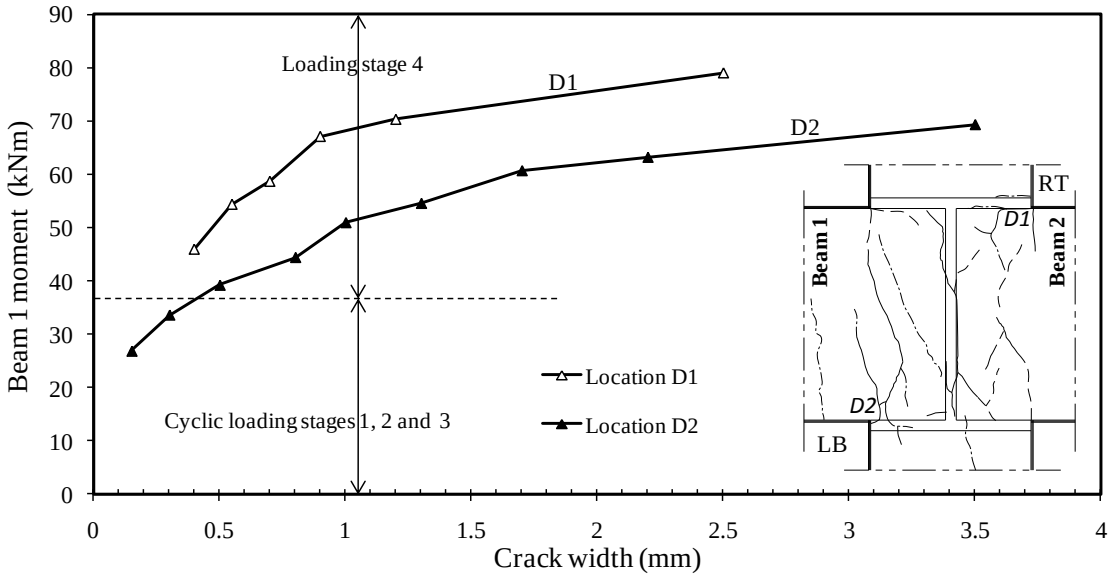

Figure 6.12 Crack width vs. beam moment in specimen SW2

6.3.2.3 Steel bar strains of SW2

In the investigated beam-column connection, the key behaviour under sway loads is the dowel action mechanism of the column bars in mobilising the beam sagging moment. To trace this behaviour, the strains were recorded in the column bars at the bottom of the connection, and at the additional column link.

Figure 6.13 shows the internal forces distribution in the connection under sway loads; the inclined lines indicate the possible shear cracks orientation within the connection under different load directions. The forces at the bottom of the beam are those responsible in developing the dowel action mechanism in the column bars.

Figure 6.14a shows the strain recorded in the column bars at the LB interface (locations A1 and A2), which experienced an opening rotation in the 4th loading stage. The graph reveals that these bars reached the yielding that caused the connection failure, as is obvious from the plateau phase in the graph. This confirms the capability of the new connection reinforcement detail (T3) in developing the full dowel strength.

For a detailed investigation of the dowel bars' behaviour at location A1, Figure 6.14b provides the strain variation in the bar at the early loading stages. At the 1st loading stage (opening rotation at LB), there was only a minor change in the column bar strain up to the occurrence of the first cracks (point A in Figure 6.14b). Afterwards, a significant change happened in the strain towards being positive (tension). This reveals that the dowel bars started mobilising the beam bottom forces after the occurrence of the first cracks.

In the 2nd loading stage (closing rotation at LB), the dowel bar at location A1 was mobilising beam bottom compressive forces, which were pushing the dowel bar into the connection. The axial steel strain at location A1 continued to increase in compression up to the initiation of the crack at the other side (beam 2). After that point (point B in Figure 6.14b), the strain changed its trend and started to increase towards the positive direction (less compression). That behaviour is attributed to losing the counteraction effect from the other side beam (beam 2) to balance the compressive forces. In the 3rd loading stage, there was a stable behaviour, as the cracked concrete section was active.

For the column bars at location A3 (Figure 6.15), a similar behaviour was observed at the early loading stages. In the 3rd and 4th loading stage, in spite of presence of compressive forces at the bottom of beam 2, tensile strains happened at location A3. This indicates that Beam 1 did not provide the support required to prevent the occurrence of the dowel action at location A3.

In the new connection reinforcement detail T3 in specimen SW2, additional links were provided at the bottom of the connection around the column bars to work as an additional bridge in transmitting the dowel forces in the column bars and preventing

splitting cracks within the lower column. Figure 6.16 shows that these links contributed in mobilising the dowel forces in the column bars but without reaching the yielding.

Figure 6.8a, Figure 6.11b and Figure 6.12 showed that, in spite of having a direct continuity in the beam top steel bars, there was a large crack opening at RT interface with a large relative beam-column rotation close to that observed at LB interface. To investigate what happened there, the strains recorded in the beam top continuity steel bars are reported in Figure 6.17. The maximum strain occurred at location B (beam 2, at the column face) as predicted, but unexpectedly it reached the yield strain there. This explains the large crack width and the large relative beam-column observed at RT interface (Figure 6.11b).

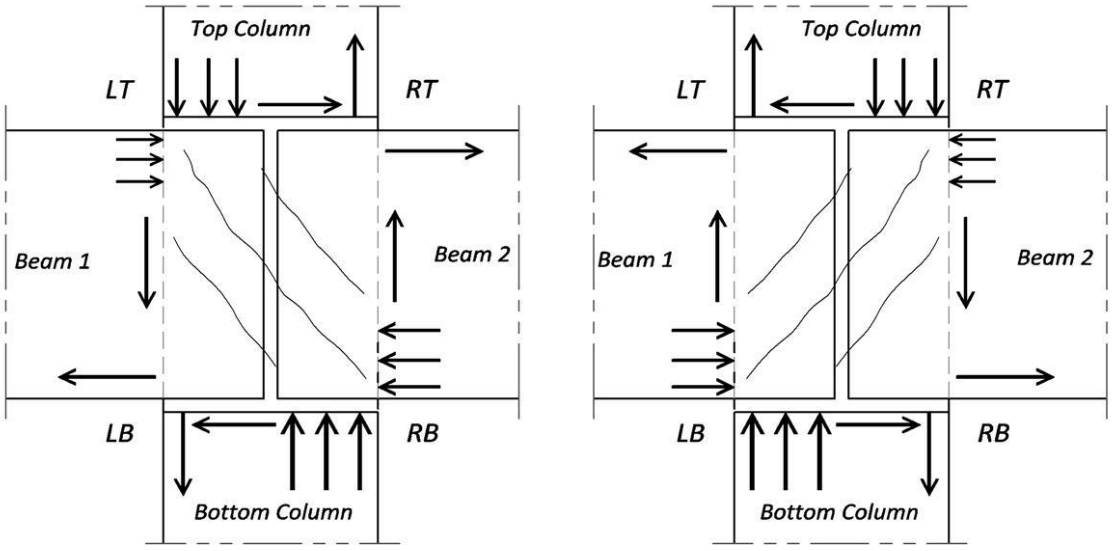

Figure 6.13 Internal forces at the connection under sway loads

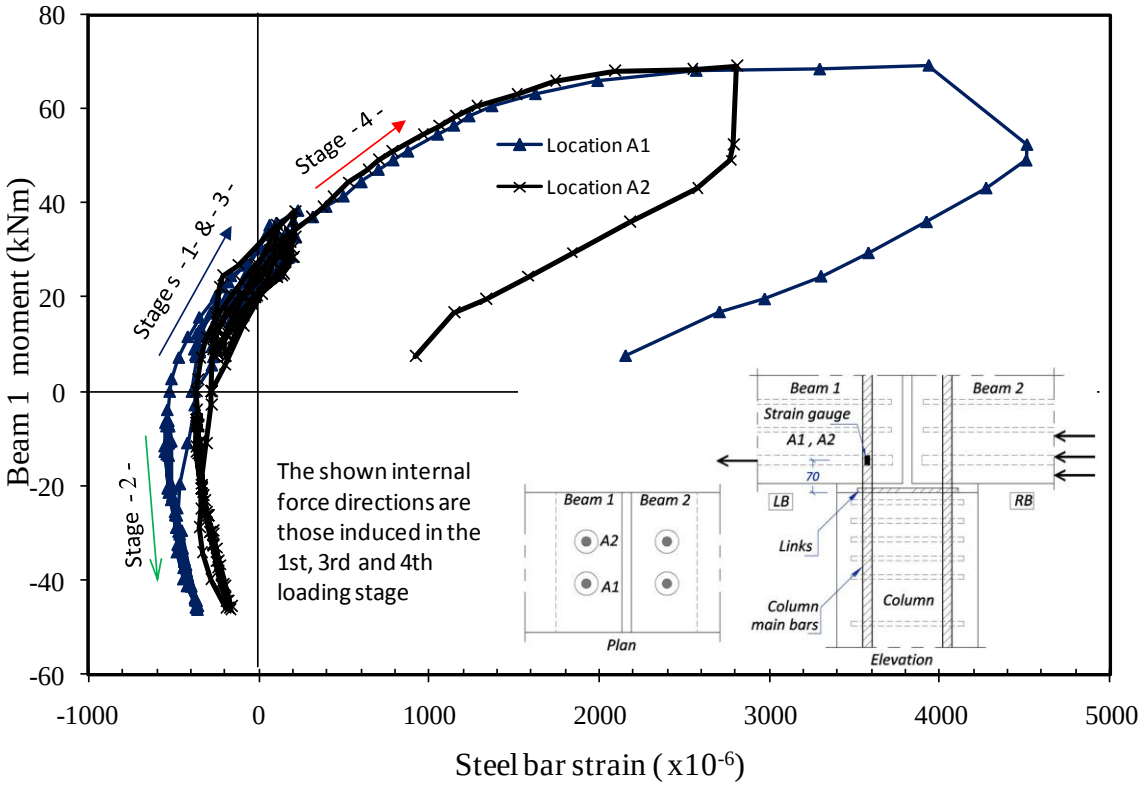

a) The whole loading stages (locations A1 and A2)

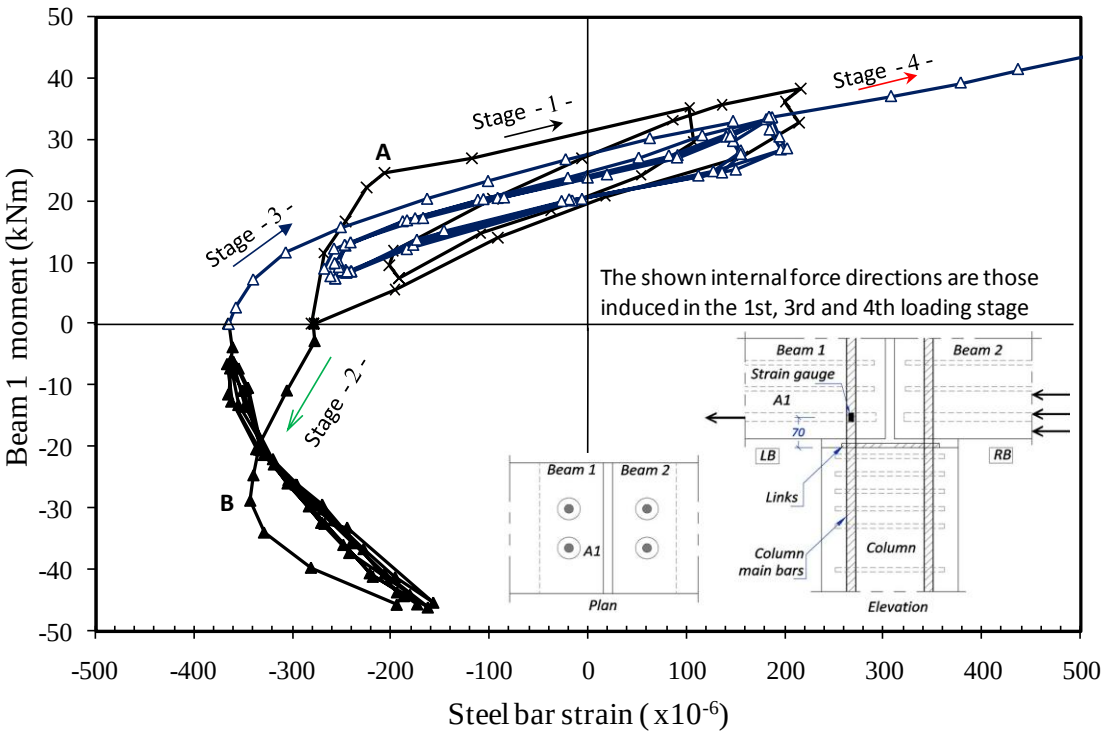

b) Enlargement of the early loading stages (location A1)

Figure 6.14 Dowel bar strain at locations A1 and A2 vs. beam 1 moment in specimen SW2

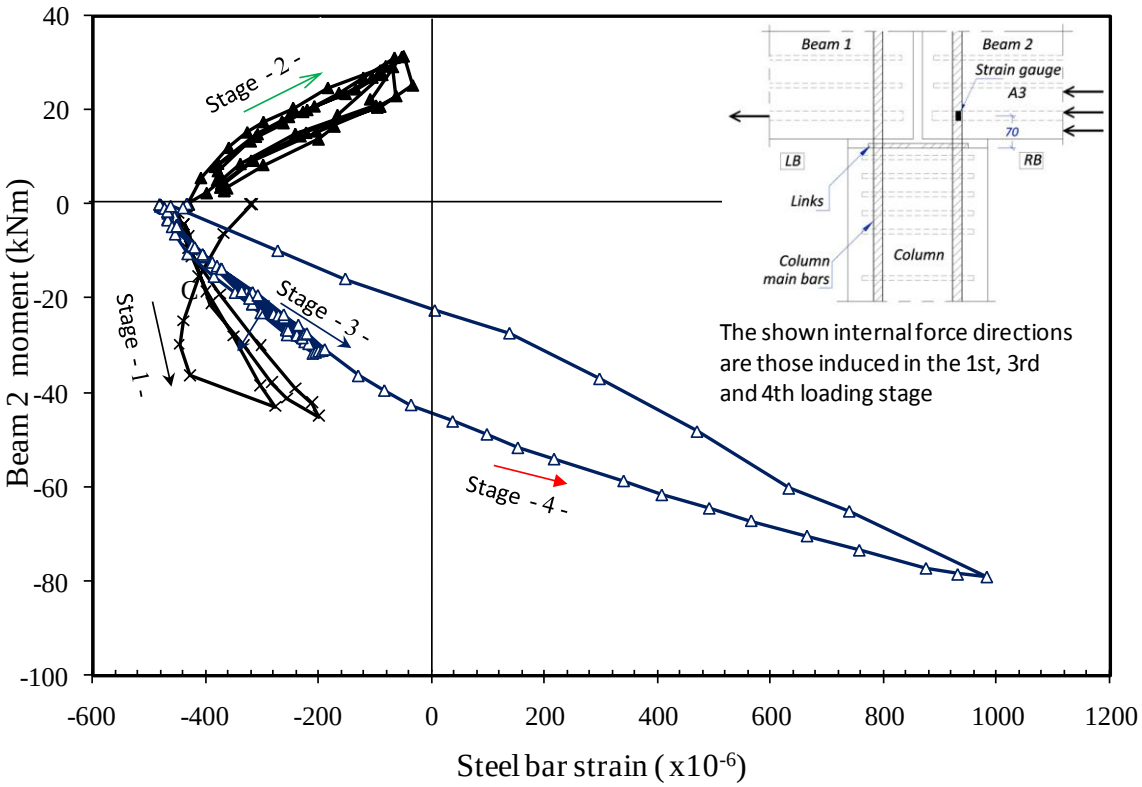

Figure 6.15 Dowel bar strain at location A3 vs. beam 2 moment in specimen SW2

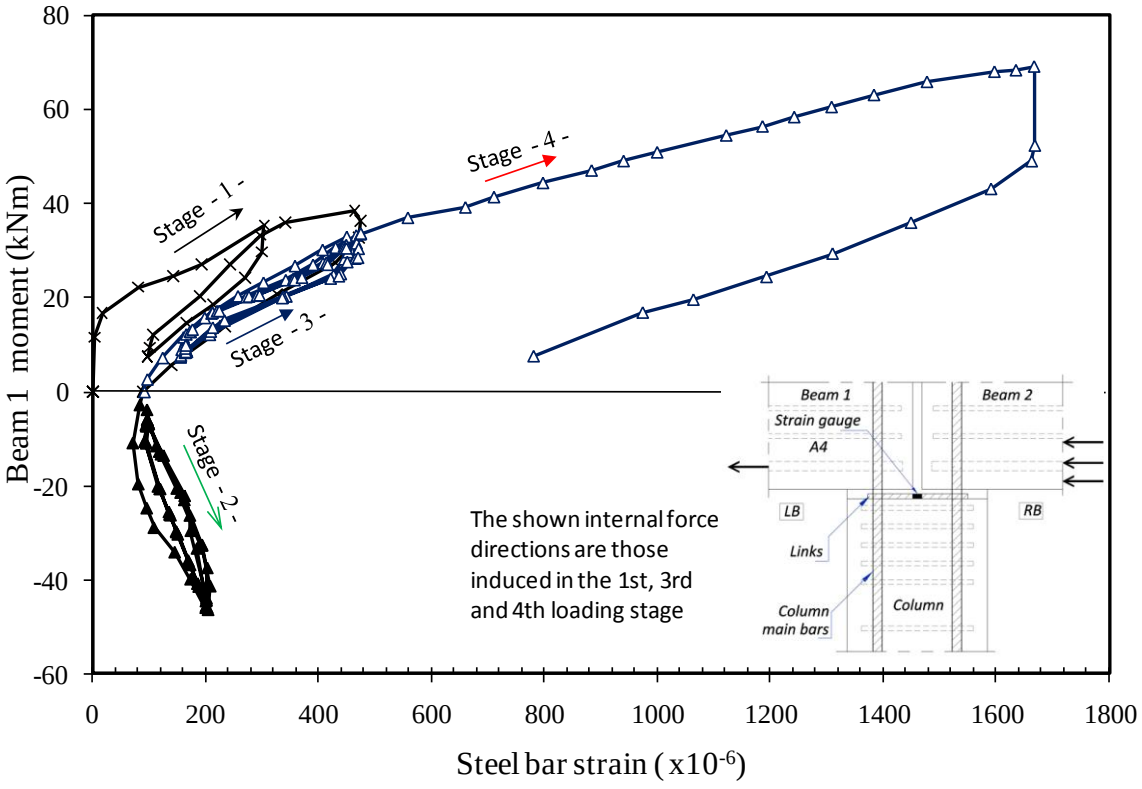

Figure 6.16 Additional link strain at location A4 vs. beam 1 moment in specimen SW2

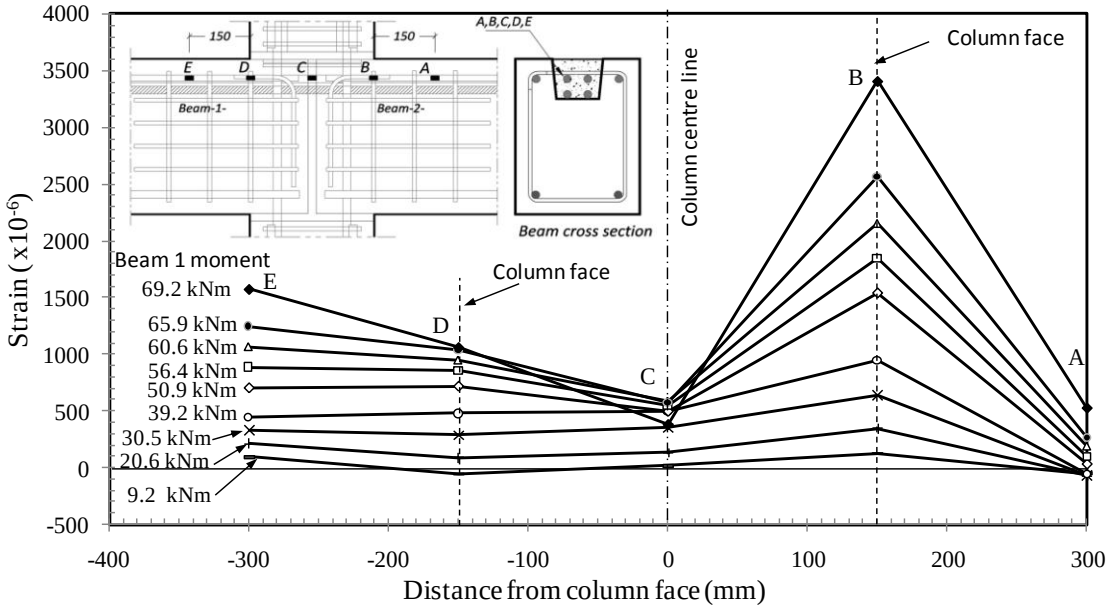

Figure 6.17 Top beam steel bar strain variation across the connection in 4th loading stage (specimen SW2)

6.3.2.4 Column axial strain distribution of SW2

Under sway loads, the axial strain distribution in the column is affected by moments induced at both the beam and column in addition to the strain resulted from column axial load. As shown in Figure 6.18, the experimental strain distribution matches the internal force distribution at the connection (Figure 6.13). After the yielding of the left side column dowel bars, the axial strain in the bottom column increased significantly, indicating an increase in the stress concentration at the middle of the bottom column due to the extension of cracks into LB interface (Figure 6.11c).

The results presented in Figure 6.18b reveal that the bottom column experienced a high axial stress due to the opening sagging moment at the LB interface without having direct continuity in the beam bottom reinforcement.

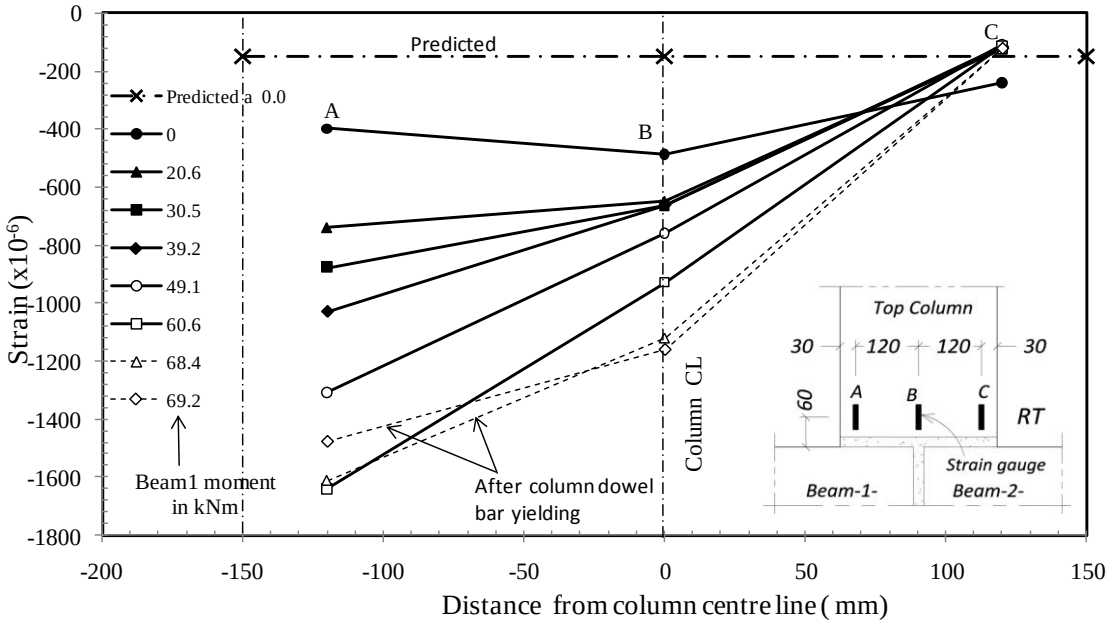

a) Top column

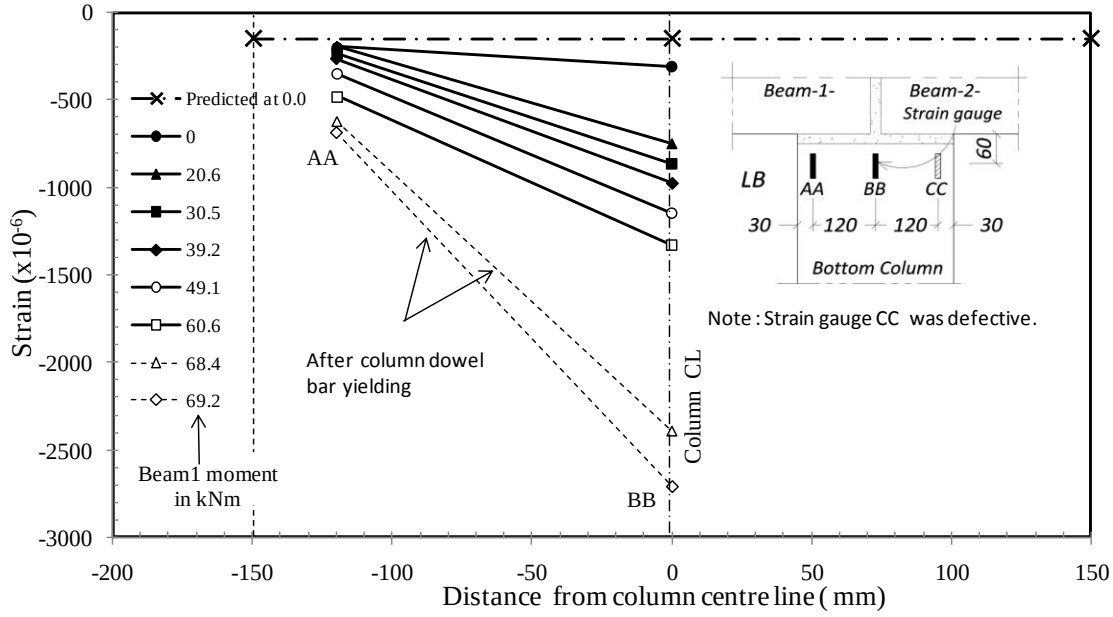

b) Bottom column

Figure 6.18 Axial column strain distribution in 4th loading stage (specimen SW2)

6.4 Preliminary connection evaluation

The test results of series SW showed that the modified connection reinforcement detail (type T3) used in specimen SW2 was successful in developing the full dowel action in the column bars and distributing the crack along the beam and column;

however, it could not prevent the crack concentration at the column face, which resulted in a low rotational stiffness. The crack width ranged from 0.3 at 50% of the ultimate moment capacity to 3.5 mm at failure. These observations suggest that the beam-column connection investigated in the current study cannot be used in unbraced frames when the permanent hogging moments generated from dead loads are surpassed by the temporary sagging moments generated from temporary wind loads.

To evaluate the rotational stiffness obtained from specimen SW2, the fixity factor of a single beam of varied span length is calculated (Figure 6.19) using Monforton's formula (1963) (refer to Section 2.7). The calculations were based on two values for E_cI for the beam: (i) full E_cI value; and (ii) 0.35 E_cI, as suggested by the ACI-code (ACI, 2008a) for beams in frames subjected to sway loads. Referring to the case of using 0.35 E_cI for the beam, based on the EC3 (2005b) classification system, it is apparent that the connection is classified as pinned connection:

(i) for spans less than 7.8 m in case of using the yield secant rotational stiffness (S_y = 1278 kNm/rad) obtained at the left-bottom (LB) interface under sagging moment;

(ii) for spans less than 6.7 m in case of using the secant rotational stiffness (1610 kNm/rad) obtained at the right-top (RT) interface under sagging moment.

The dimensions of the connection specimens (SW1 and SW2) were based on the analysis of a frame with beam span lengths of 7.3 m (Appendix A); therefore, the member sizes used in the specimens are only relevant to spans in this range. Accordingly, it is suggested that the beam-column connection tested in the current study behaves as a pinned connection under sway loading. This statement will be evaluated in detail in Chapter 8 using S_y equal to 1278 kNm/rad.

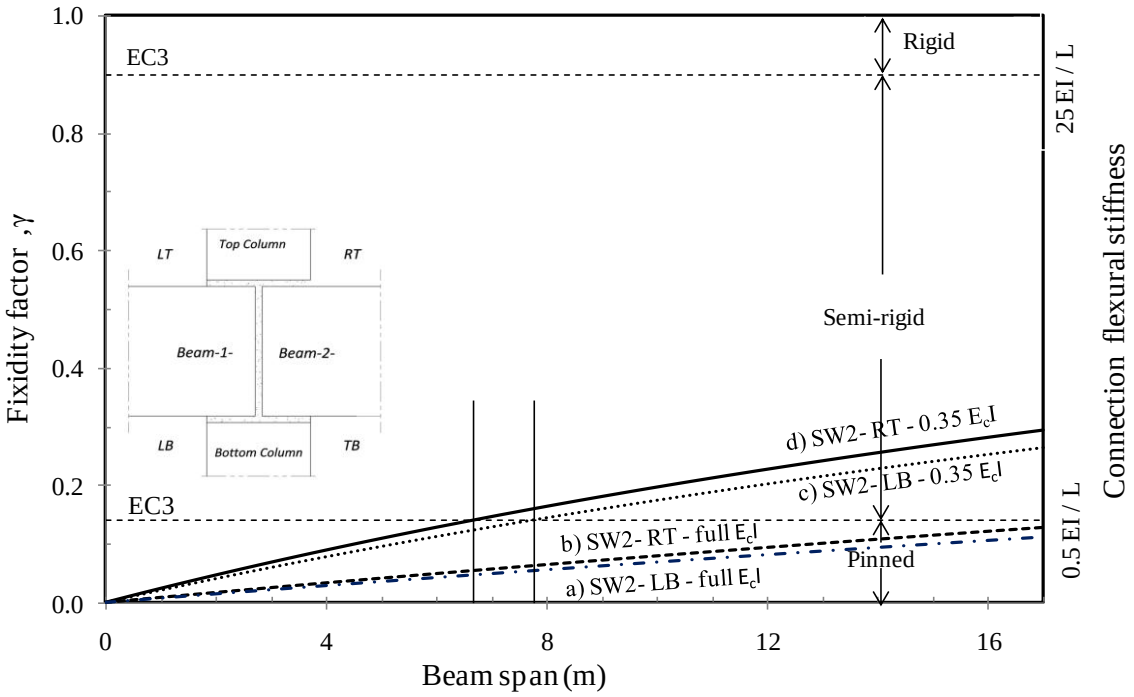

Figure 6.19 Classification of specimen SW2

6.5 Summary and conclusion

The results of two full-scale discontinuous beam-column connections (specimens SW1 and SW2) subjected to sway loads have been presented in this chapter. The main variable was the connection reinforcement detailing (details T1 and T3). Based on the experimental evidences observed in this study, the following conclusions could be summarised.

A) Using the original connection reinforcement detail (type T1):

1) The connection was neither capable of mobilising the beam sagging moment nor capable of developing the dowel action mechanism in the column dowel bars under sway loads.
2) The connection showed a poor behaviour mechanism with only a few cracks developing in the beam before the crack concentration at the column face.

3) These results showed that not bending the beam bottom bars horizontally around the column dowel bars was the reason for this behaviour.

B) Using the modified connection reinforcement detail (type T3):

1) The reinforcement detail was capable of mobilising the beam sagging moment and achieving the full dowel action capacity of the column bars under sway loads. This was achieved by bending the beam bottom bars horizontally around the column dowel bars.
2) The connection showed adequate crack propagation in the beam and the column prior to failure.
3) In spite of the crack propagation, the maximum crack widths remained at the column faces with a crack width of 3.5 mm at the LB interface and 2.5 mm at the RT interface.
4) The failure happened through yielding of the column bars under the dowel action mechanism at the LB interface.
5) The connection exhibited a low rotational stiffness under sway loads, which was found to be between 1278 kNm/rad (dowel action mechanism at the bottom of the connection) and 1610 kNm/rad (hogging bending mechanism at the top of the connection).
6) The connection is classified as pinned.
7) The proposed discontinuous precast concrete beam-column connection provided a sagging moment capacity exceeded the calculated values by 15.8%.
8) The sway measured at the top column was 378% higher than a parent rigid beam-column connection.

CHAPTER 7

FINITE ELEMENT MODELLING

7.1 Introduction

This chapter presents the finite element modelling of the semi-rigid behaviour of the discontinuous beam-column connections tested under gravity loads using the ANSYS-V11 FE analysis software package (2004). This is to provide a numerical model that can be used to investigate the effects of further parameters on the behaviour of the connection. First, the FE model was calibrated against the results of a monolithic beam-column connection tested experimentally by Ferreira (1999). Then, it was used to simulate the behaviour of the semi-rigid behaviour of specimens GR1 and GR2 tested experimentally in the current study.

The chapter presents the element types used in the FE model, material constitutive models, failure criteria, loading and boundary conditions, and non-linear analysis procedures and convergence criteria followed by the presentation and discussion of the FE modelling results. In this chapter, only the details relevant to the present analysis are presented; for further details about the basic concepts of the finite element technique, the reader could refer to a wide variety of analysis textbooks.

7.2 Finite element model

7.2.1 Concrete and grout

A 3D isoparametric, eight-node solid brick element (Solid65) was used to model the concrete and grout (Figure 7.1a), which has three degrees of freedom at each node; translations in the nodal X, Y and Z directions. For isoparametric elements, the same interpolation function (shape function) is used to define element shape coordinates (X, Y and Z) and to approximate the nodal displacements (u, v and w).

$$X = \sum_{i=1}^{8} N_i(r,s,t)\, X_i\ ; \quad Y = \sum_{i=1}^{8} N_i(r,s,t)\ Y_i\ ;\ Z = \sum_{i=1}^{8} N_i(r,s,t)\ Z_i \qquad (7.1)$$

$$u = \sum_{i=1}^{8} N_i(r,s,t)\ u_i\ ; \quad v = \sum_{i=1}^{8} N_i(r,s,t)\ v_i\ ;\ w = \sum_{i=1}^{8} N_i(r,s,t)\ w_i \qquad (7.2)$$

$$N1 = \frac{1}{8}(1-r)(1-s)(1-t);\ N2 = \frac{1}{8}(1-r)(1+s)(1-t);\ N3 = \frac{1}{8}(1-r)(1+s)(1+t)$$

$$N4 = \frac{1}{8}(1-r)(1-s)(1+t);\ N5 = \frac{1}{8}(1+r)(1-s)(1-t);\ N6 = \frac{1}{8}(1+r)(1+s)(1-t)$$

$$N7 = \frac{1}{8}(1+r)(1+s)(1+t);\ N8 = \frac{1}{8}(1+r)(1-s)(1+t) \qquad (7.3)$$

in which X, Y and Z are the global coordinates, r, s and t are the local coordinates (natural coordinates), and u, v and w are the displacement in r, s and t directions, respectively. The stress and strains are calculated and evaluated at 2 x 2 x 2 Gaussian integration points within each element. Based on the stress/strain level at these integration points, the cracking and crushing of concrete and grout are checked based on failure criteria, which will be presented in Section 7.3.1.

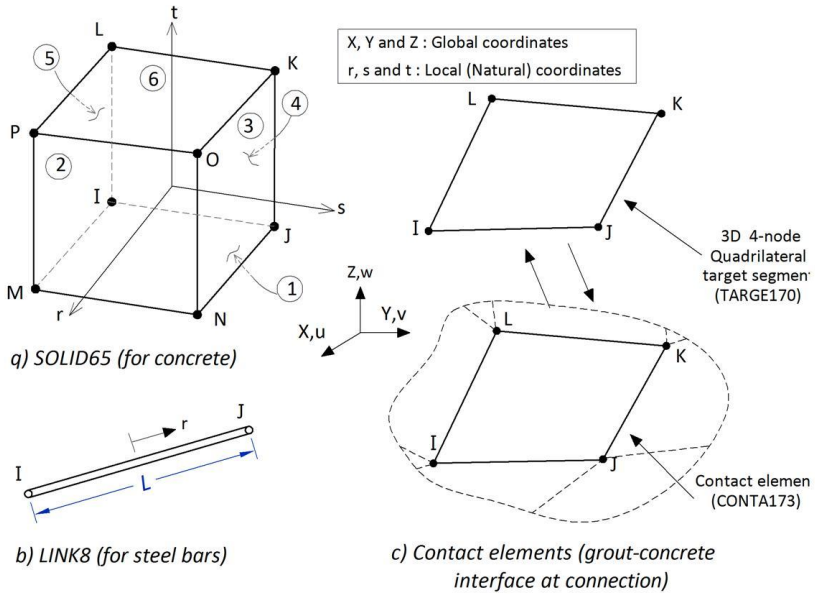

Figure 7.1 ANSYS elements used in FE modelling (ANSYS, 2004)

7.2.2 Steel

The reinforcement steel bars were modelled by using discrete bars for all types of reinforcements to reflect the effect of having many individual reinforcing bars. 3D spar element type (Link8) was used (Figure 7.1b), which has two nodes with three degrees of freedom: translations in the nodal X, Y and Z directions. This element is also capable of plastic deformation. The interpolation function is shown below.

$$u = \sum_{i=1}^{2} N_i(r)\ u_i\ ;\quad v = \sum_{i=1}^{2} N_i(r)\ v_i\ ;\ w = \sum_{i=1}^{2} N_i(r)\ w_i \tag{7.4}$$

$$N7 = \frac{1}{2}(1-r);\ \ N2 = \frac{1}{2}(1+r) \tag{7.5}$$

The reinforcement elements (Link8) are connected to the concrete element mesh nodes, meaning that the concrete and reinforcement mesh share the same nodes through shared nodes.

7.2.3 Contact

The interactions between the meshed entities were done in three ways: (i) perfect bond between steel bars and concrete/grout (Barbosa and Ribeiro, 1998; Kachlakev and Miller, 2001; Mahmood, 2007; Santhakumar et al, 2007); (ii) perfect bond between the grout and concrete in the beam trough; and (iii) using contact elements to represent the contact status between the grout and the adjoining elements (beam and columns) within the connection in specimens GR1 and GR2 (Figure 7.2). The dowel bars that are passing through the conduct sleeves within the column and beam were assumed to have perfect bond with the surrounding concrete.

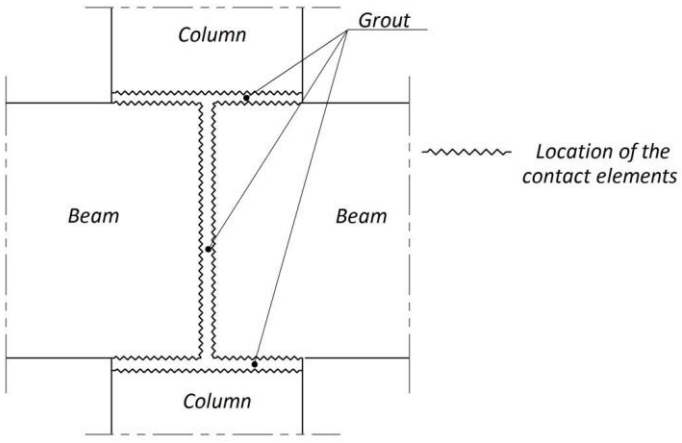

Figure 7.2 Location of contact elements in specimens GR1 and GR2

To model the contact condition between the grout and concrete, a contact element is associated with a target element (Figure 7.1c); these elements are located on the surface of 3D solids and have the same geometric characteristics as the solid elements. The target element represents a geometric entity in space that senses and

responds to contact elements moving into it. The contact element was a 3D 4-node quadrilateral contact element CONTA173, while the target element was a 3D 4-node quadrilateral contact element TARGE170. The 2 x 2 integration points (Gauss points) are the locations where the contact status is detected.

Many different algorithms have been developed to approach contact problems including penalty method, Lagrange multiplier method, and augmented Lagrangian methods. In the current FE model, the penalty contact algorithm was used to simulate the contact status through using a contact spring with a specific stiffness (contact stiffness) to establish a relationship between the contact surfaces. This algorithm modifies the stiffness matrix by adding a large term to minimise the penetration, i.e. a 'penalty' is imposed. The penalty contact algorithm requires both normal and tangent stiffness for the contact, which were taken to be equal to the stiffness of the underlying elements. The contact element has the below contact traction vector.

$$\begin{bmatrix} P_n \\ \tau_x \\ \tau_z \end{bmatrix} \tag{7.6}$$

$$P_n = \begin{cases} 0 & \text{if } U_n > 0 \\ K_n U_n & \text{if } U_n < 0 \end{cases} \tag{7.7}$$

where P_n is the normal contact pressure, K_n is the contact normal stiffness, U_n is the normal contact gap size, and τ_x and τ_Y are the contact stress in the x and y directions, respectively.

To simulate the contact behaviour in the beam-column connection, the contact surfaces between the concrete and the grout in the FE model were taken to be normal stress-free when there is a gap, and to transfer compressive stresses when there is a contact (Eq. (7.7)). The shear stresses are transferred in two forms based on whether the

contact surfaces are sticking or sliding (Eq.(7.8)). The model simulates the contact status between the concrete and grout within the precast concrete beam-column connection investigated in the current research. Based on the Coulomb friction model (ANSYS, 2004), the contact surfaces are considered as sticking as long as the equivalent shear stress 'τ_{eqv}' is less than a limited shear stress 'τ_{lim}' (

Figure **7.3**b). When τ_{eqv} exceeds τ_{lim}, the contact and target surfaces will slide relative to each other and the contact status is considered to be sliding. The sticking/sliding calculations determine when a point transitions from sticking to sliding and vice versa.

$$\tau_x = \begin{cases} K_s U_x & \text{if } \tau_{eqv} < \tau_{lim} \quad (\text{Sticking}) \\ \mu K_n U_n & \text{if } \tau_{eqv} = \tau_{lim} \quad (\text{Sliding}) \end{cases}$$
$$\tau_{eqv} = \sqrt{\tau_x^{\,2} + \tau_z^{\,2}} \;;\; \tau_{lim} = \mu P_n \qquad (7.8)$$

where K_s is the tangential contact stiffness, U_x is the contact slip distance in the x direction, and μ is the frictional coefficient.

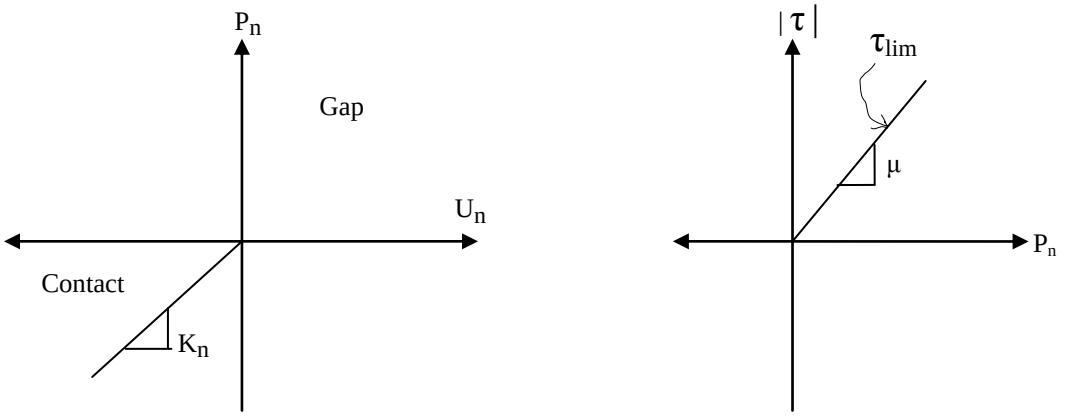

a) Normal stress transfer b) Maximum shear stress capacity in sticking status

Figure 7.3 Friction and normal stress model across contact zones

According to the PCI design hand book (PCI, 2004) the coefficient of friction between concrete and concrete in the absence of test data could be taken as 0.8, while

ACI (2008a) recommended the use of 1 as the coefficient of friction in the case of precast concrete is placed against previously hardened concrete when the interface is roughened to a full amplitude of approximately 6.4 mm. As no coefficient of friction between concrete and grout was found within the available literature, and because the concrete contact surfaces had a rough surface, the coefficient of friction between concrete and grout was taken to be 0.8 in the current study.

7.3 Material constitutive models

The correctness of the FE model of the reinforced concrete relies on the correct modelling of the stress-strain relationship of the materials (concrete and steel reinforcement), simulation of concrete cracks, and the proposed failure criteria. In order to simulate the experimental structural behaviour, the actual values of material parameters were used in the FE modelling instead of the design values.

7.3.1 Concrete and grout

The concrete and grout are quasi-brittle materials with different behaviour in compression and tension. The material constitutive model presented in this section is for concrete which is also valid for the grout considering its material properties. The concrete before cracking is assumed as linear isotropic material with the stress-strain matrix $[D_c]$ (stiffness matrix) of concrete being defined in Eqs. (7.9) and (7.10), in which $\{\sigma\}$ is the stress vector, $\{\varepsilon\}$ is the strain vector, E_c is the modulus of elasticity of concrete, and ν is the Poisson's ratio of concrete, which is taken to be equal to 0.2.

$$\{\sigma\} = [D_c]\ \{\varepsilon\}$$

$$\{\sigma\}^T = \{\sigma_x \quad \sigma_y \quad \sigma_z \quad \tau_{xy} \quad \tau_{xz} \quad \tau_{yz}\}$$

$$\{\varepsilon\}^T = \{\varepsilon_x \quad \varepsilon_y \quad \varepsilon_z \quad \gamma_{xy} \quad \gamma_{xz} \quad \gamma_{yz}\} \qquad (7.9)$$

$$[D_C] = \frac{E_c}{(1+\nu)(1-2\nu)} \begin{bmatrix} (1\text{-}\nu) & \nu & \nu & 0 & 0 & 0 \\ \nu & (1\text{-}\nu) & \nu & 0 & 0 & 0 \\ \nu & \nu & (1\text{-}\nu) & 0 & 0 & 0 \\ 0 & 0 & 0 & \frac{(1-2\nu)}{2} & 0 & 0 \\ 0 & 0 & 0 & 0 & \frac{(1-2\nu)}{2} & 0 \\ 0 & 0 & 0 & 0 & 0 & \frac{(1-2\nu)}{2} \end{bmatrix} \quad (7.10)$$

Eq. (7.10) is assumed to be valid before development of crack in tension, and up to 30% of the maximum strength in compression (Figure 7.4). Beyond that, the stiffness matrix is modified to simulate the presence of the cracks in concrete.

In tension, the concrete is modelled to behave linearly up to a limiting tensile strength (Figure 7.4), which was taken to be equal to the flexural tensile strength ($f_{ct,fl}$). A crack occurs when the principal tensile stress in any direction exceeds this limit and no tensile stress is transmitted across the crack in the subsequent load steps, where the concrete behaves as an orthotropic material. The crack is assumed to initiate at element integration points, in a plane normal to the principal stress direction, and the elastic modulus in the direction parallel to the principal stress is set to zero for the following load steps, without strain softening.

In order to prevent distorted crack patterns for the post-cracking loading stages and for a more representing FE model, retaining shear stiffness is used across the cracking plane. The shear transfer coefficient 'β' represents the condition of the crack face and the re-tension of the shear stiffness in cracked concrete; β value of 0 represents a smooth crack (no shear transfer), and 1.0 represents a rough crack face (full shear transfer). In the current study, β was taken as 0.2 (β_t) for open cracks, and as 0.7 (β_c) for closed cracks. The value of β_t used in previous studies varied between 0.2 and 0.3 (Mahmood, 2007; Wolanski, 2004). It was found that when β_t dropped below 0.2, convergence problems occurred (Kachlakev and Miller, 2001).

In the case of cracking in one direction, without tensile stress relaxation, the stiffness matrix of concrete with respect to principal stress directions with x axis perpendicular to the crack face is given in Eq. (7.11).

$$[D_c] = \frac{E}{(1+\nu)} \begin{bmatrix} 0 & 0 & 0 & 0 & 0 & 0 \\ 0 & \frac{1}{(1-\nu)} & \frac{\nu}{(1-\nu)} & 0 & 0 & 0 \\ 0 & \frac{\nu}{(1-\nu)} & \frac{1}{(1-\nu)} & 0 & 0 & 0 \\ 0 & 0 & 0 & \frac{\beta_t}{2} & 0 & 0 \\ 0 & 0 & 0 & 0 & \frac{1}{2} & 0 \\ 0 & 0 & 0 & 0 & 0 & \frac{\beta_t}{2} \end{bmatrix} \quad (7.11)$$

When the crack closes, the compressive stresses normal to the crack plan are transmitted and the shear transfer coefficient at compressive (β_c) is used, as shown in Eq. (7.12).

$$[D^s] = \frac{E_c}{(1+\nu)(1-2\nu)} \begin{bmatrix} (1\text{-}\nu) & \nu & \nu & 0 & 0 & 0 \\ \nu & (1\text{-}\nu) & \nu & 0 & 0 & 0 \\ \nu & \nu & (1\text{-}\nu) & 0 & 0 & 0 \\ 0 & 0 & 0 & \beta_c\frac{(1-2\nu)}{2} & 0 & 0 \\ 0 & 0 & 0 & 0 & \frac{(1-2\nu)}{2} & 0 \\ 0 & 0 & 0 & 0 & 0 & \beta_c\frac{(1-2\nu)}{2} \end{bmatrix} \quad (7.12)$$

When the cracking is in two directions, $[D_c]$ is expressed as given by Eq. (7.13), and when the cracks reclose in both directions, $[D_c]$ is expressed also by Eq. (7.12).

$$[D_c] = E \begin{bmatrix} 0 & 0 & 0 & 0 & 0 & 0 \\ 0 & 0 & 0 & 0 & 0 & 0 \\ 0 & 0 & 1 & 0 & 0 & 0 \\ 0 & 0 & 0 & \frac{\beta_t}{2(1+\nu)} & 0 & 0 \\ 0 & 0 & 0 & 0 & \frac{\beta_t}{2(1+\nu)} & 0 \\ 0 & 0 & 0 & 0 & 0 & \frac{\beta_t}{2(1+\nu)} \end{bmatrix} \quad (7.13)$$

7.3.1.1 Compression stress-strain relation for concrete

To simulate the non-linear elasticity of concrete under compression, multi-linear isotropic stress-strain curve for concrete under compression, Eqs. (7.14) to (7.17) were used, which were originally proposed by Desayi (1964) and were used by many researchers (Ibrahim and Huda, 2009; Mahmood, 2007; Santhakumar et al, 2007).

$$f = E_c \varepsilon \quad ; \text{for} \quad 0 \le f \le 0.3 f_c \tag{7.14}$$

$$f = \frac{E_c \epsilon}{1+\left(\frac{\epsilon}{\epsilon_{co}}\right)} \quad ; \text{for} \quad 0.3 f_c < f \le f_c \tag{7.15}$$

$$f = f_c \quad ; \text{for} \quad \varepsilon > \varepsilon_{co} \tag{7.16}$$

$$\epsilon_{co} = \frac{2 f_c}{E_c} \tag{7.17}$$

where f is stress at any strain 'ε', and ε_{co} is the strain at the ultimate compressive strength 'f_c', which was taken to be equal to the cylinder compressive strength. The simplified stress-strain curve used for concrete was constructed by connecting eight points with straight lines (Figure 7.4). From zero stress up to 0.3 f_c (point 1), the relation is taken as linear (Eq. (7.14)), while points 2 to 8 were constructed using Eq. (7.15). After point 8, the concrete is assumed to behave as perfectly plastic.

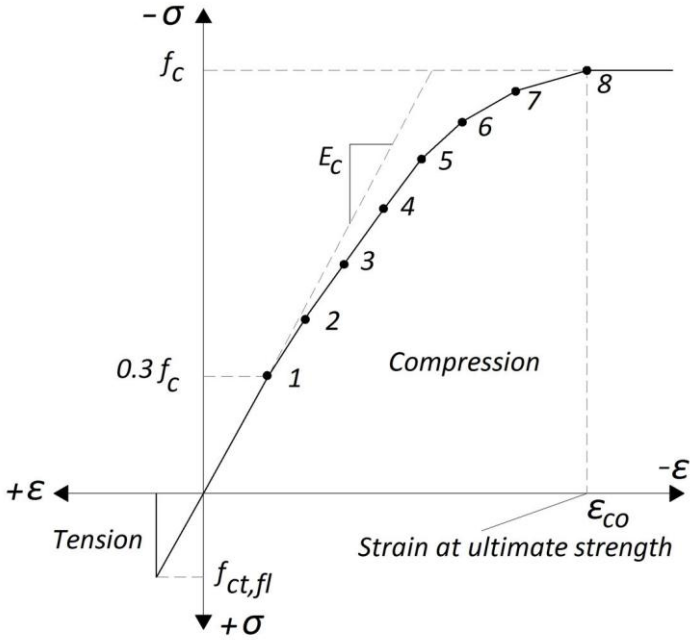

Figure 7.4 Stress-strain curve for concrete

7.3.1.2 Failure surface model for concrete

The cracking and crushing of the concrete are determined from the stress and strain evaluation at the integration points based on a failure surface for unconfined concrete under a multiaxial stress state (William and Warnke, 1975), as below.

$$\frac{F}{f_c} - S \geq 0 \qquad (7.18)$$

where:

F: function of the principal stress in x, y and z direction (σ_{xp}, σ_{yp} and σ_{zp})

f_c: uniaxial compressive strength (taken to be equal to the cylinder compressive strength)

F : failure surface defined by terms of σ_{xp}, σ_{yp} and σ_{zp} and the strength properties of concrete including the uniaxial compressive strength (f_c) and the tensile strength (taken to be equal to the flexural tensile strength, $f_{ct,fl}$).

For a state of stress that is biaxial or nearly biaxial, three failure surfaces are shown as a projection on the plane of the most significant non-zero principal stress in x and y directions (σ_{xp} and σ_{yp}). As shown in Figure 7.5, the failure mode is a function of the sign of principal stress in z direction (σ_{zp}) in the compression-compression zone. This gives two possibilities to the failure modes: (i) crushing or cracking in the case of $\sigma zp > 0$; (ii) crushing in the case of $\sigma_{zp} \leq 0$.

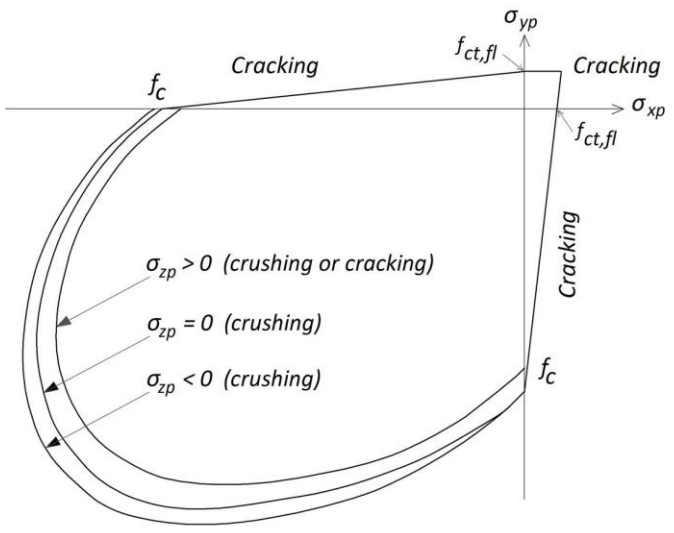

Figure 7.5 3D failure surfaces in biaxial or nearly biaxial state of stress

7.3.2 Steel reinforcement

In the finite element model, the steel reinforcement behaviour was taken as elastic-perfectly plastic material, and identical in both tension and compression (Figure 7.6). This model requires the yield stress 'f_y', modulus of elasticity 'E_s'. The reinforcement was assumed to be perfectly connected to the surrounding concrete (Barbosa and Ribeiro, 1998; Hasan, 1994; Ibrahim and Huda, 2009; Mahmood, 2007).

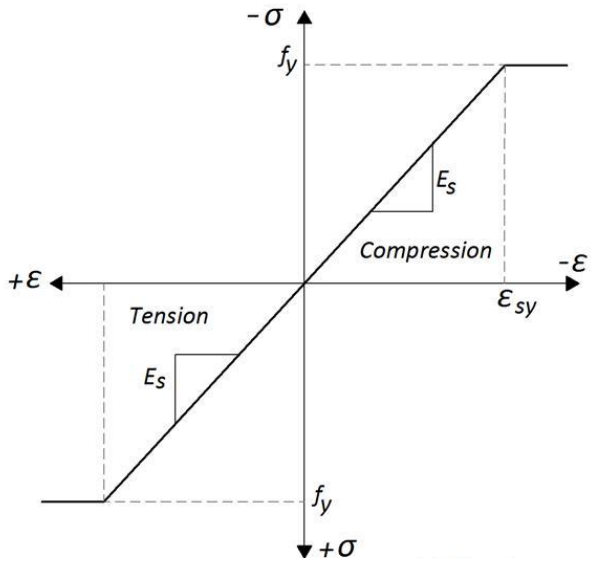

Figure 7.6 Stress-strain curves for steel reinforcement

The stiffness matrix [D^s] of the steel bar element (link8) is given in Eq. (7.19), in which, A is the element cross sectional area, E_s is the modulus of elasticity of steel, and L is the element length.

$$[D^s] = \frac{A\,E_s}{L}\begin{bmatrix} 1 & 0 & 0 & -1 & 0 & 0 \\ 0 & 0 & 0 & 0 & 0 & 0 \\ 0 & 0 & 0 & 0 & 0 & 0 \\ -1 & 0 & 0 & 1 & 0 & 0 \\ 0 & 0 & 0 & 0 & 0 & 0 \\ 0 & 0 & 0 & 0 & 0 & 0 \end{bmatrix} \quad (7.19)$$

7.4 Finite element discretisation

The FE modelling included three beam-column connections. The first one is a monolithic beam-column connection tested by Ferreira (1999), which is shown in Figure 7.7. The other two specimens are the two precast concrete beam-column specimens GR1 and GR2 (Figure 4.1a, Figure 4.3, and Figure 4.5), which have been investigated experimentally in the current study.

To obtain the mesh, first the corners of the concrete macro-elements and the ends of the steel bars were defined and, by using them as reference points, 3D blocks (to represent concrete and grout) and 1D lines (to represent steel bars) were constructed. These blocks and lines were automatically meshed in such a way as to ensure that the concrete, grout and steel bar nodes coincide with each other. The FE mesh details of the three specimens modelled in the current study are shown in Figures 7.8 to 7.10.

The size of the element used in the FE modelling are shown in Figure 7.11, while the total number of elements, number of elements of each type, and the total number of nodes are listed in Table 7.1. One element size was used in specimen M1 (Figure 7.11a), while for the two precast concrete specimens (GR1 and GR2) had different element sizes at the connection zone due to the existence grout layers (Figure 7.11b).

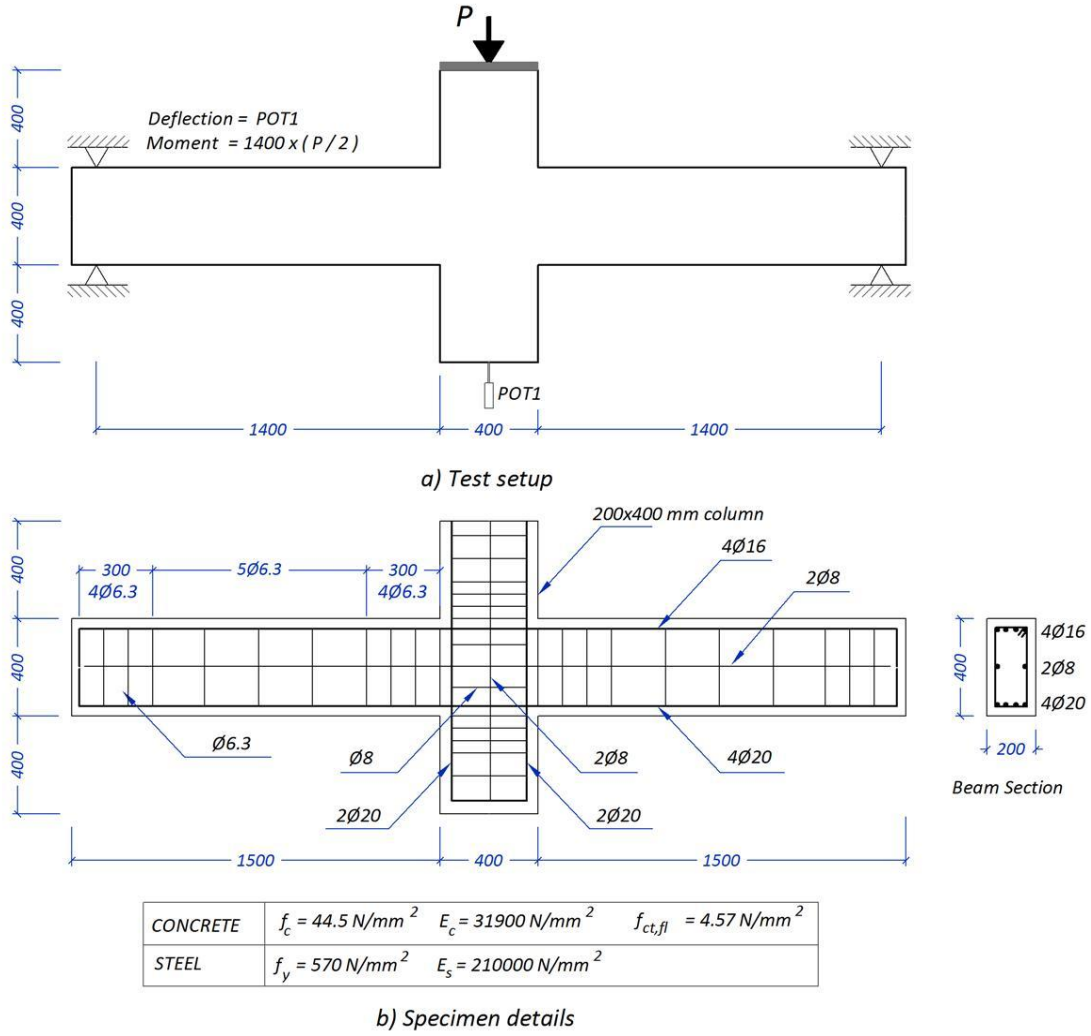

Figure 7.7 Geometry of beam-column specimen (M1) tested by Ferreira (1999)

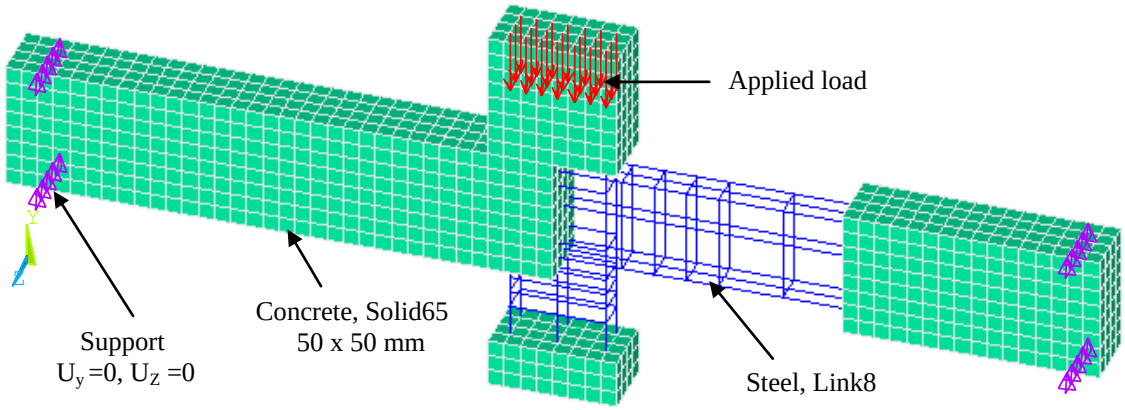

Figure 7.8 Finite element mesh of specimen M1
(some of Solid65 elements are removed to illustrate the reinforcement details)

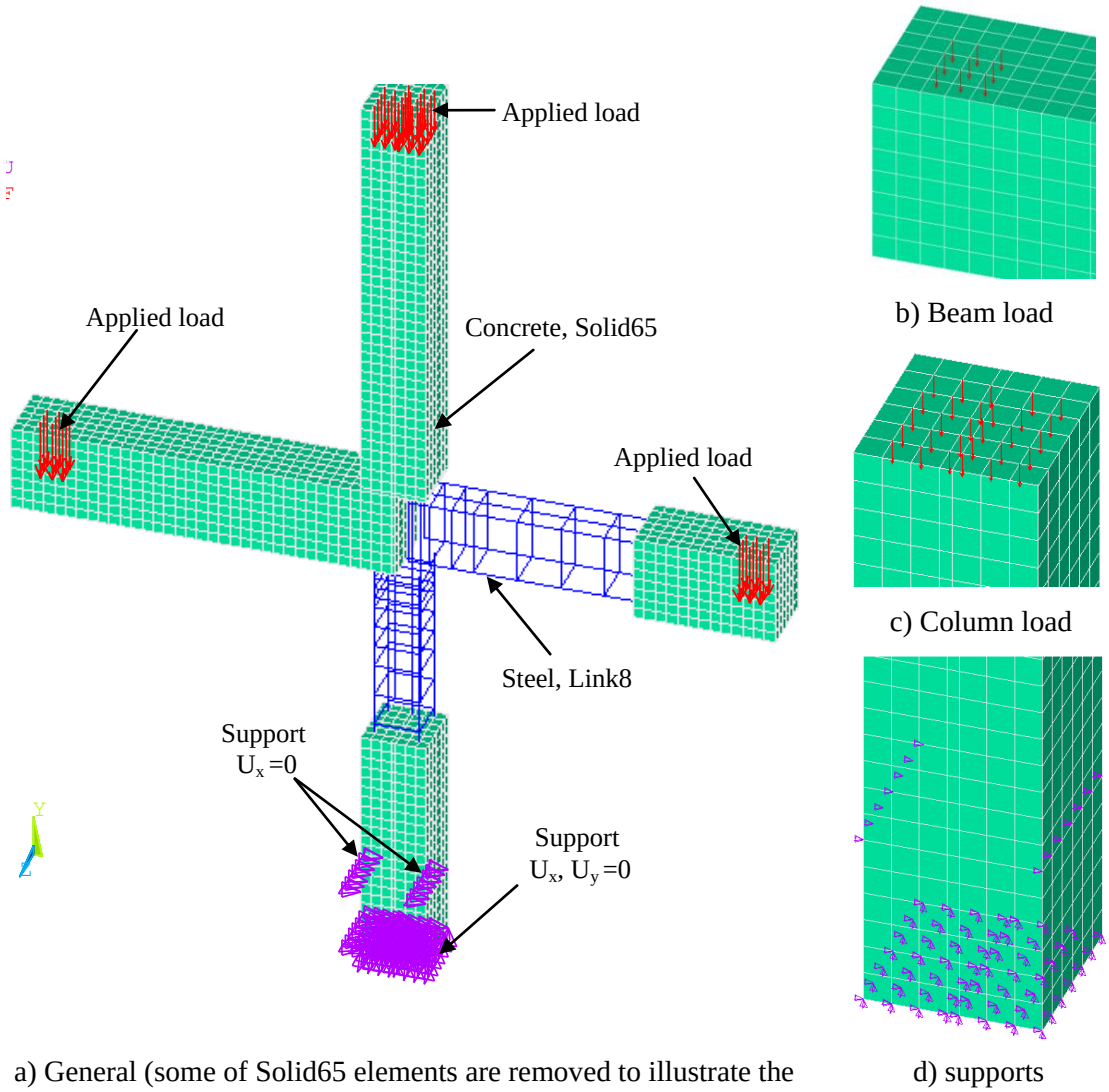

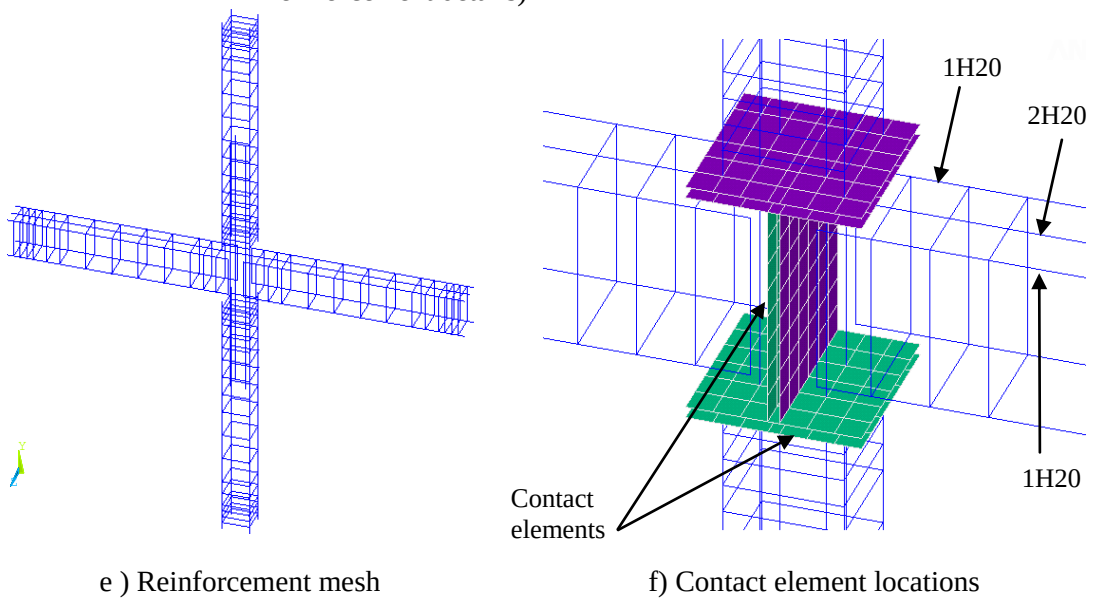

Figure 7.9 Finite element mesh of specimen GR1

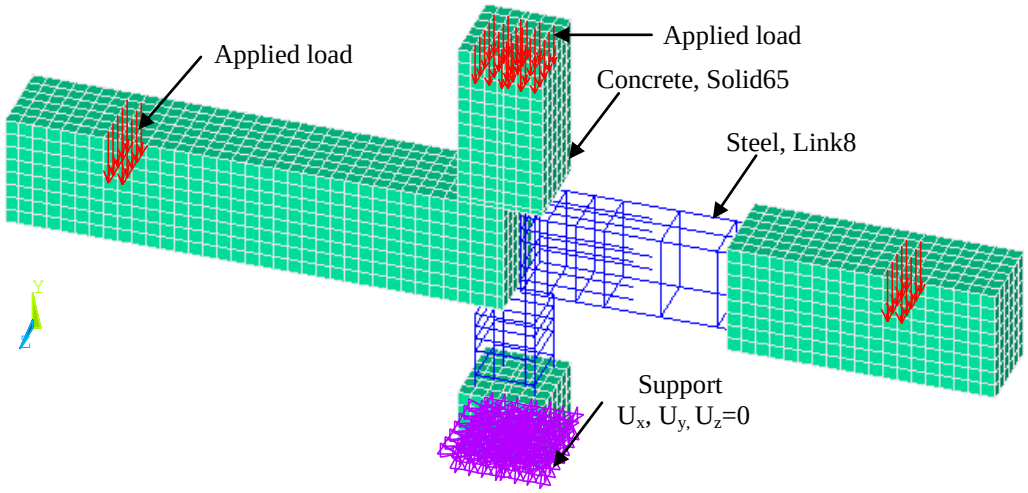

a) General (some of Solid65 elements are removed to illustrate the reinforcement details)

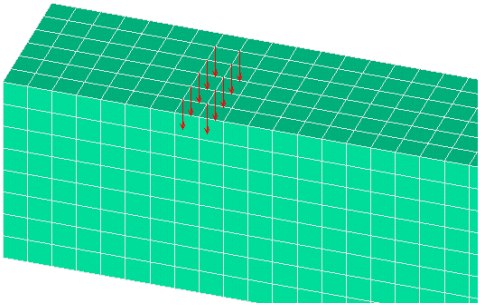

b) Beam load

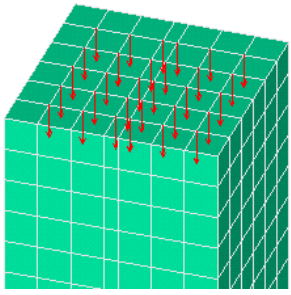

c) Column load

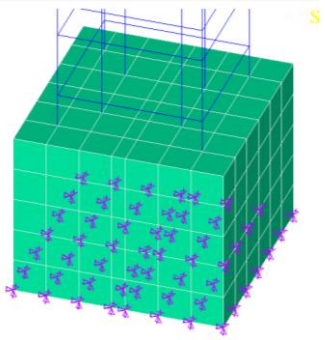

d) Lower column support

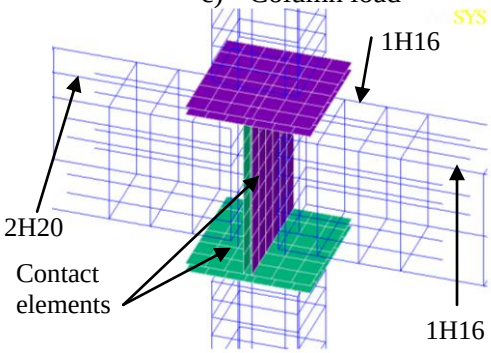

e) Contact element location

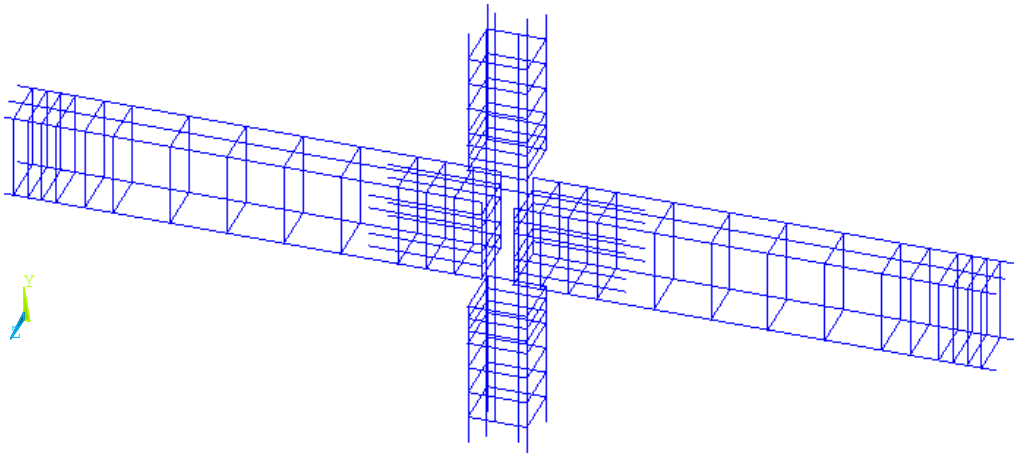

f) Reinforcement mesh

Figure 7.10 Finite element mesh of specimen GR2

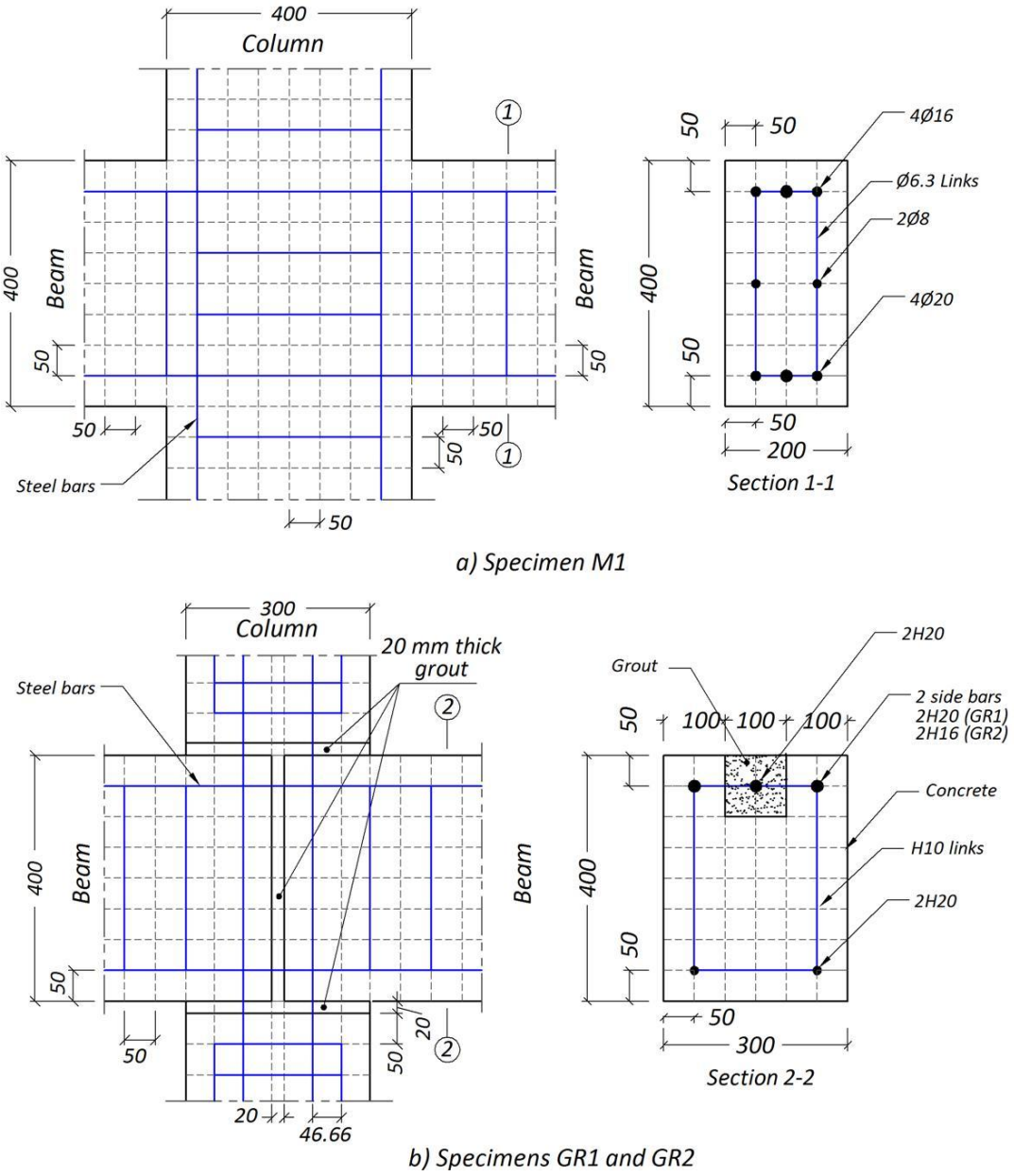

Figure 7.11 Element sizes in the FE mesh of specimens M1, GR1 and GR2

Table 7.1 FE mesh details of specimens M1, GR1 and GR2

Test	Number of elements					Number of Nodes
	TOTAL	SOLID65	LINK8	TARGE170	CONTA173	
M1	3891	2688	1203	------	------	3915
GR1	9315	6768	2019	264	264	11574
GR2	6571	4500	1543	264	264	7794

7.5 Boundary conditions and loading

The loads in the experiments were applied through two sizes of steel plates: (i) a size equal to the column cross-section in the case of column axial load (all specimens), and (ii) 150 x 150 mm steel plate in the case of beam loads (specimens GR1 and GR2). In the FE model, the loads were applied to the model through nodes within an area smaller than the area of the plates, where no loads were applied through the nodes at the edges of the steel plates. No steel plates were provided in the FE model, as no stress concentration problems occurred.

Regarding the boundary conditions, in the FE model of specimen M1, a single line support (preventing the vertical movement) was used at each of the steel plate centrelines (Figure 7.8). In the other two specimens (GR1 and GR2), the whole lower column end was prevented from vertical movement and horizontal movement (pinned); in addition, in specimen GR1, two single line supports ($U_x = 0$) were provided at two sides of the lower column (Figure 7.9d)

7.6 Non-linear solution procedure

The non-linear analysis of reinforced concrete is based on the Newton-Raphson solution procedure, where the total load of the finite element model is applied in a series of load increments (F_i, F_{1+1}, ... F_n), as shown in Figure 7.12. For each load increment, the equilibrium is satisfied through an iteration procedure; the stiffness matrix for the first iteration is adjusted based on the stress level in the previous load increments; then, the stiffness matrix is updated in every iteration. The iteration procedure continues until the convergence criteria are satisfied. The converged solution (within a load increment) is considered to be in equilibrium within some tolerance 'T_C'.

The convergence criteria used in this study was based on the force using SRSS norm, which is the 'Square Root of the Sum of the Square values of the terms'. The default tolerance in ANSYS is 0.005 for force checking. However, it was found that the convergence for non-linear behaviour of reinforced concrete solution models was difficult to obtain using the default limits (Kachlakev and Miller, 2001; Perera, 2005; Zhang, 2004). Therefore, it was suggested to increase the tolerance limit to a maximum of five times the default tolerance limits, which was used also in this study.

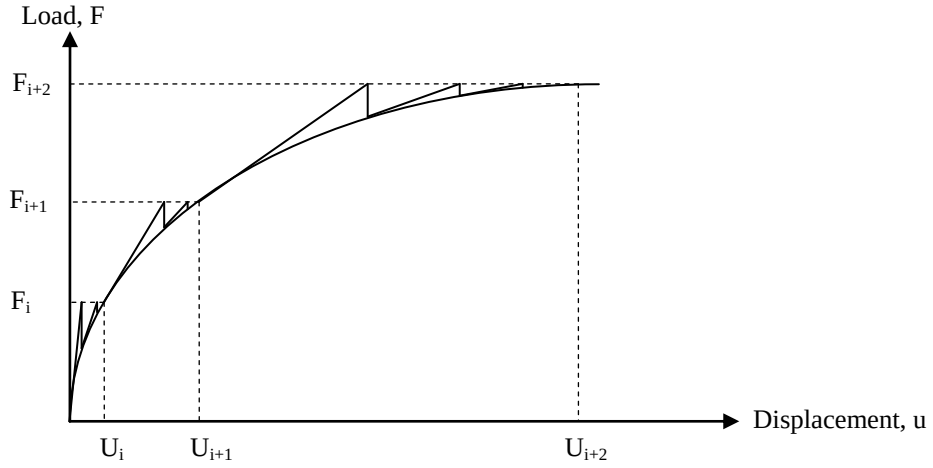

Figure 7.12 Newton-Raphson non-linear solution procedure

At each load increment (Figure 7.13), after the first iteration, the out-of-balance force vector F^o is calculated based on the difference between the restoring force vector 'F^r' and the applied force vector 'F^a'. F^r is calculated based on the element stresses. In the next iteration, F^o is applied and a linear analysis is performed using the latest stiffness matrix, and the convergence criterion is checked again. If the convergence criterion is satisfied compared to a specified tolerance, the solution will go to the next load increment; otherwise, a new F^o is calculated and applied again. The convergence is reached when Eq. (7.20) is satisfied (ANSYS, 2004).

$$\sqrt{\sum (F^o)^2} \quad < \quad T_c \ \sum \text{Abs} \ (F^a) \tag{7.20}$$

In the current study, the iteration limit was set to be 100 per load sub-step, and the load steps ranged between 5 to 0.5 kN. The failure was assumed to happen when the iteration limit was reached at the lowest load step (0.25 kN) before the equilibrium tolerance was satisfied.

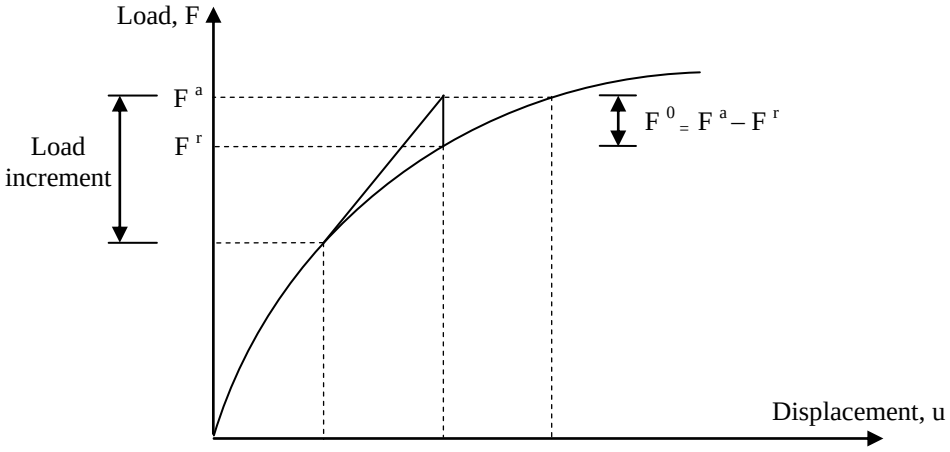

Figure 7.13 Convergence checking for force within load increment

7.7 FE modelling results

7.7.1 Monolithic beam-column specimen

As the beam-column connection investigated in the current study contains many discontinuity interfaces that do not exist in monolithic connections, it was necessary to validate the FE model against a monolithic connection first. For this purpose, the monolithic cruciform specimen tested experimentally by Ferreira (1999) was modelled.

The results showed that the FE model agrees well with experimental results with respect to the deflection in the elastic range and the yielding moment capacity 'M_y' (Figure 7.14). The numerical value of M_y is only 2.2 % higher than the experimental one, and the numerical deflection at 325 kN load (the experimental M_y) is 12.6% less than the experimental one. The difference in the deflection is attributed to the assumed perfect bond between concrete and reinforcement, which led to the overall stiffness in the FE model being higher than the actual beam stiffness. Considering the above results,

it could be stated that the 50 x 50 x 50 mm element size is adequate for modelling beam-column connection under flexure bending.

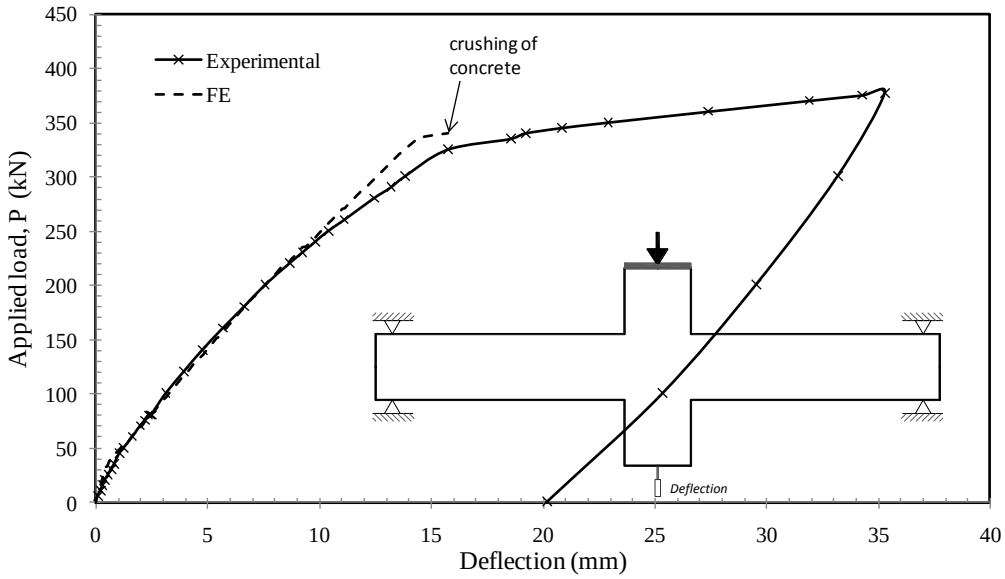

Figure 7.14 Load vs. deflection in specimen M1 (experimental results and FE results)

7.7.2 Precast beam-column specimens

Based on the preliminary FE modelling, a 50 mm element size was chosen to be used as the maximum element size in the meshing of the precast specimens (GR1 and GR2). The FE modelling (FE model 1) results compared with the experimental results are presented in this section for specimen GR2, while for specimen GR1, the comparison could be found in Appendix G.

7.7.2.1 Specimen GR2

The comparison includes deflections, beam-column relative rotations, concrete and steel bar strains, and the crack patterns, as shown in Figures 7.15 to 7.20. The comparison shows a good agreement in the early loading stage; however, there is a discrepancy prior to yielding and the FE model failed to predict the behaviour at the yielding stage and the ultimate load, as could be seen in Table 7.2. In the elastic region, the FE model anticipated well the locations of the first cracks (Figure 7.19) and the crack pattern at yielding stage (Figure 7.20). Further results of the specimen with

respect to the contact status between the grout and concrete, contact stresses, sliding and gap distances within the connection are presented in Section 7.8.2.3.

Table 7.2 FE modelling results of specimens GR1 and GR2

Specimen	Ultimate moment, M_u (kNm)		
	Experimental*	FE model	Ratio (%)
GR1	138.25	188.7	136.5
GR2	152.35	195.7	128.5
* The experimental moments are the average of beam 1 and beam 2 sides			

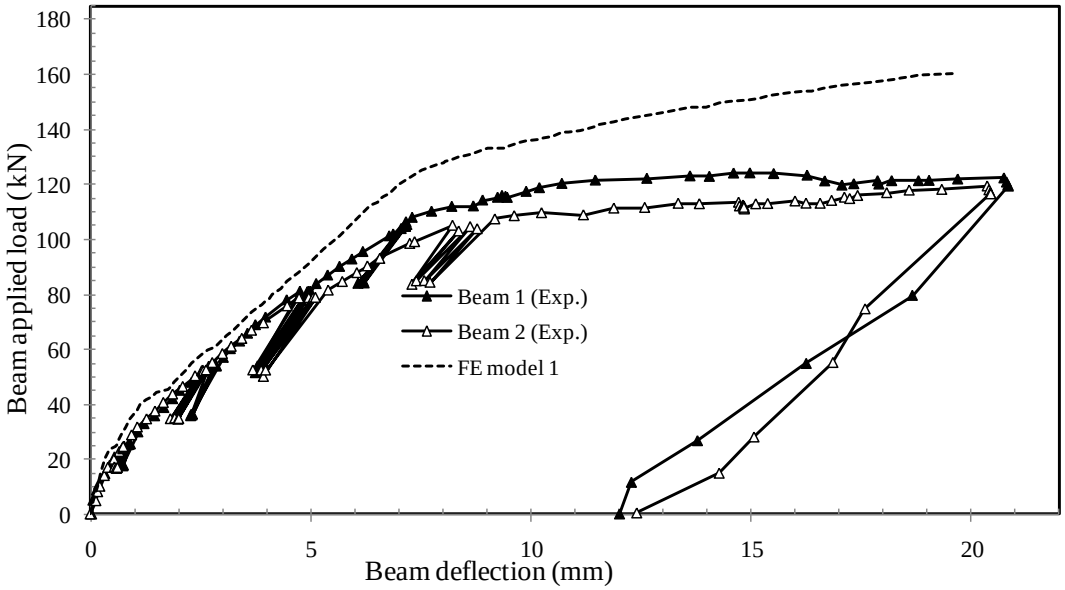

Figure 7.15 Load vs. deflection in specimen GR2
(experimental results and FE model 1 results)

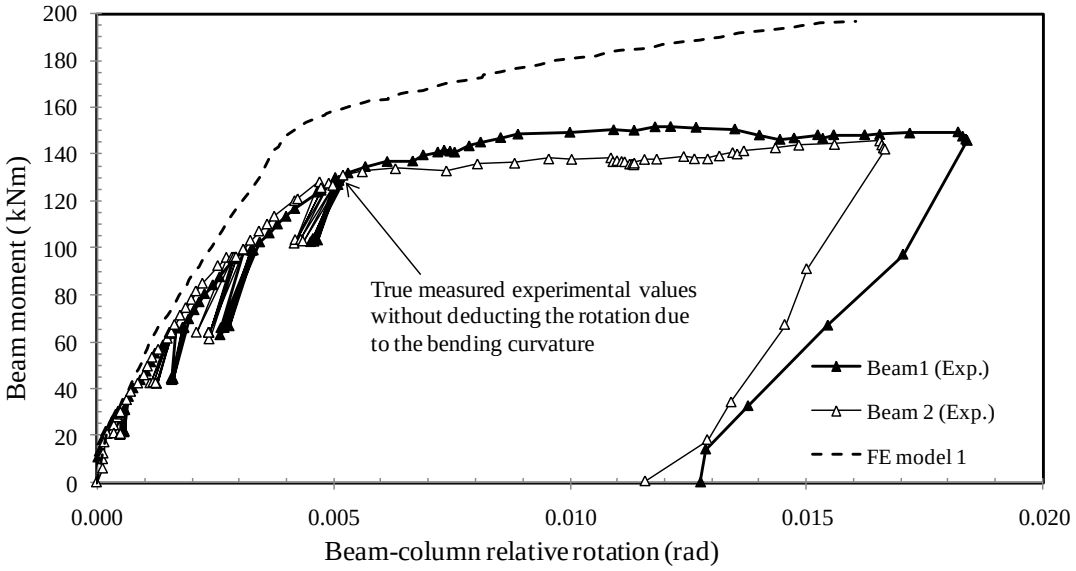

Figure 7.16 Beam moment vs. relative beam-column rotation in specimen GR2
(experimental results and FE model 1 results)

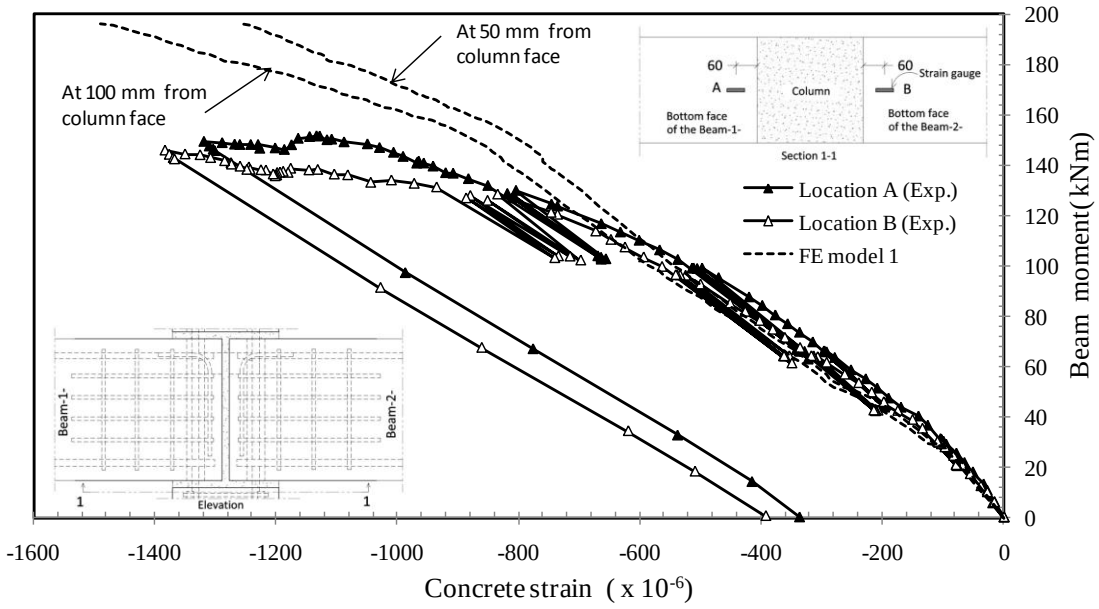

Figure 7.17 Beam moment vs. concrete strain in specimen GR2
(experimental results and FE model 1 results)

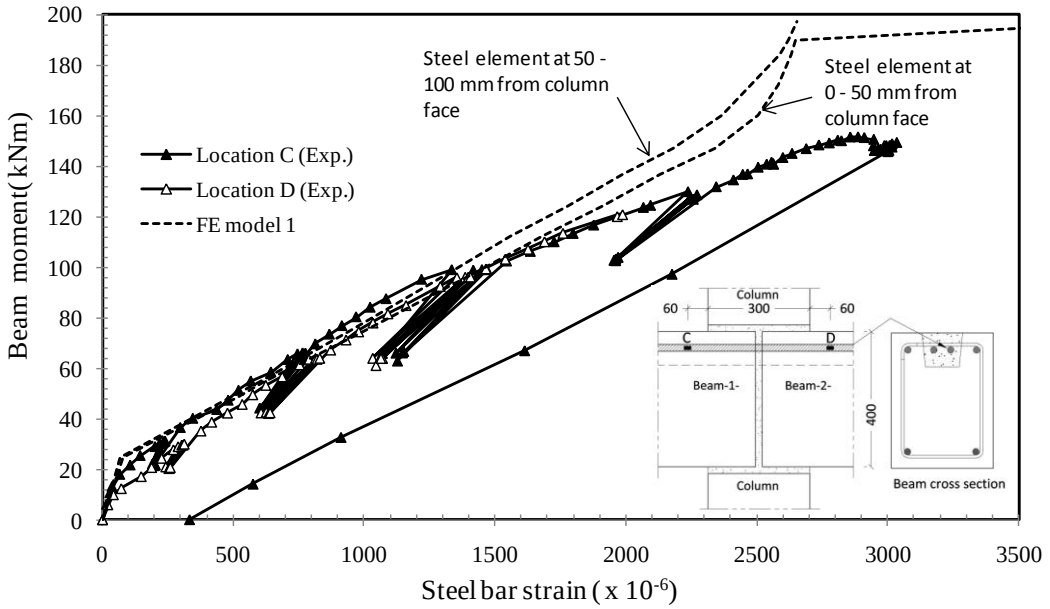

Figure 7.18 Beam moment vs. steel strain in specimen GR2
(experimental results and FE model 1 results)

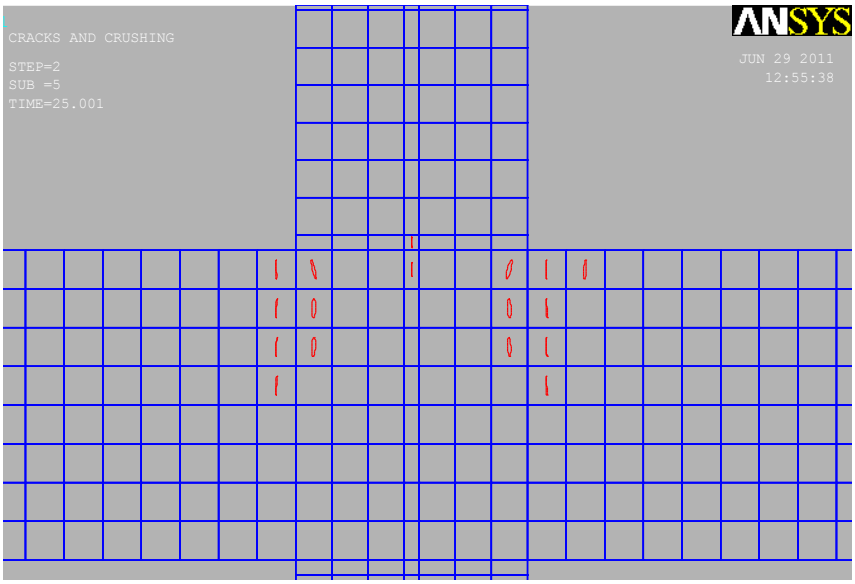

a) Numerical (FE model 1) at 25 kN beam load

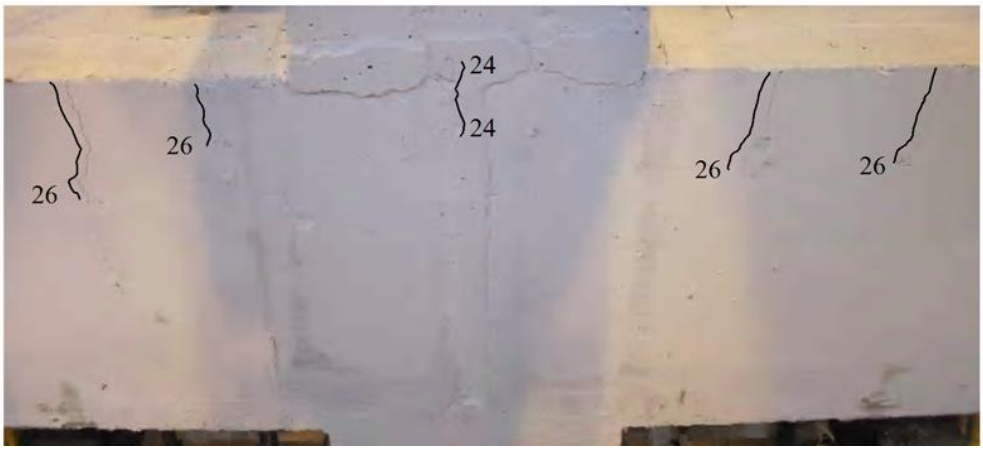

b) Experimental

Figure 7.19 Comparison of early crack pattern in specimen GR2

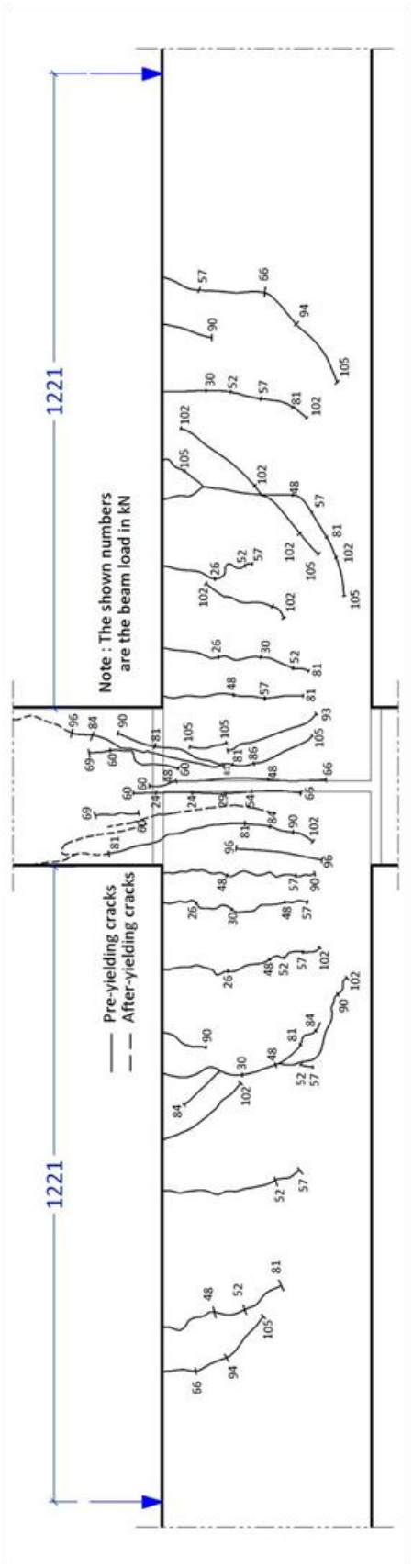

a) Experimental at yielding load and at failure

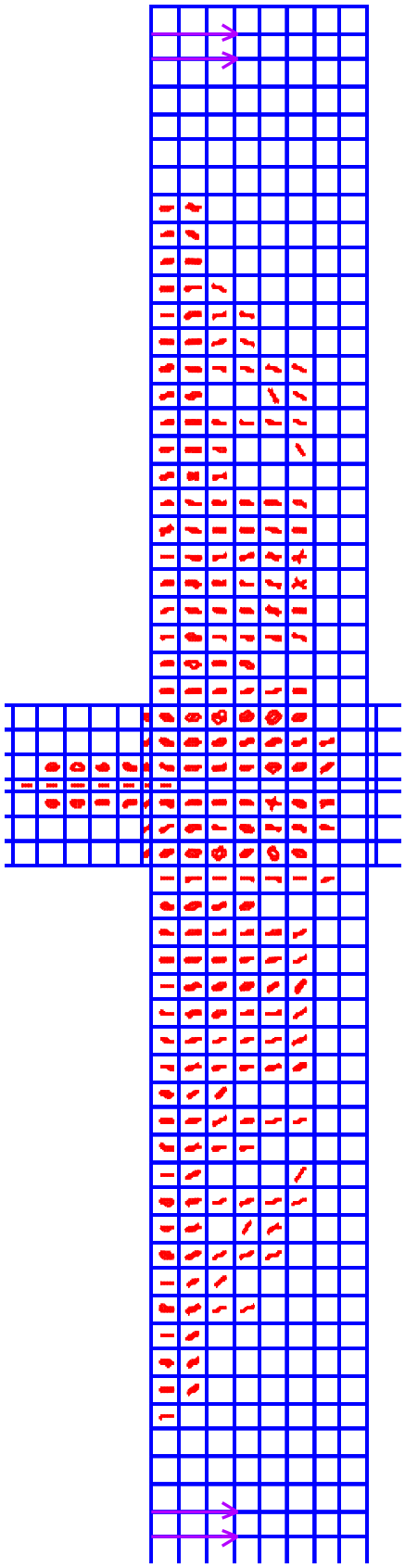

b) Numerical (FE model 1) at 116.77 kN beam load

Figure 7.20 Comparison of crack patterns at yielding load level in specimen GR2

7.7.2.2 Discussion of results

The FE model 1 could not anticipate the behaviour close to the yielding moment and could not predict the failure mode and consequently the ultimate moment capacity of the beam (specimens GR1 and GR2). To investigate the weakness of the model, it is essential to identify the influential features of the connection that might not have been modelled accurately, which are listed below.

a) The bent-ends of the 2H20 side bars at the top of the beam (specimen GR1, Figure 7.21) were very close to the corrugated sleeves, which were wrapped with plastic tapes to prevent any leakage of concrete to the sleeves during construction of the beam. Also, the perimeters of the sleeves themselves are potential locations for cracks. These two features weaken the bond of the bent bars at this region, and therefore it is believed that the internal part of the 2H20 is not contributing to either the beam stiffness or the ultimate moment capacity of the beam.

b) The interface between the perimeters of the corrugated sleeves and the concrete at the beam-ends (specimens GR1 and GR2, Figure 7.21) are potential locations for cracks and weaknesses in the connection at the yielding stage. These interfaces are necessary to be modelled using horizontal springs with stiffnesses simulating the behaviour.

c) The end of the non-continuous 2H16 side bars at the top of the beam (specimen GR2, Figure 7.21); this feature is similar to point i with one difference being that the cut end is overlapped with the L-shaped H10 steel bars. This aspect is believed to have the same effects as point i.

Due to the lack of calculation models for the above components, within the available sources, they were not incorporated in the FE model 1. To investigate the effects of point c, the 2H16 side bars in specimen GR2 were modelled in a new FE model (called FE model 2) assuming that they are continuous up the column face only and they have no overlapped length with the L-shaped H10 steel bars (Figure 7.22).

The comparison of the FE model 2 with the original model (FE model 1) is shown in Figure 7.23 considering the deflection. It is obvious that ignoring the internal parts of the 2H16 side bars adjusted the numerical behaviour to be closer to the actual behaviour and resulted in a lower yield point (point P1 in Figure 7.23) in the continuous 2H20 steel bars; however, it did not capture the behaviour after the first yielding. According to the experimental observations, after point P1, the weakness at the interfaces between the corrugated sleeves and the surrounding concrete at the beam-ends (point b in Figure 7.21) controlled the behaviour and forced the failure to happen there without a significant increase in the moment capacity.

To examine the behaviour of the beam-column connection modelled in the FE model 2, the stress in the steel bars is shown in Figure 7.24 at three different loading stages. These stages are: (P1) yielding of the continuous 2H20 top bar (Figure 7.24a); (P2) yielding of the 1st layer of the U-shaped links (Figure 7.24b); and (P3) yielding of the 2nd layer of the U-shaped links (Figure 7.24c). These three loading stages are shown graphically on the load-deflection curve in Figure 7.23.

Figure 7.24 reveals that after point P1 there was an increase in the stress in both the U-shaped horizontal beam links and the top column steel links (Figure 7.24b and 7.22c). This indicates that there was a bridge for transferring tensile stresses between

the U-shaped links and the top column links in the FE model, which did not happen experimentally as explained above.

From the above discussion, it could be stated that the current FE modelling could not capture the correct behaviour at the first yield point and therefore it does not offer the facility required to determine the ultimate moment capacity of the connection. However, the FE model provided valuable facts regarding the critical components in the connection that need to be incorporated in the FE model.

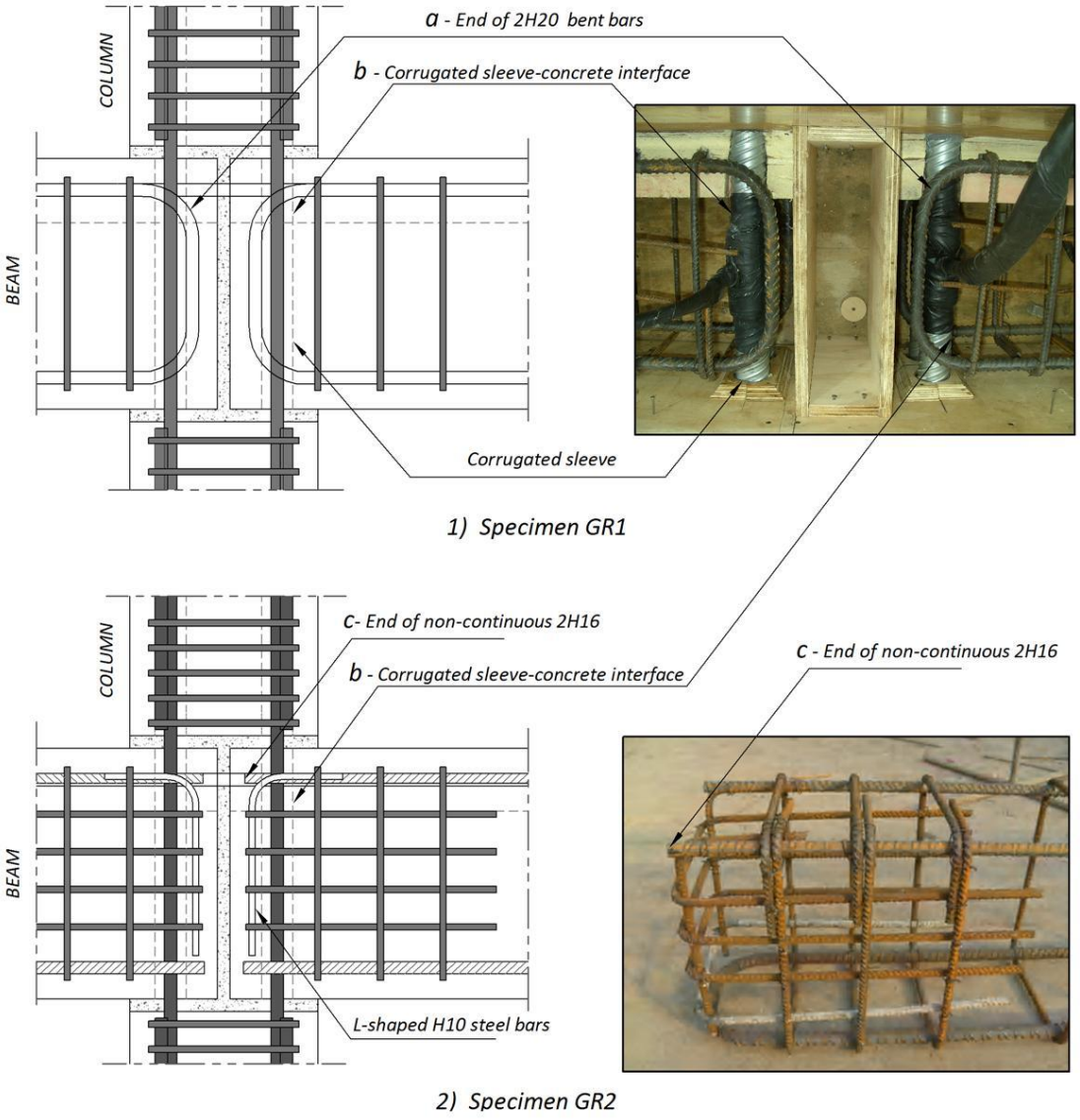

Figure 7.21 Critical connection components in FE modelling of specimens GR1 and GR2

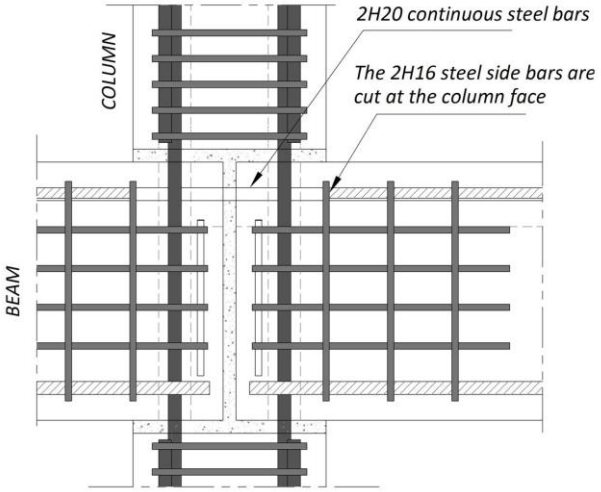

Figure 7.22 Proposed FE model 2 for Specimen GR2

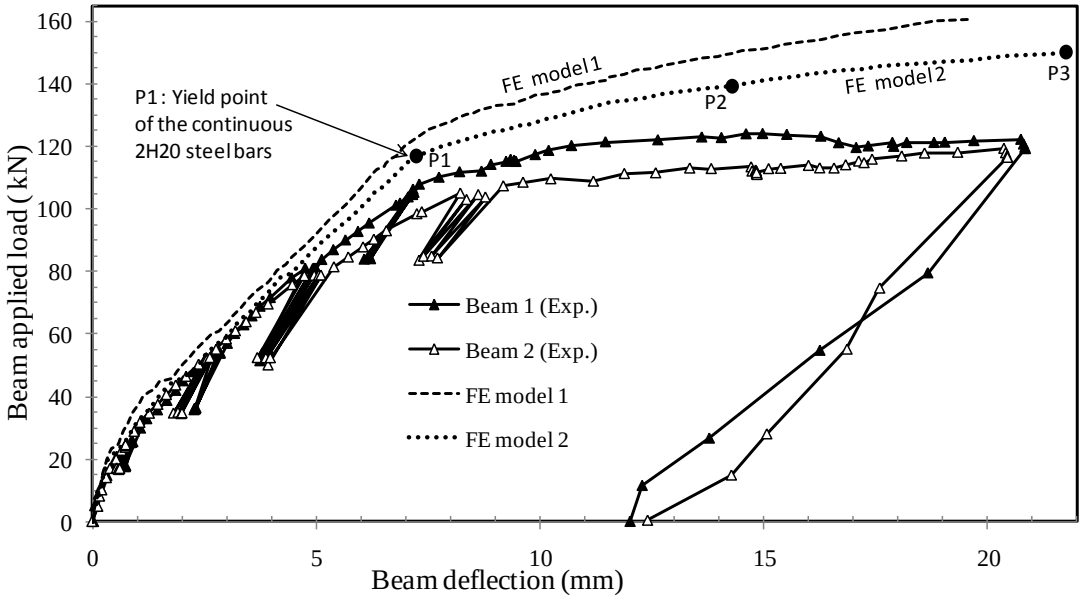

Figure 7.23 Effect of FE model 2 on numerical beam load-deflection relation in specimen GR2

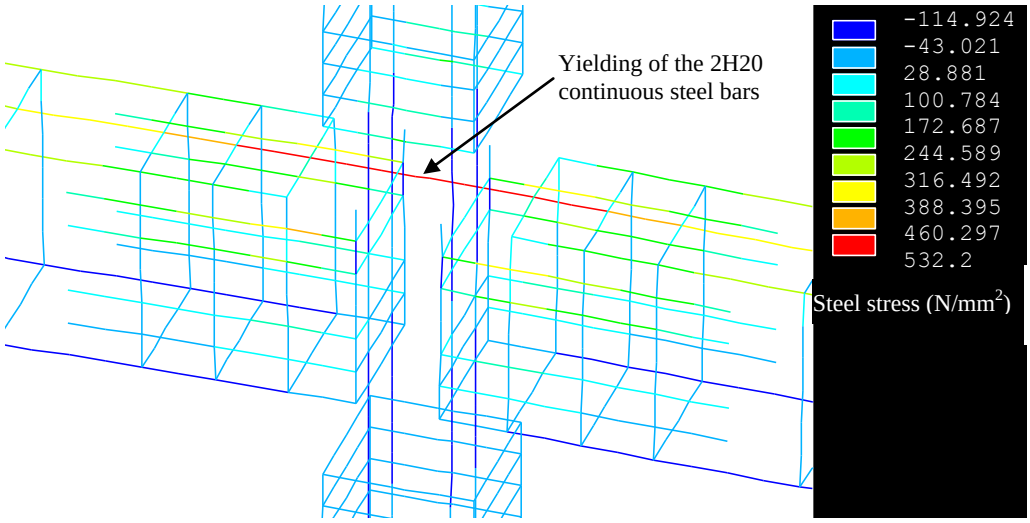

a) At 116.8 kN load (point P1: yielding of the continuous steel bars)

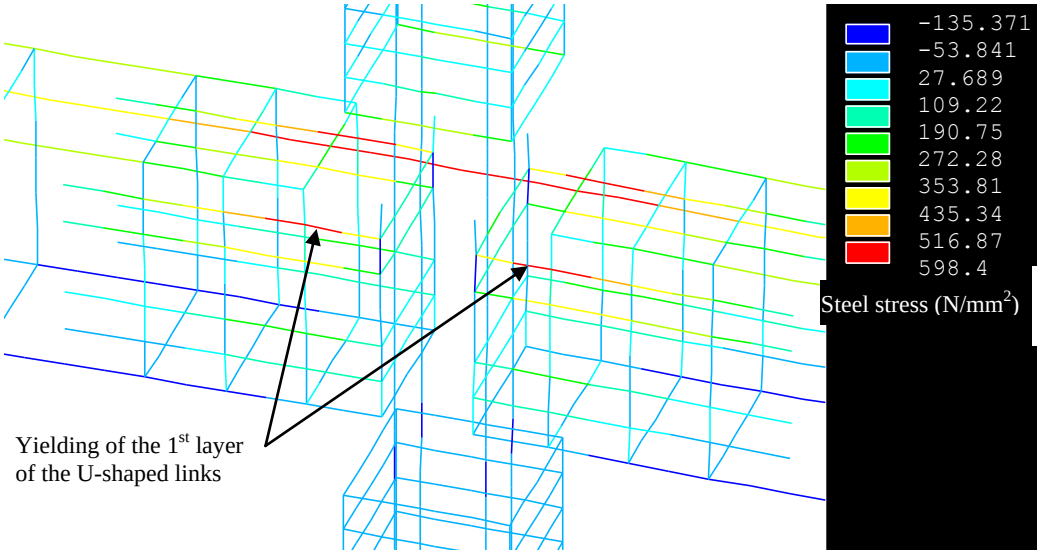

b) At 138.8 kN load (point P2: yielding of the 1st layer of the U-shaped links)

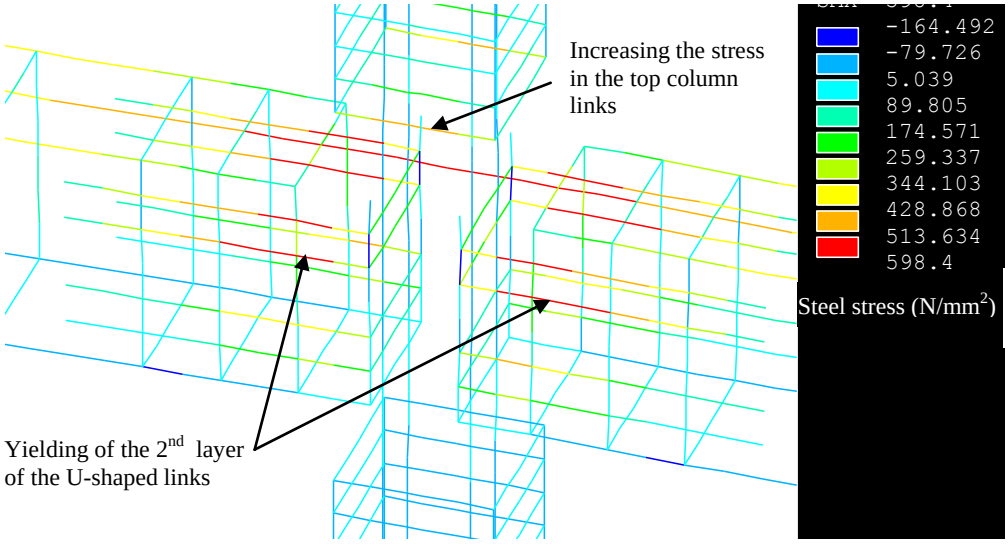

c) At 150.0 kN failure load (point P3: yielding of the 2nd layer of the U-shaped links)

Figure 7.24 Steel bar stresses in FE model 2 of specimen GR2

7.7.2.3 Contact elements

The results of the FE model 1 with respect to the contact elements in specimen GR2 are presented in this section for a comprehensive investigation of the joint status within the connection. The contact element characteristics reported in Figure 7.25 are those recorded at the 116.8 kN beam load (refer to Figure 7.15). The locations of the contact elements within the connection are shown in Figure 7.2.

As shown in Figure 7.25a to Figure 7.25c, there were gaps between the grout and concrete at places where normal tension stresses exist. The maximum gap size was 0.235 mm occurring in the vertical joint between the vertical grout and beam-ends at 300 mm beam height. Regarding the sliding, the maximum value happened at the right and left edges of the top contact elements between the top column and beam, with a maximum value of 0.323 mm.

The maximum normal and friction stresses occurred at the right and left edges of bottom contact between the bottom column and beam, with 17.0 N/mm^2 as maximum normal stress and 7.8 N/mm^2 as maximum friction stress. Assuming a uniform stress distribution, the theoretical normal stress at this beam load level (116.8 kN) is 8.2 N/mm^2. It is worth mentioning that the author conducted a complementary FE test (FE model 3) to investigate the effect of removing the contact elements in the FE model 1 and assuming a full contact instead. The effect was very noticeable, as could be seen in Figure 7.26. For instance, by using the contact elements, there was an increase in the deflection at 116.8 kN beam load by 10% in comparison to the rigid FE model. Overall, the use of the contact elements helped the FE model to move towards the correct behaviour.

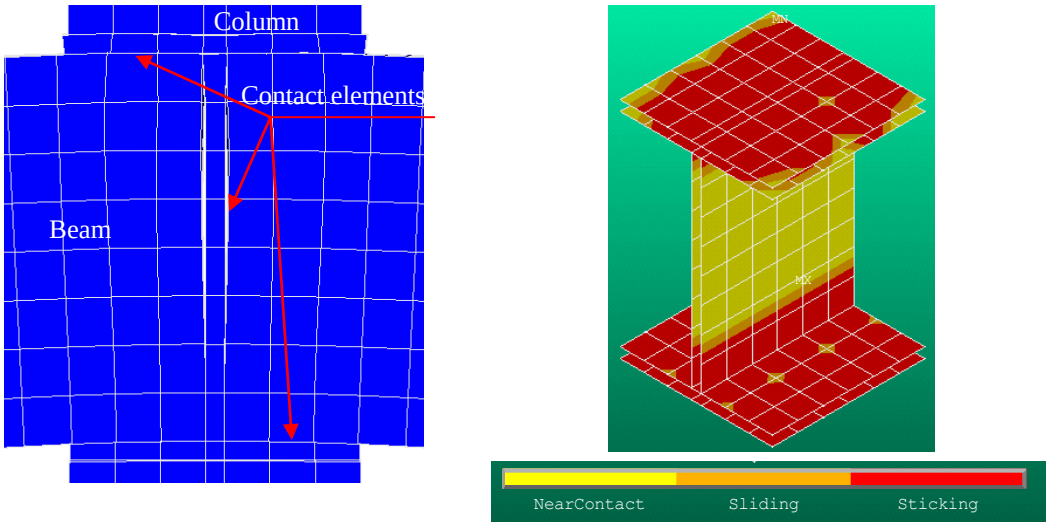

a) Deflected shape of the connection (deflections, sliding and gap distances are enlarged 40 times)

b) Contact status at the interfaces between the concrete and grout layers within the connection

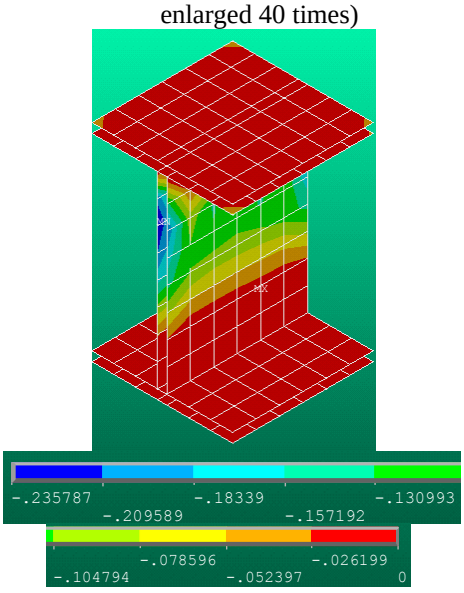

c) Contact gap distance

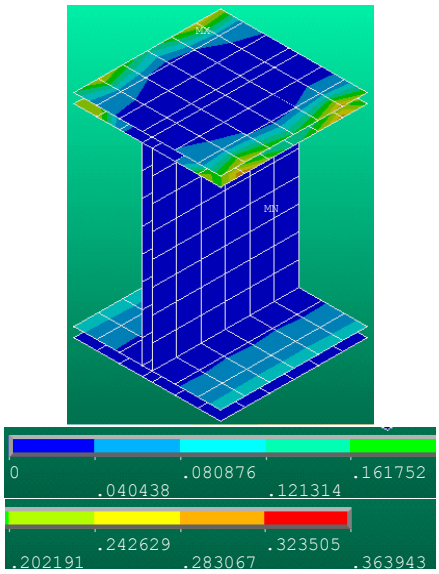

d) Contact sliding distance

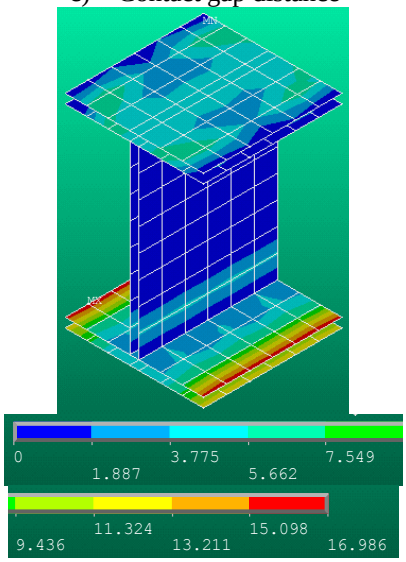

e) Contact normal stress

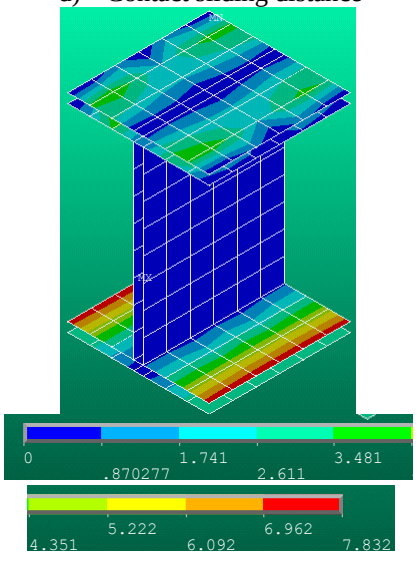

f) Contact friction stress

Figure 7.25 Contact element characteristics in specimen GR2 at 116.8 kN beam load

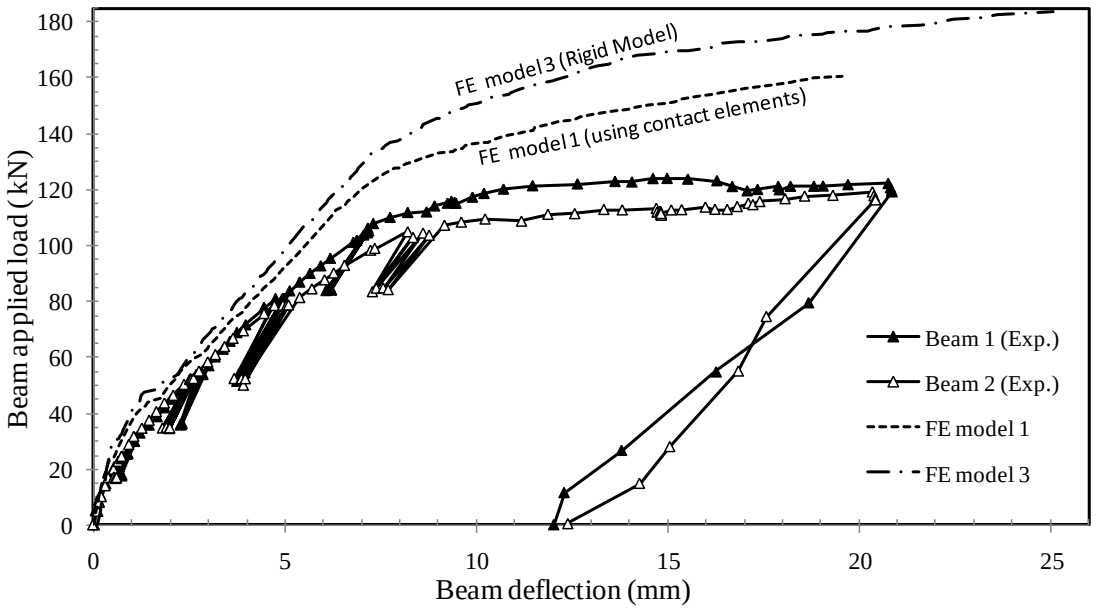

Figure 7.26 Comparison of FE model 1 with FE model 3

7.8 Summary and conclusion

In this chapter, the discontinuous precast concrete beam-column specimens tested under gravity loads in the current study were modelled using FE analysis to replicate the experimental results. The FE modelling included only the specimens that showed semi-rigid behaviour (GR1 and GR2). Based on the results obtained from the FE modelling, the following conclusions can be drawn.

1) The use of contact elements between the concrete and grout within the connection adjusted the FE model behaviour towards matching the experimental results.
2) The FE model was able to predict the behaviour in most of the elastic region.
3) The FE model was able to predict the location of the first cracks, and the crack pattern at the experimental yielding load level.
4) The FE model was not able to predict the failure modes and consequently the ultimate load capacity. The is due to the lack of available calculation models to help in providing springs at interface between the external perimeter of the corrugated sleeves and the surrounding concrete within the connection.

CHAPTER 8

ANALYSIS AND DESIGN CONSIDERATIONS

8.1 Introduction

The key parameter in the response of beam-column connections is the rotational stiffness 'S_y', which characterises the flexibility of the connection and affects the moment distribution as well as the sway drift in framed structures. To quantify such effects, the experimental S_y values obtained from the current study have been used in semi-rigid analyses of framed structures under gravity and sway loadings. Under gravity loading, the effects of S_y of specimens GR1 and GR2 on the moment distribution were examined for beam span lengths from 1 to 16 m, two beam loading patterns, and two relative beam's EI to column's EI. Under sway loading, the effects of S_y of specimen SW on the moment distribution and sway deflections were investigated for beam span lengths from 1 to 16 m.

The results of the semi-rigid analyses have been used to examine the applicability of using the so-called *single span beam approach* in classifying connections (refer to Section 5.3.4.3) considering the three variables mentioned above under gravity loading. In addition, this chapter presents the design considerations for implementing the precast concrete beam-column connection investigated in the current study in practice under gravity and sway loadings.

8.2 Semi-rigid frame analysis

The flexibility of the beam-column connections is incorporated in semi-rigid frame analyses by assigning rotational springs with no physical dimension to the member-ends. These springs have rotational stiffnesses that would affect the stiffness matrix of individual members, and consequently the global stiffness matrix of the

frame. To incorporate connection rotational flexibilities into a computer-based semi-rigid frame analysis, three methods were used:

i) semi-rigid frame analysis using the ANSYS software package (2004) by assigning rotational springs at the beam-ends;
ii) Visual Basic program (prepared by the researcher) using correction matrices, which reflects the connection flexibility of the connections, to modify the conventional stiffness matrices of rigid-end members;
iii) simplified semi-rigid analysis using the conventional rigid analysis by assigning small stubs at the beam-ends with weakened stiffnesses (EI) reflecting the rotational stiffness of the connections.

The results of the semi-rigid analysis shown in this chapter have been obtained using the first method (ANSYS), while the Visual Basic program has been used to verify the results. The simplified semi-rigid analysis has been validated against the other two methods as a way to provide a suitable tool for day-to-day design purposes.

8.2.1 Conventional semi-rigid frame analysis

The derivation of the modified elastic stiffness matrix of a member 'K' (Eq. (8.7)) is based on the conjugate-beam analogy (Figure 8.1) and the introduction of a fixity factor for the member-ends *i* and *j* (Eq. (8.1) and Eq. (8.2)), which associate the connection rotational stiffness of the member ends (S_{yi}, S_{Yj}) with the beam stiffness (3EI/L) and could be easily merged into a conventional frame analysis. The use of a fixity factor concept simplifies the semi-rigid frame analysis and introduces a meaningful value that shows how the connection will behave in real frames (refer to Section 2.7).

$$\gamma_i = \left(\frac{1}{1+\frac{3\,EI}{S_{yi}\,L}}\right) \tag{8.1}$$

$$\gamma_i = \left(\frac{1}{1+\frac{3\,EI}{S_{yj}\,L}}\right) \tag{8.2}$$

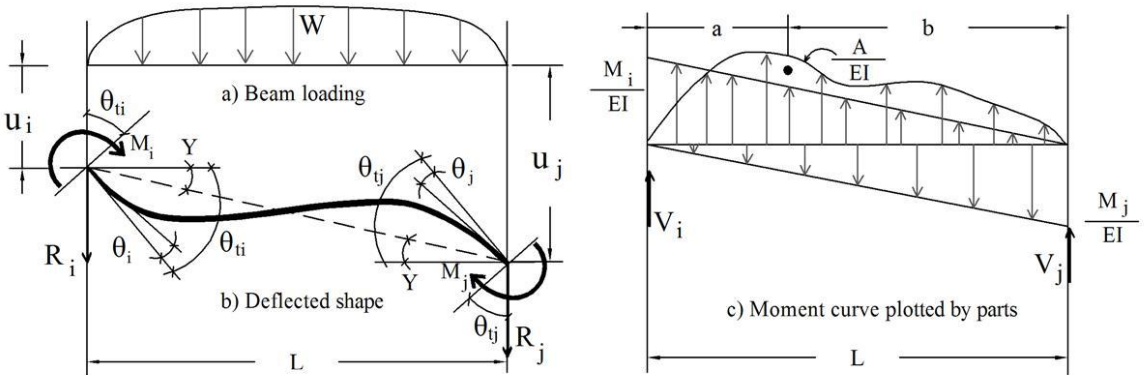

Figure 8.1 Conjugate-beam analogy (Monforton and Wu, 1963)

According to Monforton and Wu (1963), the equilibrium equations at the beam-ends (M_i, M_j) using fixity factors (γ_i, γ_j) are given as below:

$$M_i = \left(\frac{6EI}{L}\right)\left(\frac{\gamma_i}{4-\gamma_i\gamma_j}\right)\left[2\,\theta_{ti} + \gamma_j\,\theta_{tj} - (2+\gamma_j)\,Y\right] - \left(\frac{6A}{L^2}\right)\left(\frac{\gamma_i}{4-\gamma_i\gamma_j}\right) \tag{8.3}$$

$$M_j = \left(\frac{6EI}{L}\right)\left(\frac{\gamma_j}{4-\gamma_i\gamma_j}\right)\left[2\,\theta_{tj} + \gamma_i\,\theta_{ti} - (2+\gamma_i)\,Y\right] - \left(\frac{6A}{L^2}\right)\left(\frac{\gamma_j}{4-\gamma_i\gamma_j}\right)(2a - \gamma_i\,b) \tag{8.4}$$

With re-arrangement of the above equations, the end-moments could be expressed as:

$$M_i = \left(\frac{6EI}{L^2}\right)\left(\frac{\gamma_i(2+\gamma_j)}{4-\gamma_i\gamma_j}\right)u_i + \left(\frac{4EI}{L}\right)\left(\frac{3\,\gamma_i}{4-\gamma_i\gamma_j}\right)\theta_{ti} - \left(\frac{6EI}{L^2}\right)\left(\frac{\gamma_i(2+\gamma_j)}{4-\gamma_i\gamma_j}\right)u_j + \left(\frac{2EI}{L}\right)\left(\frac{3\,\gamma_i\gamma_j}{4-\gamma_i\gamma_j}\right)\theta_{tj} \tag{8.5}$$

$$M_j = \left(\frac{6EI}{L^2}\right)\left(\frac{\gamma_j(2+\gamma_i)}{4-\gamma_i\gamma_j}\right)u_i + \left(\frac{2EI}{L}\right)\left(\frac{3\,\gamma_i\gamma_j}{4-\gamma_i\gamma_j}\right)\theta_{ti} - \left(\frac{6EI}{L^2}\right)\left(\frac{\gamma_j(2+\gamma_i)}{4-\gamma_i\gamma_j}\right)u_j + \left(\frac{4EI}{L}\right)\left(\frac{3\,\gamma_j}{4-\gamma_i\gamma_j}\right)\theta_{tj} \tag{8.6}$$

Thus, the modified elastic stiffness matrix of a member 'K' with two semi-rigid end-connections with rotational stiffness of S_{yi} and S_{yj} is given as by Eq. (8.7):

$$\begin{pmatrix} Fx_i \\ Fy_i \\ M_i \\ Fx_j \\ Fy_j \\ M_j \end{pmatrix} = \begin{pmatrix} \frac{EA}{L} & 0 & 0 & \frac{-EA}{L} & 0 & 0 \\ 0 & \boldsymbol{c_1}\frac{12\,EI}{L^3} & \boldsymbol{c_2}\frac{6\,EI}{L^2} & 0 & \boldsymbol{c_1}\frac{-12\,EI}{L^3} & \boldsymbol{c_4}\frac{6\,EI}{L^2} \\ 0 & \boldsymbol{c_2}\frac{6\,EI}{L^2} & \boldsymbol{c_3}\frac{4\,EI}{L} & 0 & \boldsymbol{c_2}\frac{-6\,EI}{L^2} & \boldsymbol{c_5}\frac{2\,EI}{L} \\ \frac{-EA}{L} & 0 & 0 & \frac{EA}{L} & 0 & 0 \\ 0 & \boldsymbol{c_1}\frac{-12\,EI}{L^3} & \boldsymbol{c_2}\frac{-6\,EI}{L^2} & 0 & \boldsymbol{c_1}\frac{12\,EI}{L^3} & \boldsymbol{c_4}\frac{-6\,EI}{L^2} \\ 0 & \boldsymbol{c_4}\frac{6\,EI}{L^2} & \boldsymbol{c_5}\frac{2\,EI}{L} & 0 & \boldsymbol{c_4}\frac{-6\,EI}{L^2} & \boldsymbol{c_6}\frac{4\,EI}{L} \end{pmatrix} \cdot \begin{pmatrix} Ux_i \\ Uy_i \\ \theta_{ti} \\ Ux_j \\ Uy_j \\ \theta_{tj} \end{pmatrix} \tag{8.7}$$

$$c_1 = \frac{\gamma_i + \gamma_j + \gamma_i \gamma_j}{4 - \gamma_i \gamma_j} \; ; \; c_2 = \frac{\gamma_i (2 + \gamma_j)}{4 - \gamma_i \gamma_j} \; ; \; c_3 = \frac{3 \gamma_i}{4 - \gamma_i \gamma_j} \tag{8.8}$$

$$c_4 = \frac{\gamma_j (2 + \gamma_i)}{4 - \gamma_i \gamma_j} \; ; \; c_5 = \frac{3 \gamma_i \gamma_j}{4 - \gamma_i \gamma_j} \; ; \; c_6 = \frac{3 \gamma_j}{4 - \gamma_i \gamma_j} \tag{8.9}$$

8.2.2 Semi-rigid frame analysis using ANSYS

In ANSYS (2004), linear semi-rigid analysis is conducted by assigning rotational springs, representing the connection rotational stiffness, at the beam-ends. A two-node beam element, *Beam3*, was used to model the beams and columns, and a 1D linear spring damper, *Combin14*, was used to model the rotational springs (Figure 8.2). The *BEAM3* element is a uniaxial element with three degrees of freedom: translations in the X and Y directions and rotation about the Z-axis. An ANSYS code has been written to analyse building frames for any geometry or loading (gravity loads, lateral loads, nodal loads, surface loads); they have either rigid connections or semi-rigid connections.

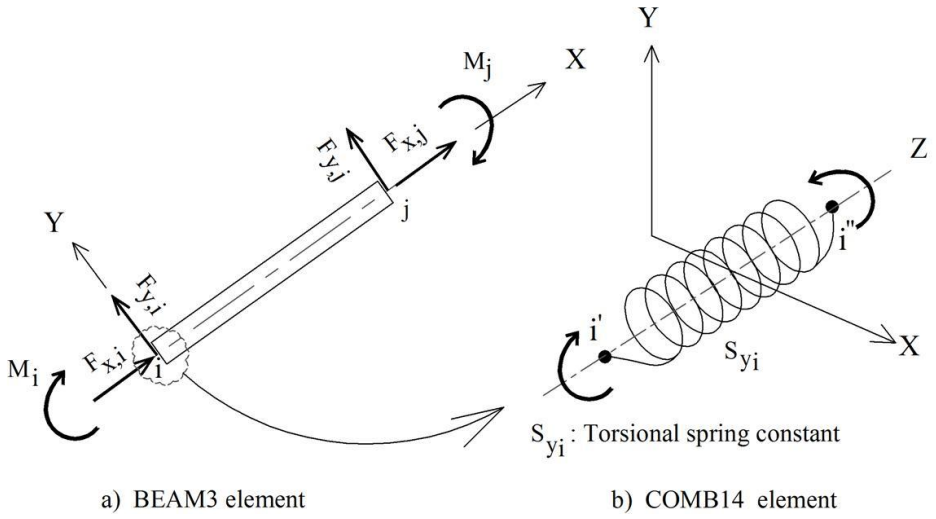

Figure 8.2 ANSYS element types used to model semi-rigid behaviour in frame analyses

8.2.3 Simplified semi-rigid frame analysis

The simplified semi-rigid analysis approach is conducted using conventional rigid frame analysis (Staad Pro software, for example) with locating short stubs of length Ls_i and stiffness EI_{si} as calculated in Eq. (8.10) (Huber et al, 1998). The stub stiffness EI_{si} reflects the rotational stiffness S_{yi} of the connection, which could be obtained either

experimentally or analytically. In the derivation of EI_{si} (Figure 8.3), the bending moment is assumed to be constant along the stub (Huber et al, 1998); therefore, it was advised to use short length stubs to minimise the deviation to the actual behaviour.

$$EI_{si} = S_{yi} \quad Ls_i \tag{8.10}$$

In the available literature, there is no clear indication with respect to the stub length effect. For this reason, a complementary work was conducted to calibrate the stub length, as presented in Appendix H. In this respect, three different stub lengths (Ls_i) were examined, starting from the less convenient one for handling in analysis (10 mm) to the most convenient one (1000 mm). The simplified method was calibrated for both gravity and sway loadings considering both first order and second order analyses. The outcomes from the calibration showed that the 10 mm stub length gives results very close to that obtained using ANSYS or the conventional semi-rigid frame analysis. Under gravity loading, the maximum difference in the moments was 1.44 kNm for moments ranging from 0.5 to 582 kNm. Under sway loading, the maximum difference in the column base moments was ±1.7%, and the maximum difference in the sway of the right top corner was also ±1.7%.

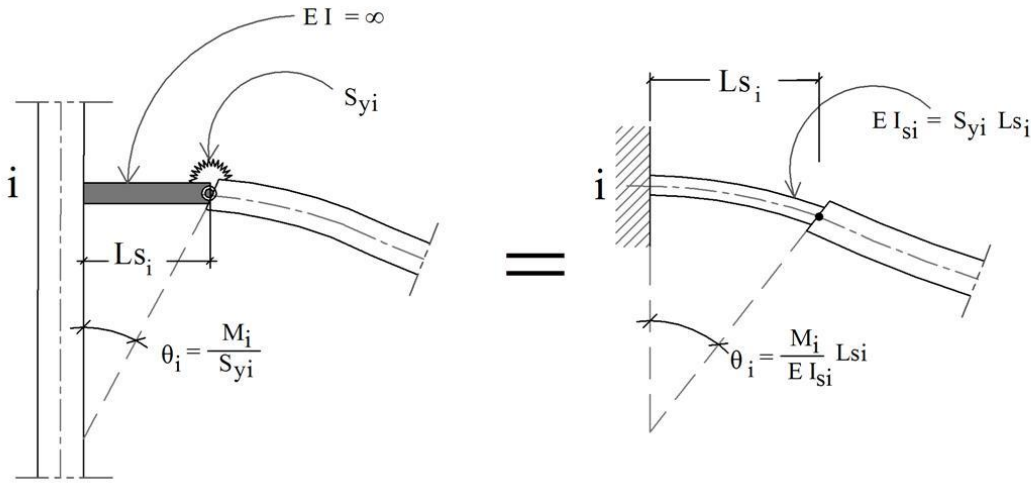

Figure 8.3 Equivalent stub concept (Huber et al, 1998)

8.3 Connection evaluation under gravity loads

This section aims to assess the effects of following parameters on the moment distribution: (i) column size; (ii) load pattern, iii) beam-column rotational stiffness; and (iv) span length. The results of beams in real frames were compared with the EC3 (CEN, 2005b) classification system. For this purpose, frame F1 was examined, which has beam dimensions the same as specimens of series GR, and geometry as shown in Figure 8.4. The frame was analysed for four cases, as shown in Table 8.1, for equal beam spans varying from 1 m to 16 m, using full EI for columns and 0.5 EI for beams.

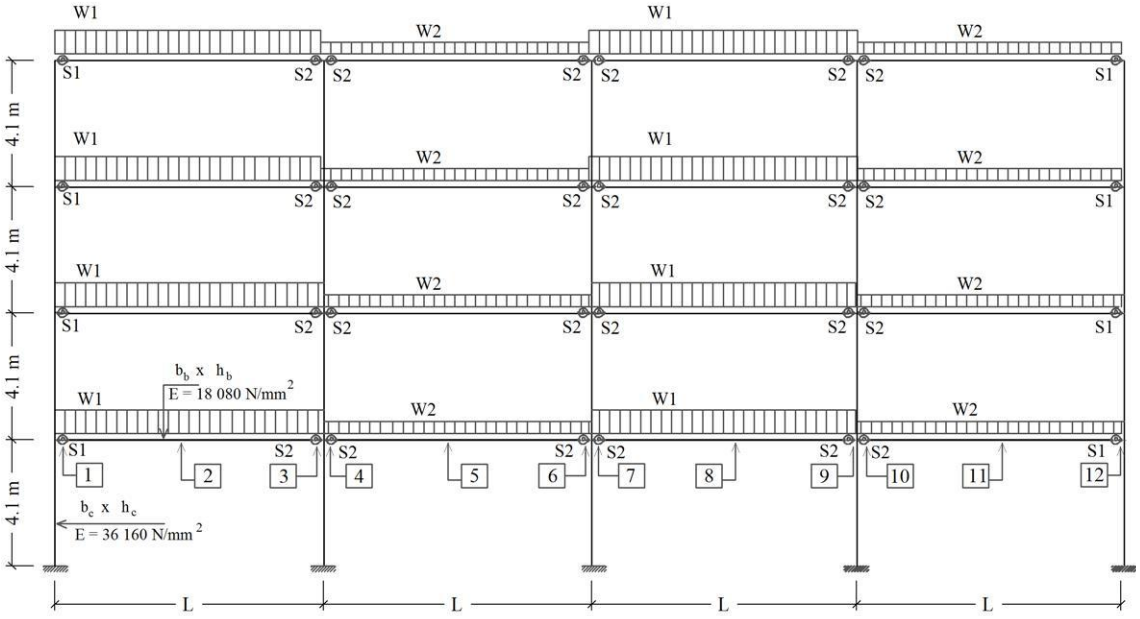

Figure 8.4 Geometry and loading of frame F1

Table 8.1 Analysed cases of frame F1

Case	W1 (kN/m)	W2 (kN/m)	S_1, S_2 (kN.m/rad)	b, h (mm)	b_c, h_c (mm)	Notes
F1-A	60	60	30160 (GR1)	300 x 400	300 x 600	Reference frame
F1-B	60	60	30160 (GR1)	300 x 400	300 x 300	Normal column size
F1-C	60	30	30160 (GR1)	300 x 400	300 x 300	Alternative loading pattern
F1-D	60	30	106905 (GR3)	300 x 400	300 x 300	Higher rotational stiffness

The results of the analyses are shown in Figures 8.5 to 8.8, wherein the normalised moments are plotted against span length. The normalised moments were

calculated by dividing the semi-rigid moments by moments obtained at corresponding locations in a parent rigid analysis. In all cases, the behaviour turned out to be classified as rigid, based on EC3 (CEN, 2005b) limits for braced frames, around almost the same span length as that determined using the single span beam approach (refer to Section 5.3.4.3). Also, as shown, semi-rigid connections turned out to be close to rigid behaviour with an increase in the span length.

As would be expected, the beams in the reference frame F1-A behaved in a very similar way to a single beam regarding the moments generated at the ends and mid-spans; this is because of the stiff columns and applying equally distributed loads on all beam spans.

However, the use of a smaller column size in the F1-B led to some discrepancy, especially at the external spans, such as locations 1 and 2 in Figure 8.6. In frame F1-C, in addition to the use of small columns, the alternative beam loading pattern was used, which led to more discrepancy. However, all the discrepancies were in favour to boost the semi-rigid behaviour to be closer to the rigid analysis (the rigid behaviour line in the figures). The only location that had a different behaviour is location 5 in frames F1-C and F1-D, which is the mid-span moment in a span loaded with the lower load, while the adjacent spans are loaded with the maximum load. This case could be disregarded because is not the critical case for determining the mid-span moments due to these reasons:

i) under load patterns of cases F1-C and F1-D, the mid-span moments are low in small spans and it is surpassed by the minimum reinforcement requirement;

ii) the design moment at location 5 will be governed by another load case (W1=30 kN/m and W2=60 kN/m).

From the above discussion, it became clear that using the single span beam approach (refer to Section 5.3.4.3) to classify a semi-rigid connection is a conservative approach. This is because the semi-rigid behaviour moves further towards the rigid behaviour in the frame analysis in comparison to a single beam analysis. This is because of the flexibility of the columns in real frames, especially at external spans, which decrease the moments generated at beam-ends even in rigid analysis.

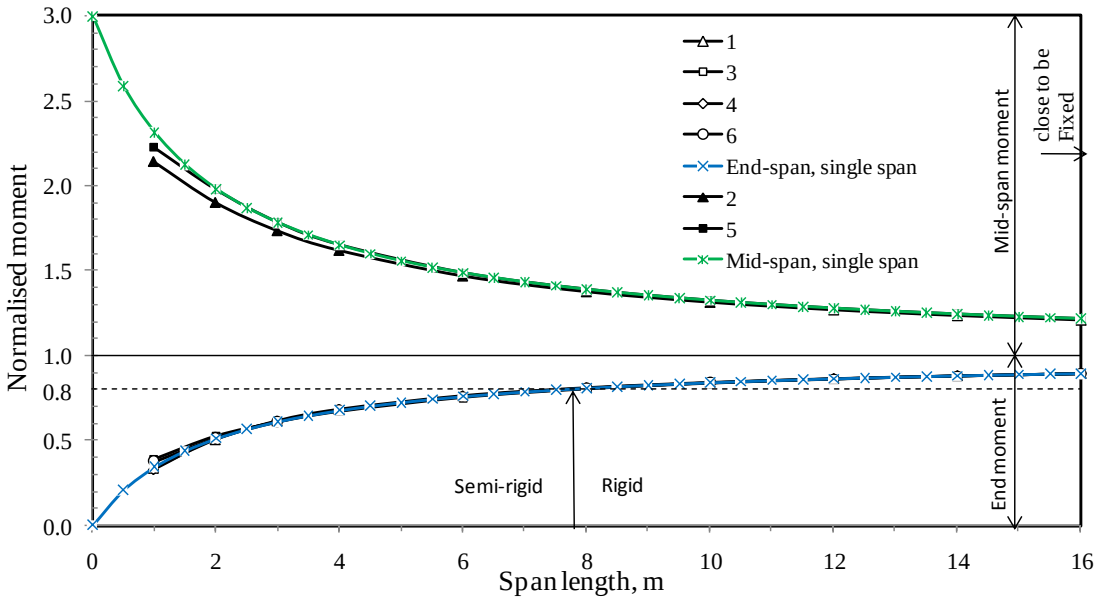

Figure 8.5 Normalised moment vs. span length variation in frame F1-A

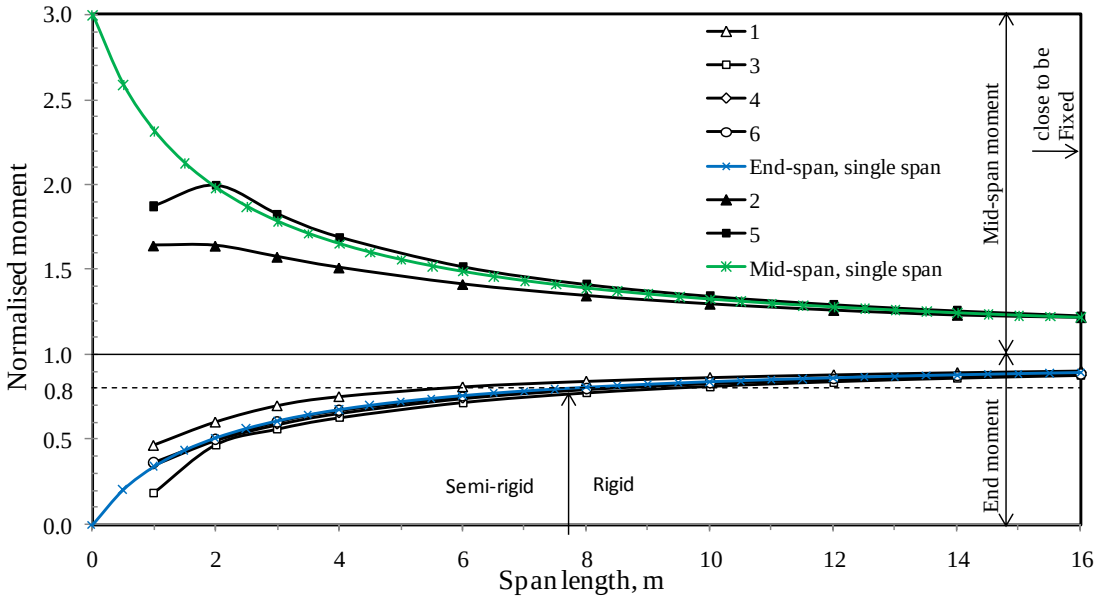

Figure 8.6 Normalised moment vs. span length variation in frame F1-B

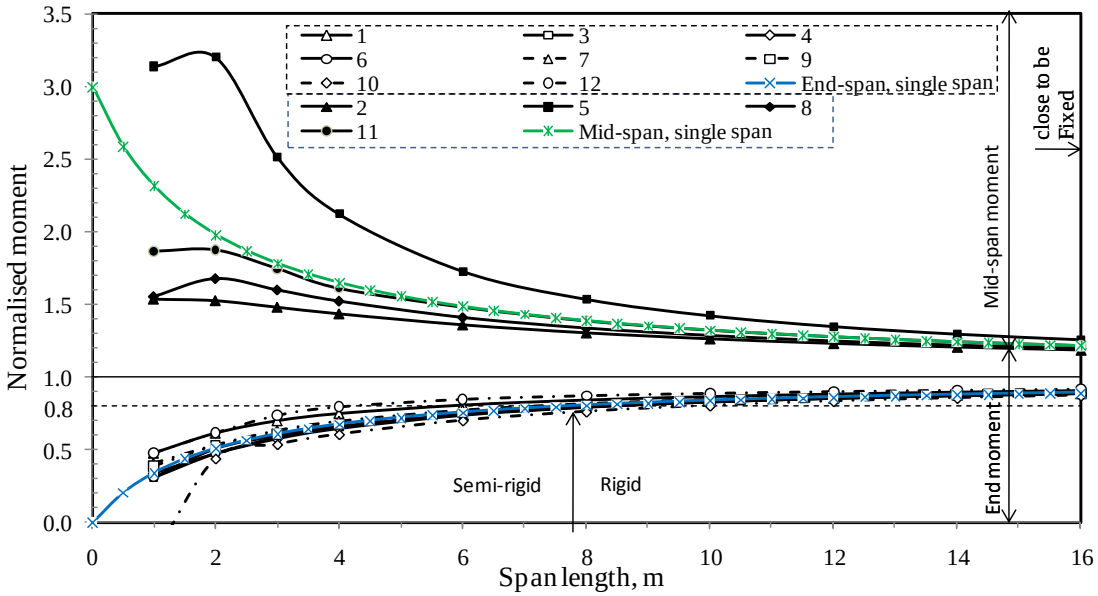

Figure 8.7 Normalised moment vs. span length variation in frame F1-C

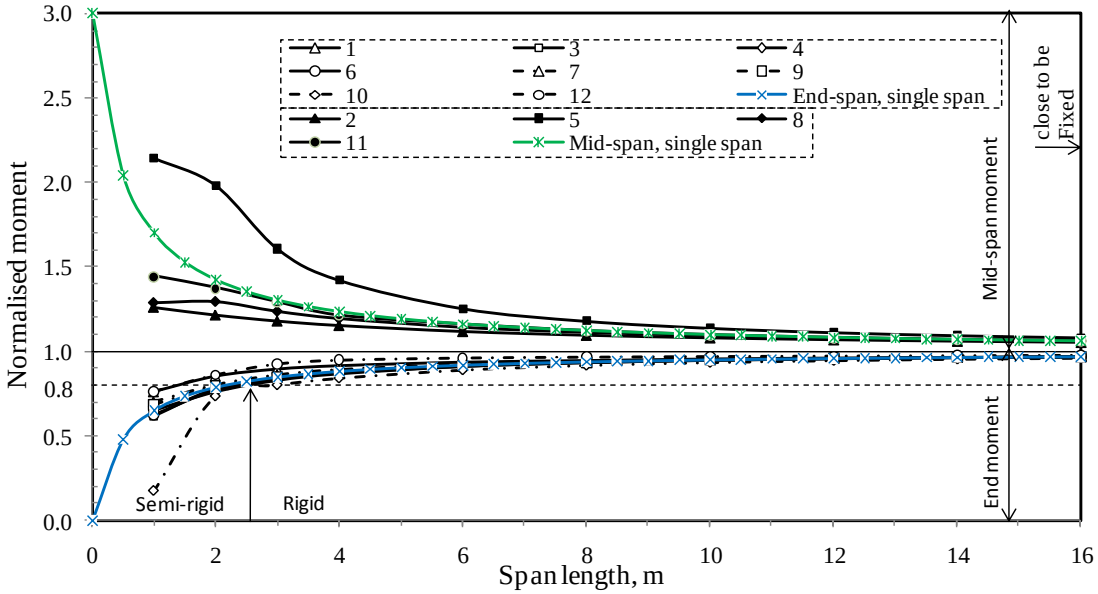

Figure 8.8 Normalised moment vs. span length variation in frame F1-D

8.4 Connection evaluation under sway loads

To find out the effects of using the beam-column connection studied in the current research in a real unbraced frame, a 2D frame F2 was analysed for the loading and geometry shown in Figure 8.9 in four different cases, as listed below, taking the beam span 'L' as the variable within each case.

1) First order rigid analysis (reference frame 1) assuming full rigid beam-column connections.
2) Same as 1, but with second order analysis (reference frame 2).
3) First order semi-rigid analysis using the experimental yield secant rotational stiffness 'S_y' obtained from testing specimen SW2 (1278 kNm/rad). For this purpose, springs were assigned only at the beam-ends.
4) Same as 3, but with second order analysis.

As seen in Figure 8.9, the moments resulting from sway loading were separated from those generated from gravity loading; this is because the intention was to investigate the resulting moments and sway in the unbraced frame due to sway loading only. Therefore, as column axial loads play an essential role in generating second order column moments, the column axial loads due to gravity loading were imposed at the connection joints. The results show that:

A) Considering first order analysis and in comparison to the parent rigid frame, the increase in the span length in the semi-rigid frame led to:
   1- a decrease in the semi-rigid column moments (Figure 8.10);
   2- no significant effect to the semi-rigid beam moments (Figure 8.10);
   3- a decrease in the semi-rigid sway (Figure 8.12).
B) Considering second order analysis and in comparison to the parent rigid frame, the increase in the span length in the semi-rigid frame led to:
   1- a significant increase in the semi-rigid column moments (Figure 8.11);
   2- a moderate increase in the semi-rigid beam moments (Figure 8.11);
   3- a little decrease in the semi-rigid sway (Figure 8.12), followed by a sharp increase at larger span lengths.

Considering the first order analysis, the above observations shows that using the beam-column connection (specimen SW2) in longer spans increases the fixity factor of the connections and consequently increases the rigidity of the frame. Conversely, considering the second order analysis, using the proposed connection in longer spans produces very high column-base moments and sway.

The semi-rigid column-base moments in the case of beam spans of 7.3 m (which is the span that the connection is designed for, see Appendix A) was found to be very high in comparison to a parent rigid frame. This ratio ranges from 2.03 to 2.23 in the case of first order analysis (Figure 8.10), and 3.20 to 3.55 in the case of second order analysis (Figure 8.11).

Regarding the sway experienced at the top of the frame, by using the rotational stiffness obtained from specimen SW2, there was also a very significant increase in comparison with the parent rigid frame (Figure 8.12). For beam spans of 7.3 m, the ratio is 5.56 considering first order analysis, and 10.49 considering second order analysis.

The excessive semi-rigid column moments and sways, especially under second order analysis, suggest that the precast concrete beam-column connection tested in the current study is not providing sufficient frame action behaviour. This leads to a conclusion that it is not advisable to use the connection configuration in resisting lateral loads, if the sagging moments generated from sway loading exceed the permanent dead load hogging moments at the beam-ends.

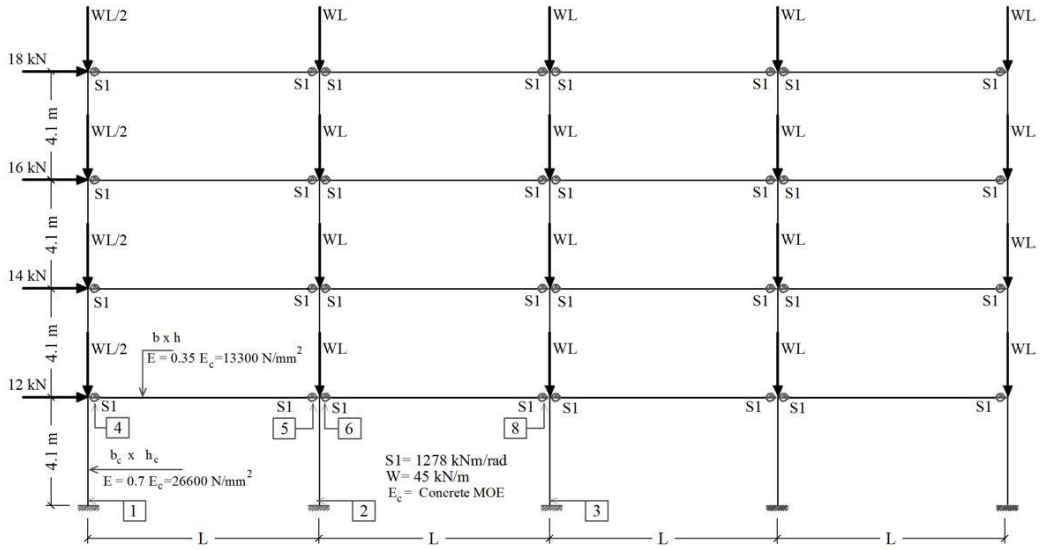

Figure 8.9 Geometry and loading of frame F2

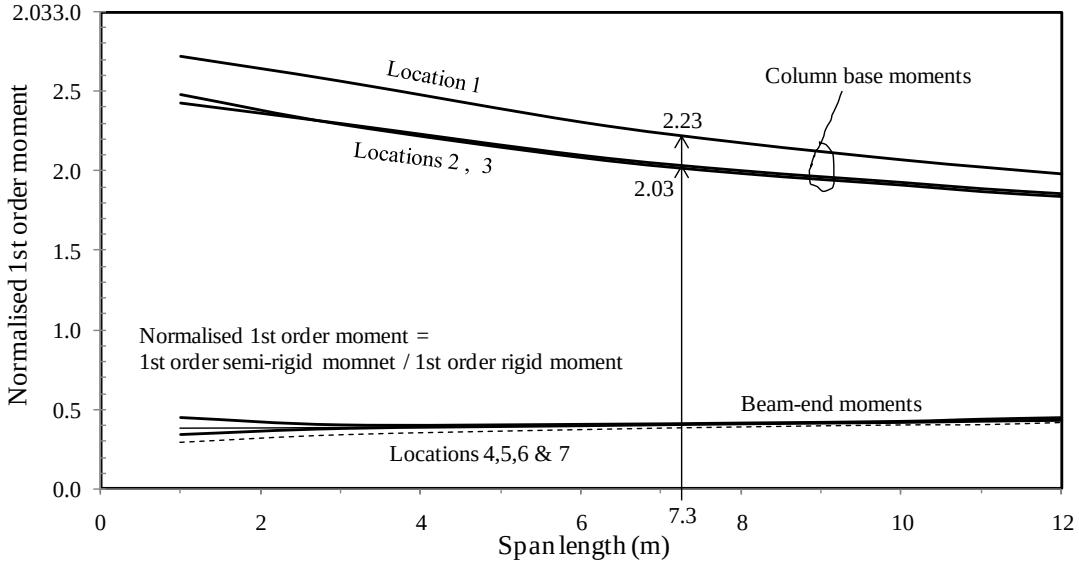

Figure 8.10 Ratio of first order semi-rigid moments in frame F2

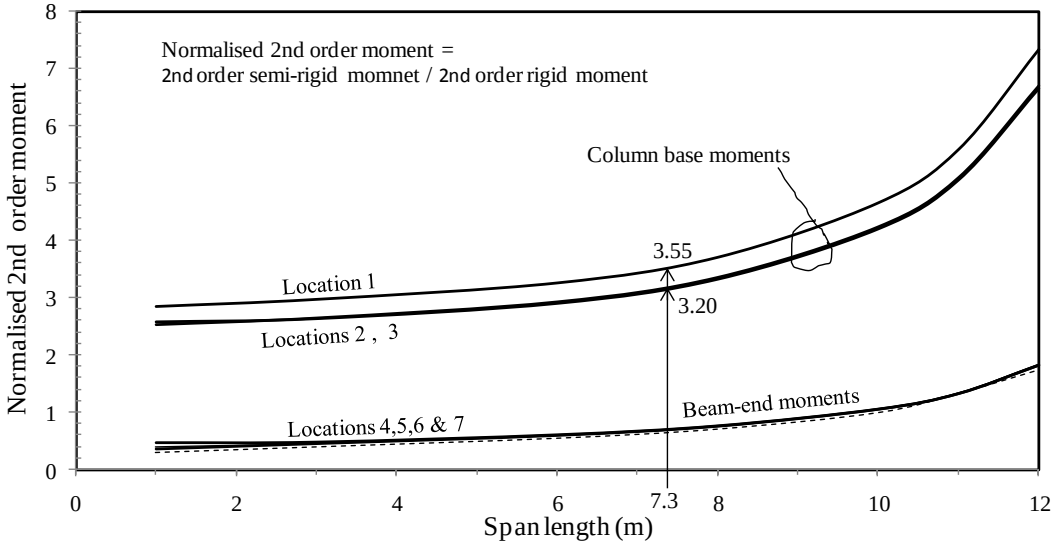

Figure 8.11 Ratio of second order semi-rigid moments in frame F2

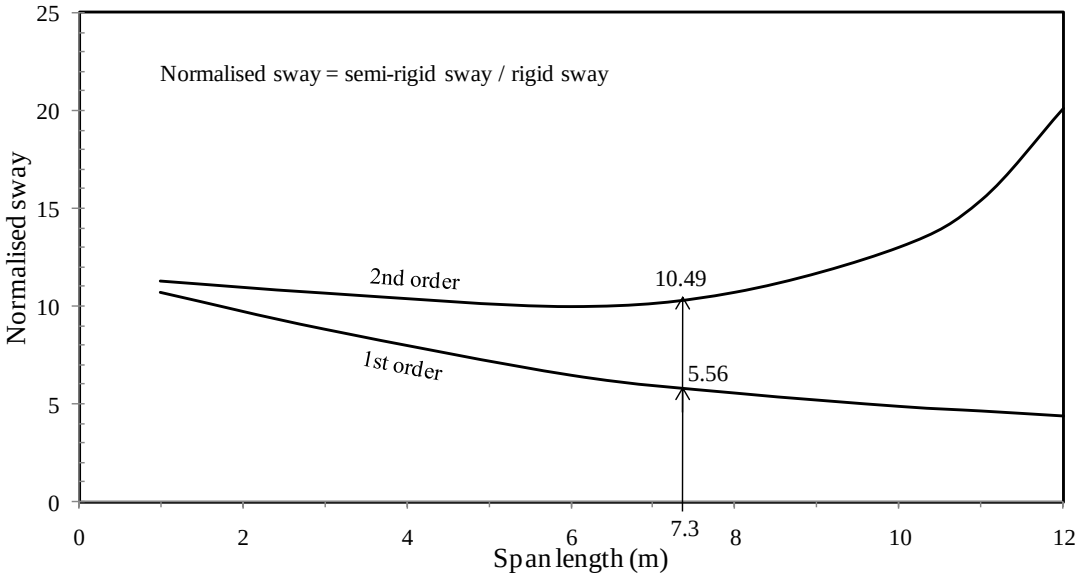

Figure 8.12 Ratio of semi-rigid sway in frame F2

8.5 Design considerations under gravity loads

The tests conducted under gravity loading (test series GR, Chapter 5) revealed two types of behaviour within the span length (7.3 m) the connection was designed for:

i) semi-rigid behaviour in specimens GR1 and GR2;

ii) equivalent monolithic behaviour in specimen GR3.

Each one of these two cases needs a different design approach, which is presented in the next two subsections.

8.5.1 Semi-rigid behaviour

The moment-rotation relation for a semi-rigid connection could be determined either experimentally or through analytical modelling, as has been shown in Section 5.4. For instance, Figure 8.13 shows this kind of relation of specimen GR1, where the secant rotational stiffness is determined at M_y ($S_y = M_y / \theta_y = 131.1/.0044 = 30160$ kNm/rad). For the frame analysis, this S_y is used in semi-rigid frame analysis by assigning S_y to rotational springs (element *COMB14* in ANSYS, for example) at the beam-ends. In spite of the fact that the use of S_y would overestimate the positive moments at mid-span, it

gives the compatible solution at the yielding stage. This is a straightforward and conservative approach, and the only criterion is to ensure that the hogging moment obtained from the semi-rigid frame analysis does not exceed the yield moment capacity of the connection.

For a more precise semi-rigid analysis, for moments lower than M_y, the rotational stiffness is higher than S_y due to the non-linear response of the moment-rotation relation. To account for this non-linearity, either the full moment-rotation relation is required to be used in frame analysis (using the non-linear spring element *COMB39* in ANSYS, for example), or by specifying a more representative rotational stiffness from the intersection of the curve with a line called the beam-line. This stiffness could be used in the semi-rigid analysis either by using Eqs. (5.15) and (5.16) for single span beams, or used in a full semi-rigid analysis using one of the methods presented in Section 8.2.

The beam-line method was presented by PCI (1988) as a way to determine the status of the compatible elastic strength 'M_E' and rotation 'θ_E', secant rotational stiffness 'S_E' and the ductility index (θ_u/θ_E) for beams with semi-rigid connections. To construct a beam-line, it is necessary to know the span length and the applied load, then points M_F and θ_R are determined. M_F represents the full fixity end-moment of the beam, while θ_R represents the beam-end rotation under zero fixity status (see Figure 8.13).

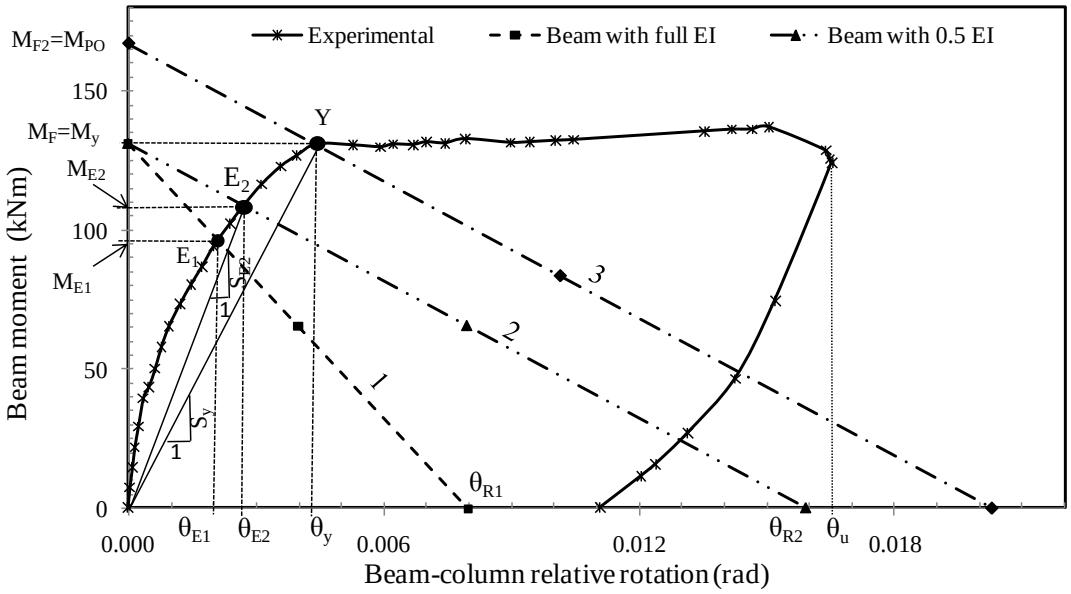

Figure 8.13 Experimental moment-rotation relation and the beam line concept for specimen GR1

For instance, for a 7.3 m long beam (L/h = 18.25, the span length in the prototype frame, Appendix A) with 29.52 kN/m distributed load, two beam-lines are drawn in Figure 8.13, which are beam-line 1 using full EI and beam-line 2 using 0.5 EI. According to Section R8.7.1 in the ACI Code of Practice (2008a), these values are proposed to be suitable for the analysis of structures subjected to non-lateral loads. As an alternative for these two values of EI, Elliot et al (2003a) used the flexurally cracked second moment of area in constructing the beam-line, which might underestimate the beam stiffness. In Figure 8.13, the intersection of the experimental moment-rotation curve with beam-line 1 gives point E_1, and with beam-line 2 gives point E_2. The compatible moment and rotation, in addition to the secant stiffness and the ductility index at these points are listed in Table 8.2, with a comparison with the characteristics at the yield moment.

Table 8.2 Results of beam-line analysis of specimen GR1

Point	θ (rad)	M (kNm)	S (kNm/rad)	Ductility index
E_1	0.00210	97.5	46429	7.8
E_2	0.00270	108.4	40148	6.1
Y	0.00435	131.1	30160	3.8

From the above, as a non-linear nature of the moment-rotation relation, it is apparent that the connection rotational stiffness is starting with a very high stiffness at the uncracked-stage, and declining gradually to the yield secant rotational stiffness. By comparing points E1 and E2, it is clear that the weakening in the beam stiffness (being 0.5 EI due to cracks) would give rise to the actual semi-rigid hogging moment. This demonstrates that semi-rigid analysis based on full members' EI underestimates the hogging moments.

Many researchers defined M_F as the moment of resistance of the beam (Elliot et al, 2003b; Gorgun, 1997) and therefore, based on that, no beam-line could be constructed beyond line 2 in Figure 8.13. However, it seems that the beam-line method could be extended to determine the ultimate load on that 7.3 m span beam by constructing a new beam-line 3, which is parallel to beam-line 2 and passes through point y.

From line 3, a new M_{F2} (could be called potential moment M_{po}, which is the fixed end moment of the member taken to have rigid ends) is determined = 166.9 kNm, and with back calculation, the uniformly distributed load (UDL) could be found to be 37.6 kN/m. This 166.9 kNm moment is the potential hogging moment under 37.6 kN/m (UDL), if the beam-end is rigid. For specimen GR1, this 37.6 kN/m UDL produces the hogging moment of 131.1 kNm at the beam-end, assuming there is sufficient

reinforcement at the mid-span. This shows that the full hogging moment capacity at the beam-ends could develop if required, which will be very valuable to produce moment capacity after the starting of plastification in the mid-span.

It is worth mentioning here that the beam-line method as a graphical solution tool could determine the compatible moment and rotation at the ends of a single beam with semi-rigid ends. It gives a reasonable estimation for the moment in real frames under gravity loads. However, as shown in Section 8.3, this statement is very sensitive to the span location (external or internal), loading arrangement, and relative beam-column stiffness; therefore, for an accurate moment calculation, a semi-rigid frame analysis is required. To serve in this respect and to provide a simple tool for such analyses, the simplified approach has been presented in Section 8.2.3.

8.5.2 Rigid classification of connections in steel construction

As mentioned earlier, based on EC3 (CEN, 2005b), in braced frames, a semi-rigid beam-column connection capable of achieving a hogging moment not less than 80% of that achieved in a parent rigid connection could be considered as rigid connection in braced frames. However, before applying this approach to concrete structures, it is necessary to understand the principle behind it.

In steel structures, the steel section is mostly kept unchanged along the member length; consequently, the beam will have the same moment capacity along the full span, meaning that in a steel beam with rigid ends there is 50% an extra moment capacity at the mid-span (see Figure 8.14b).

Under gravity loads, semi-rigid connections with a fixity factor of 0.67 produce an end-moment ($M_E = WL^2/16$) equal to 75% of the parent moments ($M_F = WL^2/12$), and a semi-rigid mid-span moment 'M_S' equal to $WL^2/16$ (Figure 8.14c, and for further

details regarding the equations used in the analysis, refer to Section 5.3.4.3). This situation would produce plastic hinges at the mid-span and at the beam-ends simultaneously, which is not an ideal structural condition, as it is advised to have a sequence of plasticisations in the structure.

On the other hand, the fixity factor 0.73, which is proposed by EC3 as a minimum limit to treat a connection as a rigid in braced frames, would produce an end-moment ($M_E=WL^2/15$) equal to 80% of the parent rigid moments, and a semi-rigid mid-span moment ($M_s=WL^2/17.2$) equal to 140% of the parent rigid moment ($WL^2/24$) (see Figure 8.14d). This situation would ensure locating the first plastic hinge at the supports, with clear plastic behaviour until the occurrence of the second plastic hinge at the mid-span. Therefore, it is the author's belief that choosing 0.73 fixity factor by EC3 as the limit for considering a connection as rigid in steel frames under gravity loads works in this direction.

It should be mentioned here that EC3 classifies connections based on the rotational stiffness 'S', as multiples of EI/I. To consider a connection as rigid under gravity loads, S should be not less than 8EI/L. In the above discussion this term has been transformed to the fixity factor concept, which gives a better quantification for the behaviour as the values of the fixity factor range between 0 and 1. This aspect has been presented in detail in Chapter 2.

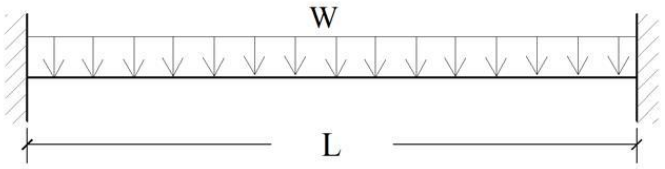

a) Beam loading

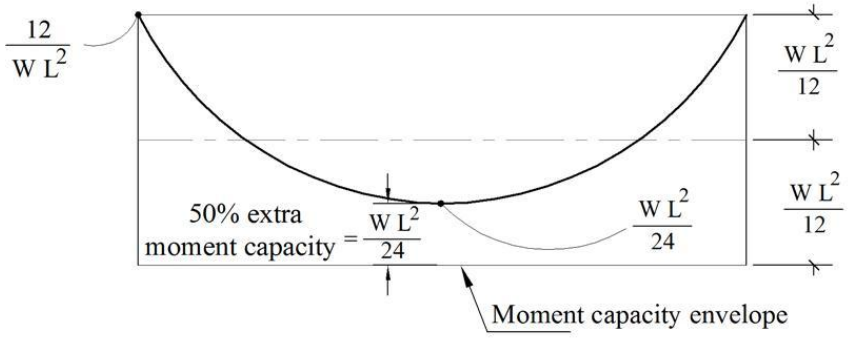

b) Moment diagram with fully rigid ends

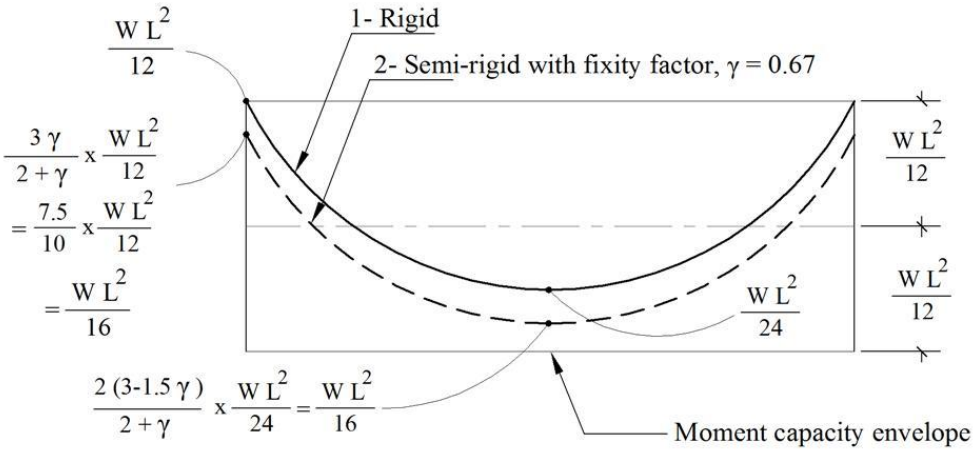

c) Moment diagram shift with fixity factor equal to 0.67

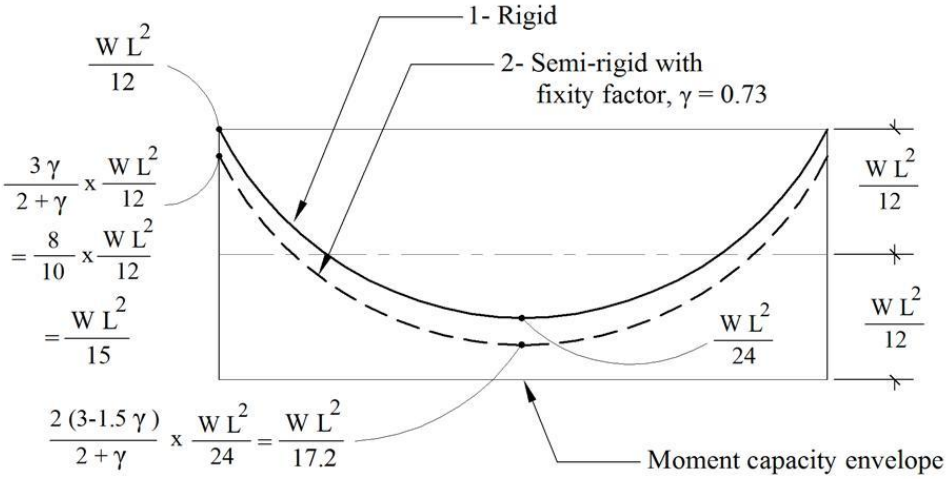

d) Moment diagram shift with fixity factor equal to 0.73

Figure 8.14 Semi-rigid moments achieved in a single span beam with fixity factors of 0.67 and 0.73

8.5.3 Rigid classification of connections in concrete construction

8.5.3.1 Moment redistribution

As a principle, from the point of view of the ultimate strength, the actual moment values that separate beam sections can sustain are not important as long as the summation of the moment capacities at the mid-span and support is capable of carrying the 'free' moment (Glanville and Thomas, 1933). In this trend, the beam-end hogging moments are reduced while the mid-span sagging moment is increased in order to make a balance in the reinforcement quantities. However, it is also permitted to reduce the mid-span moment and re-distribute it to the beam-ends within specific limits as long as the static equilibrium is maintained after redistribution (ACI, 2008a).

The codes of practice allow for moment redistribution as recognition of the inelastic behaviour in continuous flexural members (statically-indeterminate systems) resulting from large deformations. However, in spite of the fact that this recognition is proposed for the ultimate strength state, it has been shown that the redistribution of moments has an elastic component below the yield-point (Mattock, 1959; Scott and Whittle, 2005). This elastic component is attributed to the variation in the EI along the member due to variations in the reinforcement layout and the influence of cracking in contrast to the assumed constant EI in the conventional elastic analysis (Scott and Whittle, 2005).

The maximum permissible moment reduction 'Rm' in EC2 (CEN, 2004b) is 30% using steel reinforcement of class B or C, which corresponds to $\delta m=0.7$ (the ratio of the moment after redistribution to the elastic bending moment). For steel of class A, Rm is 20%. Using EC2 limitations, Fillo (2011) concluded that the maximum value of Rm,

using steel class B or C, could be guaranteed within the following maximum steel reinforcement ratios 'ρ' (Figure 8.15).

i) For concrete strength class ≤C50/60

ρ≤1.2% in case of considering only the tension reinforcement 'A_{S1}'

ρ≤3.1% in case of considering both the A_{S1} and compression reinforcement 'A_{S2}', and taking A_{S2}=0.5A_{S1}.

ii) For concrete strength class C80/90

ρ≤0.9% in case of considering only A_{S1}

ρ≤1.3% in case of considering both the A_{S1} and A_{S2}, and taking A_{S2}=0.5A_{S1}.

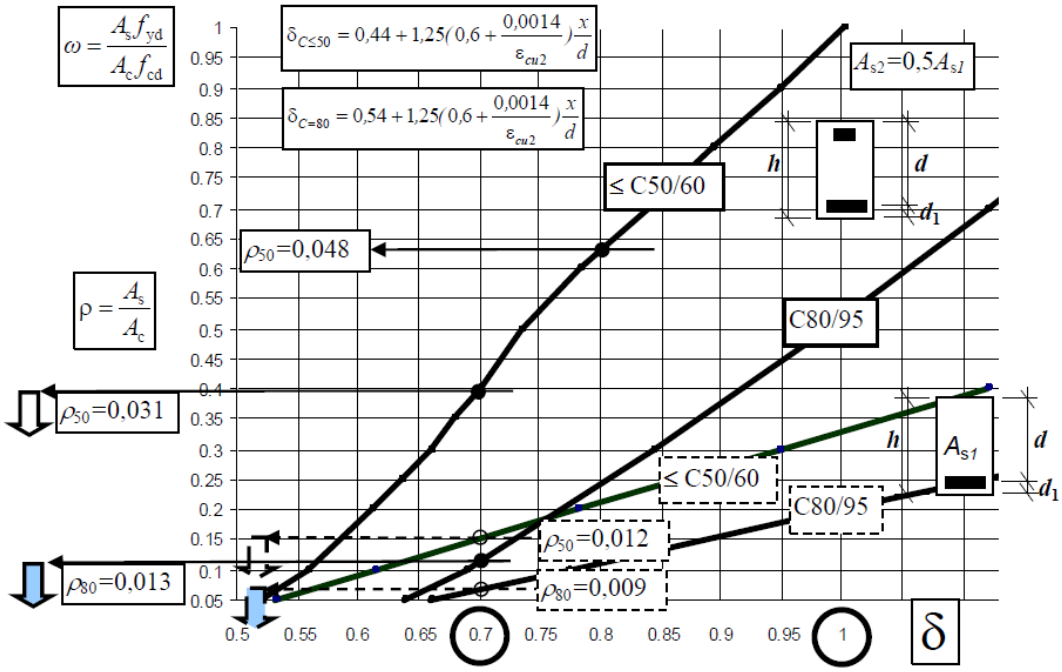

Figure 8.15 Permissible moment redistribution versus reinforcement ratio for steel class 500B according to EC2 (Fillo, 2011).
(In this graph, δ refers to the δm used in the current research)

8.5.3.2 General considerations

The classification approach mentioned in Section 8.5.2 (considering connections as rigid when the fixity factor is ≥ 0.73) could be applied directly to precast concrete beam-column connections in the case of keeping the beam section and reinforcement without change along the whole member length. Accordingly, a straightforward rigid

analysis could be performed for connections with fixity factor 'γ' greater or equal to 0.73 (80% end-moment restraint) by designing all the beam sections for the maximum moment obtained along the member length. However, the use of this approach in beams with sections of different reinforcement, which is the case in the vast majority of concrete beams, needs to be taken with a caution and a different design approach needs to be considered.

The above-mentioned 80% end-moment restraint matches well the 30% maximum permissible Rm in EC2 (CEN, 2004b) using steel reinforcement of class B or C. This achievement of end moments is accompanied by a 140% mid-span moment as a ratio of the parent rigid mid-span moment (Figure 8.16). This means, if we accept the outcomes of the rigid analysis for connections with γ equal to 0.73, there is already 28% moment redistribution (Rm=0.28) from the mid-span to the supports. This ratio comes from the difference between the rigid mid-span moment ($WL^2/24$) and the real semi-rigid mid-span moment ($WL^2/17.2$), meaning that δm is equal to ($WL^2/24$) / ($WL^2/17.2$) = 0.72, and Rm = 1- 0.72 = 0.28. Based on that, in order to consider a connection with γ equal to 0.73 as rigid, the moment redistribution required from the mid-span to supports 'Rm_r' is less than 0.28 as shown in Figure 8.17.

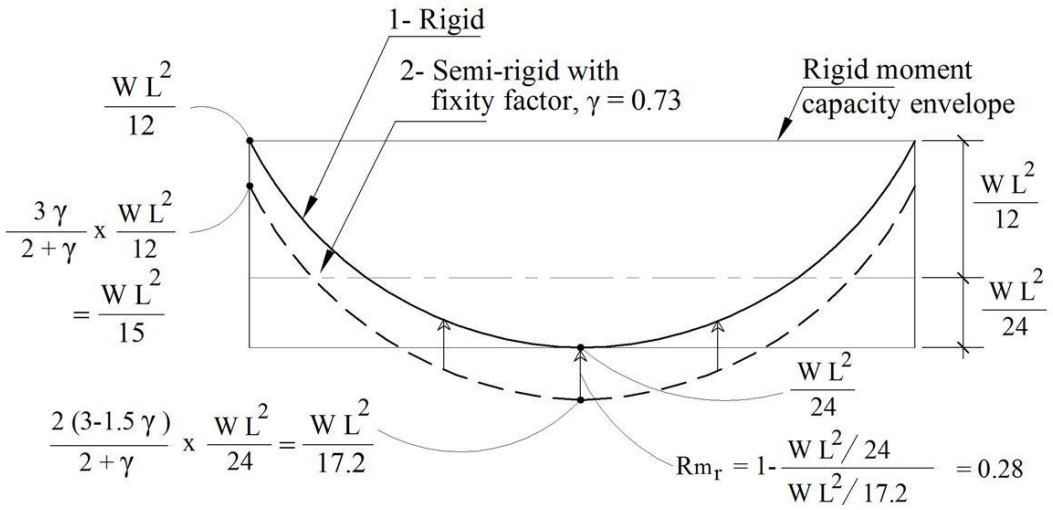

Figure 8.16 Mid-span moment redistribution demand for semi-rigid connections with γ=0.73

For connections with higher values of γ, Rm_r is lower, as shown in Figure 8.17. The relation between γ and Rm_r is given in Eq. (8.11c), which is derived from the relation between semi-rigid mid-span moment 'M_S' and the rigid mid-span moment ($M_F = WL^2/24$), as presented in Eq. (8.11a). In Figure 8.17, the γ–Rm_r relation is dividing the region for $\gamma \geq 0.73$ into two zones: (i) rigid zone, when the available moment redistribution 'Rm_a' is higher than the Rm_r; and (ii) semi-rigid, when Rm_a is lower than Rm_r. The available moment redistribution (Rm_a) depends on the beam section properties including A_s, f_y and f_c (refer to Appendix I)

$$M_S = \frac{w\,L^2}{24} \cdot \frac{2\,(3 - 1.5\,\gamma)}{2 + \gamma} \tag{8.11a}$$

$$\delta m_r = \frac{1}{\dfrac{2\,(3 - 1.5\,\gamma)}{2 + \gamma}} \tag{8.11b}$$

$$Rm_r = 1 - \delta m_r = 1 - \frac{1}{\dfrac{2\,(3 - 1.5\,\gamma)}{2 + \gamma}} \tag{8.11c}$$

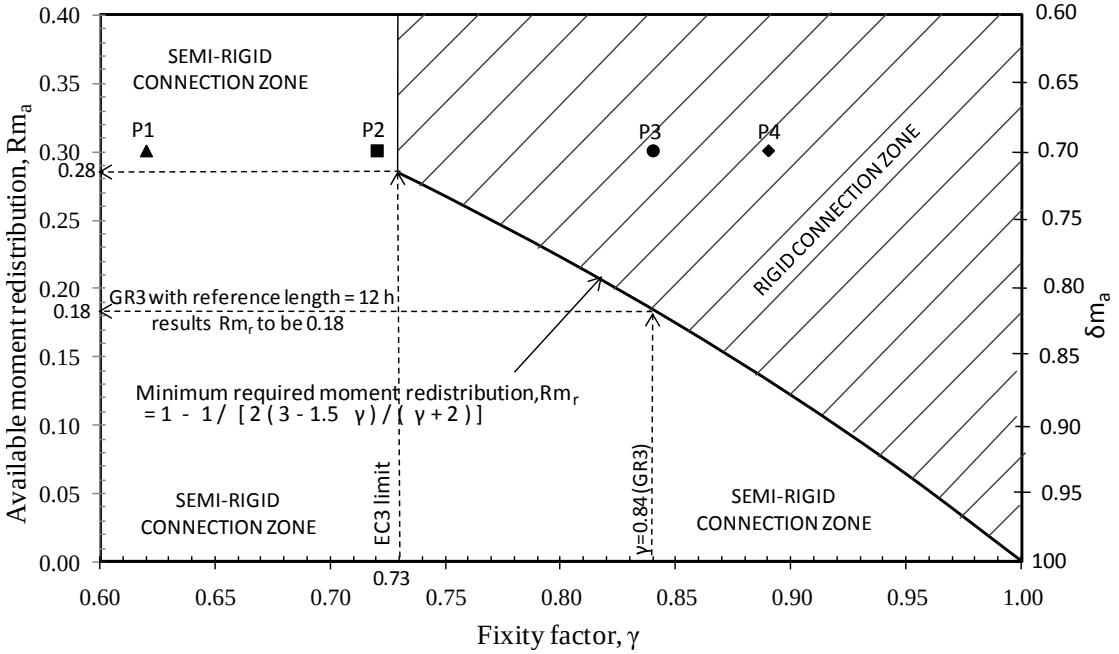

Figure 8.17 Concrete beam-column connection classification zones for γ not less than 0.73

As shown in Figure 8.17, for γ equal to 0.73, the value of Rm_r is 0.28, which is less than the maximum permissible moment reduction (Rm = 0.3). Therefore, to guarantee this moment redistribution in beam sections, the reinforcement ratio in the

beam sections needs to be kept lower than certain values, as has been shown in the previous section. For higher steel reinforcement ratios, as the Rm_a will be lower; therefore, the value of γ should be higher than 0.73 to consider a connection as rigid. In the next section, the application of this proposed approach will be applied to the specimens tested under gravity loads within series GR.

It should be stated that the above-mentioned considerations for the semi-rigid behaviour in concrete beam-column connections is based on the simplified linear moment-rotation relation (S_y) presented in Figure 8.13. If the full non-linear behaviour of concrete is considered in the frame analysis, the concrete beam-column connection will behave in a way closer to the rigid behaviour at the early loading stages in comparison with the behaviour at the yielding stage. The implications of using the full non-linear beam-column rotation result in a lesser beam deflection (in comparison to that calculated using S_y at the same early loading stage) and a larger beam-end moment/mid-span moment ratio under service loads in comparison with the case of using the linear moment-rotation relation. This feature has been also mentioned in Section 8.5.1 within the introduction to the semi-rigid behaviour.

8.5.3.3 Specimens of series GR

Using the rotational stiffness obtained from specimens GR1 and GR3, the required moment redistribution 'Rm_r' was calculated for two beam spans: (i) a reference beam span of 4.8 m, which is equal to 12h (h: beam total depth), and (ii) the span length (7.3 m) of the prototype frame (Appendix A). The calculations for Rm_a and Rm_r are presented in Appendix I, and the outcomes are tabulated in Table 8.3.

Points P1 to P4 in Figure 8.17 represent the four study cases in Table 8.3. From the projection of these points, it is clear that specimen GR1 is classified as semi-rigid in

both span cases, while specimen GR3 is classified as rigid in both span lengths. This would mean that, if we accept the rigid frame analysis for a connection of type GR3 in a 4.8 m span (point P3), there is already 18% moment redistribution assumed to happen from the mid-span to the support (Figure 8.18).

Table 8.3 Moment redistribution evaluation in specimens GR1 and GR2

Specimen	Point in Figure 8.17	L/h	γ	Achieved moment (semi-rigid/rigid)		δm_r	Rm_r	Rm_a
				End-span	Mid-span			
GR1	P1	12.00	0.63	0.71	*1.57*	1/1.57=0.64	*0.36*	*0.3*
	P2	18.25	0.72	0.79	*1.42*	1/1.42=0.71	*0.29*	*0.3*
GR3	P3	12.00	0.85	0.89	*1.22*	1/1.22=0.82	*0.18*	*0.3*
	P4	18.25	0.89	0.93	*1.15*	1/1.15=0.87	*0.13*	*0.3*

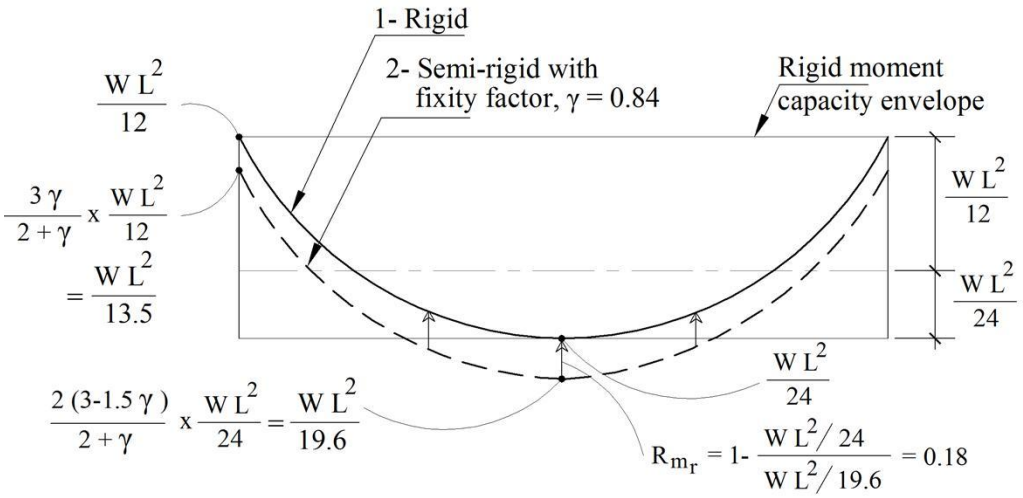

Figure 8.18 Rm_r of specimen GR3 in 4.8 m beam span (L/h=12)

Based on the above discussion, it could be stated that, in precast concrete construction, to classify a beam-column connection as rigid under gravity loading, the below steps should be followed.

1) The fixity factor should be greater than or equal to 0.73.
2) Perform a rigid-analysis to design the beam mid-spans and end-spans.
3) Calculate the available moment distribution 'Rm_a' from the mid-span towards end-spans.

4) Project the calculated values of γ and Rm_a in Figure 8.17.
5) If the projection is within the shaded area, the assumption of performing the rigid analysis was valid; otherwise, the connection should be dealt with as semi-rigid.

In addition to the above, to ensure the strong connection concept in the connection type investigated in this study, the below points should be taken into consideration.

1- Providing additional short steel bars at the top of the beam-end within the connection, of length equal to column width 'h_c' plus 2 times the beam depth 'h' (h_c+2h) and area equal to that required based on a rigid analysis.
2- Using horizontal U-shaped beam links with spacing not greater than 100 mm within the connection zone, starting from the column face to a distance equal to the beam depth.

8.6 Design considerations under sway loads

As shown in Chapter 6, the behaviour of the beam-column connection configuration investigated under sway loads has been improved, by using the reinforcement connection of type T3, in the areas of:

i) developing the full dowel action mechanism;
ii) spreading the cracking along the beam.

However, there was a large crack width at the column-beam face accompanied by a low rotational stiffness. The effects of such stiffness were shown in Section 8.4 to be enormous with respect to the sway produced, column base moments and the second order effects. All these suggest that the connection configuration is not suitable to be relied on to provide frame actions when there is a net sagging moment at the beam-ends. In this respect, the configuration could be used in unbraced frames when the temporary

wind load end-beam sagging moments are counterbalanced by the dead load hogging moments.

8.7 Summary and conclusion

In this chapter, three different ways of incorporating beam-column flexibility in frame analysis have been presented, and they have been used to evaluate the use of the connection configuration studied in the current research in frames subjected to gravity and sway loading. Also, a new classification approach has been presented to assess the behaviour of precast concrete beam-column connections with fixity factor ≥ 0.73. Based on the evidences obtained from this chapter, the following conclusions could be drawn.

A) Semi-rigid analysis

1- A simplified semi-rigid frame analysis has been calibrated to work for 1st and 2nd order frame analyses under gravity and sway loads.

2- In semi-rigid beam-column connections, the full hogging moment achieved in a cruciform test could be obtained in real frames if the mid-span is designed adequately for the moments obtained from semi-rigid frame analysis.

3- For semi-rigid frame analyses, the yield secant rotational stiffness was suggested to characterise the flexibility of the beam-column connection.

B) Evaluation of the beam-column connection specimens tested under gravity loading

1- A new approach has been presented to deal with precast concrete beam-column connections with fixity factor $\gamma \geq 0.73$ (assumed rigid zone) based on the relation between the required moment redistribution and the available one.

2- A precast concrete beam-column connection with γ equal to 0.73 could be classified as rigid if the available moment redistribution 'Rm_a' in the mid-span is not less than 28%. For higher values of γ, lower values of Rm_a are required.

3- Specimen GR1 is classified as semi-rigid (under gravity loads).

4- Specimen GR3 is classified as rigid (under gravity loads).

C) Evaluation of the beam-column connection specimens tested under sway loading

1- Under pure sagging moments at the beam-ends, using the experimental rotational stiffnesses in frame analyses increased significantly the column-base moments and the sway.

2- However, the connection could be used in unbraced frames as long as the temporary sagging moments generated from lateral loading are counterbalanced by the permanent dead load hogging moment at the beam-ends.

CHAPTER 9

CONCLUSIONS AND RECOMMENDATIONS

9.1 Introduction

Experimental, analytical and numerical investigation has been carried out aiming to assess and modify the behaviour of the discontinuous precast concrete beam-column connection, and to develop the basis for establishing the main design principles. To achieve the aims of the study, the research accomplished the following objectives.

A- Conducted small-scale biaxial bearing capacity tests to investigate the effect of the joint infill status and the ultimate bearing capacity of the column. The outcome of this was used in the design of the full-scale beam-column tests.

B- Generated moment-rotation (M-θ) data, under separate gravity and sway loads, from experimental full-scale beam-column tests.

C- Evaluated the sufficiency of the connection under gravity and sway loading conditions by implementing the M-θ data in frame analysis techniques.

D- Calibrated a simplified approach replicating the true M-θ behaviour in a semi-rigid frame analysis.

E- Established a new approach to classify concrete beam-column connections as rigid.

To achieve objective B, the connection reinforcement detail was taken as the main variable, intending to achieve the full moment capacity of the beam with enhanced rotational stiffness, adequate serviceability behaviour, and sufficient ductility with limited damage at the connection zone. The reference connection reinforcement detail (T1) included the below modification in comparison with that exists in practice.

i) Providing a beam-end hogging moment resistance capability under dead loads by providing continuity top bars within a trough made at the top of the beam, which will be grouted before installing the floor system.

ii) Grouting the vertical joint in the connection.

In addition, two other reinforcement details, T2 and T3, were investigated. T2 included adding horizontal U-shaped links at the beam-ends within the connection, while T3 included, in addition to the horizontal links, using short steel bars crossing the connection at the top of the beam and using additional column links at the top and bottom levels of the beam. It should be mentioned that the beam-column moment – rotation data is only applicable to the discontinuous precast concrete beam-column type investigated in the current study.

This chapter summarises first the major experimental results in addition to the observations from the analytical and numerical study, and then presents the findings of the current research followed by recommendations for further research.

9.2 Experimental work

The main results of the experimental parts are summarised in the next sub-sections.

9.2.1 Small-scale bearing capacity tests

- The vertical joint between the beam-ends within the connection is required to be grouted to counterbalance any compression forces from the beam.
- Grouting of all the three joints at the connection using cement-based grout led to a uniform stress distribution in the adjoining members.

- The existence of the vertical grout increased the ultimate bearing capacity of the column by a ratio proportional to the ratio of its cross-section area to the column cross-section area.
- The existence of the grout layers at the horizontal joints between the column and connection had no noticeable effect on the ultimate bearing capacity of the column.
- The use of a grout with thickness equal to 1/15 of the minimum dimension of the adjoining members and of strength between 50% and 100% of that of the adjoining members produced a bearing capacity not less than 89% of that of a single concrete block without a joint.
- Based on the above-mentioned points, all the three joints in the connection within the full-scale beam-column tests were designed to be filled using cement-based grouts of geometry and strength as stated above.

9.2.2 Full-scale beam-column tests under gravity load (series GR)

- Specimen GR1: embedding the top beam main steel bars in the trough (using the reference connection reinforcement type T1) introduced the anticipated hogging moment capacity that would work under both dead and live loads. However, the capacity was accompanied by a concentration of cracks within the connection prior to yielding. This specimen was classified as semi-rigid.
- Specimen GR2: providing horizontal links at the beam ends (detail T2) led to a better crack distribution, where a controlled crack width region was observed within 300 mm from the column face, and the maximum crack width located beyond this region. However, detail T2 failed to prevent the final damage occurring within the connection. This specimen was classified as semi-rigid.

- Specimen GR3: the addition of the 2H20 short bars to the beam-ends within the connection (detail T3) prevented the concentration of the final damage occurring in the connection zone, starting at 400 mm from the column face, coincidentally where the additional 2H20 bars and the horizontal links are terminated. This specimen was classified as a rigid connection.

9.2.3 Full-scale beam-column tests under sway load (series SW)

- Specimen SW1: the reference connection reinforcement detail (T1) was found to be unsuccessful in mobilising beam sagging moments through the column dowel bars. The main improper feature in this detail was bending the beam bottom bars at the connection to the top to form the beam top bars.
- Specimen SW2: by using reinforcement detail T3, it was possible to develop the dowel action in the column bars to mobilise the beam sagging moment. The new detail was capable of reducing the crack width at the beam-column interface, but the large crack was still there with a width of 0.3 mm at 50% of the predicted moment capacity. The results showed that the critical part in the connection configuration, under sway loads, is the beam-ends rather than the column-ends.
- Specimen SW2: the experimental rotational stiffness was evaluated by conducting 1st order and 2nd order semi-rigid analysis of frames comprising such connection under sway loads. The effects were very significant in raising the column base moments and the sway.
- Specimen SW2: based on the above two observations, it was concluded that the beam-column connection tested in the current study does not provide sufficient frame action to be used in resisting beam sagging moments.

9.3 Theoretical modelling

The theoretical observations resulted from the current study are listed below.

- An analytical calculation model has been introduced to characterise the moment-rotation relation of specimens GR1 and GR2, which showed semi-rigid behaviour under gravity loading. Compared with the experimental results, the model offered a sensible estimation for the flexibility of the connection.
- An FE model has been developed to replicate the semi-rigid behaviour of specimens GR1 and GR2 under gravity loading. The FE model was able to predict the behaviour in the elastic range; however, it could not predict the behaviour beyond the yielding. This was attributed to the simplified way of modelling the interaction between the corrugated sleeves and the surrounding concrete at the beam-ends within the connection.
- In addition to the requirement of the fixity factor of a connection to be not less than 0.73, to classify a precast concrete beam-column connection as rigid, the available moment redistribution from the mid-span to the support should be higher than the difference between the rigid mid-span moment and the moment resulting from a semi-rigid frame analysis.
- In a semi-rigid frame analysis, the beam stiffness used in the analysis (whether full EI or 0.5EI is used) has a significant impact on the moment distribution under gravity loading.
- The beam-line analysis of beams with semi-rigid ends could be utilised to achieve the full yield moment capacity of the connection.

9.4 Research findings

Based on the experimental and analytical evidences gathered in the current study, the following findings can be summarised.

A) The precast concrete discontinuous beam-column connection investigated in the current study:

- provides a hogging moment capacity under dead loads as well as under live loads;
- could be dealt with as an equivalent monolithic connection under gravity loading by using the strong connection concept;
- is able to mobilise beam-end sagging moments through the dowel action mechanism of the column main bars. However, as this was accompanied by low rotational stiffness and concentration of cracks at the beam-column interfaces, the connection is not suitable to resist net sagging moments.

B) The beam-line analysis can be extended to achieve the full moment capacity of the connection.

C) The simplified semi-rigid analysis using short stubs with appropriate stiffnesses, reflecting the connection flexibility, was found to give the exact solution when the stub length approaches zero.

D) For a realistic classification of precast concrete beam-column connections as rigid, it is required to correlate the fixity factor with the moment redistribution.

E) In the FE modelling of the beam-column configuration investigated in the current study, the critical component that diverged the model from the correct response is the interaction between the corrugated sleeves and the surrounding concrete at the beam-ends within the connection.

9.5 Proposed future work

While the findings are encouraging with respect to modifying the connection configuration, there are still some issues that need to be addressed by further researches. Some of these issues are listed below.

- Conducting further experimental tests on the connection configuration by testing the effect of the following parameters: column size; beam size; beam reinforcement ratio; and the applied load ratio on adjacent beam spans.
- Conducting further experimental tests to improve the bond condition between the grout and the reinforcement in the beam trough by special means including using steel fibres.
- The analytical model presented in the study to predict the rotational stiffness of the semi-rigid connections (specimens GR1 and GR2) needs to be validated against further experimental results.
- The FE model is required to be improved by including more representative models for: (i) the interaction between conduct sleeves and surrounding concrete; and (ii) the interaction of the ends of beam side steel bars with the connection.

Appendix A - Prototype building design

The design of the components of the beam-column connection tested in the current study (Chapters 4 to 6) was based on a rigid frame analysis of a prototype building consisting of three spans and four floors (Figure A.1). The members' dimensions, material properties, dead and live loads, loading cases are tabulated in Table A.1. The bending moment diagrams resulted at joint location A for three load cases are shown in Figure A.2.

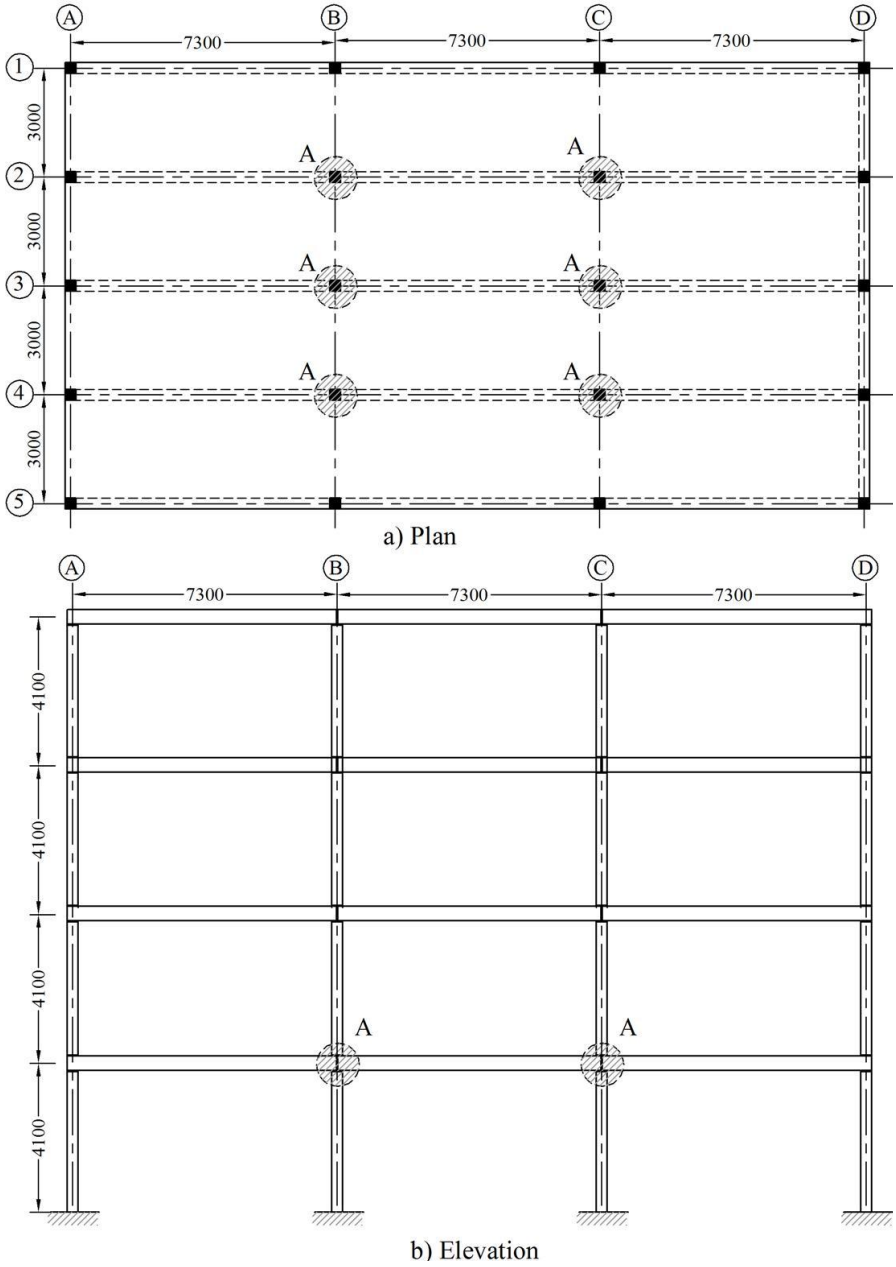

Figure A.1 Prototype building

Table A.1 Prototype building design data

Geometry and material specifications		
Beam	Width x Height (mm)	300 x 400
Column	Size (mm)	300 x 300
Main Steel	f_y (Mpa)	570
Link steel	f_y (Mpa)	570
Concrete	f_c (Mpa)	50
Loading		
Live load (LL) kN/m^2, EC1(CEN, 2004a)	Roof	1.5
	Other floors	2.0
Dead load (DL) kN/m^2	Roof	3.5
	Other floors	3.5
Wind load (WL)*	Wind velocity	40 m/s
	Size coefficient	1
	Dynamic coefficient	1
	Force coefficient	1
Load cases, EC0 (CEN,2002)		
Load case 1		1.35 DL + 1.50 LL
Load case 2		1.00 DL + 1.50 WL
Load case 3		1.00 DL + 1.05 LL + 1.50 WL
*The wind load is calculated using Equation $q_s = 0.625 * V^2$, EC1 (CEN, 2005a), q_s in N/m^2, in m/s		

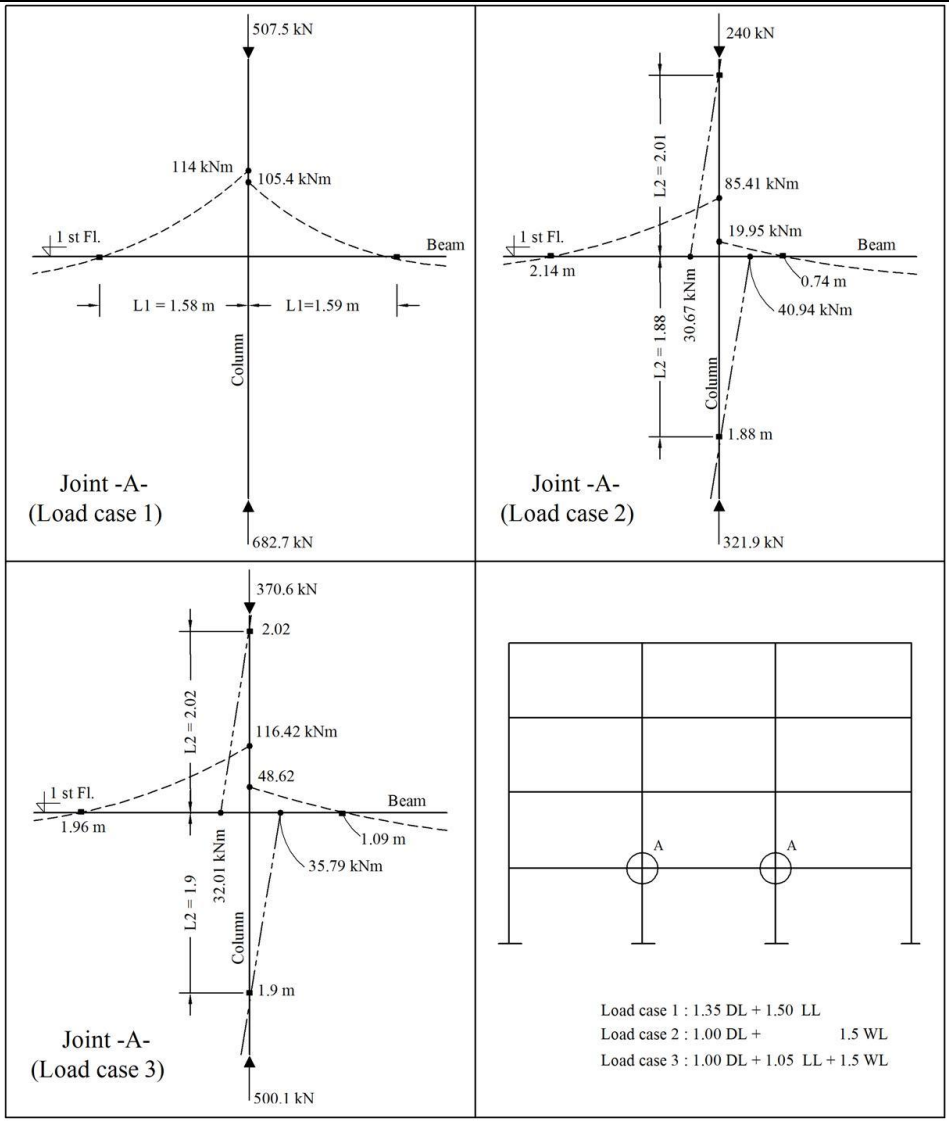

Figure A.2 Moment diagram at joint A for all load cases

The reinforcement design for the member section was done using EC2 (CEN, 2004b), and the outcomes of the design regarding the beam are shown in Table A.2.

Table A.2 Beam design results in the pprototype frame at joint A

		Design result	Used	Notes
Main	Top	2H20	2H20	
	Bottom	2H20	2H20	
Links		12H10@ 276 mm	H10: 3@100 mm, 6@200 mm	To test the beam for bending moment only

Regarding column main bars, the analysis showed that only minimum reinforcement is required. In spite of this, 2H20 were provided at each column face the same as beam bottom bars. The reason behind this was to investigate the capability of the connection to mobilise beam sagging moments.

Regarding column links, close spacing was used at the ends where the splitting failure might occur; elsewhere, minimum link spacing was provided.

The distances L1 and L2 in Figure A.2 were used as lever arms for applying the loads in series GR and SW, respectively (see Figure 4.1)

Appendix B – Construction details of full-scale tests

The assembly of the sub-frames (beam-column connections) was conducted in two ways: horizontally (four tests, GR1,GR3, SW1, and SW2); and vertically (one test, GR2). The details of the test setup are presented in the below order:

i) The test setup of specimens GR1 and GR3 is shown in Figure B.1 to Figure B.3

ii) The test setup of specimen GR2 is shown in Figure B.4 to Figure B.6

iii) The test setup of SW is shown in Figure B.7 to Figure B.9.

In all tests, first, the bottom column was put in place, and then the two beams were assembled on the column by passing the steel bars protruding from the lower column through conduct sleeves in the beam within the connection. Then, the beam-continuity bars were passed through the beam trough and tied with the beam links. After that, the top column was set in place and received the lower column steel bars in pre-made conduct sleeves; 20 mm gaps were left between adjoining beams and columns. These gaps in addition to the beam trough and the conduct sleeves were filled with in situ self-compacted grout to form a composite beam-column connection.

Thick packed steel plates were provided at the locations of load application and reaction points to prevent local bearing failures throughout the test. In addition, before testing, the specimen faces were white painted to facilitate the crack inspection. It is worth mentioning that in the horizontal mode of assembling, and in order to reduce the friction between the members and the ground, contact was made through small contact areas using oiled hard wooden pieces, as shown in Figure B.2 and Figure B.8.

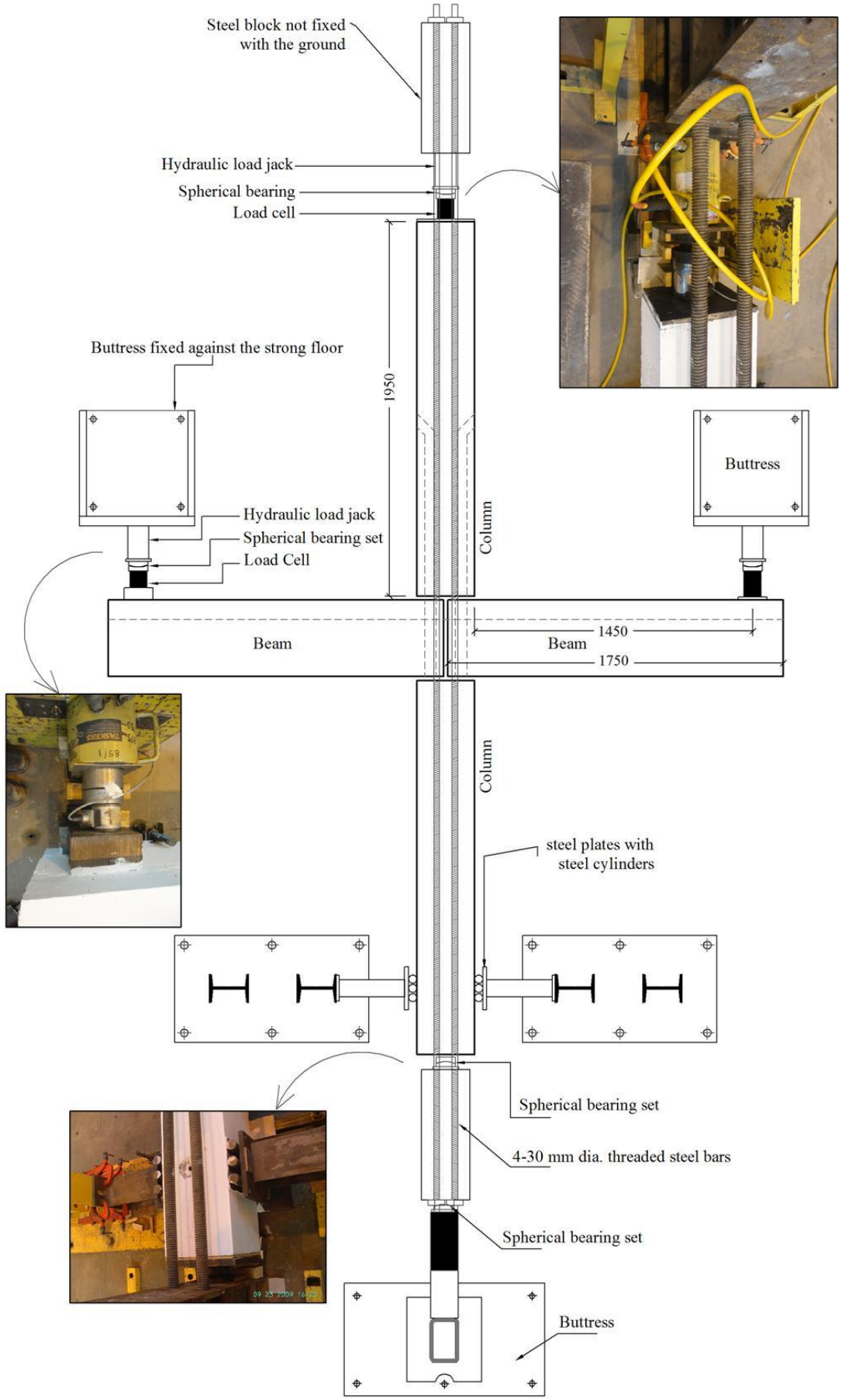

Figure B.1 Test rig plan of specimens GR1 and GR3

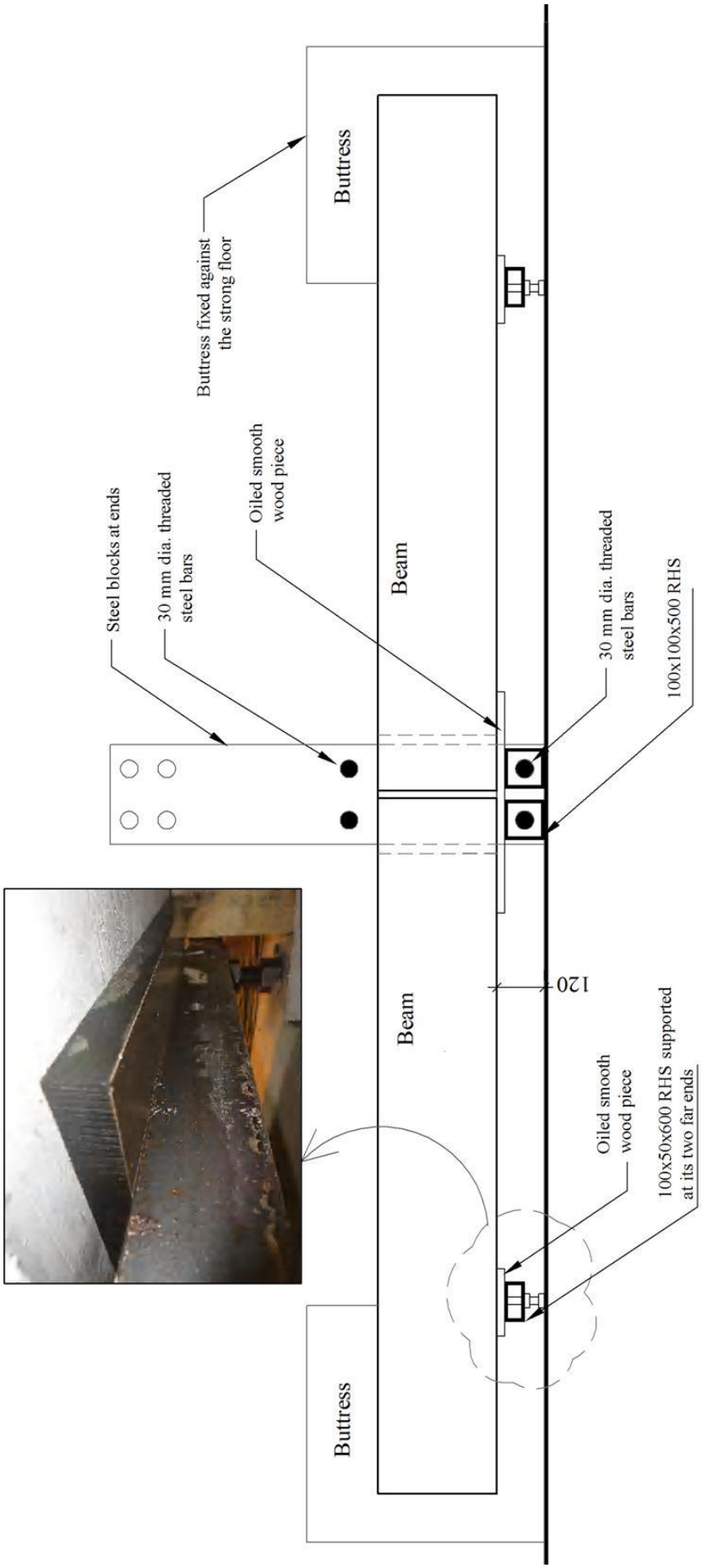

Figure B.2 Test rig elevation of specimens GR1 and GR3 (longitudinal section through the beam)

a) Form work for grouting

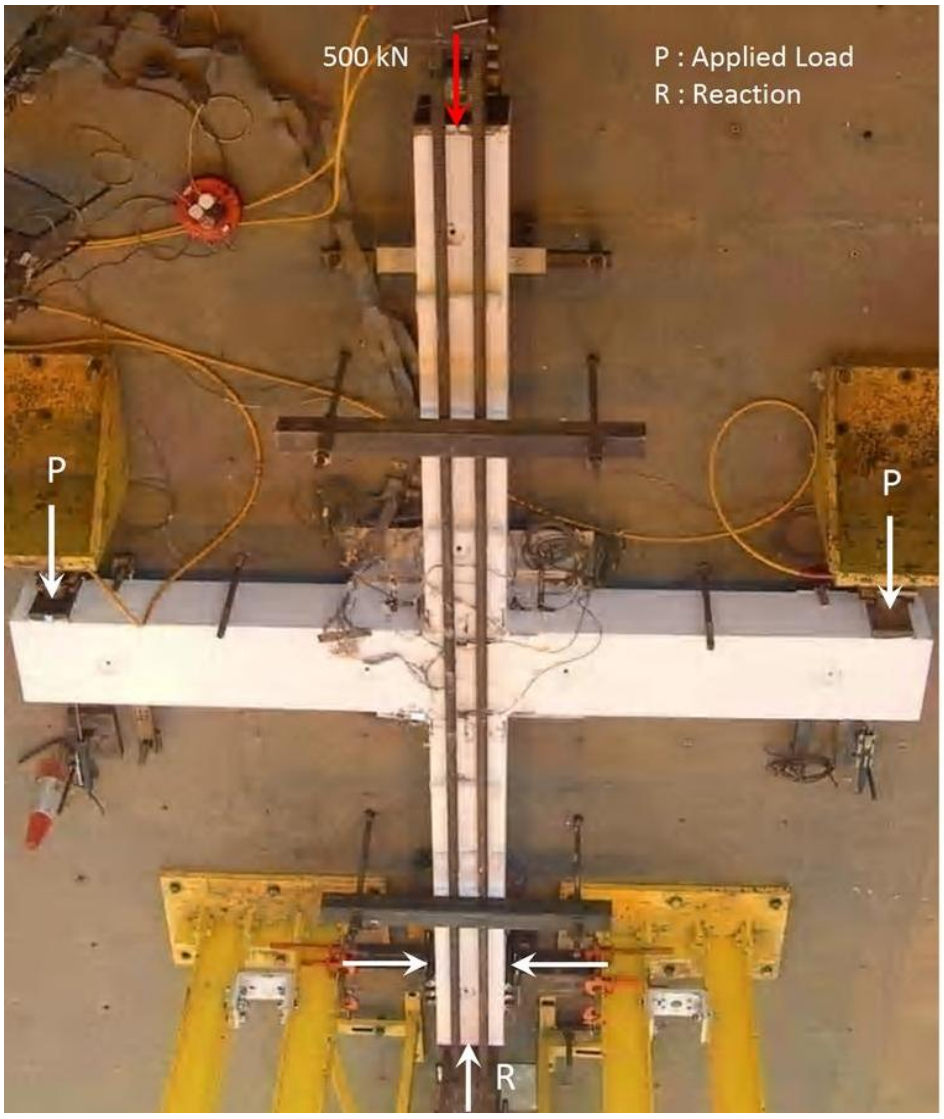

b) Loading configuration

Figure B.3 General set up of specimens GR1 and GR3

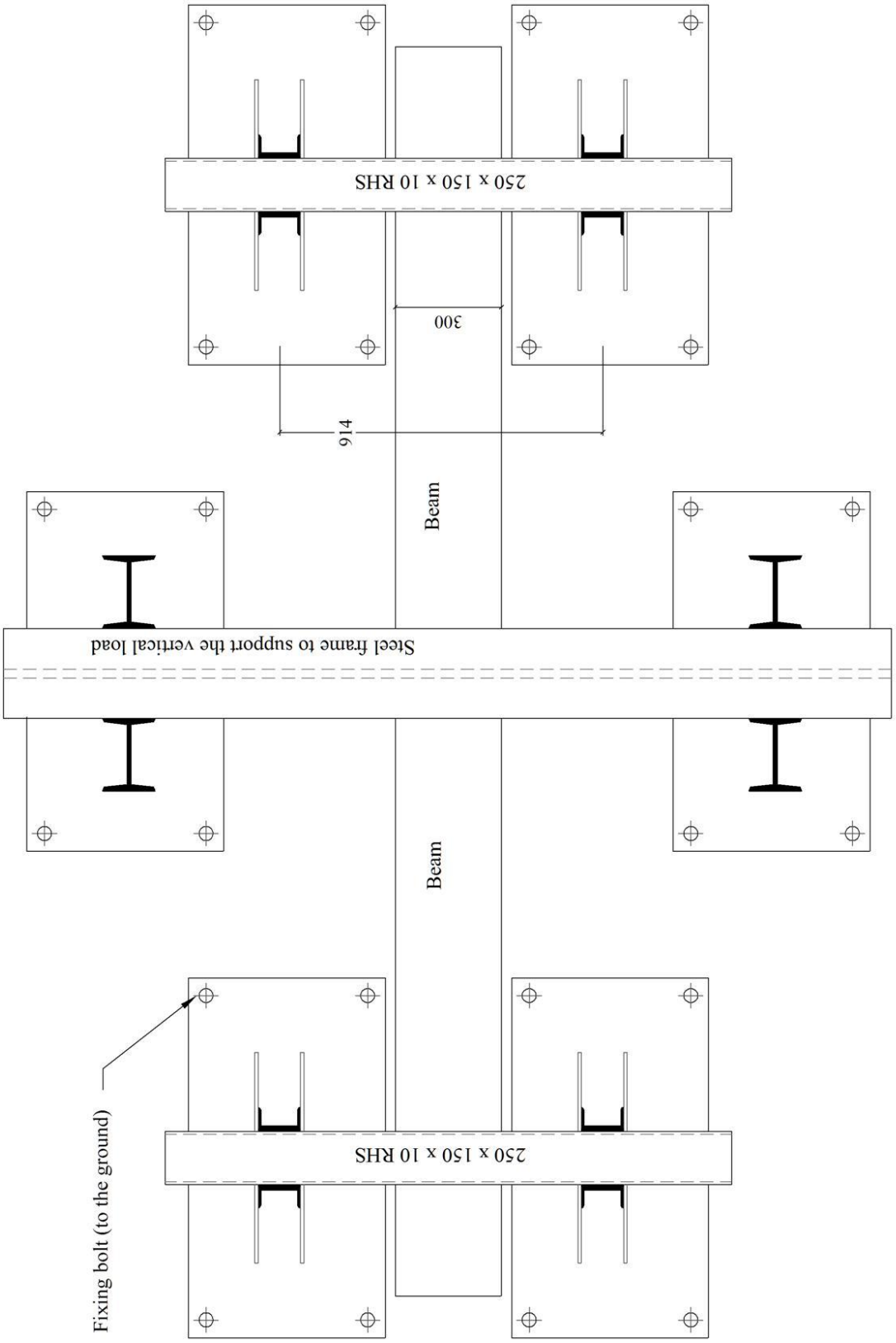

Figure B.4 Test rig plan of specimen GR2

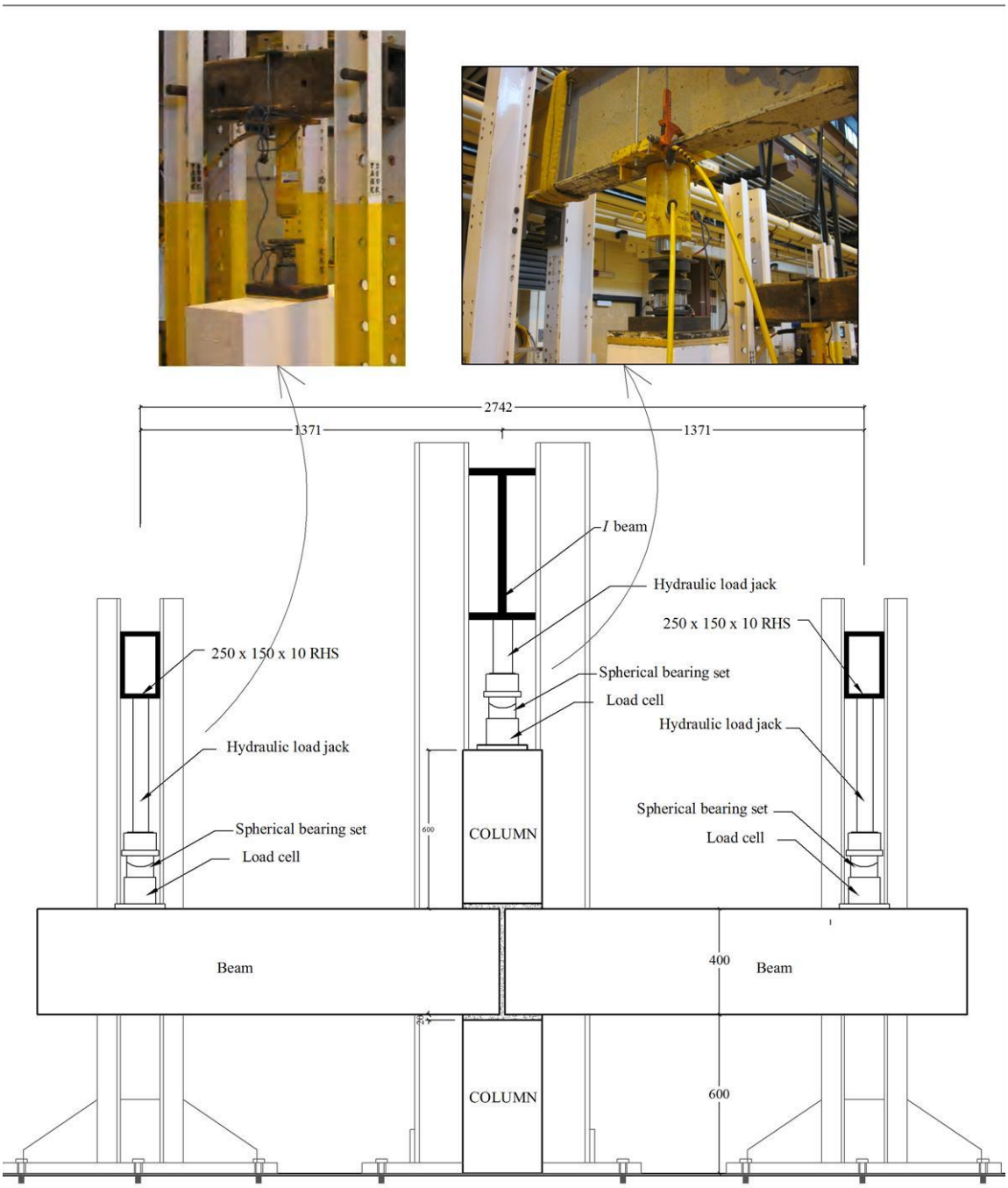

Figure B.5 Test rig elevation of specimen GR2
(longitudinal section through specimen)

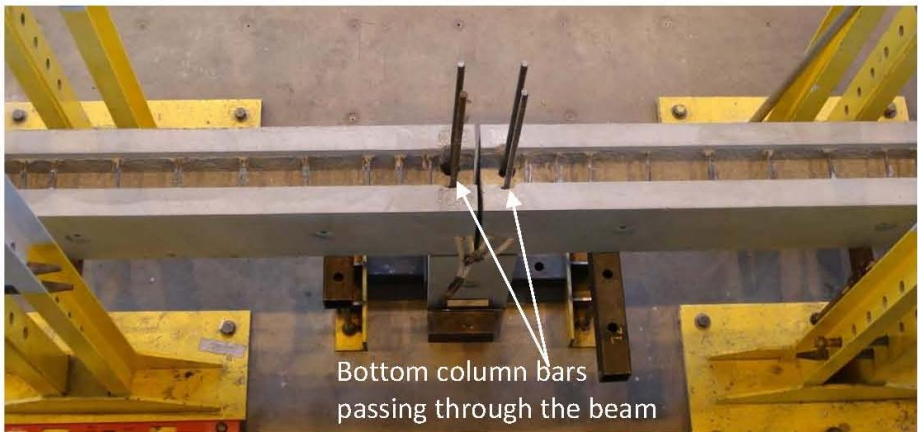

a) Assembling of the beams

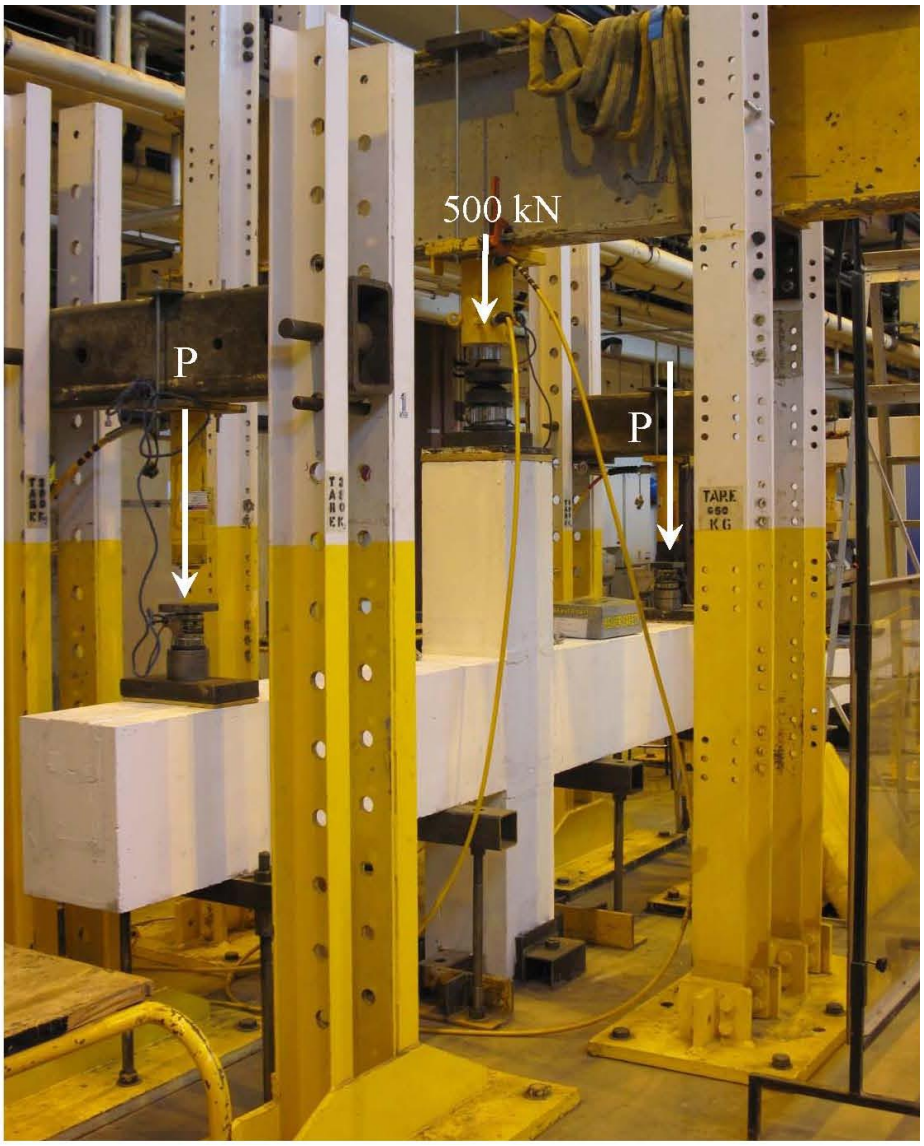

b) Loading configuration

Figure B.6 General set up of specimens GR2

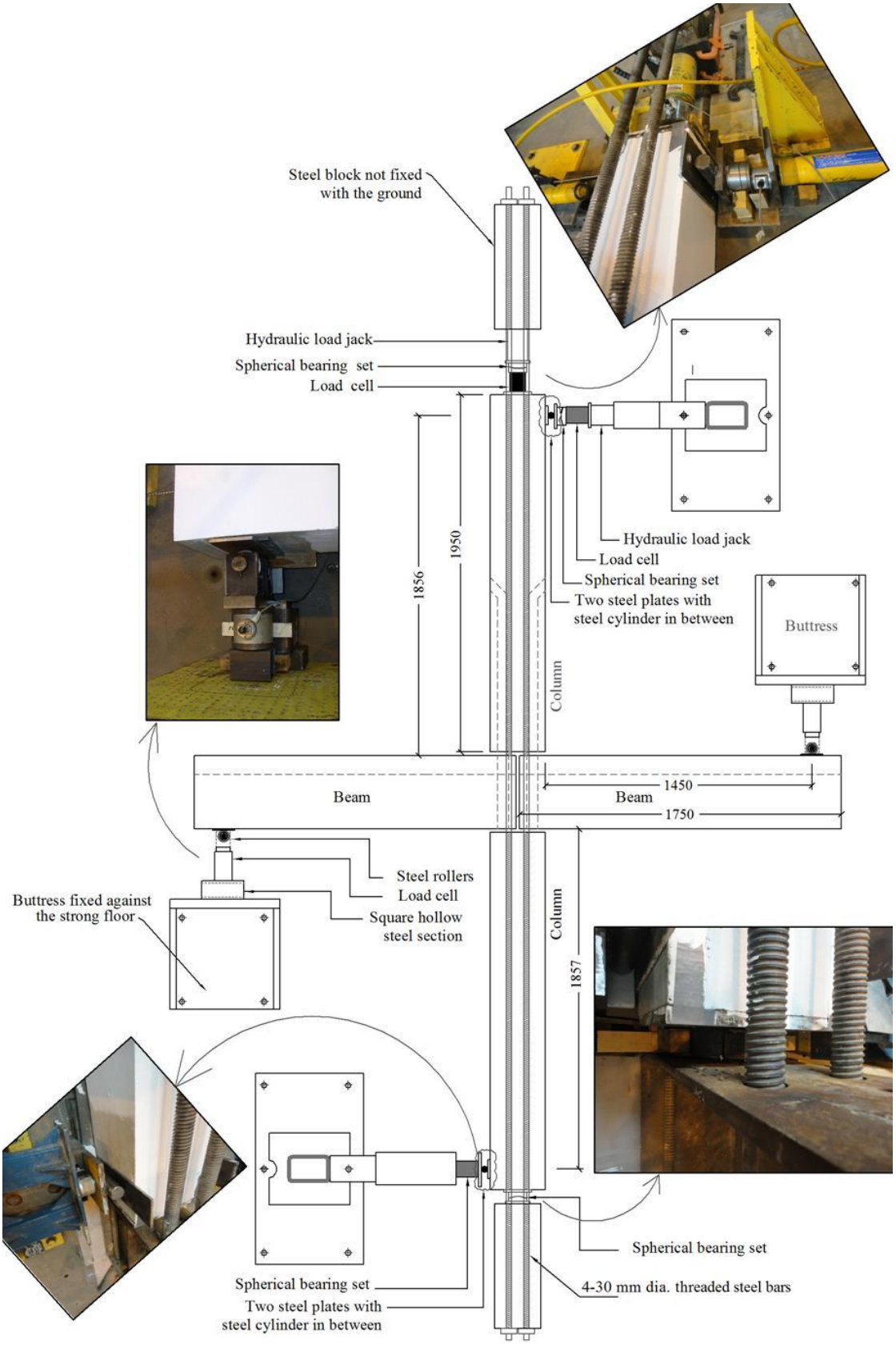

Figure B.7 Test rig plan for series SW

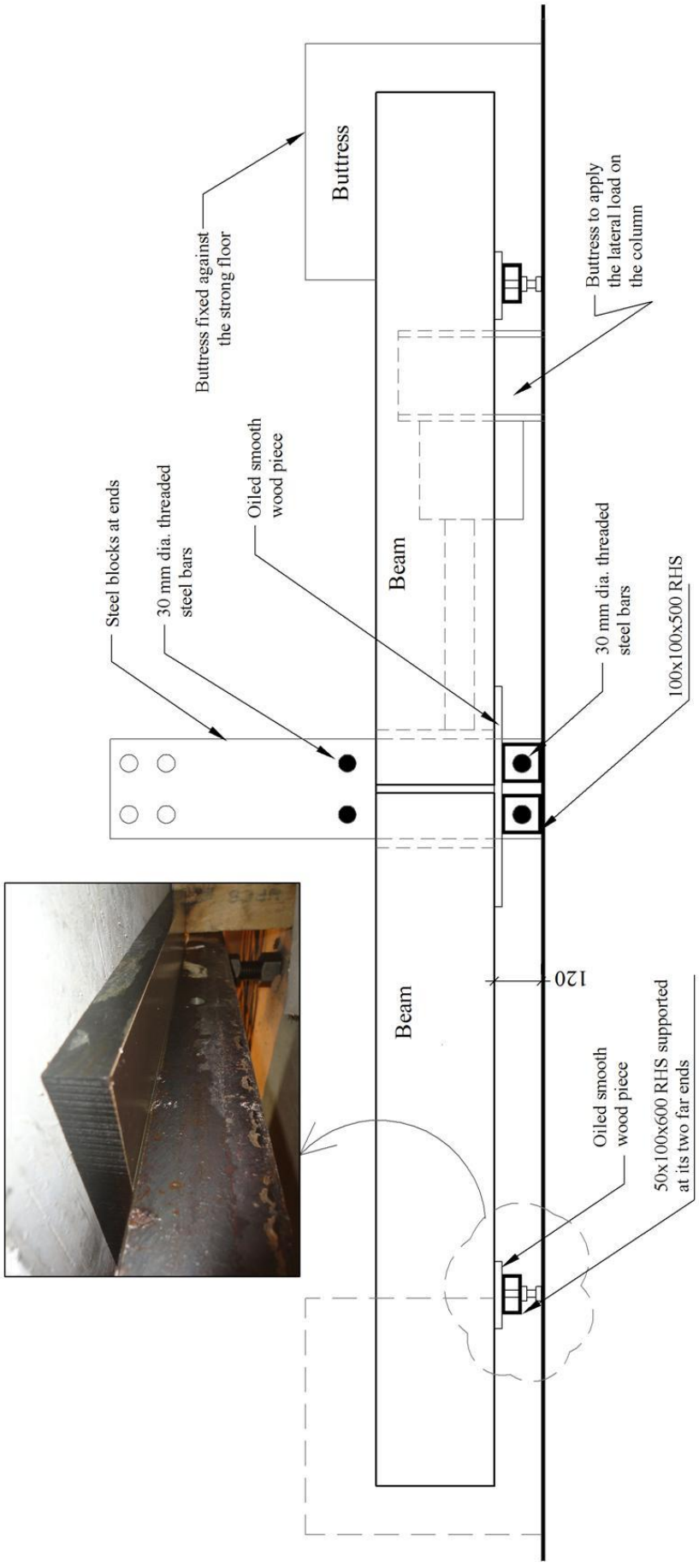

Figure B.8 Test rig elevation of series SW (longitudinal section through the beam)

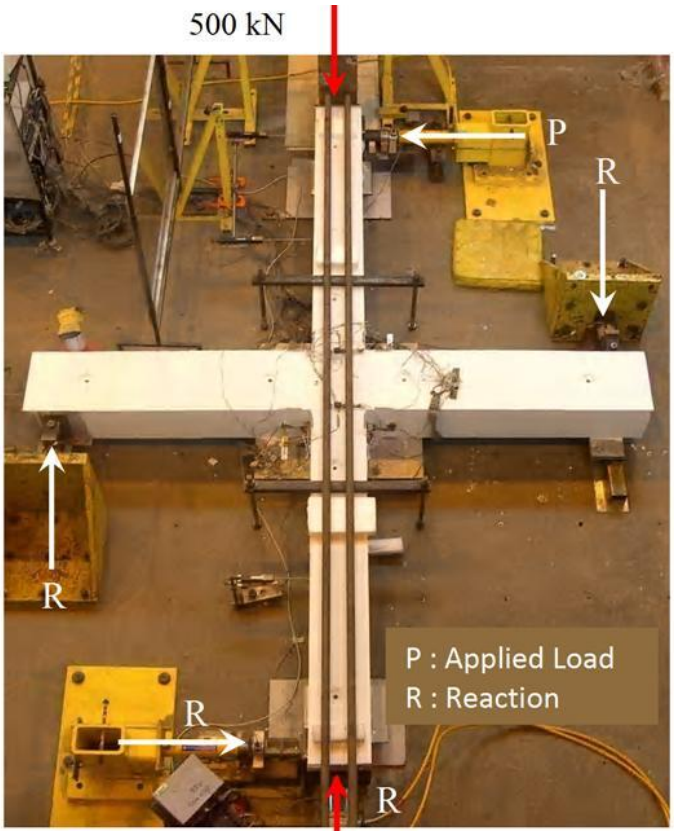

a) Cycles with the top column being applied to the left

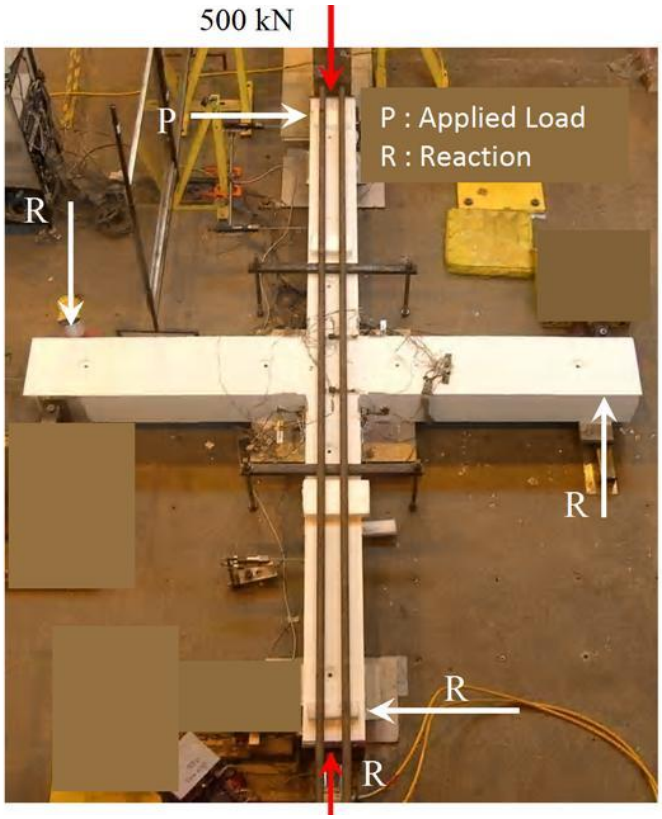

b) Cycles with the top column being applied to the right

Figure B.9 Loading configuration in series SW

Appendix C - Instrumentation of full-Scale Tests

In the tests carried out in series GR and SW within the full-scale beam-column programme (Chapters 4, 5 and 6), measurements of strains in reinforcing bars and concrete near to the joints and displacements of the beams and columns were recorded. For concrete, strain gauges of 60 mm length (as triple the size of the maximum coarse aggregate) of the PL-60-11 type were used, while for the reinforcing bars, strain gauges of 10 mm length of the FLA-10-11 type were used.

The displacements were recorded using potentiometer transducers with a different measured displacement range (15 mm, 20 mm, 50 mm). In addition, the relative beam-column rotations were calculated based on the relative displacements at the beam-column interfaces. The data were recorded using a multi-channel computer-operated data acquisition system (3531D, F & G).

The readings of strain gauges and potentiometers were recorded at zero loads, then at the end of each load increment. During the load increments, close inspection was made by naked eye to locate the crack propagation.

In test series GR, three load cells were used to record the magnitude of loads applied on beam 1, beam 2, and the top column. The axial load magnitude on the column was monitored so that it was constantly kept at 500 kN, during applying the beam loads. The testing and inspection process took about 3-4 hours. The instrumentation layout and sensor functions in specimens GR1, GR2, and GR3 are shown in Figure C.1 to Figure C.3, and Table C.1 to Table C.3.

In test series SW, five load cells were used to record: (i) the two applied loads at the top column (constant 500 kN axial load, and variable lateral load); (ii) the two

vertical reactions at the beam ends, and (iii) the lateral reaction at the bottom column. The axial column load magnitude was monitored so that it was constantly kept at 500kN, during applying the beam loads. The testing and inspection process took about 2-3 hours for each half cycle. The instrumentation layout and sensor functions in specimens of series SW are shown in Figure C.4 and Table C.4.

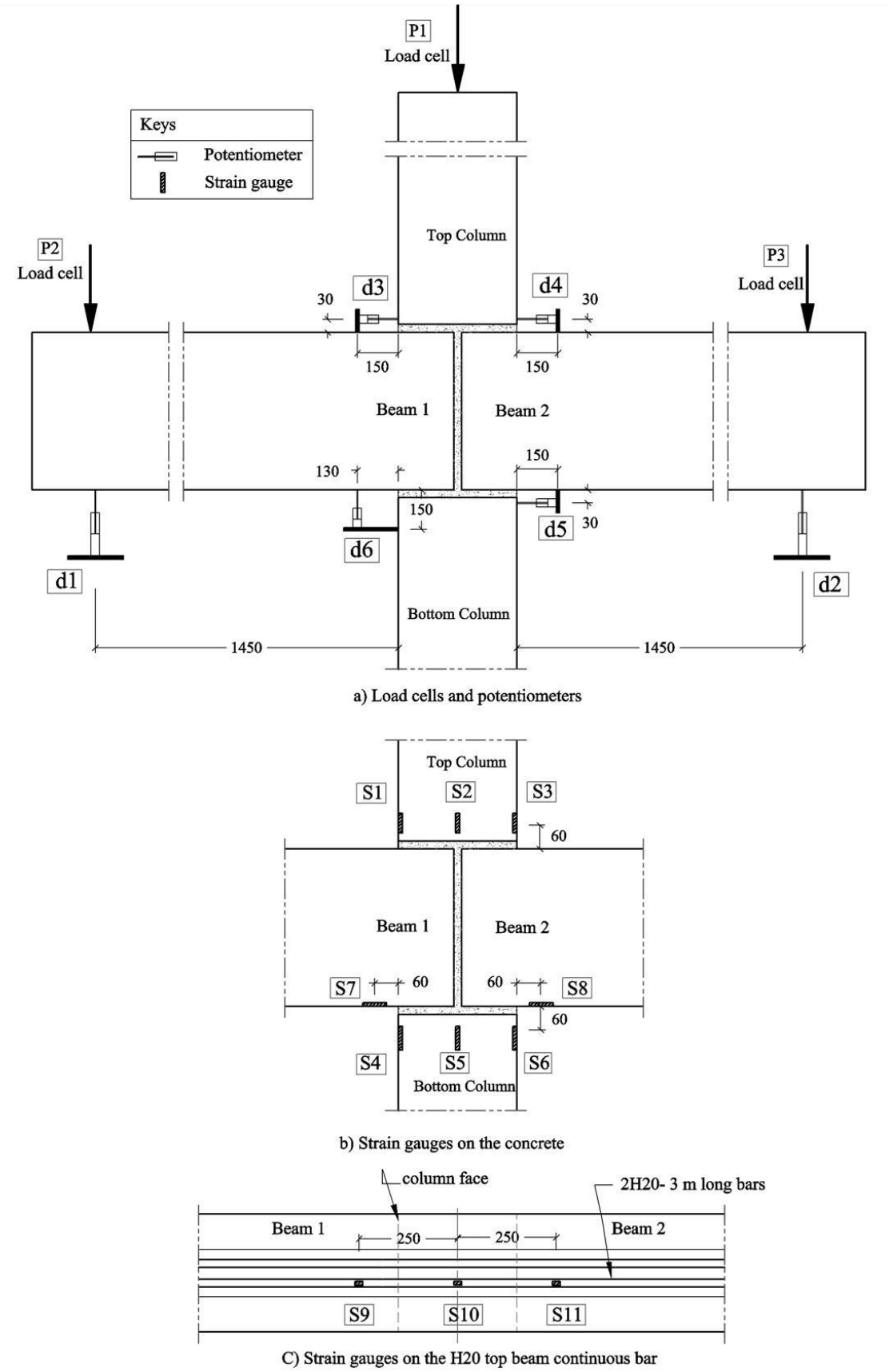

Figure C.1 Instrumentation layout in specimen GR1

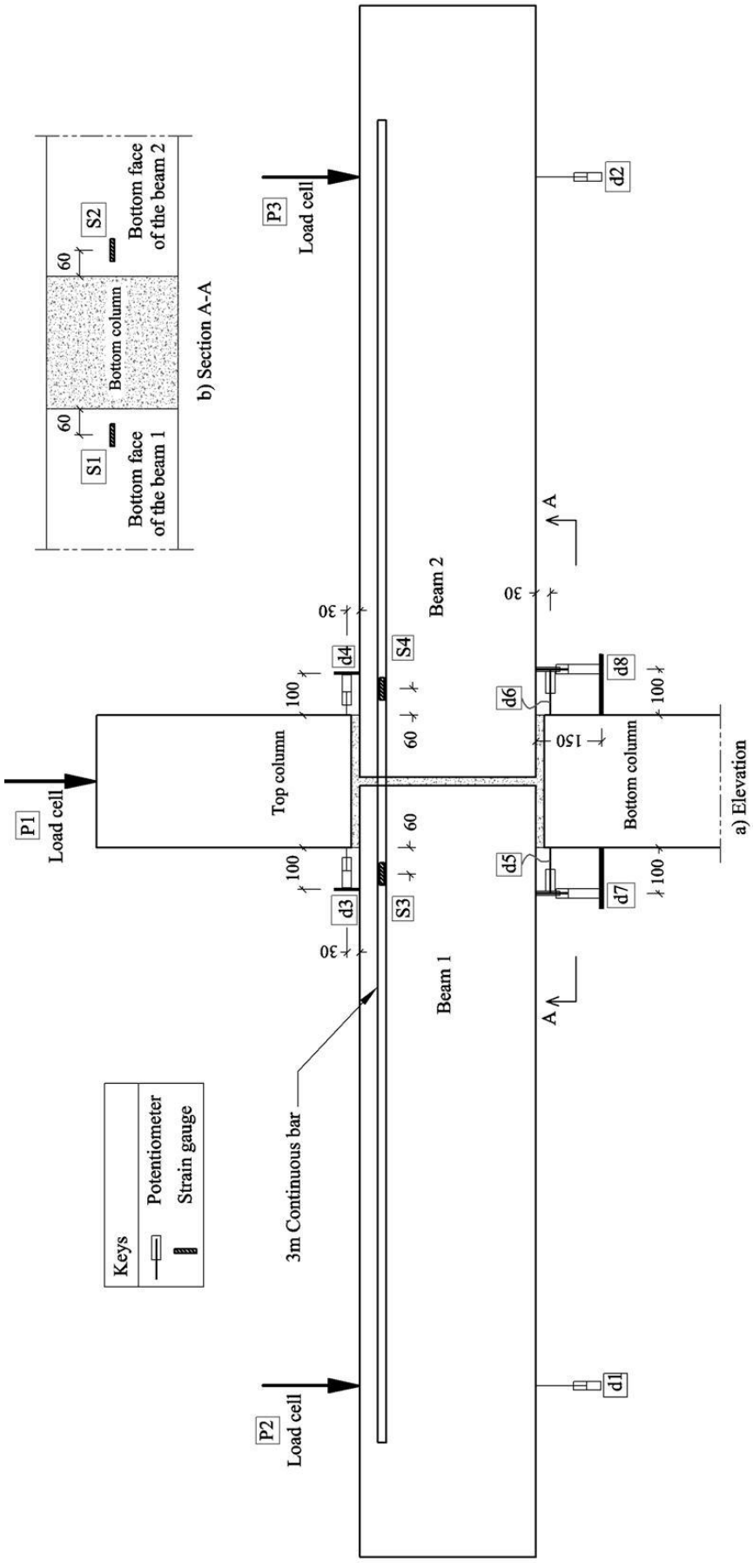

Figure C.2 Instrumentation layout in specimen GR2

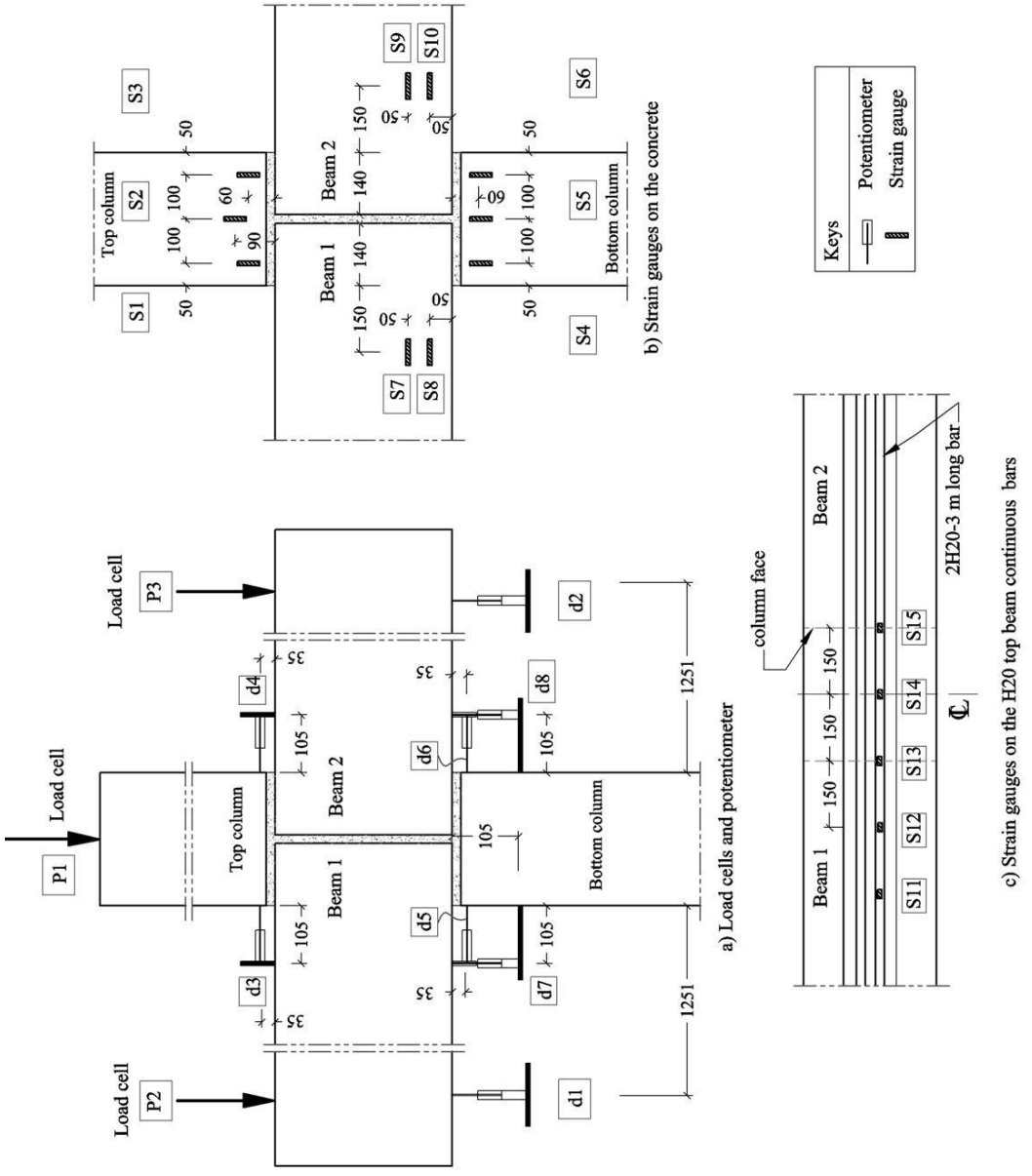

Figure C.3 Instrumentation layout in specimen GR3

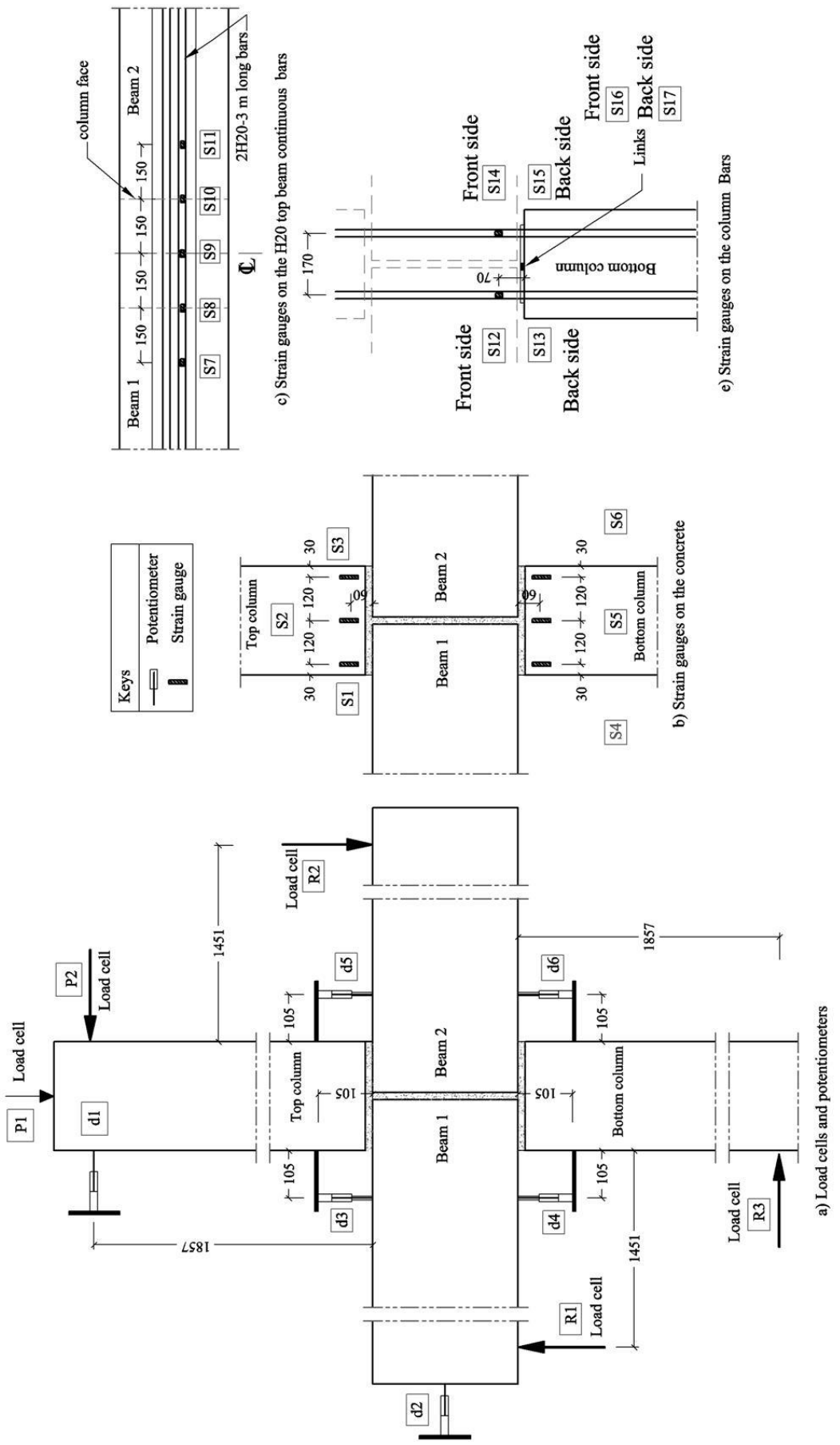

Figure C.4 Instrumentation layout in series SW

Table C.1 Function of sensors in test GR1

Instrument	Function
P1	Load cell records the magnitude of the axial load applied at the top column
P2	Load cell records the magnitude of the load applied at the end of beam 1
P3	Load cell records the magnitude of the load applied at the end of beam 2
d1*	Potentiometer records the displacement of beam 1 under the applied load
d2*	Potentiometer records the displacement of beam 2 under the applied load
d3	Potentiometer records the crack opening at beam 1- top column interface
d4	Potentiometer records the crack opening at beam 2- top column interface.
d5	Potentiometer records the compressive deformation at the bottom of beam 2
d6	Potentiometer records the beam deflection to calculate the relative beam 1-bottom column rotation (rotation = d6 / 130)
S1 to S3	60 mm length strain gauge records the concrete strain at the top column
S4 to S6	60 mm length strain gauge records the concrete strain at the bottom column
S7	60 mm length strain gauge records the concrete strain in beam 1
S8	60 mm length strain gauge records the concrete strain in beam 2
S9 to S11	10 mm length strain gauge records the strain in beam top steel bars
*The beam deflections reported in chapter 5 were taken from theses readings (d1 and d2) minus the rig displacement, which was monitoring during the test. All other displacements (d3 to d6) are relative measurements between the column and beam.	

Table C.2 Function of sensors in test GR2

Instrument	Function
P1	Load cell records the magnitude of the axial load applied at the top column
P2	Load cell records the magnitude of the load applied at the end of beam 1
P3	Load cell records the magnitude of the load applied at the end of beam 2
d1	Potentiometer records the displacement of beam 1 under the applied load
d2	Potentiometer records the displacement of beam 2 under the applied load
d3	Potentiometer records the crack opening at beam 1- top column interface
d4	Potentiometer records the crack opening at beam 2- top column interface
d5	Potentiometer records the compressive deformation at the bottom of beam 1
d6	Potentiometer records the compressive deformation at the bottom of beam 2
d7	Potentiometer records the beam deflection to calculate the relative beam 1-bottom column rotation (rotation = d7 / 100)
d8	Potentiometer records the beam deflection to calculate the relative beam 2-bottom column rotation (rotation = d8 / 100)
S1	60 mm length strain gauge records the concrete strain in beam 1
S2	60 mm length strain gauge records the concrete strain in beam 2
S3 to S4	10 mm length strain gauge records the strain in the beam top steel bars

Table C.3 Function of sensors in test GR3

Instrument	Function
P1	Load cell records the magnitude of the axial load applied at the top column
P2	Load cell records the magnitude of the load applied at the end of beam 1

P3	Load cell records the magnitude of the load applied at the end of beam 2
d1*	Potentiometer records the displacement of beam 1 under the applied load
d2*	Potentiometer records the displacement of beam 2 under the applied load
d3	Potentiometer records the crack opening at beam 1- top column interface
d4	Potentiometer records the crack opening at beam 2- top column interface
d5	Potentiometer records the compressive deformation at the bottom of beam 1
d6	Potentiometer records the compressive deformation at the bottom of beam 2
d7	Potentiometer records the beam deflection to calculate the relative beam 1-bottom column rotation (rotation = d7 / 105)
d8	Potentiometer records the beam deflection to calculate the relative beam 2-bottom column rotation (rotation = d8 / 105)
S1 to S3	60 mm length strain gauge records the concrete strain at the top column
S4 to S6	60 mm length strain gauge records the concrete strain at the bottom column
S7 to S8	60 mm length strain gauge records the concrete strain in beam 1
S9 to S10	60 mm length strain gauge records the concrete strain in beam 2
S11 to S15	10 mm length strain gauge records the strain in the beam top steel bars.
*The beam deflections reported in chapter 5 were taken from theses readings (d1 and d2) minus the rig displacement, which was monitoring during the test. All other displacements (d3 to d8) are relative measurements between the column and beam.	

Table C.4 Function of sensors in series SW

Instrument	**Function**
P1	Load cell records the magnitude of the axial load applied at the top column
P2#	Load cell records the magnitude of the lateral load applied at the top column
R1#	Load cell records the magnitude of the reaction at the end of beam 1
R2#	Load cell records the magnitude of the reaction at the end of beam 2
R3#	Load cell records the magnitude of the reaction at the end of the bottom column
d1#	Potentiometer records the column sway
d2#	Potentiometer records the beam sway
d3	Potentiometer records the beam deflection to calculate the relative beam 1-top column rotation (rotation = d3 / 105)
d4	Potentiometer records the beam deflection to calculate the relative beam 1-bottom column rotation (rotation = d4 / 105)
d5	Potentiometer records the beam deflection to calculate the relative beam 2-top column rotation (rotation = d5 / 105)
d6	Potentiometer records the beam deflection to calculate the relative beam 2-bottom column rotation (rotation = d6 / 105)
S1 to S3	60 mm length strain gauge records the concrete strain at the top column
S4 to S6	60 mm length strain gauge records the concrete strain at the bottom column
S7 to S11	10 mm length strain gauge records the strain in the beam top steel bars
S12 to S15	10 mm length strain gauge records the strain in the column dowel bars
S16 to S17	10 mm length strain gauge records the strain in the additional H8 mm links
# The direction of measurement shown in Figure C.4 is with respect to the half load cycles with the top column lateral load being applied to the left. For the other load direction, these reading were located at the other member side.	

Appendix D - Grout mix design

For grouting the sleeves and troughs in the beam and column in the full-scale beam-column connection tests, it was required to design a grout mix that possesses both a targeted cube compressive strength of 60 N/mm^2 (close to the compressive strength of the concrete used) at 10 days age with sufficient fluidity. The fluidity is expressed in slump diameter in a slump test according to EN 12350-2 (CEN, 2000b). For this purpose, eight trial mixes were carried out; trial mix C2 was chosen to be used for the grouting.

Table D.1 Grout trial mix results

Mix Ref.		Mix proportion					Results		
		Cement (kg/m^3)	Sand (kg/m^3)	Water (kg/m^3)	Super-plasticiser (*l*t./m^3)	Shrinkage reducing admixture (*l*t./m^3)	Slump diameter (mm)	Cube compressive strength, f_{cu} (N/mm^2)	
								10 days	28 days
A1	Ratio	1	1	0.35	**0.006**	0.015			
	Weight	923.4	923.4	323.2	4.6	13.9	470	-----	-----
A2	Ratio	1	1	0.35	**0.008**	0.015			
	Weight	923.4	923.4	323.2	6.2	13.9	550	-----	-----
A3	Ratio	1	1	0.35	**0.010**	0.015			
	Weight	923.4	923.4	323.2	7.7	13.9	640	**50.7**	**56.6**
B1	Ratio	1	1	0.3	**0.01**	0.015			
	Weight	943.5	943.5	287.0	8.0	14.4	375	-----	-----
B2	Ratio	1	1	0.3	**0.012**	0.015			
	Weight	943.5	943.5	287.0	9.6	14.4	425	-----	-----
B3	Ratio	1	1	0.3	**0.016**	0.015			
	Weight	943.5	943.5	287.0	12.8	14.4	565	**58.5**	**66.0**
C1	Ratio	1	1	0.28	**0.016**	0.010			
	Weight	951.8	951.8	266.5	12.7	9.5	665	**56.3**	**62.5**
C2	Ratio	1	1	0.28	**0.017**	0.010			
	Weight	951.8	951.8	266.5	13.5	9.5	790	**57.5**	**63.4**

Cement: CEM II /B-V 32.5 N

Sand : River sand passing through 2.8 mm sieve (see Appendix E for the sieve analysis results)

Superplasticiser: SP1, Grace Concrete Products, Density = 1.2 kg / litre

Shrinkage reducing admixture: Sika Control 40, Density = 1.0 kg / litre

a) Grout mix A1

b) Grout mix A2

c) Grout mix A3

d) Grout mix B1

e) Grout mix B2

f) Grout mix B3

g) Grout mix C2

Figure D.1 Consistincy of the grout trial mixes

Appendix E - Material testing results

E1 Fine Aggregate

Table E.1 Grading of sand (fine aggregate)

Concrete and grout for the small-scale biaxial loading tests (chapter 3) *		Grout for full-scale tests (Chapter 4,5 and 6)	
Sieve size (mm)	Passing (%)	Sieve size (mm)	Passing (%)
5.6	100	2.8	100
4	87	2.0	91.7
2.8	77	1	73.9
2.0	63	0.5	46.5
1	54	0.25	11.6
500 um	43	0.063	0.2
250 um	14	Pan	0
Pan	0	----------	----------
Oven-dried Density = 2.56 Mg/m^3		Oven-dried density = 2.6 Mg/m^3	
Surface-dried density = 2.59 Mg/m^3		Surface-dried density = 2.63 Mg/m^3	
Apparent Density = 2.64 Mg/m^3		Apparent density = 2.67 Mg/m^3	
The sieve analysis was performed according to EN 933-1 (CEN, 1997)			
The densities were determined according to EN 1097-6 (CEN , 2000a)			

E2 Steel bars

The tensile testing of the steel bar was performed according to EN ISO 6892-1(CEN, 2009)

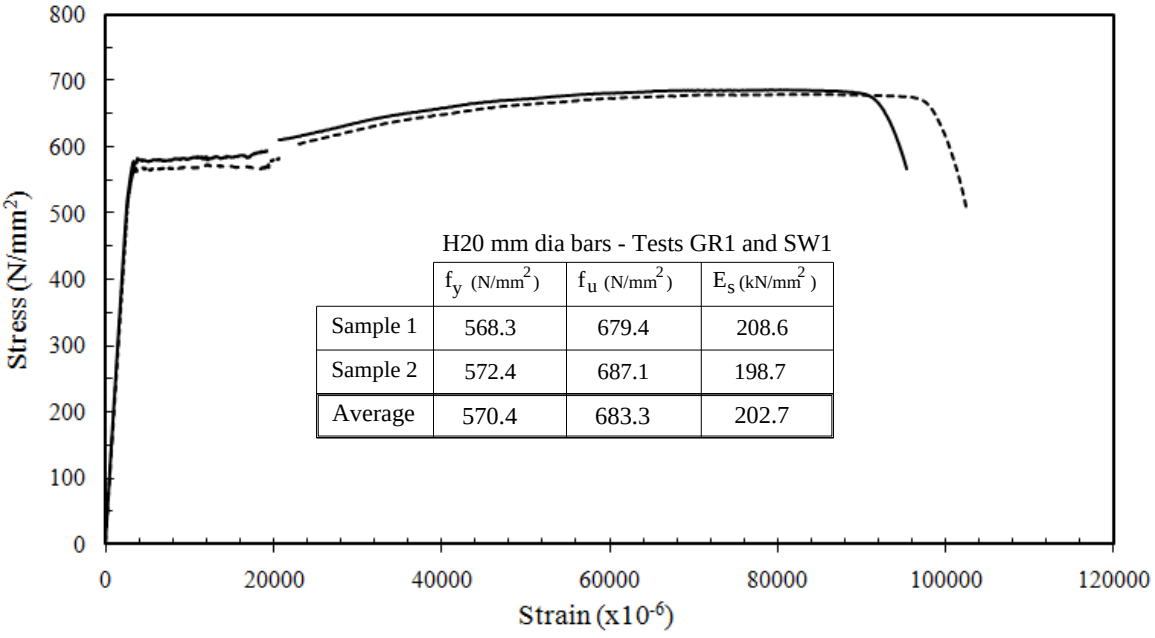

Figure E.1 Tensile strength test results of H20 steel bar type used in specimens GR1 and SW1

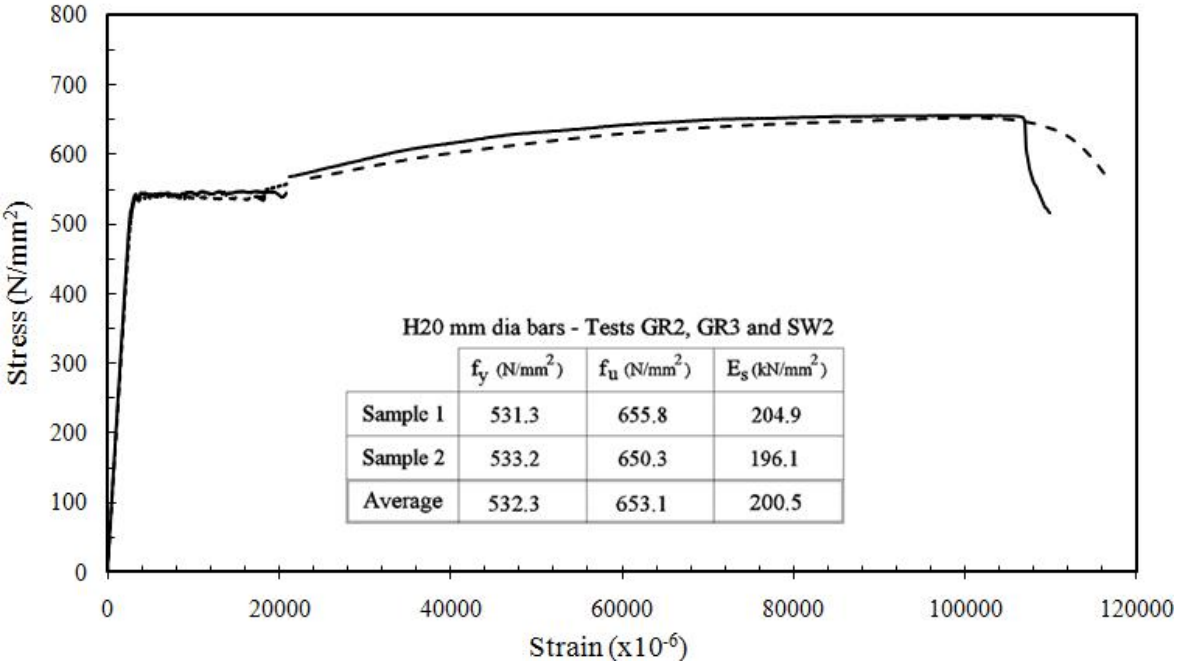

H20 mm dia bars - Tests GR2, GR3 and SW2

	f_y (N/mm^2)	f_u (N/mm^2)	E_s (kN/mm^2)
Sample 1	531.3	655.8	204.9
Sample 2	533.2	650.3	196.1
Average	532.3	653.1	200.5

Figure E.2 Tensile strength test results of H20 steel bar type used in specimens GR2,GR3 and SW2

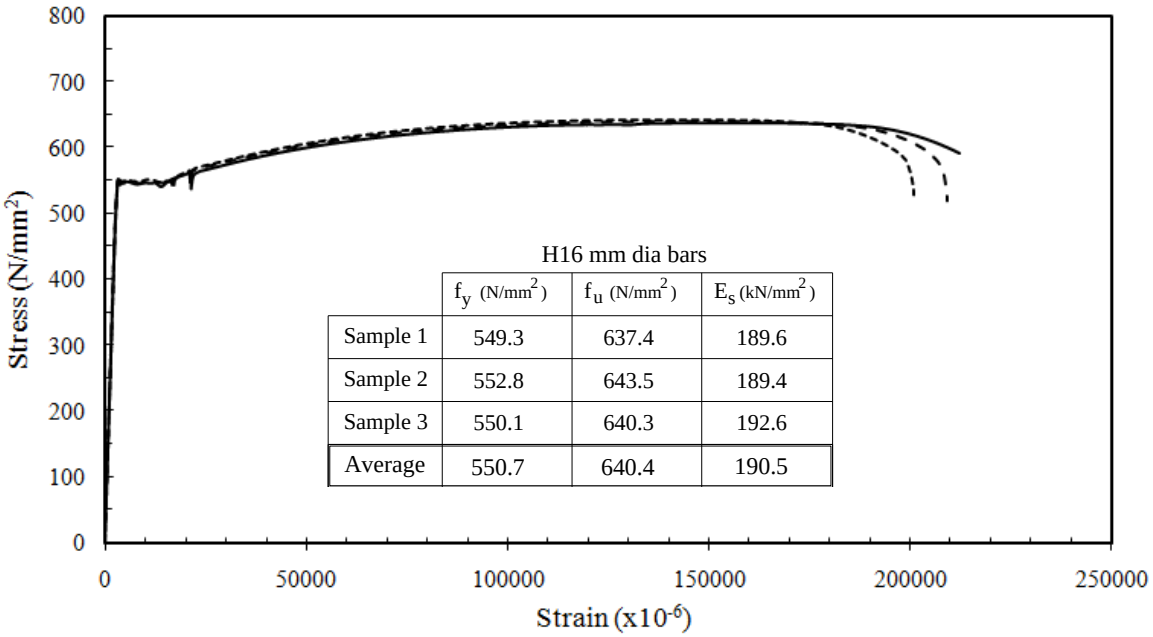

H16 mm dia bars

	f_y (N/mm^2)	f_u (N/mm^2)	E_s (kN/mm^2)
Sample 1	549.3	637.4	189.6
Sample 2	552.8	643.5	189.4
Sample 3	550.1	640.3	192.6
Average	550.7	640.4	190.5

Figure E.3 Tensile strength test results of H16 steel bar type used in specimens GR2,GR3 and SW2

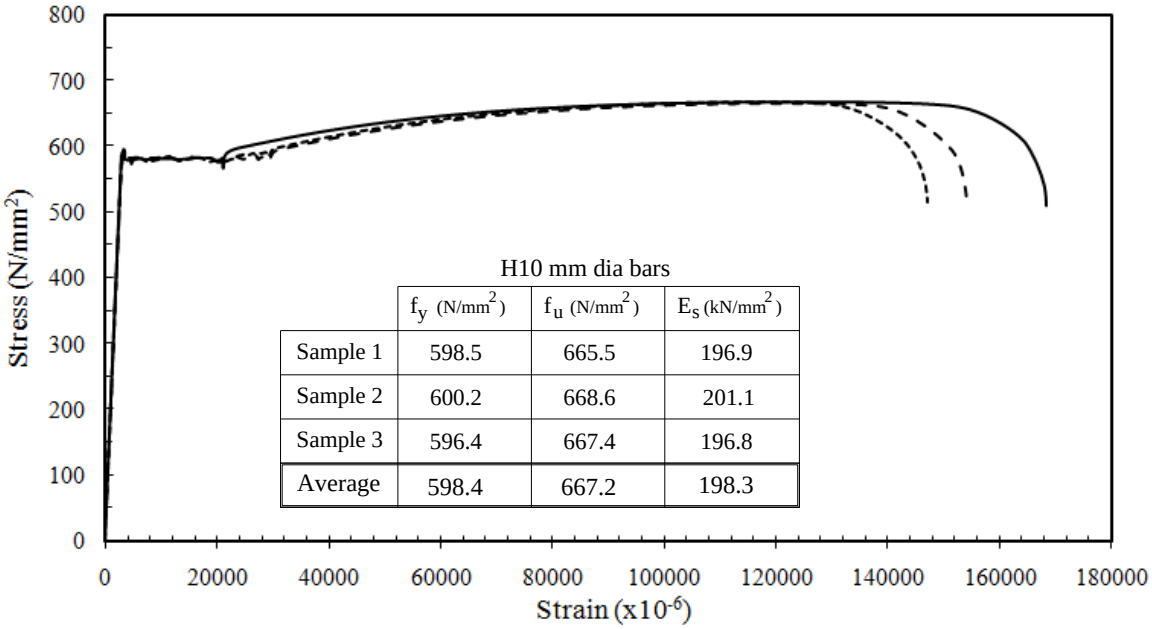

H10 mm dia bars

	f_y (N/mm^2)	f_u (N/mm^2)	E_s (kN/mm^2)
Sample 1	598.5	665.5	196.9
Sample 2	600.2	668.6	201.1
Sample 3	596.4	667.4	196.8
Average	598.4	667.2	198.3

Figure E.4 Tensile strength test results of H10 steel bar type

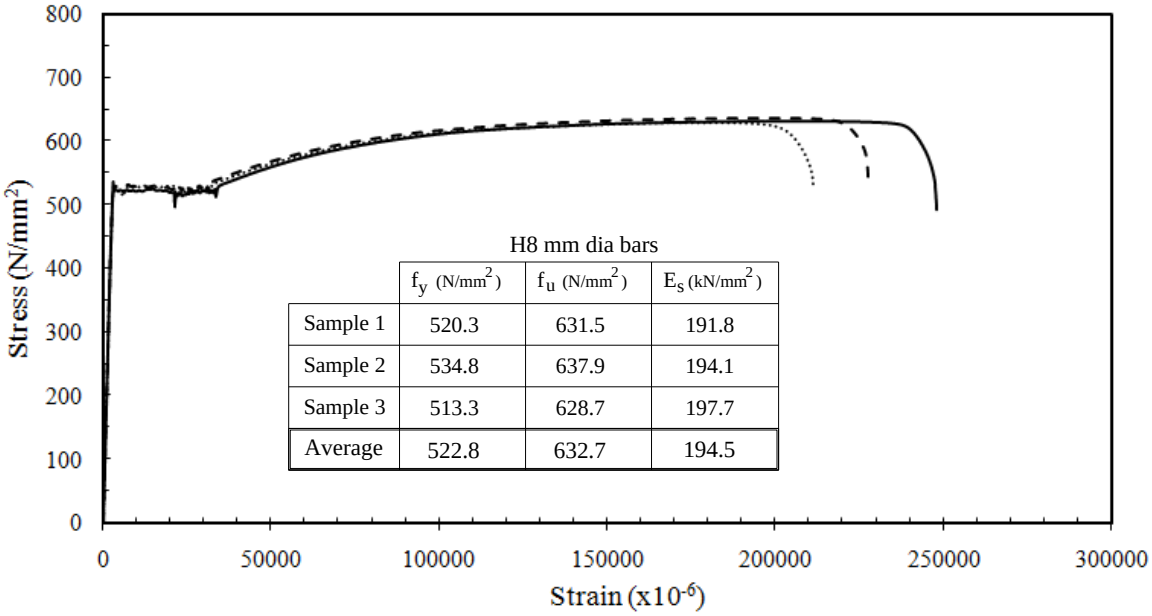

H8 mm dia bars

	f_y (N/mm^2)	f_u (N/mm^2)	E_s (kN/mm^2)
Sample 1	520.3	631.5	191.8
Sample 2	534.8	637.9	194.1
Sample 3	513.3	628.7	197.7
Average	522.8	632.7	194.5

Figure E.5 Tensile strength test results of H8 steel bar type used in specimens GR3 and SW2

Appendix F- Pull-out tests and modulus of elasticity tests

F1 Pull-out tests

Within the available sources, no slip-bond relation was found for cement-based grout and steel bars that could be used to determine the maximum bond strength 'τ_{max}' required in the analytical modelling of the beam-column connection investigated in the current study.

The CEB-FIP 1990 model code (1993) provides an analytical model to represent the bond between concrete and steel (refer to Section 2.5) that requires the parameters λ, α, Sb_1, Sb_2, Sb_3, τ_f in Eq. (F.1) to Eq. (F.4) to be known. The model code recommends values for these parameters based on specifying the bond as '*confined*' or '*unconfined*', and as being in '*good bond condition*' or '*all other bond conditions*' but without indicating any values for the bond between cement-based grout and steel bars. To find out the suitable parameters to be used to represent the bond in these circumstances, two tests were conducted.

$$\tau_{max} = \lambda \sqrt{f_c} \qquad \text{(F.1)}$$

$$\tau = \tau_{max} \left(\frac{Sb}{Sb_1}\right)^{\alpha} \quad \text{for } 0 \leq Sb \leq Sb_1 \qquad \text{(F.2)}$$

$$\tau = \tau_{max} \quad \text{for } Sb_1 \leq Sb \leq Sb_2 \qquad \text{(F.3)}$$

$$\tau = \tau_{max} - (\tau_{max} - \tau_f) \frac{Sb - Sb_1}{Sb_3 - Sb_2} \quad \text{for } Sb_2 \leq Sb \leq Sb_3 \qquad \text{(F.4)}$$

The two pull-out tests were conducted to specify the parameters in Eqs. (F.1) to (F.4), and most importantly λ. The specimen details and the test setup are shown in Figure F.1, where the specimens consisted of 250 x 250 x 300 mm samples of cement-based grout with a 1H20 steel bar located in the centre of the cube. The grout and the H20 steel bars were the same as that used in the full-scale tests. The test setup was based on the

configuration used by Losberg and Olsson (*fib*, 2008) but with using an embedded length of 5Ø as recommended by EN 100080 (CEN, 2005c). The bond was prevented within the remaining 100 mm at both ends through using 25 mm diameter plastic sleeves. The 5Ø bond length was located away from the active end to eliminate the effect of the compressive reaction from the load jack.

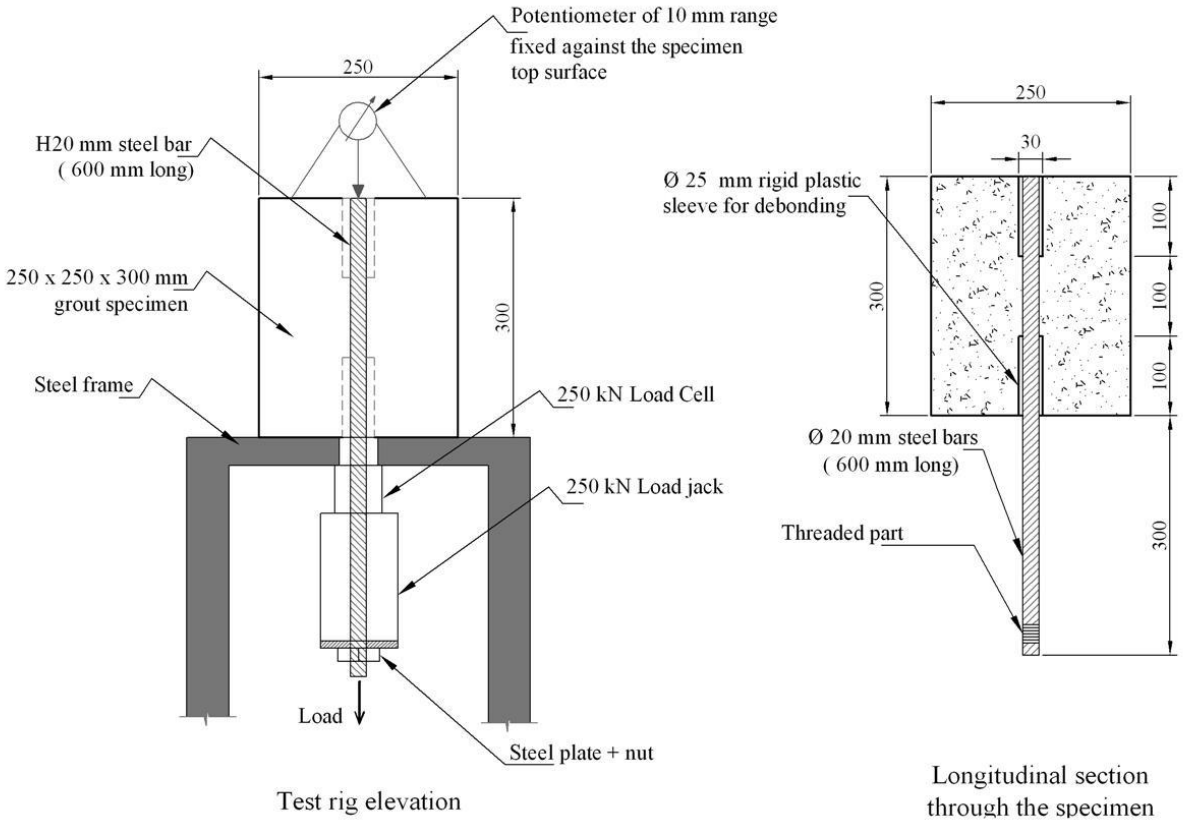

a) Test configuration and specimen details

b) Specimen form work

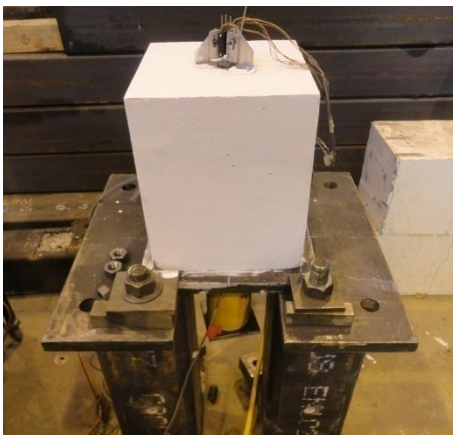

c) Testing the specimen

Figure F.1 Pull-out test details

The slip-bond stress relations resulting from the two tests are shown in Figure F.2 with a suggested model to characterise the behaviour using Sb_1 = 1.0 mm, Sb_2 = 3 mm, Sb_3 = 10 mm, $\lambda = 2$, $\alpha = 0.15$, and $\tau_f = 0.4\,\tau_{max}$. The f_c of the grout specimens was 52.5 N/mm^2 (average of two cylinders).

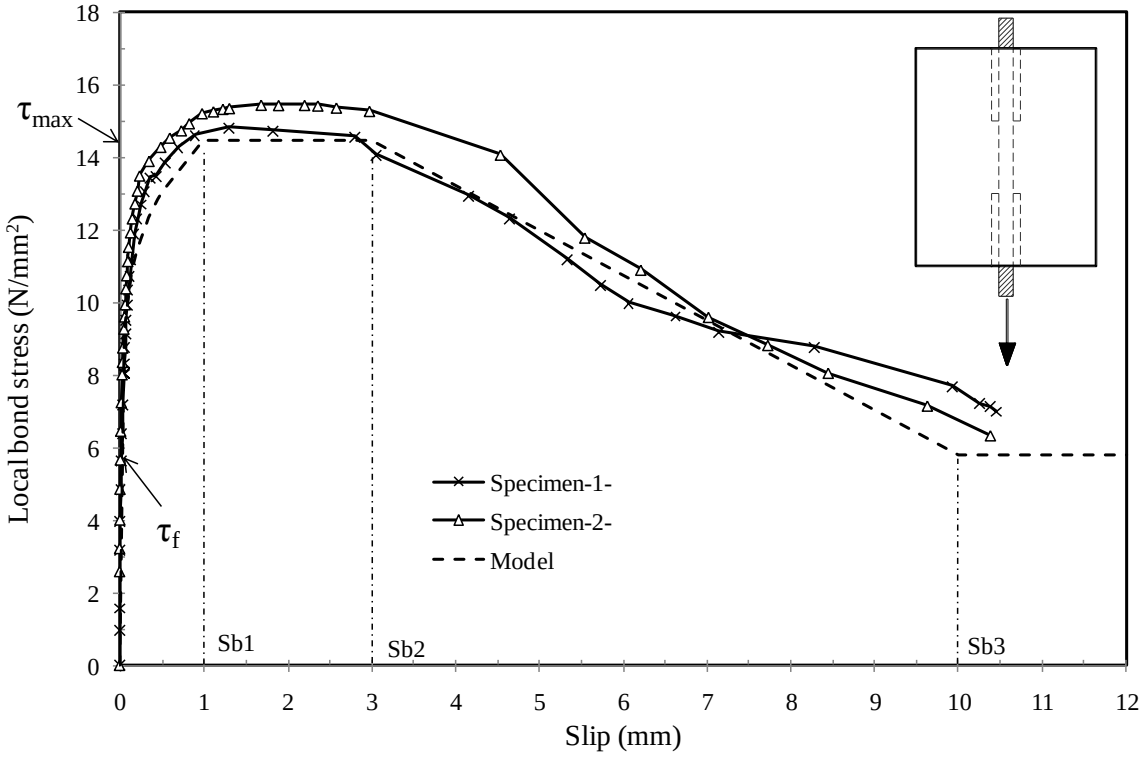

Figure F.2 Pull-out test results

F2 Grout modulus of Elasticity

EC2 (CEN, 2004b) presents Eq. (F.5) to calculate the modulus of elasticity of concrete with quartzite aggregates. For concrete with other aggregate types, EC2 provides some factors to be used with Eq. (F.5).

$$E_c = 22\left(\frac{fc}{10}\right)^{0.3} \qquad \text{(F.5)}$$

The provided factors do not cater for cement-based grout; therefore, it was necessary to determine this factor experimentally based on BS 1881-121 (BSi, 1983). The static modulus of elasticity for concrete in compression is taken for the range between

0.5 N/mm^2 stress and the one-third of the compressive strength of the concrete. For this purpose, two Ø150 mm x 300 mm height cylinders were tested to find out the factor needed to be used in Eq. (F.5). Table F.1 and Figure F.3 show the results of the tests, and the outcomes reveal that Eq. (F.5) could be used to determine the modules of elasticity of the used grout by using a reduction factor of 0.88.

Table F.1 Grout modulus of elasticity test results

Specimen	Cylinder compressive strength, f_c (N/mm^2)	Experimental E_c, (N/mm^2)	E_c using Eq. (F.5) (N/mm^2)	col 3 / col 4
M1	56.6	32600	37006	0.88
M2	48.4	30900	35308	0.88
Average	52.5			0.88

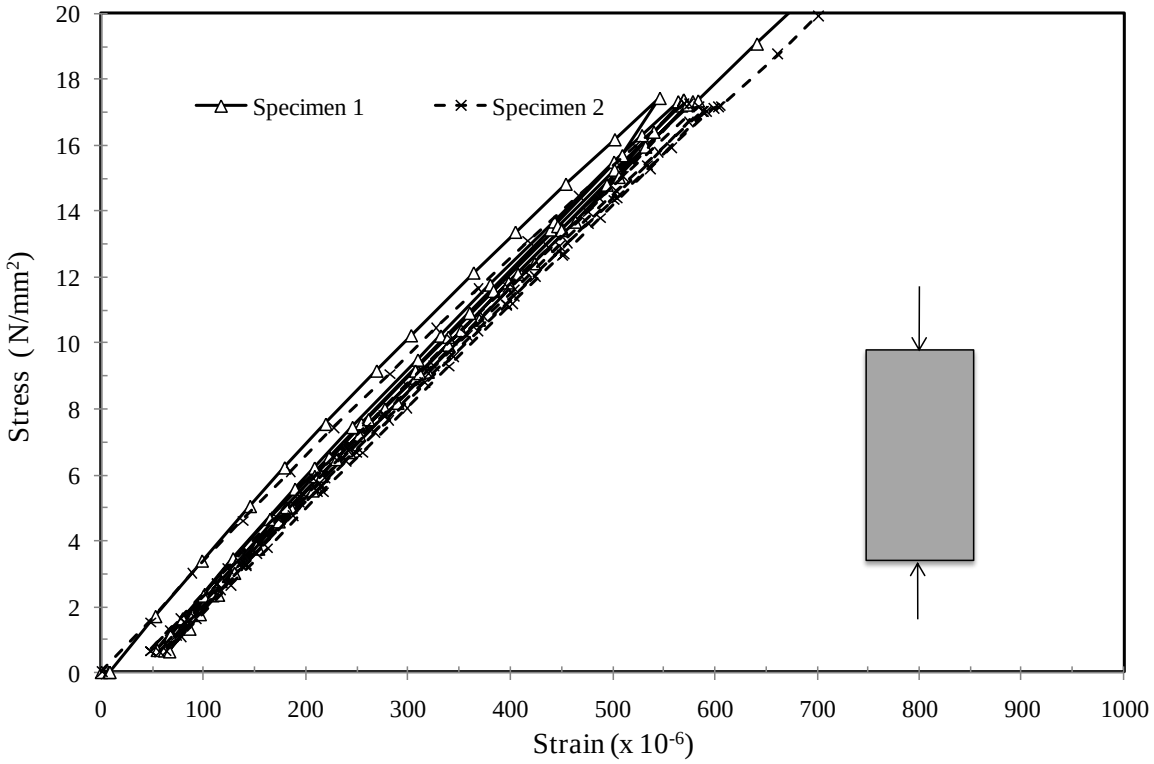

Figure F.3 Stress-strain relation of grout under compression loading

Appendix G- FE modelling results of specimen GR1

The FE modelling results of specimen GR1 compared with the experimental results are presented in this appendix. The results include deflections, beam-column relative rotations, concrete and steel strains, and the crack patterns.

The FE model results matched well the experimental results at the early loading stages; however, it failed to anticipate the behaviour close to the yielding, and did not predict the ultimate moment capacity of the connection correctly. The reasons behind these outcomes were presented in Chapter 7. The results of the FE modelling presented here include the results of two models, as listed below.

FE model 1: the reference model where all the steel bars were provided according to the experimental details.

FE model 2: the model differs from above by ignoring the internal part of the 2H20 side bars in the FE mesh.

The intention from the 2nd model was to check the effects of modelling the internal part of the 2H20 steel side bars within the connection. As shown in Figure G.1, FE model 2 provided a more representative model for the true behaviour; by cutting the 2H20 side bars at the column face, there was no means for stress transfer through the column bottom links (explained in detail in Section 7.8.3). The other FE model results reported in Figures G.2 to G.6 are those obtained from FE model 1.

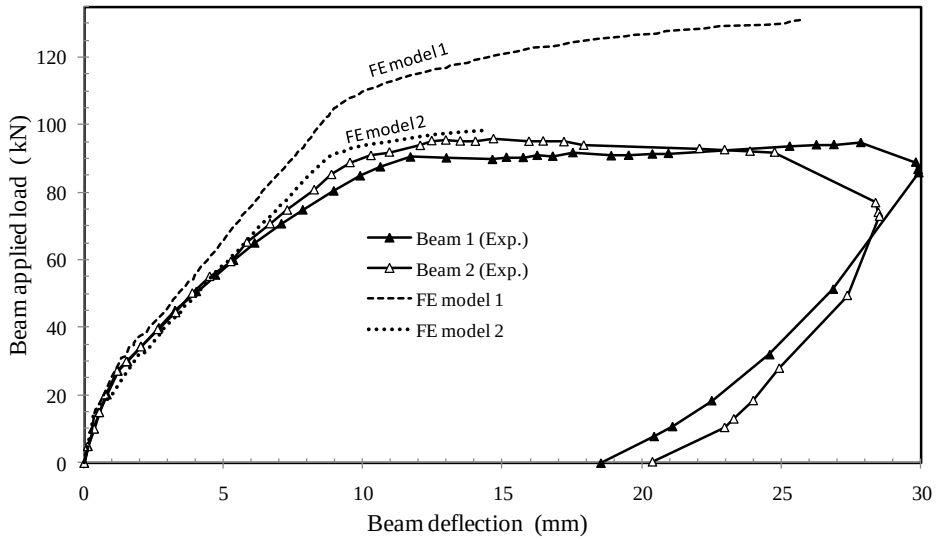

Figure G.1 Load vs. deflection in specimen GR1 (experimental results and FE results)

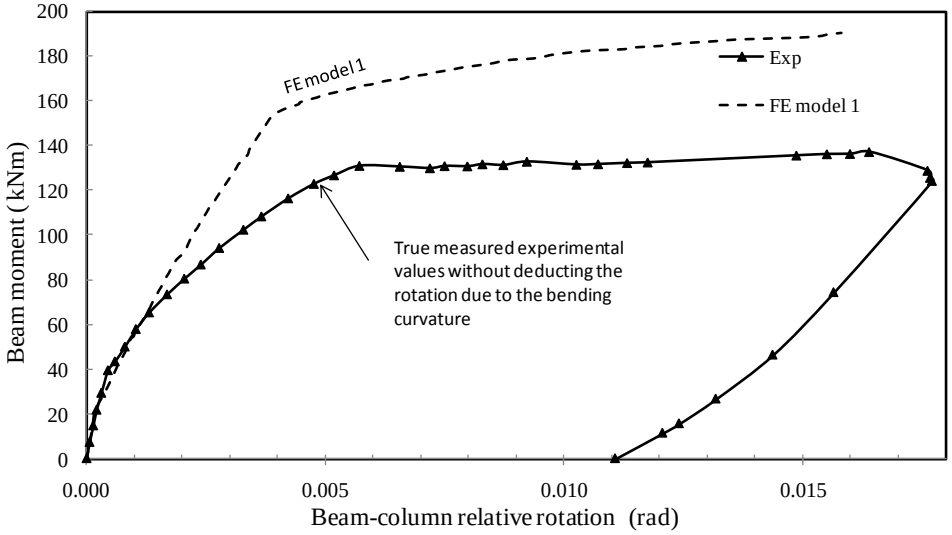

Figure G.2 Beam load vs. beam-column relative rotation in specimen GR1 (experimental results and FE results)

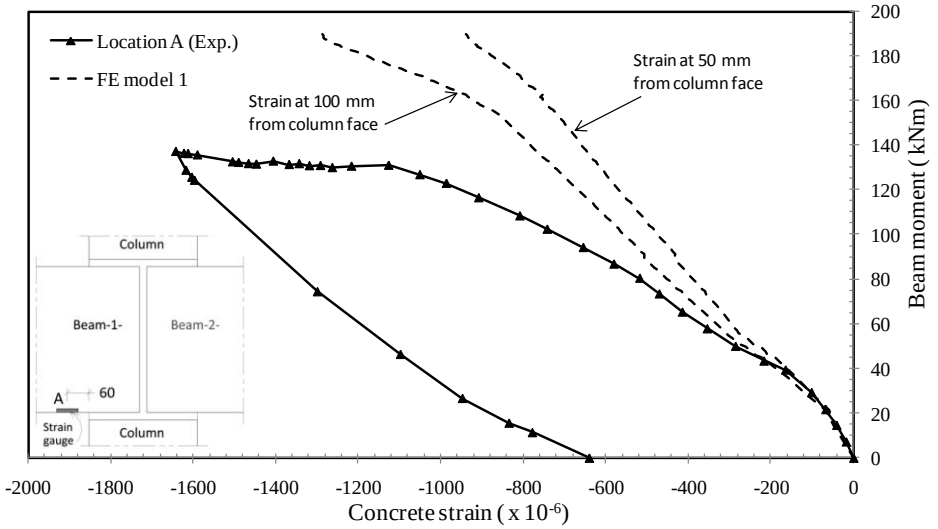

Figure G.3 Beam moment vs. concrete strain in specimen GR1 (experimental results and FE results)

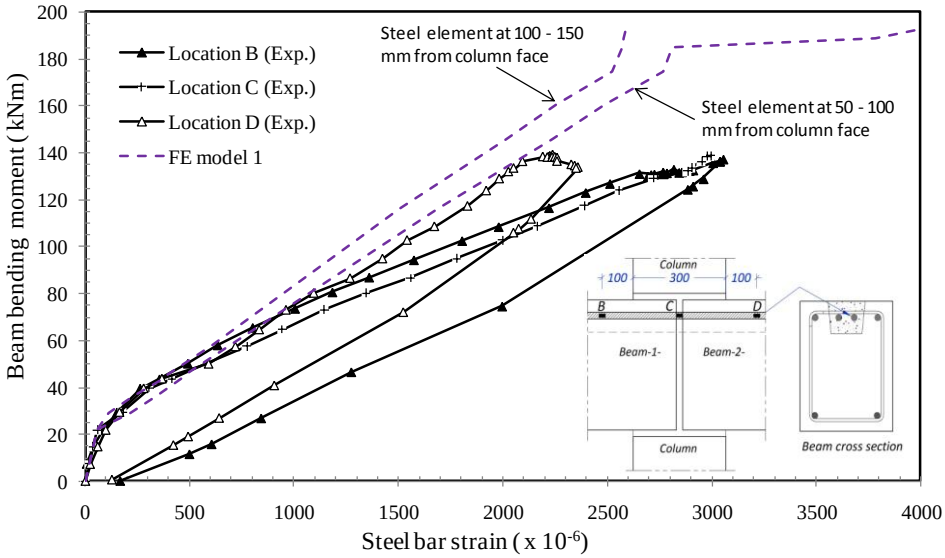

Figure G.4 Beam moment vs. steel strain in specimen GR1 (experimental results and FE results)

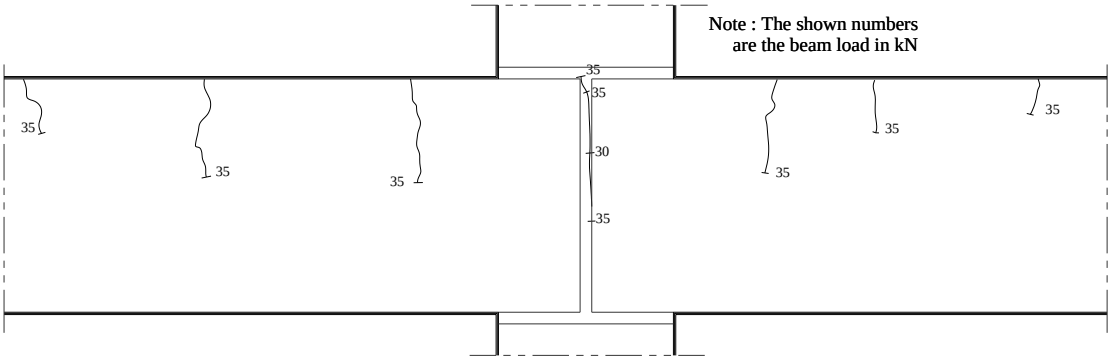

a) Experimental at 35 kN beam load

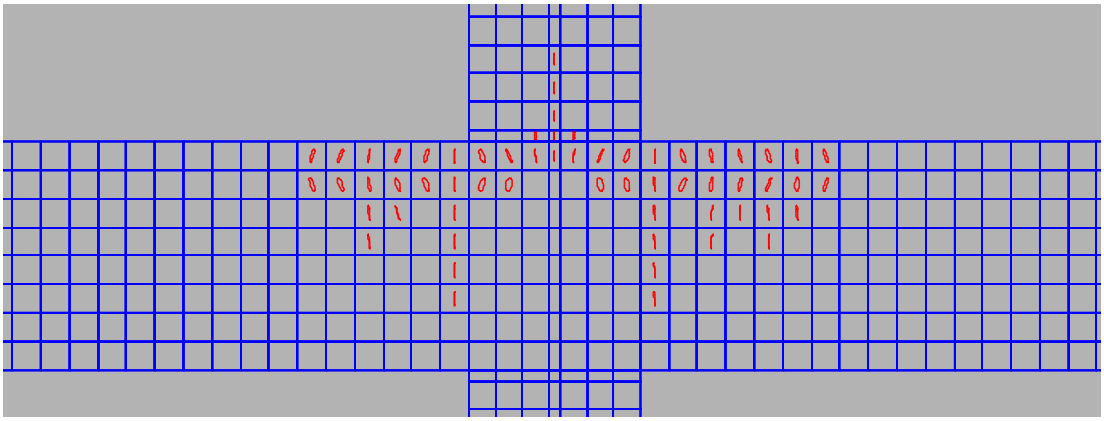

b) Numerical at 35 kN beam load (FE model 1)

Figure G.5 Comparison of the first cracks

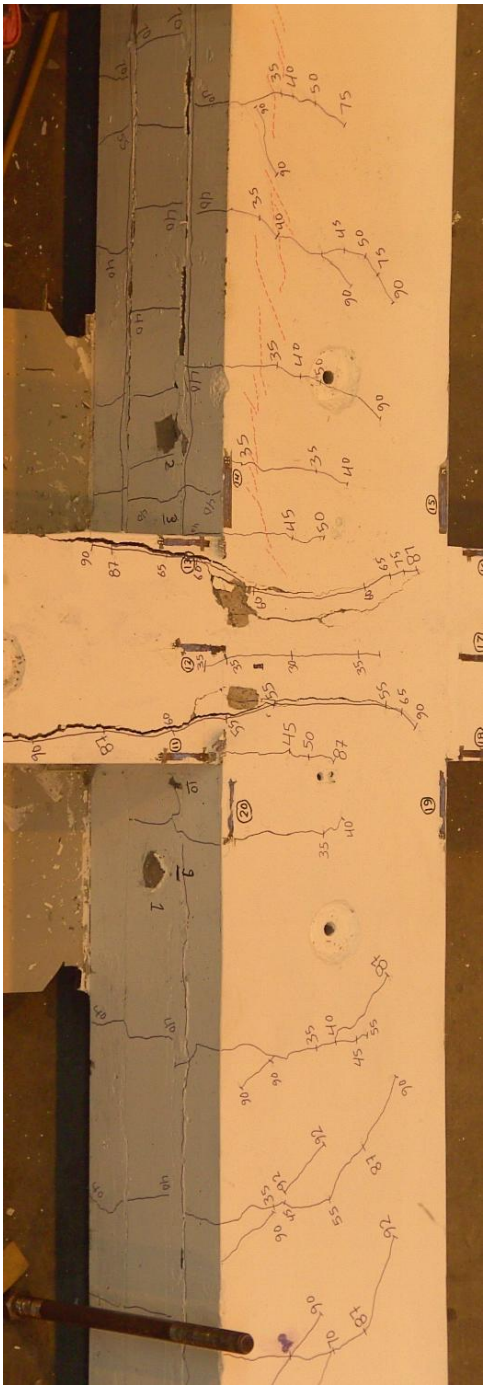

a) Experimental (at faliure, the hidden lines are the cracks that happened between the yielding load and faliure)

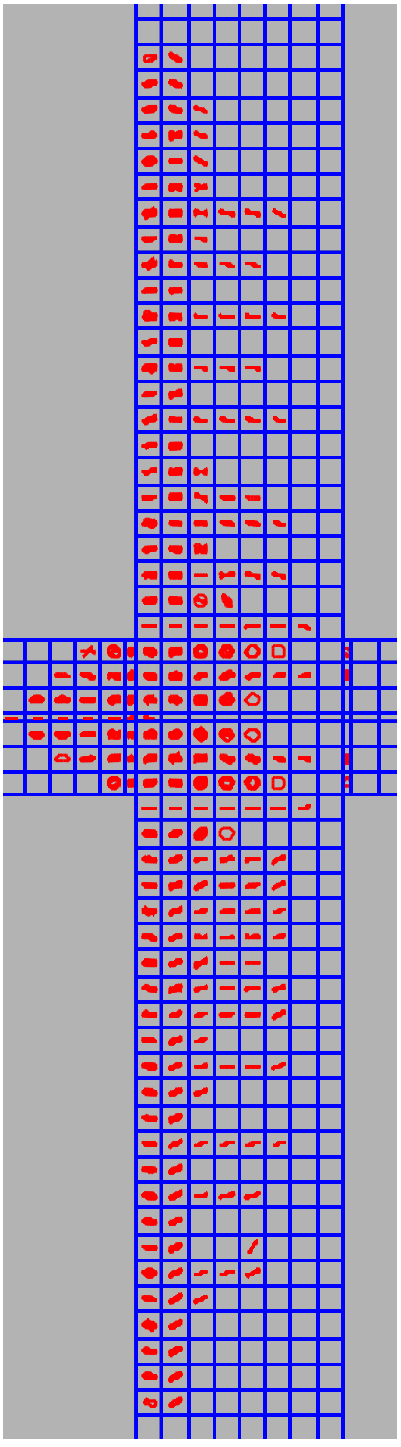

b) Numerical (FE model 1) at 90.63 kN beam load (the experimental yileding load)

Figure G.6 Comparison of the crack pattern at yielding

Appendix H
Simplified semi-rigid frame analysis calibration

In this appendix, the simplified semi-rigid frame analysis is calibrated against two other methods: (i) the ANSYS software (2004), and (ii) the conventional semi-rigid frame analysis based on Monforton's approach (1963). The calibration involved frames subjected to separate gravity and sway loads.

H1 Calibration of the simplified approach under gravity loading

For the calibration under gravity loads, frame F3 (Figure H.1) was taken as the case study. As shown, the modulus of elasticity of the beams 'E_b' has been taken as half as the modulus of elasticity of columns 'E_{col}' to account for assigning 0.5 EI to the beams. In rigid frames, using either full EI or 0.5 EI for the beams has no significant effect on the moment distribution; however, the effect is significant in semi-rigid frames (refer to Section 5.3.4.3). In frame F3, stubs were only assigned at the beam-ends using two different rotational stiffness sets in two different frame analyses, as listed below.

(i) Set A: the internal rotational stiffness was taken to be the same as the stiffness obtained from specimen GR1 (S_2= 30160 kNm/rad). For the external connections, S_1 was taken as half of S_2. The aim of this set was to validate the simplified semi-rigid analysis using a realistic connection stiffness, where the internal connections are close to being considered as rigid connections (γ = 0.41 to 0.51 for the external connections, and 0.68 to 0.78 for the internal connections).

(ii) Set B: S_2=3016 kNm/rad, and S1 = 1508 kNm/rad. The intention of this set was to validate the simplified method in the case of semi-rigid connections that are too far from being considered as rigid connections (γ= 0.06 to 0.09 for the external connections, and 0.12 to 0.26 for the internal connections).

Practically, the simplified semi-rigid frame analysis is performed in a very similar way to the rigid analysis. First, the geometry and the loadings of the frame are set. Then lengths equal to the required stub length 'Ls' are assigned at the beam ends with the 2nd moment of area of stub 'I_s' taken as equal to S_y Ls / E. For example, in set A, with Ls equal to 0.01 m, S_y = 30160 kNm/rad , and E= 18.08E6 kN/m^2, I of the internal stubs needs to be taken as I_s = 30160 *x* 0.01 /18.08E6 = 0.000016681 m^4. The same approach is applied to the external stubs, I_s = 15080 x 0.01 /1.808E7 = 0.00000834 kN/m^2. After assigning the I_s to the stubs, a normal analysis is performed and the results are the outcomes of semi-rigid frame analysis.

The analysis of frame F3 (set A) shows that the simplified semi-rigid frame analysis gave member end-moment values that were very close to the exact ones when the stub length was approaching zero (Figure H.2a, b and c). In frame F3 (set B), using the very weak beam-column rotational stiffnesses, the results were also matching the exact solution when the stub length was taken equal to 10 mm. From these, it appears that the simplified semi-rigid frame analysis produces results very close to the exact solution by using small stub lengths (10 mm as a recommended value).

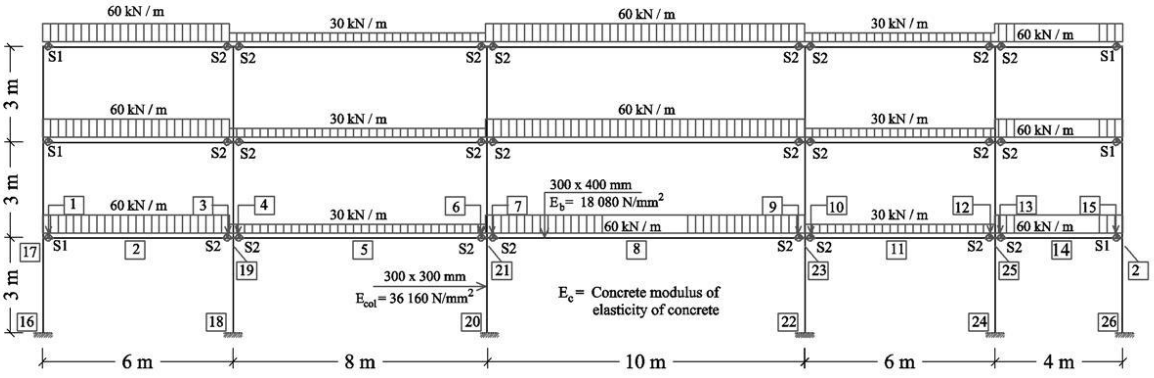

Set	S1 (kNm/rad)	S2 (kNm/rad)
A	15080	30160
B	1508	3016

Figure H.1 Geometry and loading of frame F3

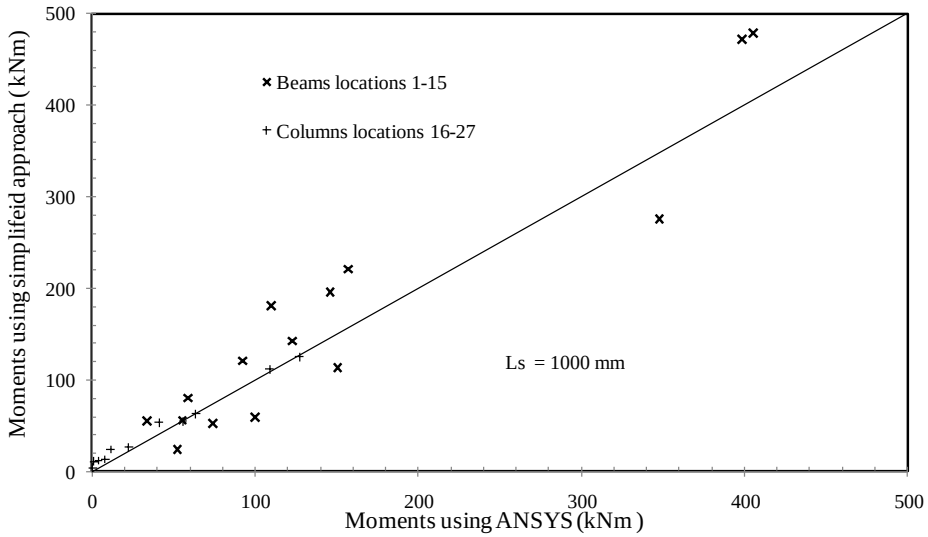

a) Using 1000 mm stub length (set A)

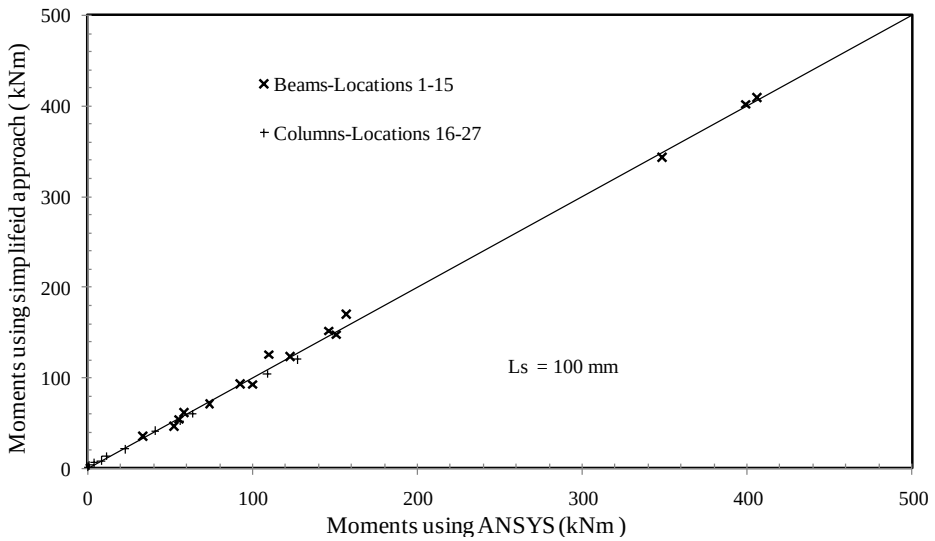

b) Using 100 mm stub length (set A)

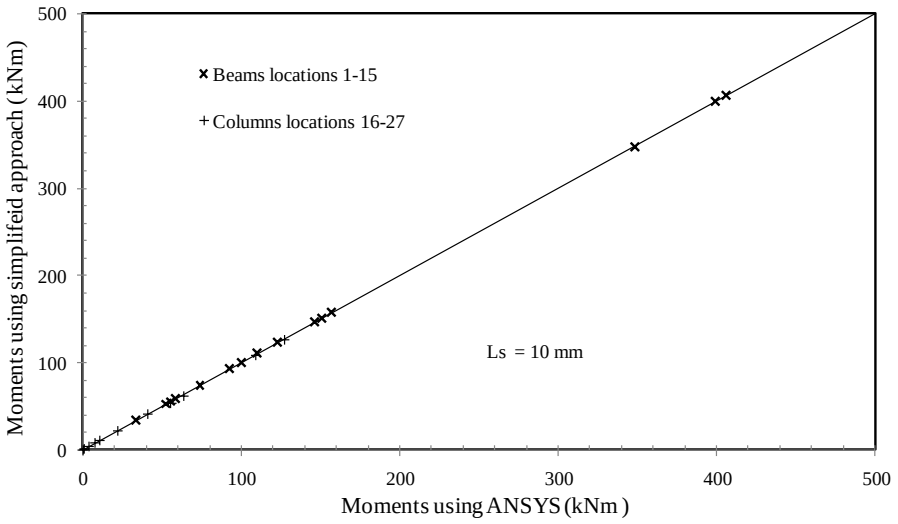

c) Using 10 mm stub length (set A)

Figure H.2 Validation of the simplified approach against ANSYS (frame F3)

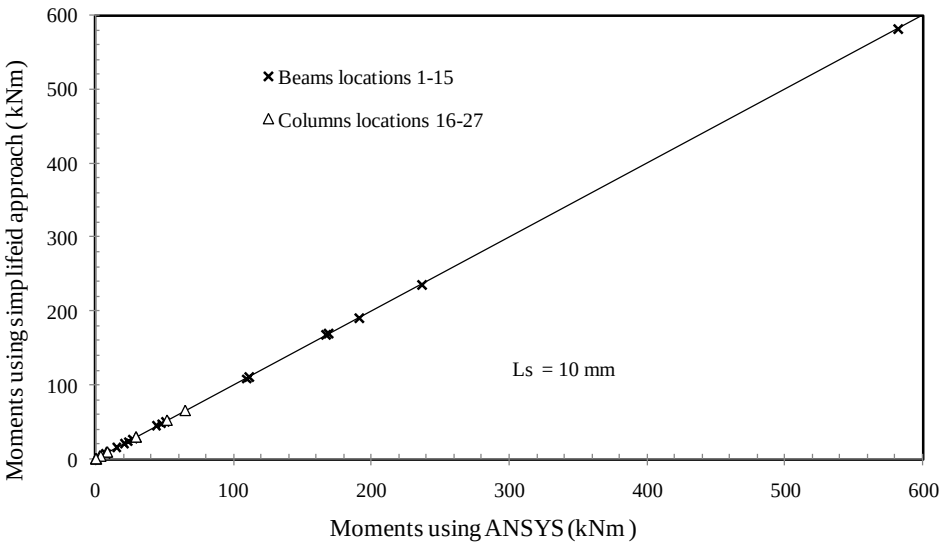

d) Using 10 mm stub length (set B)

Figure H.2 (Cont.) Validation of the simplified approach against ANSYS (frame F3)

H2 Calibration of the simplified approach under sway loading

In a similar way to that used in the previous section, the simplified semi-rigid analysis was validated under sway loads against the other two classical methods. For this purpose, frame F4 (Figure H.3) was analysed. The geometry and the member sizes of frame F4 were the same as frame F3 but with using the rotational stiffness of specimen SW2 (1278 kNm/rad, refer to Table 6.1) and being subjected to a different loading arrangement (refer to Section 8.4). As shown, the modulus of elasticity of the beams 'E_b' was taken as 0.35 E_c, while the modulus of elasticity of the column 'E_{col}' was taken as 0.7 E_c as recommended by ACI (2008a) for frame analysis under sway loads. Table H.1 compares the results of the simplified method with the results of ANSYS for both 1st and 2nd order analyses with a maximum difference being 1.7 %. The simplified semi-rigid analyses were conducted using stubs of 10 mm length (Ls) and a modified 2nd moment of area (I_s) for the stubs equal to S_y Ls / E_b.

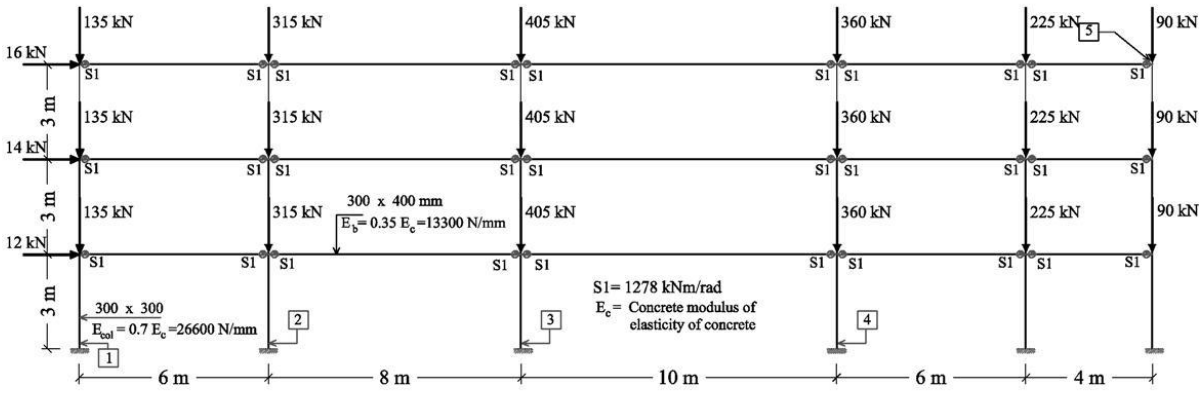

Figure H.3 Geometry and loading of frame F4

Table H.1 Results of analysis of frame F4

Location	1st order moment			2nd order moment		
	ANSYS (kNm)	Simplified (kNm)	Ratio (%)	ANSYS (kNm)	Simplified (kNm)	Ratio (%)
1	26.57	26.60	100.11	34.92	34.78	99.60
2	26.94	26.95	100.04	34.88	35.35	101.35
3	26.64	26.66	100.08	34.25	34.83	101.69
4	23.91	23.82	99.62	33.58	33.01	98.30
Location	1st order sway			2nd order sway		
	ANSYS (mm)	Simplified (mm)	Ratio (%)	ANSYS (mm)	Simplified (mm)	Ratio (%)
5	23.91	23.82	99.62	33.58	33.01	98.30

Appendix I Allowable moment redistribution in specimens GR1 and GR3

I1 Permissible moment redistribution

According to EC2 (CEN, 2004b), in continuous beam that are predominantly subject to flexure and the ratio of the adjacent spans is in the range of 0.5 to 2, bending moments could be redistributed without the need for explicit checking of the rotation capacity, using the below relations.

i) For $f_{ck} \leq 50$ MPa

$$\delta m \geq k_1 + k_2 \, x_u/d \quad ; \quad k_1 = 0.44, \; k_2 = 1.25(0.6+0.0014/\varepsilon_{cu2}) \; ; \; \varepsilon_{cu2} = 0.0035$$

ii) For $f_{ck} > 50$ MPa

$$\delta m \geq k_1 + k_2 \, x_u/d \quad ; \quad k_3 = 0.54, \; k_4 = 1.25(0.6+0.0014/\varepsilon_{cu2})$$

$$, \; \varepsilon_{cu2} = 0.0026+0.035 \, [(90 - f_{ck}) / 100)^4$$

$\delta m \geq 0.7$ where Class B and Class C reinforcement is used.

$\delta m \geq 0.8$ where Class A reinforcement is used.

x_u is the depth of the neutral axis at the ultimate limit state after redistribution

d : is the effective depth of the section

δm : the ratio of maintaining moment after redistribution

$$\delta m = \frac{\text{Section moment after redistribution}}{\text{Section moment before redistribution}} < 1$$

ε_{cu2} is the compressive ultimate strain

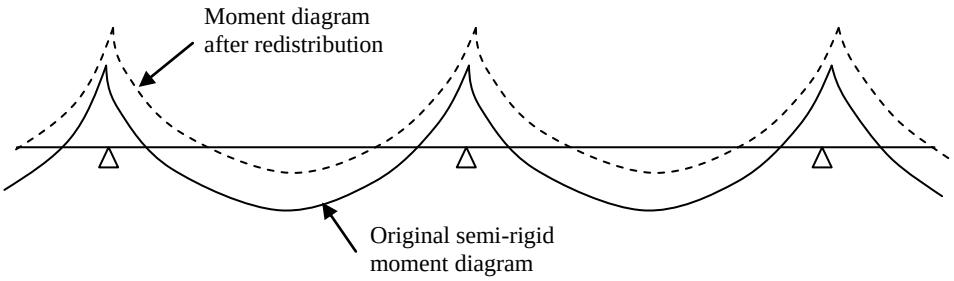

Figure I.1 Moment redistribution from the mid-spans to supports

I2 Specimen GR1

Table I.1 Specimen GR1 details

Beam width, b (mm)	300	
Beam depth, h (mm)	300	
Beam effective depth, d (mm)	350	
Main steel area at mid-span, A_s	2H20	2x314=628mm^2
$\rho = A_s / (b \cdot d)$	0.006	
f_{cu} of concrete (N/mm^2)	63.3	
f_c of concrete (N/mm^2)	52.4	
E_c of concrete (N/mm^2)	36160	
f_y of H20 (N/mm^2) - main beam bottom bars	570.4	Type B
E_s of H20 (N/mm^2) - main beam bottom bars	202700	

Moment Capacity and x_u/d at mid span

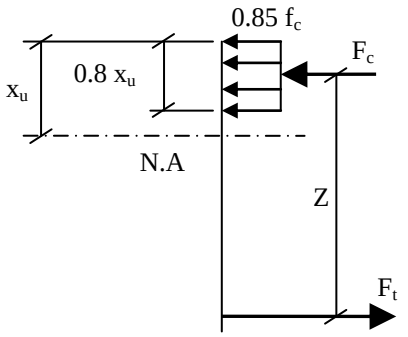

Figure I.2 Equivalent rectangular stress block

$F_t = f_y \cdot A_s = 570.4 \text{ N/mm}^2 \times 2 \times 314 \text{ mm}^2$

$F_t = 358211.2 \text{ N}$

$f_{cd} = 0.85 \cdot f_c = 0.85 \times 52.4 = 44.54 \text{ N/mm}^2$

$F_c = F_t = 358211.2 \text{ N}$

$F_c = 0.8\, x_u \cdot f_{cd} \cdot b$

$x_u = F_c / (0.8 \cdot f_{cd} \cdot b) = 358211.2 / (0.8 \times 44.54 \times 300) = 33.51 \text{ mm}$

$x_u / d = 33.51 / 350 = 0.096$

$Z = d - 0.4\, x_u = 350 - 0.4 \times 33.51 = 336.60 \text{ mm}$

$M_u = F_s \quad Z = 358211.2 \quad \times 336.6 / 1000\,000 = 120.57 \text{ kNm}$

Permissible moment redistribution

Concrete : $f_c = 52.4 \text{ N/mm}^2$

Steel bars : Type B , $f_y = 570.4 \text{ N/mm}^2$

$\delta \geq k_3 + k_4 \; x_u/d \; ; \; \delta \geq 0.7$

$k_3 = 0.54$

$k_4 = 1.25(0.6+0.0014/ \varepsilon_{cu2})$

$\varepsilon_{cu2} = 2.6 + 35 ((90 - f_c) / 100)^4$

$\varepsilon_{cu2} = 2.6 + 35 ((90 - 52.4) / 100)^4 = 3.30 ‰ = 0.0033$

$k_4 = 1.25\ [0.6+(0.0014/\ .0033)] = 1.28$

$\delta m \geq k_3 + k_4\ x_u/d$

$\delta m \geq 0.54 + 1.28\ x\ 0.096 = 0.66\ <\ 0.7$, therefore $\delta m = 0.7$ will govern

Therefore, the available moment redistribution 'Rm_a' from the mid-span towards supports is 0.3

In GR1, $S_y = 30160$ kNm/rad, $E_c = 36.16$ E6 kN/m^2

i) <u>$L = 12\ h = 12\ x\ 0.4\ = 4.8$ m, $I = 0.3\ x\ 0.4^3/12 = 0.0016$ m^4 :</u>

$$\gamma = \frac{1}{1 + \frac{3\ E_c\ 0.5\ I_I}{S_y\ L}} = \frac{1}{1 + \frac{3\ x\ 36.16E6\ x\ 0.5\ x\ 0.0016}{30160\ x\ 4.8}} = \frac{1}{1+0.6} = 0.63$$

$$\frac{M_E}{\frac{w\ L^2}{12}} = \frac{3\ \gamma}{2+\gamma} = \frac{3\ x\ 0.63}{2+0.63} = 0.71$$

$$\frac{M_S}{\frac{w\ L^2}{24}} = \frac{2\ (3 - 1.5\ \gamma)}{2 + \gamma} = \frac{2\ (3 - 1.5\ x\ 0.63)}{2 + 0.63} = 1.57$$

$\delta m_r = 1 / 1.57 = 0.64$

Required moment redistribution 'Rm_r' = $1 - \delta m_r = 0.36$

ii) <u>$L = 18.25\ h = 18.25\ x\ 0.4\ = 7.3$ m, $I = 0.3\ x\ 0.4^3/12 = 0.0016$ m^4 :</u>

$$\gamma = \frac{1}{1 + \frac{3\ E_c\ 0.5\ I_I}{S_y\ L}} = \frac{1}{1 + \frac{3\ x\ 36.16E6\ x\ 0.5\ x\ 0.0016}{30160\ x\ 7.3}} = \frac{1}{1+0.39} = 0.72$$

$$\frac{M_E}{\frac{w\ L^2}{12}} = \frac{3\ \gamma}{2+\gamma} = \frac{3\ x\ 0.72}{2+0.72} = 0.79$$

$$\frac{M_S}{\frac{w\ L^2}{24}} = \frac{2\ (3 - 1.5\ \gamma)}{2 + \gamma} = \frac{2\ (3 - 1.5\ x\ 0.72)}{2 + 0.72} = 1.42$$

$\delta m_r = 1 / 1.42 = 0.71$

$Rm_r = 1 - \delta m_r = 0.29$

I3 Specimen GR3

Table I.2 Specimen GR3 details

Beam width, b (mm)	300	
Beam depth, h (mm)	300	
Beam effective depth, d (mm)	350	
Main steel area at mid-span, A_s	2H20	2x314=628mm^2
$\rho = A_s / (b \cdot d)$	0.006	
f_{cu} of concrete (N/mm^2)	82.8	
f_c of concrete (N/mm^2)	67.8	
E_c of concrete (N/mm^2)	39070	
f_y of H20 (N/mm^2) - main beam bottom bars	532.3	Type B
E_s of H20 (N/mm^2) - main beam bottom bars	200500	

Moment Capacity and x_u/d at mid span

$F_t = f_y \cdot A_s = 532.3 \text{ N/mm}^2 \times 2 \times 314 \text{ mm}^2$

$F_t = 334\,284 \text{ N}$

$f_{cd} = 0.85 \cdot f_c = 0.85 \times 67.8 = 57.63 \text{ N/mm}^2$

$F_c = F_t = 334\,284 \text{ N}$

$F_c = 0.8\, x_u \cdot f_{cd} \cdot b$

$x_u = F_c / (0.8 \cdot f_{cd} \cdot b) = 334\,284 / (0.8 \times 57.63 \times 300) = 24.17 \text{ mm}$

$x_u / d = 24.17 / 350 = 0.069$

$Z = d - 0.4\, x_u = 350 - 0.4 \times 24.17 = 340.33 \text{ mm}$

$M_u = F_s \cdot Z = 334\,284 \times 340.33 / 1000\,000 = 113.8 \text{ kNm}$

Permissible moment redistribution

Concrete : $f_c = 67.8 \text{ N/mm}^2$

Steel bars : Type B , $f_y = 532.3 \text{ N/mm}^2$

$\delta m \geq k_3 + k_4\ x_u/d$; $\delta \geq 0.7$

$k_3 = 0.54$

$k_4 = 1.25(0.6+0.0014/ \varepsilon_{cu2})$

$\varepsilon_{cu2} = 2.6 + 35\,((90 - f_c) / 100)^4$

$\varepsilon_{cu2} = 2.6 + 35\,((90 - 67.8) / 100)^4 = 2.69 ‰ = 0.00269$ (EC2, Table 3.1)

$k_4 = 1.25(0.6+0.0014/ 0.00269) = 1.40$

$\delta m \geq k_3 + k_4 \ x_u/d$

$\delta m \geq 0.54 + 1.4 \ x \ 0.069 = 0.64 < 0.7$; therefore $\delta m = 0.7$

$Rm_a = 0.3$

In GR3, $S_y = 106905$ kNm/rad, $E_c = 39.070$ E6 kN/m^2

i) <u>L = 12 h = 12 x 0.4 = 4.8 m, I = 0.3 x 0.43/12 = 0.0016 m4 :</u>

$$\gamma = \frac{1}{1+\frac{3 \ E_c \ 0.5 \ I_I}{y_y \ L}} = \frac{1}{1+\frac{3 \ x \ 39.070 E6 \ x \ 0.5 \ x \ 0.0016}{106\ 905 \ x \ 4.8}} = \frac{1}{1+0.18} = 0.85$$

$$\frac{M_E}{M_R} = \frac{3\gamma}{2+\gamma} = \frac{3 \ x \ 0.85}{2+ 0.85} = 0.89$$

$$\frac{M_S}{\frac{w \ L^2}{24}} = \frac{2 \ (3 - 1.5 \ \gamma)}{2 + \ \gamma} = \frac{2 \ (3 - 1.5 \ x \ 0.85)}{2 + \ 0.85} = 1.22$$

$\delta m_r = 1 / 1.22 = 0.82$

$Rm_r = 1 - \ \delta m_r = 0.18$

ii) <u>L = 18.25 h = 18.25 x 0.4 = 7.3 m, I = 0.3 x 0.43/12 = 0.0016 m4:</u>

$$\gamma = \frac{1}{1+\frac{3 \ E_c \ 0.5 \ I_I}{y_y \ L}} = \frac{1}{1+\frac{3 \ x \ 39.070 E6 \ x \ 0.5 \ x \ 0.0016}{106\ 905 \ x \ 7.3}} = \frac{1}{1+0.12} = 0.89$$

$$\frac{M_E}{\frac{w \ L^2}{12}} = \frac{3\gamma}{2+\gamma} = \frac{3 \ x \ 0.89}{2+ 0.89} = 0.93$$

$$\frac{M_S}{\frac{w \ L^2}{24}} = \frac{2 \ (3 - 1.5 \ \gamma)}{2 + \ \gamma} = \frac{2 \ (3 - 1.5 \ x \ 0.89)}{2 + \ 0.89} = 1.15$$

$\delta m_r = 1 / 1.15 = 0.87$

$Rm_r = 1 - \delta m_r = 0.13$

REFERENCES

ABNT 2005, *NBR 9062: Design and Execution of Precast Concrete (in Portuquese)*, Brazilian Association for Technical Standards (ABNT), Rio de Janeiro.

ACI 2008a, *Building Code Requirments for Reinforced Concrete, ACI 318-08*, American Concrete Institute, Detroit.

ACI 2008b, *Specification for Tolerances for Precast Concrete (Draft Version), ACI Innovation Task Group 7*.

AISC 2005, *Specification for Structural Steel Buildings*, Chicago, Illinois.

Al-Shaikh, A.H. and Al-Zaid, R.Z. 1993, 'Effect of Reinforcement Ratio on the Effective Moment of Inertia of Reinforced Concrete Beams', *ACI Structural Journal*, vol 90, no. 2, pp. 144-149.

Alva, G.M., Ferreira, M.A. and Eldebs, A.L. 2009, 'Partially Restrained Beam-Column Connections in Reinforced Concrete Structures', *IBRACON Structures and Materials Journal*, vol 2, no. 4, pp. 356-379.

Al-Zaid, R.Z., Al-Shaikh, A.H. and Abu-Hussein, M. 1991, 'Effect of Loading Type on the Effective Moment of Inertia of Reinforced Concrete Beams', *ACI Structural Journal*, vol 88, no. 2, pp. 184-190.

ANSYS 2004, *ANSYS Theory Reference, Release 9*, ANSYS, Inc., Canonsburg, Pennsylvania.

Baharuddin, A., Ghazali, R.A. and Zuhairi, A. 2008, 'Comparative Study of Monolithic and Precast Concrete Beam-to-Column Connections', *Malaysian Construction Research Journal*, vol 2, no. 1.

Barbosa, A.F. and Ribeiro, G.O. 1998, 'Analysis of Reinforced Concrete Structures Using ANSYS Nonlinear Concrete Model', *Computational mechanics-New trends and applications*, Barcelona.

Barboza, A. and EL Debs, M. 2006, 'Load-Bearing Capacity of Mortar Joints Between Precast Elements', *Magazine of Concrete Research*, vol 58, no. 9, pp. 589-599.

Bhatt, P. and Kirk, D.W. 1985, 'Tests on an Improved Beam-Column Connections for Precast Concrete', *ACI Structural Journal*, vol 82, no. 6, pp. 835-843.

Bjorhovde, R., Colson, A. and Brozzetti, J. 1990, 'Classification System for Beam-to-Column Connections', *Journal of Structural Engineering, ASCE*, vol 116, no. 11, pp. 3059-3077.

Brenes, F.J. 2005, 'Anchorage of Grouted Vertical Duct Connections for Precast Bent Caps', PhD Thesis, Department of Civil Engineering, University of Texas at Austin, Texas, USA.

BSi 1983, *BS 1881-121:Testing Concrete-Part 121: Method for Determination of Static Modulus of Elasticity in Compression*.

Catoia,B., Ferreira, M., Carvalho,R. and Catoia, T. 2008, 'Analysis of the Flexural Behaviour of Precast Prestressed Beams with Semi-Rigid Connections', *ACI Special Publication of V International ACI/CANMET Conference on High Performance Concrete Structures and Materials*, American Concrete Institute (ACI) / Brazilian Concrete Institute (IBRACON).

CEB-FIP 1993, *CEB-FIP Model Code 1990, Design Code*, Thomas Telford, London.

CEN 1997, *EN 933-1: Tests for Geometrical Properties of Aggregates, Part 1: Determination of Prticle Size Distribution — Sieving Method*, Brussels.

CEN 2000a, *EN 1097-6: Tests for Mechanical and Physical Properties of Aggregates — Part 6: Determination of Particle Density and Water Absorption*, Brussels.

CEN 2000b, *EN 12350-2: Testing Fresh Concrete, Part 2: Slump Test*, Brussels.

CEN 2002, *EN 1990, Eurocode 0 : Basis of Structural Design*, Brussels.

CEN 2004a, *EN 1991-1-1, Eurocode 1: Actions on Structures - Part 1-1: General Actions - Densities, Self-Weight, Imposed Loads for Buildings*, Brussels.

CEN 2004b, *EN 1992-1-1, Eurocode 2: Design of Concrete Structures- part 1-1: General Rules for buildings*, Brussels.

CEN 2005a, *EN 1991-1-4, Eurocode 1: Actions on Structures - Part 1-4 : General Actions - Wind Actions*, Brussels.

CEN 2005b, *EN 1993-1-8, Eurocode 3: Design of Steel Structures, Part 1-8 : Design of Joints*, Brussels.

CEN 2005c, *EN 10080: Steel for the Reinforcement of Concrete – Weldable Reinforcing Steel - General*, Brussels.

CEN 2009, *EN ISO 6892-1: Metallic materials- Tensile testing Part 1: Method of test at ambient temperature*, Brussels.

Chang, A. 2010, 'Modelling of Precast Concrete Beam to Column Connection subjected to Cyclic Loading', MEng Dissertation, Civil Engineering Department, University of Nottingham, Nottingham.

Comair, F. and Dardare, J. 1992, 'Model Testing of Precast Semi-Rigid Beam-Column Connection', *Proceedings of First State of the Art Workshop, COST C1.*, Strasbourg.

Darwin, D. and Zavaregh, S.S. 1996, 'Bond Strength of Grouted Reinforcing Bars', *ACI Structural Journal*, vol 93, no. 4 , pp. 586-495.

de Chefdbien, A. and Dardare, J. 1994, 'Experimental Investigation on Current Connections Between Precast Concrete Components', *Proceedings of the 2nd Workshop, COST C1, Semi-Rigid Behaviour of Civil Engineering Structural connections* , Prague.

Desayi, P. and Krishnan, S. 1964, 'Equation for the Stress-Strain Curve of Concrete', *Journal of the American Concrete Institute*, vol 61, pp. 345-350.

Dolan, C.W. and Pessiki, S.P. 1989, 'Model testing of precast concrete connections.', *PCI Journal*, vol 32, no. 2, pp. 62-74.

Dolan, C.W., Stanton, J.F. and Anderson, R.G. 1987, 'Moment Resistance Connections and Simple Connections.', *PCI Journal*, vol 32, no. 2, pp. 62-74.

Dragosavic, M. 1978, 'Load-Bearing Capacity of Joints Between precast Elements', *Proceedings of RILEM-CEB-CIB Symposium, Mechanical and Insulating Properties of Joint of Precast Reinforced Concrete Elements*, Athens.

Dulacska, H. 1972, 'Dowel Action of Reinforcement Craossing Crack in Concrete ', *Journal of the American Concrete Institute*, vol 69, pp. 754-757.

Elliott, K.S. 2002, *Precast Concrete Structures*, Elsevier Ltd, Great Britain.

Elliott, K.S., Davies, G., Ferreira, M.A., Gorgun, H. and Mahdi, A.A. 2003a, 'Can Precast Concrete Structures be Designed as Semi-Rigid Frames: Part 1 – The Experimental Evidence', *The Structural Engineer*, vol 81, no. 16, pp. 14-27.

Elliott, K.S., Davies, G., Ferreira, M.A., Gorgun,H. and Mahdi,A.A. 2003b, 'Can Precast Concrete Structures be Designed as Semi-Rigid frames: Part 2 – Analytical Equations and Column Effective Length Factors', *The Structural Engineer*, vol 81, no. 16, pp. 28-37.

Elliott, K.S., Davies, G., Gorgun, H., and Adlparvar, M.R 1998, 'The Stability of Precast Concrete Skeletal Structures', *PCI Journal*, pp. 42-60.

Ferreira, M.A, Elliott, K.S. and Hasan, S.A. 2010, 'Precast Concrete Framed Structures with Semi-Rigid Connections', State of Art Research Report, School of Civil Engineering, University of Nottingham, Nottingham.

Ferreira, M.A. 1999, 'Deformability of Beam-Column Connections in Precast Concrete Structures', PhD Thesis, School of Eng. of Sao Carlos, University of Sao Paulo, Sao Carlos, Brazil.

Ferreira, M.A. 2001, 'Analytical Design Procedure for Semi-Rigid Connections in Precast Concrete Structures', Research Report, School of Civil Engineering, University of Nottingham, Nottingham.

fib 2003, *Seismic Design of Precast Building Structures: State of Art Report*, International Federation for Structural Concrete, Lausanne.

fib 2008, *Structural connections for Precast Concrete Building*, Lausanne.

fib 2011, *Planning and Design, Handbook on Precast Building Structures (Draft Version), Commission on Prefabrication: Task Group TG 6.12*.

Ghali, A. 1993, 'Deflection of Reinforced Concrete Members: A Critical Review', *ACI Structural Journal*, vol 90, no. 4, pp. 364-373.

Ghosh, S.K, Nakaki, S.D. and Krishan, K. 1997, 'Precast Structures in Region of High Seismisity : 1997 UBC Design Provisions', *PCI Journal*, vol 42, no. 6, pp. 76-93.

Glanville, W. and Thomas, F. 1936, 'The Redistribution of Moments in Reinforced-Concrete Beams and Frames', *Journal of the ICE*, vol 3, no. 7, pp. 291-328.

Gorgun, H. 1997, 'Semi-Rigid Behaviour of Connections in Precast Concrete Structures.', PhD Thesis, Department of Civil Engineering, The University of Nottingham, Nottingham.

Hasan, S. A. 1994, 'Finite Element Analysis of Reinforced Concrete Deep Beams', MSc Thesis, Department of Civil Engineering, Salahadeen University, Erbil.

Hegger, J., Sherif, A. and Roeser, W. 2004, 'Nonlinear Finite Element Analysis of Reinforced Concrete Beam-Column Connections', *ACI Structural Journal*, vol 101, no. 59, pp. 604-614.

Huber, G., Kronenberger, H.J. and Weynand, K. 1998, 'Representation of Joints in the Analysis of Structural Systems', *Proceedings of International Conference, COST C1*, Liege, Belgium.

Hughes, S. R. and Crisp, B. C 2010, 'Structural precast Concrete in Melbourne, Australia', *3rd fib International Congress*, Washington.

Ibrahim, A.M. and Mubarak, H.M. 2009, 'Finite Element Modeling of Continuous Reinforced Concrete Beam with External Pre-stressed', *European Journal of Scientific Research*, vol 30, no. 1, pp. 177-186.

ICBO 1997, *Uniform Building Code, Vol. II: Structural Engineering Design Provisions*, International Conference of Building Officials, Whittier, California.

Kachlakev, D., Miller, T., Yim, S. and Chansawat, K. 2001, 'Finite Element Modelling of Reinforced Concrete Structures Strengthened with FRP Laminates.', Civil and Environmental Engineering Department, California Polytechnic State University, San Luis Obispo.

Kishi, N., Hasan, R., Chen, W.F and Goto, Y. 1997, 'Study of Eurocode 3 steel Connection Classification', *Engineering structures*, vol 19, no. 9, pp. 772-779.

Korkmaz, H.H, and Tankut, T. 2005, 'Performance of a Precast Concrete Beam-to-Column Connection Subject to Reversed Cyclic Loading', *Journal of Engineering Structures*, vol 27, pp. 1392-1407.

Kuttab, A. and Dougill, W. 1988, 'Grouted and Dowelled Jointed Precast Concrete Columns: Behaviour in Combined Bending and Compression', *Magazine of concrete research*, vol 40, no. 144, pp. 131-142.

Lindberg, R. Vinha, J. Myllyviita, S. and Hellman, H. 1992, 'Beam-to-Column Connections in Storey-Height Concrete Frame.', Report 57, Department of Civil Engineering, Tampere University of Technology, Tampere, Finland.

Loo, Y.C and Yao, B.Z 1995, 'Static and Repeated Load Tests on Precast Concrete Beam-to-Column Connections', *PCI Journal*, vol 40, no. 2, pp. 106-115.

Mahdi, A.A. 1992, 'Moment-rotation behaviour of connections in precast concrete structures', PhD Thesis, Department of Civil Engineering, University of Nottingham, Nottingham.

Mahmood, M.N. 2007, 'Nonlinear Analysis of Reinforced Concrete Beams Under Pure Torsion', *Journal of Applied Science*, vol 7, no. 22, pp. 3524-3529.

Mattock, A.H. 1959, 'Redistribution of Design Bending Moment in Reinforced Concrete Continuous Beams', *Proceedings, Institution of Civil Engineers* , vol 13, pp. 35-46.

Minnert, J. 1997, 'Tests for Determination of the Bearing Behaviour of Butt Jointed Precast HSC-Columns', Leipzig Annual Civil Engineering Report, No.2, University of Leipzig, Germany.

Monforton, G.R. and Wu,T.S. 1963, 'Matrix Analysis of Semi-Rigidly Connected Frames.', *Journal of the Structural Engineering, ASCE*, vol 89, no. 6, pp. 13-42.

Nethercot, D.A., Li, T.Q. and Ahmed, B. 1998, 'Unified Cassification System for Beam-to-Column Connections', *J. Construct. Steel Re.*, vol 45, no. 1, pp. 39-65.

PCI 1988, *Design and Typical Details of Connections for Precast and Prestressed Concrete, 2nd Edition*, Precast/Prestressed Concrete Institute, Chicago IL.

PCI 2004, *PCI Design Hand Book: Precast and Prestressed Concrete, 6th Edition*, Chicago,Illinois, IL, USA.

Perera, U. 2005, 'Seismic Performance of Concrete Beam-Slab-Column Systems Constructed with a Re-usable Sheet Metal Formwork', Master Thesis, The Department of Civil and Environmental Engineering, The University of Melbourne, Melbourne, Australia.

Raynor, D.J., Lehman, D.E and Stanton, J.F. 2002, 'Bond-Slip Response of Reinforcing Bars Grouted in Ducts.', *ACI Journal*, vol 99, no. 5, pp. 568-576.

Restrepo, J.I., Park, R. and Buchanan, A.H. 1995, 'Tests on Connections of EarthquakeResisting Precast Reinforced Concrete Perimeter Frame of Buildings', *PCI Journal*, vol 40, no. 3, pp. 40-61.

Saleh, H. 2000, 'Behaviour of Butt-Jointed Precast Columns.', Leipzig Annual Civil Engineering Report, No.5, University of Leipzig, Germany.

Santhakumar, R., Dhanaraj, R. and Chandrasekaran, E. 2007, 'Behaviour of Retrofitted Reinforced Concrete Beams Under Combined Bending and Torsion : A Numerical Study', *Electronic Journal of Structural Engineering*, vol 7.

Scott, R.H. and Whittle, R.T. 2005, 'Moment Redistribution Effects in Beams', *Magazine of Concrete Research*, vol 57, no. 1, p. 9–20.

Stanton, J. F., Anderson, R.G, Dolan, C.W. and McCleary, D.E. 1986, 'Moment Resistance Connections and Simple Connections.PCI Special Research Project 1/4', Precast/Prestressed Concrete Institute, Chicago,Illinois.

Tsoukantas, S.G. and Tassios, T.P 1989, 'Shear Resistance of Connections Between Reinforced Concrete Linear Precast Elements', *ACI Structural Journal*, vol 86, no. 3, pp. 242-249.

Vambersky, J.N.J.A. 1990, 'Mortar Joints Loaded in Compression', *Proceddings of the International Seminar: Prefabrication of Concrete Structures*, Delft. The Netherlands.

Willam,K.J., and Warnke, E.D. 1975, 'Constitutive Model for the Triaxial Behavior of Concrete', *Proceedings, International Association for Bridge and Structural Engineering*, vol 19, p. 174.

Wolanski, A.J. 2004, 'Flexural Behaviour of Reinforced and Prestressed Concrete Beams Using Finite Element Analysis', Master Thesis, Marquette University, Milwaukee, Wisconsin.

Zhang, Q. 2004, 'Finite Element Application to Slab-Column Connections Reinforced with Glass Fibre-Reinforced Polymers', Master Thesis, Faculty of Engineering, University of Newfoundland, St. John's, Canada.